DOCTORAL DISSERTATION
博士論文

Multiwavelength Signals From Pulsar-Driven Supernovae

パルサー駆動超新星からの多波長シグナル

A Dissertation Submitted for the Degree of
Doctor of Philosophy

December 2020
令和2年12月博士(理学)申請

Department of Physics
Graduate School of Science
University of Tokyo
東京大学大学院理学系研究科物理学専攻専攻

Conor Michael Bruce Omand
オマンド　コナー　マイケル　ブルース

Declaration of Authorship

I, Conor Michael Bruce Omand, declare that this thesis titled, "Multiwavelength Signals From Pulsar-Driven Supernovae" and the work presented in it are my own. I confirm that:

- This work was done wholly or mainly while in candidature for a research degree at this University.
- Where any part of this thesis has previously been submitted for a degree or any other qualification at this University or any other institution, this has been clearly stated.
- Where I have consulted the published work of others, this is always clearly attributed.
- Where I have quoted from the work of others, the source is always given. With the exception of such quotations, this thesis is entirely my own work.
- I have acknowledged all main sources of help.

Abstract

Today, large surveys detect thousands of supernovae a year, and our understanding of their causes, mechanisms, and aftermath is very thorough. However, there are several other transients, including Gamma-Ray Bursts (GRBs), Hypernovae (HNe), Super-Luminous Supernovae (SLSNe), and Fast Radio Bursts (FRBs), where the causes and mechanisms are less certain or even completely unknown.

The remnant of the deaths of stars in a certain mass range is a neutron star. These dense stars can be rapidly rotating and have extremely large magnetic fields, thus emitting radiation and particles while losing their rotational energy (spinning down). These pulsars can emit more energy than the supernova explosion over their spin-down timescale, which can be as short as a few minutes. Many models predict that spin-down from pulsars with different properties can power multiple kinds of transients.

In this thesis, we explore the pulsar-powered supernova model and try and predict broadband emission from the pulsar wind nebula (PWN). Quasi-thermal optical supernova emission can not differentiate between different central supernova engines, but this non-thermal PWN emission is unique to the pulsar engine. We are interested in the detectability of this emission.

First, we calculate the PWN emission from six bright newborn SLSN-I remnants and examine the constraints placed by radio and millimetre emission. We find that the Atacama Large Millimeter/submillimetre Array (ALMA) can detect the millimetre emission from most of them in a few years after the explosion, while the Jansky Very Large Array (VLA) can detect the radio emission from a few of them in a few decades.

Next, we present our VLA observations of ten older SLSNe-I at 3 GHz. No emission was detected from nine of the ten sources, but one SLSN-I, PTF10hgi, is detected in deep imaging. This detection, along with a recent 6 GHz detection of PTF10hgi supports the interpretation that this SLSN-I is powered by a young, fast-spinning ($\sim$ ms spin period) magnetar with $\sim 15\ M_\odot$ of partially ionized ejecta. These observations exclude slow-spinning pulsars and low-ejecta mass supernovae for about half of our sample.

We then present a larger, deeper sample of observations at both radio and submillimetre wavelengths. We use an MCMC method with a different magnetar model to fit optical light curves and a modified version of the previously introduced pulsar wind nebula model to calculate radio and millimeter light curves. No new sources are detected, but these observations exclude the model for seven sources and constrain ten others, although these exclusions are not certain due to model uncertainties and parameter degeneracies.

We also introduce an indirect detection method for a young PWN: reprocessed emission from dust grains. We investigate the effect of PWN on dust formation and evolution in the supernova ejecta. We find that a pulsar can either accelerate or delay dust formation, with timescales of a few months to over 15 years, and reduce the average size of dust by a factor of ~ 10 or more compared to the non-pulsar case. We also find that infrared dust emission may be detectable in typical superluminous supernovae out to $\sim$ 100-1000 Mpc in 2-5 years after the explosion.

Finally, we present an overview of future propects and directions to study to improve our understanding of pulsar-driven supernovae.

Acknowledgements

First and foremost, I would like to thank my supervisor, Naoki Yoshida, for his guidance during my entire masters and PhD program, particularly in making sure I always had the oppotunities I needed to thrive. Next, I would like to thank my mentor and closest collaborator, Kazumi Kashiyama, who has taught me almost everything I need to perform my current research and who is a constant source of information, encouragement, and assistance.

I want to thank all my other collaborators as well, which are listed at the beginning of each chapter, as well as everyone in UTAP and RESCEU for being a constant source of both help and entertainment for me, and for their willingness to make sure I don't miss out on anything due to my lack of Japanese skill. I also want to thank those other who I have discussed these or other projects with.

I need to thank a few previous mentors and supervisors who are responsible for where I am today. In chronological order, this includes my high school physics teacher Mark Sakakibara, who made physics fun and interesting and sparked my interest in the field; my first research supervisor, Sarah Burke, who took a chance on me as a young student and taught me a lot about performing research; Michael Balogh, who supervised my first successful research project and taught me how to write and publish papers; Petr Navrátil, who supervised another successful project and taught me how to perform large calculations; Seiji Miyashita, who supervised my internship at the University of Tokyo and strongly advocated for my return; and Jeremy Heyl, who supervised my honours thesis and subsequent internship and taught me a lot about high-energy physics, much of which I still use in my current research.

Finally, I want to thank my parents, Debbie and Michael, and brother, Travis, who've put up with me my whole life and who's support has allowed me to flourish.

This work has been supported by the Grant-in-aid for the Japan Society for the Promotion of Science (18J21778).

Contents

Chapter 1

Introduction

1.1 A Historical Overview

Astronomy is considered one of the oldest sciences, as many ancient civilizations collected astronomical information in a systematic manner through observation. This information was limited to the relative positions of celestial bodies, with subjects like the structure and chemical makeup of the planets and stars not being a consideration.

The beginning of transit astronomy may have been as early as 10 000 to 20 000 years ago. In 1977, an archeologist found carving left by ancient Native Americans in Bolivia. The carvings show two groups of small circles, which resemble stellar groupings in the constellations Vela and Carina, and two large circles: one may represent the star Capella, and the other is located near the position of the Vela Supernova Remnant. The archeologist suggested this may represent the supernova explosion as witnessed by the indigenous residents (Michanowsky 1977), although this interpretation is not widely accepted and has been criticized by the academic community (Hamacher 2014; Huygh 1981).

Another possible early record of a supernova could have been viewed by unknown Indian observers in 4500 ± 1000 BCE. A stone slab showing two bright objects in the sky above a hunter spearing an animal was unearthed in Burzahama, India, where the oldest settlements are about 6500 years old (Sharma 2000). Joglekar et al. (2011) searched supernova catalogs for a supernovae with brightness comparable to the moon at peak, as well as the correct position and age, and found that HB9 satisfies the criteria.

The first confirmed record of a supernova is from 185 CE, when Chinese astronomers recorded the appearance of a bright star in the sky and observed that it took about eight months to fade (Zhao et al. 2006). It sparkled like a star and did not move across the sky, like a comet would. SN 185 may have also have been recorded in Roman literature, but no records have survived (Stothers 1977). The gaseous shell RCW 86 is suspected as being the remnant of this event, as X-ray studies show a good match for the expected age (Vink et al. 2006).

Over the span of about 2000 years, Chinese astronomers recorded a total of twenty candidate supernovae, and some later explosions were also noted by Islamic, European, and possibly Indian and other observers (Chin & Huang 1994; Clark & Stephenson 1977; Stephenson & Clark 1976; Stephenson & Green 2003, 2005). Two of the most well known and brightest were SN 1006, which is the brightest observed stellar event in recorded history (reaching one quarter the brightness on the moon) and was recorded by astronomers in China, Egypt, Iraq, Italy, Japan and Switzerland, and may also have been noted in France, Syria, and North America (Murdin & Murdin 1985; Murdin & Murdin 2011; Winkler et al. 2003); and SN 1054, the precursor to the Crab Nebula, which had brightness comparable to Venus and was recorded by Arab, Chinese, and Japanese astronomers (Brecher et al. 1983).

Supernovae were originally thought to be something in the Earth's atmosphere, since the common belief in Europe before the 1700s was the Aristotelian idea that the world beyond the Moon and planets was immutable. Tycho Brahe noted that SN 1572 remained stationary from night to night - never changing its parallax - so it must lie far away. The modern word *nova* comes from the title of his book about these observations, *De nova et nullius aevi memoria prius visa stella* (Latin for "Concerning the new and previously unseen star") (Brahe 1573). Subsequent observations of SN 1604, the most recent supernova to be seen in the Milky Way, by Johannes Kepler led to Galileo also trying, in vain, to measure the parallax of the supernova, and then also arguing against the Aristotelian view of an immutable heavens (Kepler 1606).

The first spectroscopic observations of a nova were done in 1866 by William Huggins, when he discovered lines of hydrogen in the unusual spectrum of the recurrent nova T Coronae Borealis. He proposed that a cataclysmic explosion was the underlying mechanism (Huggins 1866). In 1885, a nova-like burst was discovered in the direction of the Andromeda Galaxy, and once astronomers measured distance to the Andromeda Galaxy they realized the event must have released a much greater amount of energy than was typical for a nova. In the 1930s, Walter Baade and Fritz Zwicky postulated that the energy for these events, which they called super-novae (the hyphen was dropped before the end of the decade), was by the gravitational collapse of ordinary stars into neutron stars (Baade & Zwicky 1934; Osterbrock 2001), which was also the first postuation of the existence of neutron stars (Baade & Zwicky 1934).

In 1938, Baade was the first to identify a nebula as a supernova remnant (SNR) by associating the Crab Nebula with the remains of SN 1054 (Baade 1938). He noted that the expansion velocity was far too high to be a planetary nebula. He also proposed using what would later be called Type Ia supernova as a distance indicator. Later work refined the process and allowed Type Ia supernovae to become a type of standard candle for measuring large distances across the cosmos (Branch & Tammann 1992; Colgate 1979; Hamuy et al. 1996, 1993; Phillips 1993; Sandage et al. 1992).

While the first computer-controlled search for supernovae was begun in the 1960s, which was able to discover 14 supernovae over a period of two years (Marschall 1988), this decade also marked the birth of neutron star astronomy. At first, they were thought to be too faint to be detectable and thus largely ignored by astronomers, but Franco Pacini pointed out that if neutron stars were spinning and had large magnetic fields, they would emit electromagnetic waves (Pacini 1967). The first neutron star to be detected was found by Antony Hewish and Samuel Okoye in 1965. They saw "an unusual source of high radio brightness temperature in the Crab Nebula" (Hewish & Okoye 1965), which turned out to be the Crab Pulsar (pulsar being short for "pulsating star"). In 1967, Iosif Shklovsky found evidence in X-ray and optical observations for a neutron star accreting matter from its companion in Scorpius X-1 (Shklovsky 1967), a system that was discovered five years earlier by a team led by Riccardo Giacconi (Giacconi et al. 1962). Later that year, Jocelyn Bell and Antony Hewish discovered regular radio pulses from four sources, which were later identified as pulsars (Gold 1968; Hewish et al. 1968; Pilkington et al. 1968). Hewish was awarded the Nobel Prize in 1974 for this discovery. To date, a large fraction of known neutron stars were discovered as pulsars emitting regular radio bursts (Rosswog & Brüggen 2007).

Since the 1960s, larger telescopes, more broadband sky coverage, and coordinated surveys have led to the discoveries of thousands of supernovae and neutron stars. The first discovery of X-ray pulsars was in 1971, when the *UHURU* satellite saw periodicity in the source Cen X-3 and Her X-1 (Schreier et al. 1972; Tananbaum et al. 1972). The first binary pulsar system was discovered in 1975 (Hulse & Taylor 1975), which provided an opportunity to measure the mass of a neutron star and test for the existence of gravitational radiation; mergers of a two similar systems (GW170817 and GW190425) were recently seen by the Laser Interferometer Gravitational-wave Observatory (LIGO) (Abbott et al. 2017b, 2020a,b), with one (GW170817) also being observed by various electromagnetic telescopes (Abbott et al. 2017a; Cowperthwaite et al. 2017; Soares-Santos et al. 2017; Tanaka et al. 2017; Utsumi et al. 2017). Observations of supernovae have started to see them at earlier times after the explosion, as SN 1987A was observed within hours of its start (McCray 1993) and SN 2008D and SN 2016gkg were caught on camera just as they were exploding (Bersten et al. 2018; Soderberg et al. 2008), allowing for early multiwavelength follow-up and characterization of the shock breakout emission (Colgate & McKee 1969; Falk 1978). Peculiar classes of supernovae, such as hypernovae and superluminous supernovae, were discovered, and supernovae have also been associated with gamma-ray bursts.

Thanks to current wide-field transient surveys, including the Palomar Transit Factory (PTF), La-Silla Quest Supernova Survey (LQSS), Dark Energy Survey (DES), and a survey with the upcoming Legacy Survey of Space and Time (LSST) at Vera. C Rubin Observatory, which will lead to the discovery of hundreds of thousands of supernovae every year (Ivezic et al. 2008; Skidmore et al. 2015); the newest and next generation telescopes across the electromagnetic spectrum, including the Thirty Meter Telescope (TMT), James Webb Space Telescope (JWST), Wide-Field Infrared Survey Telescope - Astrophysics Focused Telescope Assets (WFIRST-AFTA), Square Kilometer Array (SKA), next generation Very Large Array (ngVLA), and the Five-hundred-meter Aperture Spherical Telescope (FAST); and the birth of both neutrino and gravitational wave astronomy, and thus multi-messenger astronomy; the future of supernovae and neutron star astronomy seems like it can only get brighter from here.

1.2 Supernovae and Neutron Star Formation

In the initial burning stages of a star, the hydrogen in the core is burnt into helium; this is known as the main sequence phase. Once the central hydrogen is depleted, the star contracts and heats up until the central helium ignites. The hydrogen shell is also burned off, and for stars with mass $> 0.5 M_\odot$, the helium core ignites at $\sim 10^8$ K and produces carbon and oxygen, and smaller amounts of neon, magnesium, and silicon, via the triple-alpha process. Low mass stars do not burn further, as their self-gravity is not strong enough to further ignite carbon and oxygen via contraction. Instead, these stars eject their envelopes via thermal pulses caused by the temperature dependence of helium burning (Rosswog & Brüggen 2007). These envelopes are observable as planetary nebulae, and the remains of these stars are known as white dwarfs.

Stars more massive than $\sim 8 M_\odot$ can burn carbon at $> 6 \times 10^8$ K to produce mostly oxygen, neon, and magnesium; and stars more massive than $\sim 9 - 10 M_\odot$ can burn these into silicon, sulphur, calcium, argon, and finally iron, the strongest bound nuclei (Fewell 1995). Nuclear burning is only exothermic up to iron, and further burning would cost the system energy, so no further burning takes place. At this point, the star has a mostly iron core with a onion-esque structure comprised from shells of silicon, oxygen, carbon, helium, and hydrogen.

1.2.1 Core Collapse and Compact Object Formation

Once the iron core reaches the Chandrasekhar mass $1.44 (Y_e/0.5)^2\ M_\odot$, where Y_e is the number of leptons per baryon (Bethe et al. 1979), the electrons are ultrarelativistic and can not support the core against gravitational collapse, and so the iron core, no longer stabilized by electron degeneracy pressure, begins to contract (Chandrasekhar 1931, 1935; Lieb & Yau 1987). Electron capture

$$e^- + p^+ \rightarrow n + \nu_e. \tag{1.1}$$

in the iron core reduces the pressure, and the temperatures become high enough to photodisintegrate the star through reactions like (den Hartog 2008; Rosswog & Brüggen 2007)

$$\begin{aligned} {}^{56}_{26}\mathrm{Fe}^{26+} + \gamma &\rightarrow 13\,{}^{4}_{2}\mathrm{He}^{2+} + 4n, \qquad (1.2)\\ {}^{4}_{2}\mathrm{He}^{2+} + \gamma &\rightarrow 2p^+ + 2n. \qquad (1.3)\end{aligned}$$

The collapsing core has two parts: an inner core of $\sim 0.8\ M_\odot$ (cooresponding to the Chandrasekhar mass at the local Y_e (Goldreich & Weber 1980)), which collapses homologously ($v \propto r$), and an outer, supersonically infalling core. The collapsing core is completely decoupled from the rest of the star, and the outer mantle is not affected by the collapse. In the early stages of infall, neutrinos from various weak interactions can escape the star almost unhindered, but once the density reaches $\sim 10^{12}$ g cm^{-3} and the neutrino escape time becomes comparable to the infall time, the neutrinos are dragged along with the infalling core (Epstein et al. 1988; Haxton 1988; Hayakawa et al. 2006; Woosley et al. 1990; Woosley & Haxton 1988). Once this happens, neutrino and electron captures come to an equilibrium, and the reaction in Equation 1.1 becomes reversible.

Once the density becomes comparable to $\rho_{\mathrm{nuc}} \sim 2.6 \times 10^{14}$ g cm^{-3} and the nucleons are essentially touching, the short-range repulsive nuclear force begins to dominate and stiffens to material. The nearly-incompressable nuclear matter stops the collapse and makes the infalling material bounce back, which causes an outward-moving shock that triggers the supernova explosion.

The shock forms at 20-30 km and moves through several tenths of solar masses of infalling material, breaking up the iron nuclei into neutrons and protons. These interactions cause the shock to lose energy and stall around 10-20 ms after the bounce at a radius of 100-200 km, forming a quasi-stationary accretion shock. The mass enclosed by the shock keeps increasing as matter continues to fall in, but the shock stays at a constant radius.

The bulk of the gravitational energy from the collapse is converted into neutrinos, which diffuse out of the protoneutron star on a diffusion timescale $\tau_{\mathrm{diff}} \sim 5$ s with a typical luminosity of $\sim 6 \times 10^{52}$ erg s^{-1}. Most of the neutrinos leave the star and carry away energy, but a small fraction deposit their energy in the stellar material. This deposition could serve to re-accelerate the shock and drive the explosion - this mechanism is known as the delayed explosion mechanism. This scenario is far from certain and often fails when simulated (Buras et al. 2003, 2006; Janka et al. 2007; Liebendoerfer 2005), although state-of-the-art simulations can reliably produce supernovae (Nagakura et al. 2017; Pan et al. 2016; Powell & Müller 2020). Alternative hypotheses include the standing accretion shock instability (SASI), where perturbations to the accretion shock cause oscillations which destabilize it and cause re-acceleration (Abdikamalov et al. 2015; Blondin et al. 2003), and a mechanism where acoustic waves emitted by g-mode oscillations energize the stalled shock and eventually induce an explosion (Burrows et al. 2006a, 2007b; Harada et al. 2017).

As the shock wave breaks through the star, the inner regions are heated to high enough temperatures to synthesize further elements through nuclear fusion. Parts of the silicon shell are burnt into iron-peak nuclei, parts of the oxygen shell into intermediate mass nuclei, and some carbon into oxygen. Radioactive isotopes such as ^{56}Ni and ^{57}Ni, which help power the light curve peak, ^{56}Co, which helps power the $\sim$ 30-100 day light curve, and ^{44}Ti, which helps power the late-time light curve, are also produced.

Depending on whether the neutron-degeneracy pressure and short-range strong nuclear force can withstand the extreme gravity or not, a protoneutron star will either stabilize or the core will collapse into a black hole. If the neutron star is stable, the magnetic field from the original star will be strongly amplified during the collapse due to the rapid rotation of the new compact object (Ferrario et al. 2015; Mestel 1966; Spruit 2009; Zhou et al. 2019). There are two other mechanisms which may amplify the magnetic field of a newborn neutron star. The first is the convective dynamo, where convective motion of the conducting fluid through the magnetic field produces more field, which adds to the original field (Bonanno et al. 2005; Burrows & Lattimer 1986; Duncan & Thompson 1992; Obergaulinger et al. 2014; Thompson & Duncan 1993). The other is collective magnetism, where domains of the material in the neutron star undergo a ferromagnetic transition to the Pauli-prefered triplet state at high density (Brownell & Callaway 1969; Haensel & Bonazzola 1996; Kutschera & Wójcik 1989). It is unknown which of these mechanisms dominate, or if they coexist to some extent (Lyne et al. 2013).

1.2.2 Dynamics of Supernova Remnants

Supernovae inject stellar material into the interstellar medium (ISM), which strongly affects gas distribution within galaxies. They play large roles in the heating and chemical evolution of galaxies, and their shocks can cause gas clouds to collapse and form new stars. Although the supernova itself is short, the SNR can emit electromagnetic radiation for about 100 000 years. Also, since elements heavier than helium are synthesized in star and ejected during supernovae, some material used to form the next generation of stars and planets comes from SNRs.

A SN with typical energy $E_{\rm SN} \sim 10^{51}$ erg ejects matter with a velocity

$$E_{\rm SN} \sim \frac{1}{2} M_{\rm ej} v_{\rm ej}^2, \tag{1.4}$$

$$v_{\rm ej} \sim 10^4\ {\rm km/s} \left(\frac{E_{\rm SN}}{10^{51}\ {\rm erg}}\right)^{1/2} \left(\frac{M_{\rm ej}}{M_\odot}\right)^{-1/2}. \tag{1.5}$$

The expansion of the supernova can be divided into roughly four phases, which are each dominated by a different physical principle. At first, the stellar ejecta retains its initial velocity such that the radius of the blast wave is $v_{\rm ej} t$. As the blast wave sweeps up mass, energy conservation forces it to slow down. Generally, the blast wave has swept up $M_{\rm ej}$ during this time, and the radius is

$$r_1 \sim 2\ {\rm pc} \left(\frac{\rho_{\rm ISM}}{10^{-24}\ {\rm g\ cm^{-3}}}\right)^{-1/3} \left(\frac{M_{\rm ej}}{M_\odot}\right)^{1/3}, \tag{1.6}$$

which occurs at time

$$t_1 \sim \frac{r_1}{v_{\rm ej}} \sim 200\ {\rm yr} \left(\frac{E_{\rm SN}}{10^{51}\ {\rm erg}}\right)^{-1/2} \left(\frac{\rho_{\rm ISM}}{10^{-24}\ {\rm g\ cm^{-3}}}\right)^{-1/3} \left(\frac{M_{\rm ej}}{M_\odot}\right)^{5/6}. \tag{1.7}$$

In the second phase, since energy losses from radiation are still negligible, the ejecta expands adiabatically. The constant $E_{\rm SN}$ is proportional to $\rho_{\rm ISM} r^3 v^2$, and since $v = \dot{r}$, we can write

$$E_{\rm SN}/\rho_{\rm ISM} \propto r^3 \dot{r}^2, \tag{1.8}$$

which can be integrated to give

$$r \propto (E_{\rm SN}/\rho_{\rm ISM})^{1/5} t^{2/5}. \tag{1.9}$$

This phase is known as the Sedov phase (Sedov 1946). In this second phase, the ejecta is decelerating as it expands, and since material further out decelerates earlier, the material inside runs into the outer shells, which heats up the outer shell and can produce complex flow patterns (Rosswog & Brüggen 2007).

The shocked gas still has a very high temperature. In the strong shock limit, the ratio of temperatures behind and in front of the shock is (Rosswog & Brüggen 2007)

$$\frac{T_2}{T_1} = \frac{2\Gamma(\Gamma-1)\mathcal{M}_\infty^2}{(\Gamma+1)^2} = \frac{5}{16}\mathcal{M}_\infty^2, \tag{1.10}$$

where $\mathcal{M}_\infty$ is the Mach number of the shock with respect to the sound speed of the unshocked gas. The last quantity assumes the adiabatic exponent of the gas is $\Gamma = 5/3$.

The temperatures in this phase are roughly 10^6 K. When temperatures fall below 10^6 K, some ions start to recombine and form atoms. These atoms cool strongly due to line emission, and once the radiative losses affect the kinetic energy of the ejecta, the Sedov phase is over.

In the third phase, the outer shell cools so fast from line emission that it forms a cold, dense shell that is driven by the hotter interior. This shell propagates with constant radial momentum and piles up ambient material, giving this phase the name "snowplow phase". The constant momentum can be described by

$$\frac{d}{dt}[Mv] = \frac{d}{dt}\left[\left(\frac{4\pi}{3}\right)\rho r^3 \dot{r}\right] = 0. \tag{1.11}$$

If we set the initial conditions t_o, r_o, and v_o as when the thin shell first forms, then

$$\rho r^3 \dot{r} = \rho r_o^3 v_o, \tag{1.12}$$

which, when integrated, gives

$$r = \rho r_o \left(1 + \frac{4 v_o (t - t_o)}{r_o}\right)^{1/4}, \tag{1.13}$$

which has $r \propto t^{1/4}$ at late times. In this phase, the gas has temperatures around 10^4 K, emits strong line emission, and strongly radiates in the optical band.

The final stage of the SNR is when the ejecta merges with the ISM. This happens when the ejecta speed becomes comparable to the sound speed of the ISM, usually around 10^5 years after the supernova explosion. At this point, it contributes its remaining kinetic energy to the general turbulence of the ISM flow.

1.3 Neutron Star Overview

The inner structure of a neutron star (NS) is described by the relationship between density and pressure, which gives an insight into the internal composition of the NS; the relationship is usually known as an equation of state (EoS). It is known that NSs are comprised mostly of neutrons, but also contain protons and electrons near their surface. The EoS at the centre of NSs is still an open question in NS astrophysics, and there could possibly be more exotic states of matter, such as quark-gluon plasma or quark-degenerate matter, in their ultra-dense cores (Burgio et al. 2002; Haensel et al. 2007; Pons et al. 2013). A variety of NS EoSs predict very different neutron star mass-radius relations, which allows the EoS to be constrained by observational studies. Different EoSs also predict different tidal deformabilities, which parameterize how much a neutron star can be stretched by the tidal forces from nearby compact objects, and can be tested observationally by the gravitational wave and electromagnetic signals from neutron star mergers (Choi et al. 2019; Fasano et al. 2019; Kiuchi et al. 2019; Raithel 2019).

The first NS EoS was worked out by J. Robert Oppenheimer and George Volkoff in 1939 (Oppenheimer & Volkoff 1939), using the work of Richard Chace Tolman (Tolman 1939). They assumed the neutrons formed a cold degenerate Fermi gas, and obtained a maximum NS mass of 0.7 $M_{\odot}$ (where $M_{\odot}$ = 1.98892 × 10^{33} g is the mass of the Sun) (Oppenheimer & Volkoff 1939). Recent work, which takes the strong nuclear interaction into account, leads to limiting masses between 2.0 and 3.0 $M_{\odot}$ (Bombaci 1996; Chamel et al. 2013; Kalogera & Baym 1996). This limit, now known as the Tolman-Oppenheimer-Volkoff (TOV) limit, is uncertain because the equations of state of extremely dense matter are not well known. An empirical lower bound for the maximum mass is set by the most massive known neutron star, PSR J0348+0432, at $2.14^{+0.10}_{-0.09}$ $M_{\odot}$ (Cromartie et al. 2020); this value is extremely close to theoretical values found by studying GW170817 (Margalit & Metzger 2017, 2019; Rezzolla et al. 2018), although more NS-NS mergers with electromagnetic couterparts will need to be found to further constrain this value. Reviews by Lattimer & Prakash (2007) and Weber et al. (2007) give insight into the difficulties in the quest for the EoS.

In this thesis, unless otherwise specified, we use a canonical NS with mass $M_{\rm NS}$ = 1.4 $M_{\odot}$ and radius $R = 1.2 \times 10^6$ cm = 12 km. The moment of inertia $I = kMR \sim 10^{45}$ g cm^2 is often used, and our value for k is 0.35, giving an overall value of $I = 1.4 \times 10^{45}$ g cm^2. Most pulsars have periods of 0.1 - 1 s, but some have periods as high as 10 s or as low as 1.4 ms (den Hartog 2008; Hessels et al. 2006; Manchester et al. 2005; Olausen & Kaspi 2014). The most rapidly rotating neutron stars have surface speeds of around 10% the speed of light.

There are three main subtypes of pulsars: rotation-powered pulsars, where the dipole radiation is powered by loss of rotational kinetic energy in star, causing its rotation to slow down (Rosswog & Brüggen 2007; Shapiro & Teukolsky 1983); accretion-powered pulsars, where gravitational potential energy of accreted matter powers the radiation (Zeilik & van Panhuys Smith 1987); and magnetars, where the radiation is powered by the decay of an extremely strong magnetic field (Brownlee 2003; Duncan & Thompson 1992; Heyl & Kulkarni 1998; Norris et al. 1991; Thompson & Duncan 1993; Thompson et al. 2002).

Another type of neutron star is a central compact object (CCO): these thermal X-ray sources are usually found at the geometric centre of supernova remnants and do not emit any non-thermal counterpart (De Luca 2017). Most sources do not exhibit pulsations, although weak pulsations have been found in three sources (Gotthelf & Halpern 2009; Gotthelf et al. 2005; Zavlin et al. 2000). The leading scenario for the formation of these sources is the buried field scenario, where fallback accretion of supernova ejecta onto a newly formed pulsar can bury the magnetic field of the pulsar (Benli & Ertan 2018; Shigeyama & Kashiyama 2018; Torres-Forné et al. 2016), leading to the only emission coming from thermal energy via the diffusion of trapped magnetic field. This state may be temporary, as CCOs may evolve back into pulsars at later times (Bernal et al. 2010; Muslimov & Page 1995), but this has yet to be confirmed.

1.3.1 Pulsar Spin-Down Emission

Pulsars have a dipolar magnetic field and rotate with periods between 1 ms and 10 s. Pulsars that do not accete gradually slow down, losing rotational kinetic energy; most of this energy is eventually emitted as energetic particles (called the pulsar wind) and high-energy radiation (den Hartog 2008), but there is also a pulsating radio signal from which pulsars, short for "pulsating stars", get their name. The dipole model (Ostriker & Gunn 1969; Pacini 1967, 1968) was the first model for examining the emission from pulsars, and still widely remains in use today.

The rotational kinetic energy of a NS with period P, angular frequency Ω, and moment of inertia I is

$$E = \frac{1}{2} I \Omega^2 \approx 2.76 \times 10^{52} \left(\frac{P}{1 \text{ ms}} \right)^{-2} \text{ erg.} \tag{1.14}$$

The kinetic energy loss from a NS with period derivative $\dot{P}$ yields the maximum possible spin-down luminosity of the pulsar

$$\dot{E} = -\frac{d}{dt} \frac{1}{2} I \Omega^2 = -I \Omega \dot{\Omega} = I \frac{2\pi}{P} \frac{2\pi \dot{P}}{P^2} = 4\pi^2 I \frac{\dot{P}}{P^3} \approx 5.54 \times 10^{46} \frac{\dot{P}}{P^3} \text{ erg s}^{-1}. \tag{1.15}$$

Independent of the internal field geometry, a pure magnetic dipole field at the magnetic pole of the star, B_{dip}, is related to the magnetic dipole moment $\mathbf{m}$ by

$$|\mathbf{m}| = \frac{B_{\text{dip}} R^3}{2}. \tag{1.16}$$

This configuration has a time-varying dipole moment as seen from infinity, and so radiates energy with power

$$\dot{E} = -\frac{2}{3c^3} |\ddot{\mathbf{m}}|^2. \tag{1.17}$$

Using

$$\mathbf{m} = \frac{B_{\text{dip}} R^3}{2} (\mathbf{e}_{\parallel} \cos\alpha + \mathbf{e}_{\perp} \sin\alpha \cos\Omega t + \mathbf{e}'_{\perp} \sin\alpha \sin\Omega t), \tag{1.18}$$

where $\mathbf{e}_{\parallel}$ is a unit vector parallel to the rotation axis, $\mathbf{e}_{\perp}$ and $\mathbf{e}'_{\perp}$ are fixed mutually orthogonal unit vectors perpendicular to $\mathbf{e}_{\parallel}$, and α is the angle between the rotation axis and the magnetic polar axis. Substituting this into Equation 1.17 gives

$$\dot{E} = -\frac{B_{\text{dip}}^2 R^6 \Omega^4 \sin^2\alpha}{6c^3}, \tag{1.19}$$

in which the radiation is emitted at frequency Ω.

If one assumes that the pulsar spin-down is caused by the torque of the magnetic field with its surroundings and that the emission process is completely dipole radiation, the characteristic surface magnetic field (at the poles) can be inferred by equating Equation 1.15 with Equation 1.19, giving

$$B_{\rm dip} = \sqrt{\frac{3Ic^3}{2\pi^2 R^6 \sin^2\alpha} P\dot{P}} = 4.39 \times 10^{19}\ {\rm G}\ \sqrt{P\dot{P}}, \tag{1.20}$$

Since α is generally not known, $\sin\alpha = 1$ is sometimes assumed (we take that assumption here).

The spin-down timescale $t_{\rm SD}$ of a pulsar is the ratio of the initial rotation energy and the initial spin-down luminosity

$$t_{\rm SD} = \frac{E_{\rm rot}}{\dot{E}} = \frac{\frac{1}{2}I\Omega^2}{I\Omega\dot{\Omega}} = \frac{\Omega}{2\dot{\Omega}} = \frac{2P}{\dot{P}}, \tag{1.21}$$

A NS will lose much of its energy within $t_{\rm SD}$, and the early emission will be extremely luminous. Substituting $B_{\rm dip}$ in here gives

$$t_{\rm SD} = \frac{3Ic^3}{4\pi^2 R^6}\left(\frac{P}{B_{\rm dip}}\right)^2 = 28\ {\rm days}\left(\frac{P}{1\ {\rm ms}}\right)^2\left(\frac{B_{\rm dip}}{10^{13}\ {\rm G}}\right)^{-2} \tag{1.22}$$

which allows one to calculate $t_{\rm SD}$ from the initial period and magnetic field - common parameters in models. The energy lost during the initial spin-down $E_{\rm SD} = E_{\rm rot}$ from Equation 1.14, which does not depend on period derivative or magnetic field.

This dipole model is assumed to be in vacuum, but Goldreich & Julian (1969) showed by contradiction that a pulsar can not exist in a vacuum, since a rotating magnetic dipole surrounded by a vacuum will induce a Lorentz force parallel to the magnetic field. For pulsars, this force will exceed the gravitational force by orders of magnitude, and charged particles will be forced from the surface into the magnetosphere. The particles will co-rotate with the neutron star within the light cylinder.

Radiation can be created at different sites around the pulsar. Popular models are the slot-gap model (Arons 1983; Muslimov & Harding 2003), outer-gap model (Cheng et al. 1986a; Hirotani 2006; Romani 1996), and polar-cap models which include the vacuum-gap model (Ruderman & Sutherland 1975; Usov & Melrose 1995) and the space-charge limited-flow gap model (Harding & Muslimov 1998; Usov & Melrose 1995). They are named after the sites where particle acceleration can be efficient due to an electric field parallel to the magnetic field. Mechanisms like curvature radiation, synchrotron radiation or inverse Compton scattering may play a role in creating the observed non-thermal emission ranging from radio to the gamma-ray bands (den Hartog 2008).

1.3.2 Pulsar Wind Nebulae (PWNe)

Although almost all of the spin-down energy is removed from the neutrino star via a Poynting flux dominated wind, most of that energy is eventually converted into the emission of energetic particles (electron and positrons), known as a pulsar wind. If this magnetized wind is confined by an SNR or the interstellar medium, a wind termination shock can form at the boundary, which accelerates the particles to ultrarelativistic energies, where they radiate synchrotron emission across the electromagnetic spectrum (Pacini & Salvati 1973; Rees & Gunn 1974). This confined pulsar wind is known as a pulsar wind nebula (PWN). Detailed theoretical evolution has been studied by Blondin et al. (2001); Bucciantini et al. (2003); Chevalier (1998); Reynolds & Chevalier (1984); and van der Swaluw et al. (2004).

The basic picture for the formation of pulsar winds is that a charge-filled magnetosphere surrounds the pulsar, and that particle acceleration occurs in charge-separated gaps either near the pulsar polar caps or in outer regions that extend to the light cylinder (where $R_{\mathrm{LC}} = c/\Omega$). The maximum voltage generated by the rotating magnetic field in the case where the magnetic and spin axes are co-aligned is (Goldreich & Julian 1969)

$$\Delta\Phi = \frac{B_{\mathrm{dip}}\Omega^2 R_{\mathrm{NS}}^3}{2c} \approx 10^{22}\ \mathrm{V} \left(\frac{B_{\mathrm{dip}}}{10^{13}\ \mathrm{G}}\right) \left(\frac{R_{\mathrm{NS}}}{12\ \mathrm{km}}\right) \left(\frac{P}{1\ \mathrm{s}}\right) \tag{1.23}$$

Although this current is considerably modified in subsequent models, it provides the basis for our understanding of the pulsar wind.

In almost all models, the wind leaving the pulsar magnetosphere is dominated by the Poynting flux, $F_{E\times B}$, with the particle energy flux, F_{particle}, being much smaller. The magnetization parameter, σ_B, is

$$\sigma_B = \frac{F_{E\times B}}{F_{\mathrm{particle}}} = \frac{B^2}{4\pi\rho\gamma c^2} \tag{1.24}$$

where B, ρ, and γ are the magnetic field, mass density of particles, and Lorentz factor, respectively, in the wind. Typically, wind leaving the magnetosphere has $\sigma_B > 10^4$, however, models for the structure and spectrum of the Crab Nebula (Kennel & Coroniti 1984; Rees & Gunn 1974) require $\sigma_B \sim 10^{-3}$ just behind the termination shock. The process that dissipates the magnetic energy and transfers it to particles is still unknown, and this question is commonly known as the "sigma problem" (Arons 2002; Kirk & Skjaeraasen 2004; Tanaka 2017). Two possible mechanisms are magnetic reconnection in the current sheet generated by a striped wind (Kirk & Skjæraasen 2003; Lyubarsky & Kirk 2001; Lyubarsky 2003; Sironi & Spitkovsky 2011) and a kink instability in the field (Begelman 1998; Porth et al. 2013).

When the pulsar-driven wind decelerates from expanding into the cold, slowly expanding SN ejecta, there is a wind termination shock produced, which accelerates electron/positron pairs to ultrarelativistic energies. As they move through the wound-up magnetic field of the PWN, they produce broadband synchrotron radiation. For a power-law electron spectrum, the constant injection of particles and a finite synchrotron-emitting lifetime lead to a spectral break at a frequency (Ginzburg & Syrovatskii 1965)

$$\nu_b = 10^{16}\ \mathrm{GHz} \left(\frac{B}{10^{-6}\ \mathrm{G}}\right)^{-3} \left(\frac{t}{10\ \mathrm{yr}}\right)^{-2} \tag{1.25}$$

which results in the size of the PWN decreasing with increasing frequency. The particle injection must be greater than $10^{40}\ \mathrm{s}^{-1}$ (Slane 2017), which is difficult to obtain from pair creation within pulsar magnetospheres (Timokhin & Harding 2015), suggesting that relic electrons created early in the PWN formation might be required (Atoyan & Aharonian 1996).

The highly relativistic magnetized pulsar wind inflates a bubble confined by the SN ejecta. The wind termination shock is formed at R_w, where the wind is decelerated by the slow, cold SN ejecta and the ram pressure of the wind is balanced by the internal pressure of the PWN:

$$R_w = \sqrt{\dot{E}/4\pi\omega c\mathcal{P}_{\rm PWN}} \tag{1.26}$$

where ω is the equivalent filling factor for an isotropic wind, and $\mathcal{P}_{\rm PWN}$ is the total pressure in the shocked nebular interior. Upstream of this shock, the particles flow relativistically along with the frozen-in magnetic field instead of radiating. At the shock, particles are thermalized and re-accelerated, producing synchrotron radiation (Equation 1.25) in the downstream flow (Gaensler & Slane 2006).

Particles accelerated at the wind termination shock form a toroidal structure, although some of the flow is collimated along the rotation axis and can possibly contribute to jet-like structure formation (Bogovalov et al. 2005) - both of these structures generate synchrotron emission that can usually be seen in X-ray, but also sometimes in optical (Hester et al. 1995). The emission pattern from jets or ring-like structures and the large scale geometry of the PWN provide an indication of the pulsar's orientation. The emission structures in the post-shock and jet regions provide direct insight on particle acceleration, magnetic collimation and the magnetization properties of the PWN wind (Gaensler & Slane 2006).

Since pulsars are formed with a random space velocity, due to asymmetry in the SN explosion, with typical magnitude 400-500 km s^{-1} (although sometimes reaching 1500 km s^{-1} (Arzoumanian et al. 2002)), while the SN blast wave first moves outward at a speed $> (5-10) \times 10^3$ km s^{-1}, the pulsar is located near the SNR's center at early times. The pulsar wind has extremely high pressure with respect to the SN ejecta, so the PWN expands rapidly, moving supersonically and driving the PWN forward shock into the ejecta (Gaensler & Slane 2006).

In the spherically symmetric case, the PWN evolves as (Chevalier 1977; Gelfand et al. 2009)

$$\begin{aligned} R_{\rm PWN} &\approx 1.5 \dot{E}_o^{1/5} E_{\rm SN}^{3/10} M_{\rm ej}^{-1/2} t^{6/5}, \qquad (1.27)\\ &\approx 4.4 \times 10^{-3}\ \mathrm{pc} \left(\frac{\dot{E}_o}{10^{38}\ \mathrm{erg\ s^{-1}}}\right)^{1/5} \left(\frac{E_{\rm SN}}{10^{51}\ \mathrm{erg}}\right)^{3/10} \left(\frac{M_{\rm ej}}{10\ \mathrm{M}_\odot}\right)^{-1/2} \left(\frac{t}{10\ \mathrm{yr}}\right)^{6/5} \qquad (1.28) \end{aligned}$$

where $R_{\rm PWN}$ is the radius of the PWN forward shock at time t, $\dot{E}_o$ is the spin-down luminosity at t = 0, and $E_{\rm SN}$ and $M_{\rm ej}$ are the kinetic energy and ejected mass, respectively, of the SN.

Since the PWN expansion velocity is steadily increasing, the PWN remains centered on the pulsar, and we expect to see a rapidly expanding SNR with a reasonably symmetric PWN near its center and a young pulsar near the center of the PWN. An example of this is pulsar J1833-1034, which powers the bright X-ray and radio PWN that lies at the center of SNR G21.5-0.9, which is estimated to be $\sim$ 1000 years old (Camilo et al. 2006; Gupta et al. 2005; Matheson & Safi-Harb 2010).

The PWN is often elongated along the pulsar spin axis due to the higher equatorial pressure associated with the toroidal magnetic field (Begelman & Li 1992; Lyubarsky 2002; van der Swaluw 2003). As the PWN expands, Rayleigh-Taylor instabilities form due to the fast-moving relativistic fluid accelerating the slower SN ejecta, producing dense, finger-like filamentary structures.

As the SN evolves into the Sedov-Taylor phase, the total energy becomes conserved as the ejecta cools adiabatically and is partitioned almost equally between kinetic and thermal contributions (Truelove & McKee 1999). The interaction between the SNR and surrounding medium is now more complicated, with a SN forward shock which compresses and heats ambient gas, and a reverse shock that decelerates the ejecta. The two shocks are separated by a contact discontinuity where instabilities can form. The reverse shock initially propagates outward behind the SN forward shock, but eventually begins to move inward.

In the absence of a pulsar and PWN, the reverse shock reaches the SNR center at (Reynolds & Chevalier 1984)

$$t_{\rm RS} = 7\ {\rm kyr}\ \left(\frac{M_{\rm ej}}{10\ {\rm M}_\odot}\right)^{5/6} \left(\frac{E_{\rm SN}}{10^{51}\ {\rm erg}}\right)^{-1/2} \left(\frac{n_o}{1\ {\rm cm}^{-3}}\right)^{-1/3} \tag{1.29}$$

where n_o is the number density of the ambient gas, which is assumed to be constant. At this point, the interior of the SNR is filled entirely with shock-heated ejecta and can be described by a small set of simple self-similar equations (Cox 1972).

In the presence of a pulsar and PWN, the inwardly-propagating SN reverse shock collides with the outwardly-moving PWN forward shock after a time $t_{\rm coll} < t_{\rm RS}$, typically a few thousand years (Blondin et al. 2001; van der Swaluw et al. 2001). Even in the simplest case, with a stationary pulsar, isotropic wind, and spherical SNR, the evolution is complicated. The reverse shock compresses the PWN by a large factor, increasing the magnetic pressure inside the PWN and causing the PWN to expand again. The sudden magnetic field increase during compression burns off the highest energy electrons (Blondin et al. 2001; Bucciantini et al. 2003; Reynolds & Chevalier 1984), and the alternation of compression due to ram pressure from the shocked ejecta and expansion due to the magnetic pressure inside the PWN cause the nebula to reverberate on a timescale of a few thousand years. The compression of the PWN produces Rayleigh-Taylor instabilities, which can produce a chaotic, filamentary structure (Blondin et al. 2001; Chevalier 1998).

At later times, the motion of the pulsar carries it away from the SNR center and even outside the PWN. This leads at first to a complicated three-dimensional interaction, causing large asymmetries and distortions in the shape of the PWN (Chevalier 1998; van der Swaluw et al. 2004), then a new, smaller PWN around its current position (van der Swaluw et al. 2004). The motion of the pulsar eventually becomes supersonic, and drives a bow shock through the SNR interior (Chevalier 1998; Van Der Swaluw et al. 1998). The ram pressure from the pulsar motion confines the new PWN to within 1 pc, and the PWN no longer expands steadily with time.

Eventually the pulsar will spin down to the point where their energy output is insufficient to power an observable synchrotron nebula. At this stage, a pulsar is surrounded by a static or slowly expanding cavity of relativistic material with a radius $\ll$ 1 pc confined by the thermal pressure of the interstellar medium (Arons 1983; Blandford et al. 1973); deep searches have detected these pulsar bow shock nebulae at multiple wavelengths (e.g. Gaensler et al. 2004; Ng et al. 2010; Rangelov et al. 2016, 2017).

1.3.3 Magnetars

Most pulsars have a dipole field strength of $\sim 10^{12}$ G, but a small number of neutron stars have fields as high as $\sim 10^{15}$ G. These neutron stars usually spin very slowly (with periods longer than a second) and emit more luminously than the spin-down energy can provide. These neutron stars are thought to be powered by the decay of their extremely high magnetic fields - they have thus come to be known as magnetars [1].

Quantum electrodynamic effects can become important around and above (Duncan 2001)

$$B_{\text{crit}} = \frac{m_e^2 c^3}{e\hbar} = 4.413 \times 10^{13}\ \text{G}, \tag{1.30}$$

where the nonrelativistic Landau energy $\hbar eB/m_e c$ is equal to the electron rest energy $m_e c^2$ (den Hartog 2008; Landau 1957a,b; Thompson & Duncan 2001). Such effects include the vacuum becoming anisotropic and birefringent (den Hartog 2008; Mészáros & Ventura 1979), vacuum polarization (Mészáros & Ventura 1979; Pavlov & Shibanov 1979), magnetic lensing (den Hartog 2008), and photon splitting (Adler 1971; Harding et al. 1997). Atoms in magnetic fields of this strength are stretched into long, thin cylinders (Harding & Lai 2006; Lai 2001; Thirumalai & Heyl 2009).

Magnetars were historically found as two different types of objects: the Soft Gamma-Ray Repeaters (SGRs), which were first found due to their repeated bursts in the soft gamma-ray band, and Anomalous X-ray Pulsars (AXPs), which have a persistant X-ray flux higher than predicted by dipolar spin-down. These types of objects both have very long ($P \sim$ 5-12 s) rotation periods and spin down very rapidly ($\dot{P} \sim 10^{-10}$ s s^{-1}); these properties give very large magnetic fields (Equation 1.20) and find a natural interpretation within the magnetar model. The first detection of pulsations in the persistent/quiescent emission from SGR 1806-20 was made in 1998 (Kouveliotou et al. 1998), which included measurement of the period and period derivative. The persistent X-ray flux was more than two orders of magnitude higher than the available spin-down energy (Kouveliotou et al. 1998; Rosswog & Brüggen 2007) and the period and period derivative indicate a magnetic field of $\sim 8 \times 10^{14}$ G. Because these phenomena were predicted by the magnetar model (Thompson & Duncan 1995, 1996), this was when astronomers became convinced that SGRs are indeed magnetars (den Hartog 2008).

It is not currently known how such high magnetic fields are generated, but there are several possible mechanisms. The magnetohydrodynamic dynamo, and collective magnetism mechanisms from Section 1.2.1 can all generate magnetar fields, as well as the flux freezing or fossil field mechanism, where the magnetic field of the progenitor core is amplified by stellar collapse (Kasumov et al. 2008; Ruderman 1972). Other possibilities include differential rotation with a magnetic instability (Akiyama et al. 2003; Spruit 2002) and vector spin alignment in a pion-condensated quark matter core (Bhattacharya & Soni 2007). Luckily for us, although we are not yet sure which models for generation of magnetar strength fields is correct, most observational characteristics of magnetars can be explained without using any specific field origin model.

There are several possible mechanisms involved in transporting magnetic energy from the magnetar core to its surface: Ohmic dissipation, ambipolar diffusion, and Hall drift (Goldreich & Reisenegger 1992). The dissipation timescale for Ohmic decay in the core is too long to significantly contribute to energy transportation in magnetars. Ambipolar diffusion is capable of transporting energy from the core to lower crust, while Hall drift allows magnetic field to cascade into smaller scales, which enhances the local rate of Ohmic dissipation. The force due to the magnetic field,

---

[1] Sometimes rotation-powered pulsars with magnetar-strength fields are also referred to as magnetars, even though it is not strictly correct - I do this several times in this thesis.

affected by Hall drift, can rupture the magnetar crust and give rise to a glitch or flare (Goldreich & Reisenegger 1992; Pons & Geppert 2007).

Thompson et al. (2002) studied the effects of the internal twisted toroidal magnetic field on the external poloidal field, and find that the internal field is strong enough to twist the outer one. This twisting induces currents that produce both thermal and non-thermal persistent emission, and causes extra magnetospheric current to cross the light cylinder, which increases the spin-down torque of the neutron star. This is sufficient to power magnetars for several thousand years (Durant & van Kerkwijk 2006), and also explains why no older magnetars are discovered. The absence of this internal energy is thought to be why high magnetic-field radio pulsars do not show similar behaviour to magentars.

As of December 2020, there were 24 confirmed magnetars (12 Soft Gamma-ray Repeaters (SGRs) and 12 Anomalous X-ray Pulsars (AXPs)) and 6 candidates (4 SGRs and 2 AXPS) in existence[2] (Olausen & Kaspi 2014).

SGR Flares

The first detection of an SGR was a flare from SGR 1806-20 on January 7, 1979 (Aptekar et al. 2001; Laros et al. 1986; Mazets & Golenetskii 1981). On March 5, 1979, the first SGR hyperflare was detected from SGR 0526-66, which is located in the Large Magellanic Cloud (Cline et al. 1982; Mazets et al. 1979). The hyperflare started with an extremely bright initial spike followed by a three minute decaying tail (Cline 1980). The 8 second pulsations of the magnetar were clearly visible (Barat et al. 1983). The total energy emitted during the hyperflare was $\sim 5 \times 10^{44}$ erg (assuming isotropic emission) (den Hartog 2008). The same source was then observed to repeatedly emit smaller flares (Aptekar et al. 2001; Cline et al. 1982; Mazets & Golenetskii 1981; Usov 1996). SGR 1900+14 was discovered shortly afterwards when three flares were detected on March 24, 25, and 27, 1979 from the same location (Kouveliotou et al. 1993; Mazets et al. 1981). The detection of these flares were only a few years after the first extragalactic gamma-ray bursts were detected (den Hartog 2008; Klebesadel et al. 1973). SGR 0526-66, SGR 1900+14, and SGR 1806-20 all showed recurrent non-periodic flares over the next few years (Atteia et al. 1987; Golenetskii et al. 1984; Kouveliotou et al. 1987; Laros et al. 1987), which lead to the name Soft Gamma-ray Repeater.

There have been two more recent SGR hyperflares: one on August 27, 1998 from SGR 1900+14, which was similar to the first hyperflare from SGR 0526-66 (Feroci et al. 2001; Hurley et al. 1999), and one on December 27, 2004 from SGR 1806-20, which was more than two orders of magnitude larger than the previous two ($\sim 10^{47}$ erg) (Boggs et al. 2007; Borkowski et al. 2004; Götz et al. 2006; Palmer et al. 2005; Terasawa et al. 2005). The X-rays and gamma-rays from both of these hyperflares ionized the Earth's upper atmosphere and caused the earth's ionosphere to contract to the same extent as it would from sunlight. These contractions changed the way radio waves propagated off the ionosphere (Campbell et al. 2005; Inan et al. 1999, 2007; Mandea & Balasis 2006). Radio afterglows were also observed after both hyperflares (Cameron et al. 2005; Frail et al. 1999; Gaensler et al. 2005).

The small flares from SGRs show very irregular behavior. SGRs have short periods of bursting activity, where hundreds of bursts can de detected within several weeks, followed by years of inactivity (Aptekar et al. 2001; Göğüş et al. 2001; Woods et al. 1999). The energy distribution of these flares is a power-law ($dN/dE \propto E^{-5/3}$) (Cheng et al. 1996), much like the Gutenberg-Richter law for earthquakes (Gutenberg

---

[2] http://www.physics.mcgill.ca/ pulsar/magnetar/main.html

& Richter 1956). Other similarities exist between earthquakes, solar flares, and SGR flares; they all have comparable waiting times and none of them show a correlation between energy and waiting time (den Hartog 2008; Göğüş et al. 1999, 2000; Thompson & Duncan 2001).

Because of the similarity to earthquakes, a "magnetar-quake" is regarded as a plausible mechanism for producing flares and hyperflares (Pons & Geppert 2007; Thompson & Duncan 2001). An estimate of the magnetic field energy gives ($U_B V_{\rm NS} \sim 10^{48}$ erg, while the energy released in the SGR 1806-20 hyperflare was $\sim 10^{46}$ erg, so the energy released in the burst is only a fraction of the magnetic energy inside the star, and both theory and observations of magnetar giant flares indicate that the magnetic energy can be converted to high energy photon emission (Elenbaas et al. 2017; Thompson & Duncan 1995). The restructuring of the magnetic field that causes the initial spike also radiates a hot, optically thick, electron-positron pair-plasma fireball that is trapped near the magnetar by closed magnetic field loops. This fireball is forced to rotate with the star and slowly evaporates by leaking photons, which powers the decaying tail (Duncan 2004; Paczynski 1992; Rosswog & Brüggen 2007; Thompson & Duncan 2001).

While the pair fireball is likely to form in giant flares, it is still debated wheter it can form for the lesser, short bursts (Kaspi & Beloborodov 2017; Watts et al. 2010). This is partially because the emission region sizes inferred by observations are small enough (Göğüș et al. 2000) as to be indistinguishable from the inferred sizes of hot spots on the magnetar surface (Yamasaki et al. 2019). The fireball model tends to be in good agreement with soft X-ray emission at late times but underpredicts the hard X-ray spectrum (e.g. Israel et al. 2008; Olive et al. 2004). Periodic radio emission from the magnetar is also suppressed during these short bursts (Archibald et al. 2017; Yamasaki et al. 2019). Models including resonant cyclotron scattering, normally invoked to explain quiescent magetar emission (e.g. Baring & Harding 2007; Lyutikov & Gavriil 2006; Thompson et al. 2002), have recently been developed to try and resolve this discrepancy (Yamasaki et al. 2020b).

1.4 Possible Pulsar-Driven Transients

Although supernova astronomy is thousands of years old, the advances in mulit-wavelength (and multimessenger, with the detection of gravitational waves from LIGO and VIRGO, and neutrinos from IceCube Neutrino Observatory, Kamiokande, and Super Kamiokande) astronomy over the past 50 years have led to the discovery of many different high-energy transients, including Gamma-ray Bursts (GRBs) and Fast Radio Bursts (FRBs). Improvements in optical telescopes have also led to the discovery of more luminous and energetic subclasses of supernovae, such as Hypernovae (HNe) and Superluminous Supernovae (SLSNe). Scientists have long struggled to determine the energy sources and emission mechanisms for these transients, and even though models have been developed, there is still no clear evidence from observations to support them.

Many of these models involve the death of a massive star (Bisnovatyi-Kogan 1971; Kardashev 1964; Ostriker & Gunn 1971; Shklovskii 1973, 1976). The collapsar model, where a fast rotating star with a 5-15 $M_\odot$ core collapses into a black hole and the fall-back accretion onto the black hole produces relativistic jets (MacFadyen & Woosley 1999), is often used to explain HNe and GRBs (Fujimoto et al. 2008; MacFadyen et al. 2001). The pair-instability model, where pair production in stars with masses 130-250

$M_\odot$ temporarily reduces the internal pressure supporting the star against gravitational collapse and greatly accelerates nuclear burning, causing a runaway thermonuclear explosion that leaves no remnant (Fraley 1968; Kasen et al. 2011), is often used to explain SLSNe (Cooke et al. 2012; Gal-Yam et al. 2009). Also, a circumstellar shock between SN ejecta and dense nebular material or dust close to the star is thought to be the power source for hydrogen-rich SLSNe (Gal-Yam & Leonard 2009; Smith et al. 2008). I will be overviewing these models in more detail in Section 1.5.

However, a model that can explain a wide variety of transients is the pulsar-driven model (e.g., Dai et al. 2016b; Inserra et al. 2013; Metzger et al. 2015; Nicholl et al. 2014, 2016b; Pastorello et al. 2010; Quimby et al. 2011; Wang et al. 2015). In this model, the spin-down energy of a newborn pulsar is injected into the ejecta of a supernova; this energy is thermalized and re-emitted as quasi-thermal optical radiation. A sufficiently asymmetrical explosion can also lead to jets around the pulsar poles, which can either be absorbed by the ejecta or punch a hole right through it. The diversity of possible explosions in this model follows from the diversity of possible neutron stars and environments: there is a large possible range in possible spin periods and magnetic fields, there could be a binary companion or accretion disk, the envelope can vary vastly in mass and composition, and the pulsar could have a magnetar-like twisted poloidal magnetic field.

Although the pulsar-driven model can explain all these different transients, no observational finding has been able to conclusively validate the pulsar-driven scenario so far (Kashiyama et al. 2016). The quasi-thermal optical radiation produced in HNe and SLSNe can be explained by a number of different central engines. The question is, how can we discriminate newborn pulsar engines for each type of transient by using ongoing and upcoming multi-messenger observations (Kashiyama et al. 2016)?

Figure 1.1 shows a number of different transients that are thought to be powered by newborn or young pulsars, and the expected initial spin period and dipole magnetic field of the pulsar engine. We describe the different transients individually in the rest of the section.

1.4.1 Gamma-Ray Bursts (GRBs) and Hypernovae (HNe)

Gamma-ray bursts were discovered in 1967 by the Vela 3 and Vela 4 satellites, which were originally launched to detect nuclear weapons tests in space (Katz 2002; Schilling 2002). The operation of four satellites made it possible to localize the burst to a compact region of space. Vela 5 and Vela 6 were launched in 1969 and 1970 respectively, and the six satellites were able to detect and trace 16 GRBs in the next three years, leading up to the publication of the first GRB observations by Klebesadel et al. (1973).

By 1978, there were 11 satellites, together known as the Inter-Planetary Network (IPN), in orbit around the Earth, Venus, and the Sun, attempting to detect and localize GRBs. These satellites could pinpoint GRBs to within arcminutes, but this was not enough to detect a counterpart in any other wavelength band. Three gamma-ray satellites were launched in the 1990s and early 2000s: the Burst and Transient Source Explorer (BATSE) in 1991, BeppoSAX in 1996, and the High Energy Transient Explorer 2 (HETE2) in 2000 (The first HETE lost radio contact with the Earth after one day).

The launch of BATSE was able to show the isotropy of GRBs (Meegan et al. 1992), confirming them as extragalactic, as well as showing them belonging to two distinct catagories, short GRBs (SGRBs) with periods less than two seconds and long GRBs (LGRBs) with periods greater than two seconds (Kouveliotou et al. 1993). These catagories are broad with significant overlap, and other catagories, such as ultra-long GRBs (Boër et al. 2015; Levan et al. 2014; Virgili et al. 2013), intermediate GRBs

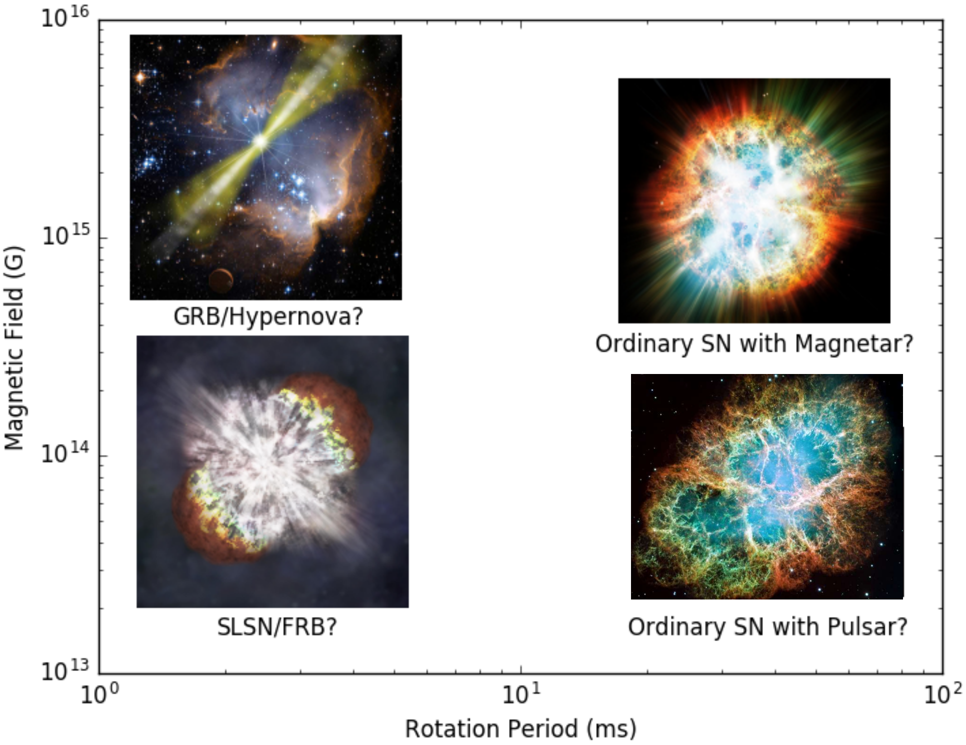

FIGURE 1.1: The diversity of transients caused by pulsar formation or young pulsars, and their approximate dependence on the initial spin period and dipole magnetic field of the pulsar. Pulsars with ms rotation periods and $\sim 10^{13}$ G magnetic fields are thought to power SLSNe during their formation, and power FRBs years or decades afters their birth (Connor et al. 2016; Cordes & Wasserman 2016; Lyubarsky 2014; Lyutikov et al. 2016; Popov & Postnov 2010a). Pulsars with ms rotation periods and $\sim 10^{15}$ G magnetic fields are thought to power HNe and GRBs during their formation (Burrows et al. 2007a; Troja et al. 2007; Zhang & Mészáros 2001). Pulsar with longer rotation periods are thought to power some ordinary Type Ibc SNe, with those with $\sim 10^{15}$ G magnetic fields having a central magnetar and those with smaller field having a central pulsar.

(Horváth et al. 2006; Mukherjee et al. 1998), and low-luminosity GRBs (LL-GRBs) (Virgili et al. 2009), have also been suggested based on theoretical and observational grounds (Chattopadhyay et al. 2007; Hakkila et al. 2003; Horváth 1998).

The best hope for the detection of a counterpart would rely on the localization of a GRB afterglow at lower wavelengths (Fishman & Meegan 1995; Paczynski & Rhoads 1993). In February 1997, BeppoSAX discovered GRB 970228, a gamma-ray burst with fading X-ray emission (Costa et al. 1997), and optical telescopes were able to detect a fading counterpart as well (van Paradijs et al. 1997). With a location identified, later deep observations were able to identify a distant, faint host galaxy for the GRB; the discovery of the distance scale and environments where GRBs occur revolutionized the study of GRBs (Frontera & Piro 1999).

Although radio emission from GRBs was originally thought to be too faint to be detectable (Meszaros & Rees 1993), the afterglow of GRB 970508 was detected by the Very Large Array (VLA) (Frail et al. 1997). This observation determined that the source of radio waves had expanded almost at the speed of light. There was also a very complete spectrum for this event, which allowed Wijers & Galama (1999) to determine the total energy of the burst (assuming isotropic emission) and particle density of the surrounding medium as 3×10^{52} erg and 30 000 particles per cubic meter respectivity. Although they did not consider their results to be incredibly reliable, they were able to show that it would be possible, in principle, to determine the physical characteristics of GRBs based on their spectra (Schilling 2002).

The next important GRB was GRB 971214, which would have emitted 3×10^{53} erg if isotropic. This amount of energy was higher than predicted by any model and would have been the most energetic explosion observed since the Big Bang, which earned it the nickname "Big Bang 2". After this, astronomers concluded that GRBs were highly focused explosions, with most of the explosion energy collimated into a narrow jet (Abdo et al. 2009; Rykoff et al. 2009). The approximate width of the jet can be estimated by observing the achromatic "jet breaks" in afterglow light curves, where the afterglow decays rapidly as the jet slows and can no longer beam its radiation effectively (Burrows et al. 2006b; Frail et al. 2001; Sari et al. 1999). This implies that for every burst observed on earth, several hundred occur which are not observed because their beams are not pointed towards earth (Schilling 2002).

GRBs were predicted to be associated with core-collapse supernovae (Paczynski 1997), and in 1998, the first supernova to be coincident with a gamma-ray burst, SN1998bw, was discovered (Galama et al. 1998; Vreeswijk et al. 2000), although it was never confirmed that the events were related. This type of supernova came to be known as a hypernova (HN), which has an explosion energy too high for only neutrino deposition, but is only slightly more luminous than a regular supernova (Iwamoto et al. 1998) - HNe tend to have extremely high kinetic energies. Hypernovae are typically broad-lined Type Ic supernovae (Woosley et al. 1999), although some hydrogen rich supernovae share similar energetic properties (Terreran et al. 2017). In 2003, the connection was confirmed with the detection of GRB 030329 in gamma-ray (Vanderspek et al. 2003), X-ray (Marshall & Swank 2003), optical (Peterson & Price 2003), and radio (Berger et al. 2003), and subsequent detection of SN2003dh in the afterglow (Matheson et al. 2003; Stanek et al. 2003), with spectral features similar to previous hypernovae (Iwamoto et al. 2000; Patat et al. 2001).

A natural prediction of jetted GRBs with more isotropic afterglows is that is that some afterglows should be observed that are not associated with prompt GRB emission; these are referred to as orphan afterglows (OAs) (Piran 2004). OAs could be used to infer the true rate of GRBs (Rhoads 1997; Totani & Panaitescu 2002), since they are less sensitive to relativistic beaming than the prompt emission, but afterglows decay quickly post-break and should be difficult to detect without a prompt trigger (Dalal et al. 2002; Nakar et al. 2002). X-ray flashes are thought to be an intermediate between classical hard GRBs and OAs (Granot et al. 2002; Urata et al. 2015; Yamazaki et al. 2002, 2003), but so far no optical OAs have been detected (Huang et al. 2020). Ofek (2017) identified a number of sources in the Very Large Array FIRST catalog that may be related to FRB persistent sources, and Law et al. (2018a) showed that one of these sources, FIRST J141918.9+394036 is a slowly declining radio transient wih properties similar to either a PWN or OA. Marcote et al. (2019) were able to resolve the source using Very Long Baseline Interferometry (VLBI) observations, and the source properties they found support the OA hypothesis.

Until recently, photons from GRBs above 100 GeV had never been observed, but observations of GRB 180720B and GRB 190114C with the Major Atmospheric Gamma Imaging Cherenkov (MAGIC) telescope and High Energy Stereoscopic System (HESS) array have reported detections of photons above that energy during the afterglow phase (Abdalla et al. 2019; MAGIC Collaboration et al. 2019a,b). HESS observations of GRB 180720B detected photons between 100 GeV and 1 TeV at 10-12 hours after the GRB burst trigger (Abdalla et al. 2019), while MAGIC observations of GRB 190114C detected photons above 1 TeV for 20 minutes after the GRB burst trigger (MAGIC Collaboration et al. 2019b). Observations of GRB 190114C were also conducted using 15 ground telescopes and 6 satellites during the first 10 days post-trigger, giving a frequency range of more than 17 orders of magnitude (MAGIC Collaboration et al. 2019a). The origin of this emission is well explained by synchrotron self-compton radiation (Derishev & Piran 2019; Fraija et al. 2019; Wang et al. 2019b), which produces the observed double peaked spectrum in GRB 190114C (Zhang 2019), and can lead to strong constraints on physical parameters associated with the afterglow emission (Derishev & Piran 2019).

The central engine for SGRBs has long been thought to be binary neutron star mergers (Blinnikov et al. 1984; Eichler et al. 1989; Nakar 2007; Narayan et al. 1992; Paczynski 1986, 1991) due to their lack of association with star-forming regions and galaxies (Bloom et al. 2006; Gehrels et al. 2005; Prochaska et al. 2006), and were hypothesized to produce also optical emission, known as a kilonova (Tanvir et al. 2013), due to the decay of heavy radioactive elements (Berger et al. 2013; Metzger et al. 2010), as well as radio emission (Hurley et al. 2002; Piran 2004) and gravitational waves (Cutler & Flanagan 1994; Flanagan & Hughes 1998; Nakar 2007; Phinney 1991). This was confirmed by the multimessenger observations of GW170817 and GRB 170817A (Abbott et al. 2017c), as it produced a gravitational wave signal (Abbott et al. 2017b), short- to intermediate-duration GRB (Abbott et al. 2017a), UV/optical/ infrared kilonova (Cowperthwaite et al. 2017; Nicholl et al. 2017c; Smartt et al. 2017; Valenti et al. 2017), and radio emission (Alexander et al. 2017; Hallinan et al. 2017). This event appears to show cocoon-like shock breakout behaviour (Bromberg et al. 2017; Gottlieb et al. 2017; Ioka & Nakamura 2017; Kisaka et al. 2017; Lamb & Kobayashi 2017; Mooley et al. 2017; Piro & Kollmeier 2017), as detailed below. Since there has only been one detection and it does not resemble a "typical" short GRB in terms of its luminosity and spectra (Bégué et al. 2017; Horvath et al. 2017; Palmese et al. 2017), there has been much discussion of the possibility of multiple types of SGRB progenitors, including magnetar hyperflares from nearby galaxies (Frederiks et al. 2008; Hurley et al. 2005; Tong & Yu 2017), black hole-neutron star mergers (Mochkovitch et al. 1993; Nakar 2007; Narayan et al. 1992), or even certain types of black hole-black hole mergers (de Mink & King 2017; Loeb 2016).

LGRBs are unambiguously associated with star formation and the deaths of massive stars (Pontzen et al. 2010; Woosley & Bloom 2006), but the central engine is yet unclear, and could be a collapsar (Fujimoto et al. 2008; Gendre et al. 2013; Ioka et al. 2016; MacFadyen & Woosley 1999; MacFadyen et al. 2001), tidal disruption event (Bloom et al. 2011; Ioka et al. 2016; Krolik & Piran 2011; Levan et al. 2011), or newborn magnetar (Bucciantini 2012; Greiner et al. 2015; Ioka et al. 2016; Thompson et al. 2004; Usov 1992; Wheeler et al. 2000), among other possibilities (Cline 1996; MacFadyen et al. 2006; Vietri & Stella 1998; Winterberg 2001). In the millisecond magnetar model, the rotational energy of $\sim 10^{52}$ erg is extracted in ~ 100 s with a field of $\sim 10^{15}$ G.

During magnetar formation, the proto-NS cools via neutrino emission in the thermal Kelvin-Helmholtz timescale $\tau_{\mathrm{KH}} \sim 10 - 100$ s (Pons et al. 1999). About 1 s after the core bounce, a neutrino driven wind develops due to a density decrease around the proto-NS (Thompson et al. 2001). For regular pulsars, this wind carries little energy (Thompson et al. 2001), but for magnetars, the wind is magnetocentrifugally accelerated and far more energetic, eventually reaching relativistic speeds (Bucciantini et al. 2006; Thompson et al. 2004). In the first ~ 1 s, the wind has typical thermal speeds of $\sim 0.1c$. In the next ~ 10 s, the proto-NS relaxes to a radius of around 20 km and begins to spin down, and the magnetization parameter σ_B increases from ~ 1 to ~ 10; the neutrino wind becomes more energetic, but the bulk of the neutrinos are still confined within the proto-NS. After most of the neutrinos break out of the proto-NS, they start to accelerate in the stellar material and σ_B increases to $\sim 10^2 - 10^3$. These neutrinos ablate baryons from the surface of the NS as they break out, and these baryons are accelerated by the magnetar fields and collimated into a jet by a compressed toroidal magnetic field in the nascent magnetar wind nebula that expands in the polar directions (Del Zanna et al. 2004; Komissarov & Lyubarsky 2004) as well as by the cocoon mechanism decribed below (Bromberg & Tchekhovskoy 2016; Bromberg et al. 2017); the toroidal magnetic field collimation process has been shown to work under various assumptions (Bucciantini et al. 2007, 2008, 2009; Komissarov & Barkov 2007) and is sometimes known as the "tube of toothpaste" effect (Bucciantini 2012), but can lead to magnetic field shearing (Alves et al. 2014). After ~ 100 s, the neutrino luminosity drops below the threshold to drive a baryon-loaded wind, which is replaced by a leptonic wind once the density in the magnetosphere drops below the threshold for pair production (Metzger et al. 2011). The magnetized wind can also drive a shock into the expanding SN ejecta, depositing up to $\sim 10^{52}$ erg into the ejecta. The fraction of energy that escapes with the GRB and the fraction that is deposited in the ejecta is still unknown, with some astronomers claiming most of the energy escapes (Bucciantini 2012; Bucciantini et al. 2009; Komissarov & Barkov 2007) and some claiming most goes into the ejecta (Thompson et al. 2004).

The jets for GRBs need to break through the ejecta surrounding the central engine in most models, even those for SGRBs. Once this highly-relativistic jet collides with the non-relativistic ejecta, its advance is slowed and most of its energy during this phase is deposited into a surrounding cocoon (Ramirez-Ruiz et al. 2002; Waxman & Mészáros 2003; Zhang et al. 2003). The jet propagates through the dense ejecta and mixes with it, lowering the kinetic energy of the jet and increasing the energy of the cocoon. If the ejecta is thin enough, the jet will punch through the ejecta and propagate with relativistic speed, leading to a collimated gamma-ray burst with a small amount of off-axis emission due to the cocoon. If the ejecta is thick, the jet will choke and it will be thoroughly mixed and break through the ejecta as a mildly relativistic or trans-relativistic cocoon fireball, and emit highly luminous optical, UV, and X-ray emission almost isotropically (De Colle et al. 2017; Mizuta & Ioka 2013; Nakar & Piran 2017).

1.4.2 Superluminous Supernovae (SLSNe)

SLSNe have only been discovered recently, with the first one being SN1999as around 20 years ago (Knop et al. 1999); to date there have only been around around 150 confirmed SLSNe. Although they are extremely rare, accounting for 1 out of every 10^3-10^4 supernovae (Quimby et al. 2011), they are the most luminous optical/UV transients associated with the deaths of massive stars, being generally around 100 times brighter than regular supernovae. While Type II SLSNe show narrow spectroscopic features, like Type IIn SNe, consistent with strong interaction with the circumstellar medium, Type I SLSNe do not exhibit these features, have blue continua at maximum light, a distinctive feature due to [O II] at early epochs, and at about 30 days after peak, they are spectroscopically similar to normal or broad-lined SNe Ic at peak luminosity (Inserra et al. 2016a; Pastorello et al. 2010). They are found predominantly in low metallcity dwarf galaxies with high rates of specific star formation (Lunnan et al. 2014; Vreeswijk et al. 2014) and extreme emission lines (Leloudas et al. 2015b), although this is not always the case (Chen et al. 2017a).

Early time bumps (pre-peak, double peaks, or excess emission), which can be explained by shock-cooling or circumstellar medium (CSM) interaction models (Chatzopoulos et al. 2012; Nakar & Sari 2010; Piro 2015; Rabinak & Waxman 2011), have been observed for SLSNe-I such as SN2006oz (Leloudas et al. 2012), LSQ14bdq (Nicholl et al. 2015b), PTF12dam and iPTF13dcc (Vreeswijk et al. 2017), and DES14X3tza (Smith et al. 2016), and may be common among SLSNe (Nicholl & Smartt 2016). The precursor lasts for 5-10 days with a blackbody temperature of around 30 000 K before fading for about 5 days, then rising again to the SN peak (Moriya et al. 2018b). Late-time (post-peak) bumps have also been observed in a few cases, such as SN2007bi (Gal-Yam et al. 2009) iPTF13ehe (Yan et al. 2015), PS1-14bj (Lunnan et al. 2016), and SN2015bn (Nicholl et al. 2016a). Undulations in late-time decay have been observed in a few slowly declining SLSNe (Inserra et al. 2017). Late emergence of hydrogen emission has been detected in a few cases, which can be explained by substantial mass loss shortly before the progenitors exploded (Yan et al. 2015, 2017). Liu et al. (2017a) showed that these light curves could be explained by a multiple-shell CSM interaction model. The diversity observed so far in H-poor SLSNe seem to indicate that multiple processes may contribute to powering their light curves (De Cia et al. 2018).

These SNe are too luminous to be powered by the neutrino mechanism detailed in Section 1.2.1 - magnetohydrodynamic models usually require these supernovae to have an explosion energy of $\sim 10^{52}$ erg, while models show that neutrinos are unlikely to be able to explain supernovae with explosion energies $\gtrsim 2 \times 10^{51}$ erg because of the neutrino's small cross section (Janka 2012; Müller 2017; Terreran et al. 2017). Also, bright supernovae usually indicate that a large amount of ^{56}Ni was synthesized in the explosion, as its radioactive decay serves to keep the ejecta hot during its early rapid expansion. However, late-time observations suggest that the M_{Ni} is much lower than required to match the SLSN luminosity (Chen et al. 2013; Inserra et al. 2013; Pastorello et al. 2010; Quimby et al. 2011), and estimated ejecta masses are much lower than the necessary core mass to synthesize a large amount of ^{56}Ni (Moriya et al. 2010; Nicholl et al. 2015b). These mandate the need for a central engine or other power source; hydrogen-rich SLSN are likely powered by SN ejecta and the hydrogen-rich envelope (e.g., Chatzopoulos et al. 2012; Chevalier & Fransson 1994; Chevalier & Irwin 2011; Chugai & Danziger 1994; Inserra et al. 2016b; Ofek et al. 2013; Smith & McCray 2007), while hydrogen-poor SLSN are likely powered by central engine, possibly a fast-rotating pulsar.

Although most SLSN models are spherically symmetric, a pulsar-powered SN should have some intrinsic asymmetry characterized by a dominant polarization angle as observed for other types of stripped-envelope SNe (e.g., Maund et al. 2007; Tanaka et al. 2012; Wang et al. 2001). A strong magnetic field could lead to larger asymmetries than normal stripped-envelope SNe, and detection of this asymmetry could suggest magnetar energy injection as the source. Asymmetry in the ejecta could hide signatures of hydrogen or helium in SLSN-I spectra (Kozyreva & Blinnikov 2015), as well as ionization (De Cia et al. 2018; Mazzali et al. 2016). Axisymmetric ejecta could be the consequence of aspherical energy and momentum production during the explosion due to magnetohydrodynamic jets (Khokhlov et al. 1999), magnetoturbulence (Mösta et al. 2014), accretion flow around the pulsar (Chevalier 1989), asymmetric neutrino emission (Müller 2015; Wheeler & Akiyama 2010), clumping of the ejecta material, or a combination of these (Inserra et al. 2016a).

In the pulsar-driven model for SLSNe, the engine timescale in the SLSN must be comparable to the ejecta diffusion timescale ($\sim$ 50 days), so most of the energy in the SLSN can go into quasi-thermal optical radiation rather than driving a jet (Metzger et al. 2015; Nicholl et al. 2016a). The large required injection energy also requires that pulsar initially rotates with a millisecond time scale (see Equation 1.14). From Equation 1.21, we find that these criteria prohibit pulsars with extremely high magnetic fields ($\geq 10^{15}$ G) from being the possible SLSN progenitor, and require the field to be around $10^{13} - 10^{14}$ G.

1.4.3 Fast Radio Bursts (FRBs)

FRBs, which are luminous, coherent bursts of radio emission, were discovered in 2007 using the Parkes Radio Telescope (Lorimer et al. 2007), but astronomers were initially skeptical until a population was found using the Arecibo and Green Bank Telscopes (Spitler et al. 2014; Thornton et al. 2013). FRBs are typically ≤ 1 ms, and can not be temporally resolved by most receivers (Katz 2016). To date, around 120 burst sources have been found [3] (Petroff et al. 2016); most of which appear to have been one time events, while around 20 have been seen to repeat (CHIME/FRB Collaboration et al. 2019b, 2020; Fonseca et al. 2020; Gajjar et al. 2017; Kumar et al. 2019; Mann 2017; Scholz et al. 2016; Spitler et al. 2016); differences between repeating and non-repeating FRBs likely indicates multiple populations, progenitors, and emission mechanisms (Caleb et al. 2018a; CHIME/FRB Collaboration et al. 2019b; Cui et al. 2020; Dai et al. 2020; Fonseca et al. 2020; Palaniswamy et al. 2018; Petroff et al. 2019; Ravi 2019).

The dispersion measure

$$\mathrm{DM} = \int_{\mathrm{Source}}^{\mathrm{Object}} n_e dl \tag{1.31}$$

which causes a frequency-dependent time delay in the signal, can be used to roughly estimate the source distance; the DM for FRBs was found to be too high to come from a Galactic source (Bannister et al. 2017), which established the bursts as being extragalactic (Caleb et al. 2017). This dispersion may be partially due to a dense magnetic plasma (Masui et al. 2015) or PWN surrounding the source (Kashiyama & Murase 2017); in the case of the PWN, the density puts a lower limit of the age of the source (Kashiyama & Murase 2017). The all-sky rate of FRBs with a fluence above around 2-5 Jy ms is estimated to be around 1000 - 10 000 per day (Bhandari et al. 2018; Champion et al. 2016; Crawford et al. 2016; Lawrence et al. 2017; Petroff et al. 2019; Rane et al.

---

[3] http://frbcat.org/

2016; Shannon et al. 2018; Spitler et al. 2014; Thornton et al. 2013) or volumetically $\sim$ 1000 Gpc^{-3} yr^{-1} (Luo et al. 2020; Petroff et al. 2019).

FRBs show large variations in pulse profiles, with some showing multiple peaks and some only showing a single peak (Petroff et al. 2019). The pulse widths are usually between 1-10 ms, with some peaks having < 10 μs structure (Farah et al. 2018) and the widest peaks being around 30 ms (Farah et al. 2017; Josephy et al. 2019). Most single bursts have their spectrum modeled as a power law $\propto \nu^{\alpha}$, but α is usually not well constrained, may be modified by propagation effects, and this simple model may not be indicative of the intrinsic FRB emission process (Hessels et al. 2019). Polarization properties can vary among bursts as well, with some showing no polarization, some showing only circular polarization, some showing only linear polarization, and some showing both (Caleb et al. 2018b; Petroff et al. 2019, 2015). The differences in FRB polarization properties do not necessarily reflect different physical origins, and may be a consequence of time-variable emission properties, different viewing geometries, or different local environments. There was no detection of circularly polarised radio emission from repeating FRBs (Dai et al. 2020), which could have been a way to discriminate between repeating and non-repeating FRBs and give some clues as to their origin, until two bursts from SGR J1935+2154 were detected with roughly equal linear and circular polarization (Kirsten et al. 2020b).

Some of these FRB properties can be of use to those doing cosmology. Strongly lensed FRBs could be used as cosmological probes (Zhou et al. 2014) to constrain the Hubble constant H$_o$ with a 0.91% uncertainty from 10 localized systems observed with SKA (Li et al. 2018) and model independently constrain cosmic curvature to a precision of $\sim$ 0.076, which can can directly test the validity of the cosmological principle and break the degeneracy between the cosmic curvature and dark energy (Li et al. 2018; Zhou et al. 2014). FRBs strongly lensed by MACHOs of masses larger than $\sim 20\ M_{\odot}$ would result in repeated FRBs with an observable time delay (Muñoz et al. 2016), and by combining time delays with their time derivatives, uncertainties arising from the unknown mass distribution of gravitational lenses can effectively be eliminated, which could allow us to used these lensed FRBs as a Galactic interferometer (Wucknitz et al. 2020). FRBs may be uniquely suited to breaking the optical depth degeneracy of the kinematic Sunyaev-Zeldovich (kSZ) effect (Madhavacheril et al. 2019), to probe turbulence in the ISM (Xu & Zhang 2020), and to study the clustering of free electrons via angular cross correlation of FRBs with known galaxies, which can also help constrain the FRB redshift distribution independently of DM (Rafiei-Ravandi et al. 2020). The DMs and rotation measures (RMs) of fast radio bursts can be used to measure intergalactic magnetic fields, and a sample of $\gtrsim 10^3$ unlocalized fast radio bursts with extragalactic RM ≥ 1 rad m^{-2} can be enough to improve the current upper limits on the strength of intergalactic magnetic fields (Hackstein et al. 2019, 2020). A future sample of 500 FRBs out to $z \approx 5$ can shed light on the epoch of helium reionization, when quasar black hole activity and the cosmic star formation rate were nearing their peak (Linder 2020). FRBs can also be used to take on the missing baryon problem, which arises because more than 75% of the Universe's baryonic content lies in a difficult to detect highly diffuse state; Macquart et al. (2020) reported a measurement of the baryonic content of the Universe by using the dispersion of localized fast radio bursts, and found that their independent measurement is consistent with values derived from both Big Bang nucleosynthesis and the cosmic microwave background (Cooke et al. 2018; Planck Collaboration et al. 2016).

The nature of FRBs is still unknown due to their isolated nature and there is no generally accepted explanation, but there have been many models proposed. Some of these models involve cataclysmic events, such as collisions and mergers of compact massive objects such as white dwarves, neutron stars, or black holes (Kashiyama et al. 2013; Margalit et al. 2019; Ravi & Lasky 2014; Totani 2013; Yamasaki et al. 2020c; Zhang 2016), blitzars (Falcke & Rezzolla 2014; Thornton et al. 2013), the dark matter-induced collapse of pulsars (Bramante & Linden 2014; Fuller & Ott 2015), quark novae (Shand et al. 2016), the collapse of the magnetospheres of Kerr-Newman black holes (Barrau et al. 2014; Liu et al. 2016; Zhang 2016), and the accretion-induced collapse of a white dwarf (Margalit et al. 2019). Other models involve non-cataclysmic events, such as giant neutron star pulses (Connor et al. 2016; Cordes & Wasserman 2016; Lyutikov et al. 2016), magnetar hyperflares (Champion et al. 2016; Kulkarni et al. 2015; Lyubarsky 2014; Popov & Postnov 2010b), intermittent Roche lobe overflow in a neutron star-white dwarf binary (Gu et al. 2016), or pulsars interacting with planets (Mottez & Zarka 2014), asteroids (Dai 2020; Dai et al. 2016a; Geng et al. 2020), comets (Geng & Huang 2015), or other small bodies (Buckley et al. 2020; Mottez et al. 2020). They have even been proposed to come from extragalactic civilizations (Lingam & Loeb 2017). Since the discovery of several repeating FRBs, we know that there is a population of FRBs caused by non-cataclysmic events. However, due to there being differences in the pulse widths between repeating and non-repeating sources (CHIME/FRB Collaboration et al. 2019b; Fonseca et al. 2020), and the number of bursts coming from the sources that do repeat, it has been proposed that the repeating bursters might be a seperate subclass of FRB with a different physical mechanism entirely. A review of FRB models was done by Platts et al. (2019), who keep an updated repository of theories and predictions online[4].

Magnetar hyperflares are predicted to emit energy in three channels: in thermal heat, in the bulk motion of plasma, and in energetic non-thermal particles (Lyutikov 2002). Solar flares are often accompanied by radio bursts (Bastian et al. 1998), which are signatures of electrons accelerated along coronal magnetic field lines that cause electrostatic plasma turbulence and the subsequent collision of plasma waves (Lyutikov 2002); magnetars are predicted to exhibit similar behaviour. However, the radio non-detection of the 2004 SGR 1806-20 hyperflare gives a fluence limit that is inconsistent with all but one of the first fifteen FRBs (Tendulkar et al. 2016); however, due to the variability in magnetar and FRB properties and possible dependence on the circum-magnetar medium, the hyperflare hypothesis has yet to be discarded by the community.

The giant pulses arise from young neutron stars, and arise in an outer magnetosphere acceleration gap (Cheng et al. 1986b; Romani & Yadigaroglu 1995). Photon production is maintained by synchrotron radiation in the gap itself, where high magnetic fields enchance synchrotron emissivity and pair-production (Johnston & Romani 2004). This dense pair plasma promotes instabilities which create enhancements in particle coherence and thus the giant radio pulses (Johnston & Romani 2004). Giant pulses have been observed in 11 sources so far (Kuzmin 2007), most notably the Crab pulsar (Argyle & Gower 1972; Staelin & Reifenstein 1968) and millisecond pulsar PSR B1937+21 (Wolszczan et al. 1984). It is worth noting that these pulsars have extremely high magnetic fields at their light cylinder (Johnston & Romani 2004). The brightness temperature 5×10^{39} K, from a giant pulse from PSR B1937+21, is the highest observed brightness temperature in the Universe (Soglasnov et al. 2004). However, these pulses are extremely short (Hankins et al. 2003; Soglasnov et al. 2004), with one pulse from the Crab pulsar being only 2 ns long (Hankins et al. 2003). If the pulse duration t is interpreted as the maximum size of the emitting region $r < ct$, then 2

---

[4] frbtheorycat.org

ns corresponds to a maximum size of only 60 cm, the smallest entity ever detected outside our solar system (Kuzmin 2007).

Over the past four years, several discoveries have led to vast improvements in our understanding of FRBs. Until 2017, there was no localization or association of FRBs with other sources. However, observations of the first repeating fast radio burst, FRB 121102, led to the localization of its host galaxy at $z = 0.193$ and the discovery of a persistent radio counterpart, which was seen by VLA and the European VLBI Network (Chatterjee et al. 2017; Marcote et al. 2017; Tendulkar et al. 2017). The radio counterpart from FRB 121102 is consistent with a young PWN from a neutron star engine with sub-magnetar field strength and a millisecond initial rotation period (Kashiyama & Murase 2017), similar to SLSNe (see Figure 1.1 for the overlap). The source is coincident with the star forming region in the galaxy (Bassa et al. 2017), which strongly suggests a possible connection between FRBs and the deaths of massive stars, similar to SLSNe and GRBs (DeLaunay et al. 2016; Deng & Zhang 2014; Zhang 2014). FRB 121102 shows a 100% linear polarization and a high and variable rotation measure, which decreased from $+1.46 \times 10^5$ rad m^{-2} to $+1.33 \times 10^5$ rad m^{-2} over a span of 7 months in the source frame, which indicates a highly dynamic magneto-ionic environment around the progenitor (Michilli et al. 2018). FRB 121102 has bursted over 150 times (Gajjar et al. 2017; Mann 2017; Scholz et al. 2016; Spitler et al. 2016) and shows some frequency range variation; some bursts were detected above 5 GHz (Gajjar et al. 2018) while some were detected only at lower frequencies (Josephy et al. 2019; Pearlman et al. 2020b). These bursts have complex time-frequency structures, including subbursts with finite bandwidths, which is consistent with the progenitor being embedded within a dense nebula (Hessels et al. 2019). Hidden within the sea of erratic interstellar scintillations, there is a periodic structure in the spectra of 121102: a set of (95 ± 16) MHz-equidistant peaks with seemingly frequency-independent interpeak distance, which can be explained by diffractive lensing of the FRB wave (Levkov et al. 2020). Due to the clustering of detected bursts, there have also been tentative reports of a periodicity of $\sim$ 160 days in the burst repetitions (Cruces et al. 2020; Rajwade et al. 2020), altough others find that the underlying pattern of bursts does not appear to be periodic, instead having a logarithmic repetition pattern (Tabor & Loeb 2020); more observations will be needed to determine the precise nature of the FRB 121102 repetition pattern.

Most of the discoveries over the past 3 years have been made by the Canadian Hydrogen Intensity Mapping Experiment (CHIME). CHIME is a radio interferometer at the Dominion Radio Astrophysical Observatory in British Columbia, Canada, consisting of four 100×20 cylindrical parabolic reflecting antennae with 1024 dual-polarization radio recievers suspended above them. The telescope was originally designed to measure the large scale neutral hydrogen power spectrum at the redshift range between 0.8-2.5 (Bandura et al. 2014), which is the period in the history of the Universe where the ΛCDM cosmological model predict that dark energy started to dominate the energy density of the Universe, and thus the expansion of the Universe transitioned from decelerating to accelerating. However, due to the telescope having a large instantaneous field of view (about 200 square degrees), a wide bandwidth (400-800 MHz), high sensitivity, and a powerful correlator, it proved to be ideal to search for FRBs (CHIME/FRB Collaboration et al. 2018).

Even during pre-commissioning, CHIME proved to be prolific at finding FRBs, observing 13 during that period at frequencies down to 400 MHz; FRBs had not previously been seen below 700 MHz (CHIME/FRB Collaboration et al. 2019c). One of its early discoveries was the second repeating fast radio burst, FRB 180814, which had subpulse frequency structure, drifting and spectral variation similar to that of FRB

121102, suggesting there could be similar emission mechanisms or propagation effects (CHIME/FRB Collaboration et al. 2019a). CHIME has subsequently discovered 17 other repeating FRBs (CHIME/FRB Collaboration et al. 2019b; Fonseca et al. 2020), which have an indistinguishable DM distribution from non-repeating FRBs, suggesting that both their distribution in space and associated local environments do not strongly differ (Fonseca et al. 2020). However, the pulse widths of repeating bursts are sigificantly wider than non-repeating bursts, suggesting that there may be an inherent difference in emission mechanisms and/or local environments (CHIME/FRB Collaboration et al. 2019b; Fonseca et al. 2020). The number of bursts detected by CHIME has given strong constraints or energy distribution and activity level of the repeaters (Lu et al. 2020b).

The second precise localization of a repeating FRB was FRB 180916.J0158+65 (less formally known as FRB 180916), which originates from a star-forming region in a nearby ($z = 0.0337 \pm 0.0002$) massive spiral galaxy (Marcote et al. 2020). From September 16, 2018, to 4 February 4, 2020, 38 bursts were recorded which showed a periodicity of 16.35 ± 0.15 days; all bursts arrive within a five day phase window, while 50% of the bursts arrive within a 14 hours phase window (CHIME/FRB Collaboration et al. 2020). Some of the bursts were detected as low as 328 MHz, the lowest frequency detection yet (Pilia et al. 2020). Due to the 2.3-mas localization of FRB 180916, follow-up observation with the Hubble Space Telescope (HST) and Gran Telescopio Canarias could probe the FRB environment with 30-60 pc resolution (Tendulkar et al. 2020). The Hα constraint shows that any stellar companions of FRB 180916 should be a cooler, less massive spectral type than O6V; the FRB is 250 pc away (in projected distance) from the brightest pixel of the nearest young stellar clump, its probable birthplace, which is $\sim$ 380 pc in size (Tendulkar et al. 2020). Given the typical kick velocity of a pulsar, magnetar, or neutron star in a binary (60-750 km s^{-1}), this FRB would need 800 kyr to 7 Myr to traverse the observed distance from that stellar clump, which is longer than the active ages of magnetars ($\lesssim$ 10 kyr). The inferred age is more consistent with high-mass X-ray binaries and gamma-ray binaries and the observed separation their separations from their nearest OB associations (Tendulkar et al. 2020). Deep optical observations during a more recent burst detected no transient optical emission down to m$_i$ = 24.7 mag (Kilpatrick et al. 2020)

Several theories were posited to explain the periodicity of FRB 180916. Some involved a neutron star binary systems, where the approximately 16 day period is the orbital period of that system (Ioka & Zhang 2020; Lyutikov et al. 2020; Zhang 2020b). The periodicity of the emissions in these models is a consequence of the FRB being in a binary, with the stellar wind of the neutron star may open up a window in the the normally radio-obscuring wind of the companion, allowing the FRBs to escape (Zhang 2020b). The FRBs could be produced by a highly magnetized pulsar whose field is combed by the strong wind of the companion (Ioka & Zhang 2020; Zhang 2017), either a millisecond pulsar or massive star, like an early OB-type star (Lyutikov et al. 2020). Other models involved the FRB-producing neutron star to be deformed, with the emission region precessing like a gyroscope due to stresses from magnetic flares (Levin et al. 2020), neutron star free precession (Zanazzi & Lai 2020), or orbit-induced spin precession (Yang & Zou 2020). Other models included an ultra-long period magnetar (Beniamini et al. 2020), similar to the CCO and magnetar candidate at the centre of supernova remnant RCW 103 which possesses an astonishing 6.67 hour period (De Luca et al. 2006), or the Lense-Thirring precession of a debris disk around a newborn millisecond pulsar, which can produce the observed radio burst luminosity for around 400 years (Chen 2020).

The Galactic magnetar SGR J1935+2154 spins with a period $P = 3.24$ s and a period derivative $\dot{P} = 1.43 \times 10^{-11}$ s s^{-1}, which gives an estimated surface dipole magnetic field strength $B_p = 2.2 \times 10^{14}$ G (Israel et al. 2016). On April 27, 2020, the magnetar entered an active period and emitted hundreds of X-ray bursts within a few hours (Younes et al. 2020). One of these bursts was detected at 18-60 keV by AGILE (Tavani et al. 2020a), at 1-250 keV by Insight-HXMT (Li et al. 2020a), at 20-200 keV by Imager on-board INTEGRAL (IBIS) instrument (Mereghetti et al. 2020), and at 20-500 keV by Konus-Wind (Ridnaia et al. 2020a); this burst was special because it coincided with an FRB from the same source, which was observed by CHIME with a light curve that had a double peak structure with two components $\sim$ 5 ms wide separated by $\sim$ 30 ms (The CHIME/FRB Collaboration et al. 2020), and by STARE2 at 1281-1468 MHz as a single narrow spike with a width of 0.61 ms (Bochenek et al. 2020b). Both radio detections found the same DM $\sim$ 332.7 pc cm^{-3} (Bochenek et al. 2020b; The CHIME/FRB Collaboration et al. 2020). A summary of the timeline of detections is shown in Yamasaki et al. (2020a) Figure 1, and the delay time between the two radio and X-ray peaks is consistent with the dispersion delay of FRB 200428 (Li et al. 2020a). Only one coincident burst was detected, given the stringent upper limits from FAST coincident with other X-ray bursts (Lin et al. 2020b). If the FRB-associated burst were randomly drawn from this magnetar burst population, its occurrence rate would be at most around 0.014%. Given that this X-ray burst showed a different spectrum than the other bursts, it perhaps seems indicative of an uncommon location for the origin of the FRB-associated burst (Younes et al. 2020). Both ANTARES and ICECUBE found no neutrinos accociated with the burst (Coleiro & Dornic 2020; Vandenbroucke 2020), but an archival search of 2014 and 2016 Chandra data discovered an X-ray transient feature consistent with a magnetar wind nebula or outflow near SGR 1935+2154, although the origin is not completely clear (Kong et al. 2020).

Since then, there has been an intense follow-up campaign to try and detect more emission from SGR J1935+2154. The day after Lin et al. (2020a) reported the initial non-detection upper limits from FAST, Zhang et al. (2020a) reported the FAST detection of a highly linearly polarized burst with RM = +112.3 rad m^{-2}, consistent with typical values of pulsars at a distance of 9 kpc (Han et al. 2018); this burst was not coincident with a detected X-ray burst (Li et al. 2020b). Several radio telescopes performed burst searches over the next few weeks; including the Low-Frequency Array (LOFAR) at 110-180 MHz (Bassa et al. 2020); the Deep Space Network (DSN) at 2.3 and 8.5 GHz (Pearlman et al. 2020a); the VLA at 6 and 22 GHz (Ravi et al. 2020a,b); the Medicina Northern Cross (MNC) radio telescope at 408 MHz (Naldi et al. 2020); the Arecibo Observatory at 0.327, 1.4, and 4.5 GHz (Palliyaguru et al. 2020; Surnis et al. 2020a), the Green Bank Telescope (GBT) at 1.1-1.9, 1.8-2.7, and 3.8-8 GHz (Surnis et al. 2020a); the upgraded Giant Metrewave Radio Telescope (uGMRT) at 300-500, 550-750, and 1250-1450 MHz (Bera et al. 2020; Roy et al. 2020; Surnis et al. 2020b,c); the European VLBI network at 1.66 GHz (Nimmo et al. 2020); and the Murchison Widefield Array (MWA) at 154.24 and 184.96 MHz (An et al. 2020); but no bursts were detected. The VLA, uGMRT, and VLBI were also able to place $\sim$ 20-100 μJy upper limits on emission from a coincident persistent source in their respective bands (Bera et al. 2020; Nimmo et al. 2020; Ravi et al. 2020a,b; Surnis et al. 2020b,c). During this period, several millisecond duration X-ray bursts were detected by the Nuclear Spectroscopic Telescope Array (NuSTAR) and Neutron Star Interior Composition Explorer (NICER) (Borghese et al. 2020), several bursts were detected by the Swift Burst Alert Telescope (BAT) (Tohuvavohu 2020a,b), and about 100 bursts were discovered in the preliminary data of Insight-HXMT (Zhang et al. 2020b). On May 10th, two short X-ray bursts were detected by Konus-Wind and other X-ray observatories (Hurley et al. 2020; Ridnaia et al. 2020b) when radio observations were simultaneously being performed by

Westerbork telescope, Onsala Space Observatory (OSO), and Torun telescope, but no radio bursts were detected (Kirsten et al. 2020a).

No further radio emission was detected from SGR J1935+2154 until later in May, when two bursts were detected by the Westerbork telescope, Onsala Space Observatory (OSO), and Torun telescope on May 24 at a central observing frequency of 1324.0 MHz (Kirsten et al. 2020b). These bursts have the same dispersion measures as the previous CHIME, STARE2, and FAST bursts, but were unique in that they were the first detections of circular polarization from a repeating FRB; the linear and circular polarizations were both about 8% for the first burst (considered non-significant by the authors), and both around 30-40% for the second burst. There was no X-ray burst detected, even though the source was in the Swift, NICER, and Fermi Gamma-ray Burst Monitor (GBM) fields of view (Kirsten et al. 2020b). Shortly after, on May 30, the MNC detected periodic radio pulsations at 408 MHz from SGR 1935+2154 at 7σ with flux density $\sim$ 4 mJy (Burgay et al. 2020). The MNC had other non-detections of pulsed emission with 3 and 6 mJy upper limits (Burgay et al. 2020), and the CHIME flux density upper limit from later that day was $\sim$ 0.2 mJy at 600 MHz - around 20 times lower than that of MNC (Tan & Chime/Pulsar Collaboration 2020); this suggests that the radio pulsations have an active window of less than a day. The period observed by MNC is 0.3 ms longer than that observed by NuSTAR (Borghese et al. 2020) and implies an average $\dot{P} = 1.2 \times 10^{-10}$ s s^{-1} - about an order of magnitude larger than that derived by Israel et al. (2016), but this is likely just due to timing irregularities in radio emitting magnetars (Archibald et al. 2018; Camilo et al. 2016), which are not uncommon.

After the first month post-FRB discovery, there were a few months without any new detections from SGR J1935+2154. However, on October 8, CHIME detected three bursts from the magnetar with the first and second bursts separated by 0.954 s and the second and third by 1.949 s, indicating that all three occurred within one 3.24 second rotation period (Good & CHIME/FRB Collaboration 2020). The burst was not detected by STARE2 between 1.28 GHz and 1.53 GHz (Bochenek et al. 2020a), although the CHIME fluences are consistent with the upper limits derived from the STARE2 telescope (Pleunis & CHIME/FRB Collaboration 2020). No simultaneous X-ray or gamma-ray counterparts were detected with Swift/BAT (Tohuvavohu 2020c,d) or INTEGRAL (Savchenko et al. 2020). FAST observed SGR J1935+2154 on October 9 at 1.25 GHz and detected multiple radio pulses and periodic radio emission with a period of 3.24781(1) s (Zhu et al. 2020), the same as the magnetar; the pulses were aligned to within 0.03 of the spin phase. Zhu et al. (2020) speculated that these emissions could signal a possible transition to a rotation-powered pulsar phase. October 16 observations at 820 MHz and 2 GHz using the GBT did not detect any significant periodic or single-pulse emission (Straal et al. 2020). A recent re-analysis of 2009 X-ray and radio observations of 1E 1547.0-5408, a different Galactic magnetar, found the detection of two radio bursts during an X-ray active phase (Israel et al. 2020). The two radio bursts are neither aligned with the latter radio pulsations nor with the peak of the X-ray pulse profile, and while in SGR J1935+2154, the radio burst appears to lead the X-ray burst by no more than $\sim$ 8 ms, in 1E 1547.0-5408 the X-ray burst leads the first radio burst by $\sim$ 1 s.

These recent discoveries have had a profound effect on our modelling and constraints of FRB progenitors and emission mechanisms. An FRB model should include both an energy source model that accounts for the universal properties of FRBs - such as energetic, redshift distribution, event rate density, host galaxy properties, location within the host galaxy, as well as properties of the immediate environment, such as DM, RM, persistent source, etc. - and a radiation mechanism model which can explain the observed properties of the coherent radio emission - such as duration, brightness temperature, spectral and temporal features, and polarization. The models should also ideally make a testable prediction: models that invoke the disruption of an asteroid (Dai 2020; Geng et al. 2020) in a pulsar/magnetar magnetosphere can interpret all the features of the Galactic FRB and X-ray burst self-consistently, but are tough to rule out due to the lack of a smoking-gun prediction (Zhang 2020a). Many models (more than fifty) can account for an energy source, but there are only a few possible radiation mechanisms, which can be discussed regardless of the source. There are two general types of FRB radiation models, ones which invoke the magnetosphere of a compact object (usually a pulsar or magnetar), and ones which invoke relativistic shocks launched from a compact object; Zhang (2020a) refers to these as "pulsar-like" and "GRB-like" respectively, due to the similarities with how radiation is proposed to be emitted in those systems.

There have been around a dozen pulsar emission models discussed in the literature, which all suffer from criticisms either observationally or theoretically (Melrose 2017). When applied to FRBs without any modifications, none of these pulsar models reproduce the much higher brightness temperatures of FRBs compared with pulsars (Lu & Kumar 2018). One plausible scenario is that a magnetic pulse generated in the inner magnetosphere of a magnetar propagates into the outer magnetosphere and triggers magnetic reconnection (Lyubarsky 2020). Another involves coherent curvature radiation by bunches of charged particles (Ruderman & Sutherland 1975). This model requires a continuous generation of sparks throughout the duration of the FRB due to the short cooling timescale of the charged bunches (Katz 2014; Kumar & Bošnjak 2020; Kumar et al. 2017; Lu & Kumar 2018; Lu et al. 2020a; Yang & Zhang 2018; Yang et al. 2020), which requires a strong electric field component parallel to the local magnetic field in the FRB emission region; the formation of plasma "solitons" due to a two stream plasma instability in the polar cap sparking mode can maintain the observed timescale (Melikidze et al. 2000; Zhang 2020a). There is also a low-twist model (Wadiasingh et al. 2020; Wadiasingh & Timokhin 2019), where magnetic field dislocations or oscillations in the neutron star surface can lead to a pair cascade, but since this is the same dislocation that results in X-rays bursts, this model predicts that all FRBs should be associated with short magnetar bursts, which is inconsistent with observations (Margalit et al. 2020a). These models all predict highly polarized emission, up to nearly 100% linear polarization (Zhang 2020a).

Models that invoke either internal or external shock, similar to those introduced to explain both the prompt emission and afterglow of GRBs, were first proposed for FRBs by Lyubarsky (2014). These models require an ultra-relativistic outflow and need a compact object (a magnetar in most models) to power the FRB. The most straightforward of these is a vacuum model where plasma effects are ignored (Ghisellini 2016). One more complicated version favours weakly magnetized neutron stars (Long & Pe'er 2018), where negative absorption in a weakly magnetized plasma occurs below the generalized Razin plasma frequency where the energy spectrum of the electrons hardens substantially (Waxman 2017), but this does not predict emission with strong linear polarization. Another more complicated model involves a highly magnetized ejecta with an ordered magnetic field in the pre-shock medium (Beloborodov 2017, 2020; Lyubarsky 2014; Metzger et al. 2019; Plotnikov & Sironi 2019) - these are the so-called "synchrotron maser blast wave" models (Margalit et al. 2020a), of which there are three main varieties. The first proposes FRB production occurs as an ultra-relativistic flare ejecta collides with the PWN (Lyubarsky 2014). This model is only marginally consistent with observations, as the inferred synchrtron maser efficiency is far lower than simulations (Plotnikov & Sironi 2019), and requires high pair-loading, which pushes the high energy thermal synchrotron counterpart to lower frequencies, peaking in the optical/UV band (Margalit et al. 2020a); therefore, this model requires the X-rays from the flare must be created by a process not directly related to the FRB mechanism. Another variety proposes that the outflow collides with an electron/positron plasma from the spin-down powered component of the pulsar wind (Beloborodov 2017, 2020). This scenario might seem disfavoured due to the low spin-down power of SGR 1935+2154, but an updated model with low-amplitude Alfvén waves from a magnetar quake propagating to the outer magnetosphere and converting to "plasmoids" (closed magnetic loops) that accelerate from the star, driving blast waves into the magnetar wind, can produce a variable wind far stronger than the normal spin-down wind from a magnetar (Yuan et al. 2020). Simulations of this model predict a narrow (a few milliseconds) X-ray flare generated in the magnetosphere, which arrives almost simultaneously with the FRB emitted far outside the magnetosphere (Yuan et al. 2020). The final synchrotron maser blast wave model has the magnetar flare collides with matter ejected from a recent, earlier flare (Metzger et al. 2019). This model predicts a ratio $\eta \equiv E_{\text{radio}}/E_{\text{X}} \sim 10^{-5}$ for expected values of the maser efficiency (Plotnikov & Sironi 2019), which matches well with observations. Since the peak frequency of the high-energy flare scales with the characteristic synchrotron frequency, extending this model to more energetic cosmological FRBs predicts that flare emission for these bursts will occur at much higher energies (MeV-GeV), which will unfortunately be too faint to see with Fermi and Swift (Chen et al. 2020a; Margalit et al. 2020a,b; Metzger et al. 2019). These models predict nearly 100% linear polarization with a constant polarization angle across the pulse. These models in general require a huge energy budget and predict a brighter high-energy counterpart than the pulsar-like models, and predict a minimum wait time of > 100 s between FRBs (Metzger et al. 2019).

We have learned from observations of SGR J1935+2154 that at least some, perhaps most, even all, FRBs can be produced by magnetars; that magnetic energy, not spin-down energy, provides the source of the FRB, since the FRB luminosity greatly exceeded the spin-down luminosity of the magnetar, the FRB was associated with an SGR burst which is believed to be triggered by a magnetic dissipation event within the magnetar (Thompson & Duncan 1995), and radio pulsars are $\gtrsim 100$ times more common than Galactic magnetars (accounting for their effective active lifetime), making it extrememly unlikely that a spin-down-powered "FRB" would be first detected from a Galactic magnetar; and that making a detectable FRB from an SGR burst requires a special set of conditions, since the success rate is less than one out of a hundred (Zhang 2020a). If the X-ray emission originates from the magnetosphere of a magnetar (Thompson & Duncan 1995), a pulsar-like mechanism is favoured for FRB200428 (Katz 2020), but if X-ray emission of magnetar flares arises from thermal synchrotron radiation from internal shocks, which is broadly consistent with previous observations (van der Horst et al. 2012), then a GRB-like mechanism is favoured for FRB200428. If all FRBs are generated by magnetars, then the existence of two populations of magnetars is required (Lu et al. 2020a): a large population of regular magnetars (similar to Galactic magnetars) that contribute the bulk of FRBs and a small population of special magnetars (those born from extreme explosions such as GRBs and SLSNe) that power active repeaters and have a much shorter lifetime (Margalit et al. 2020a; Zhang 2020a). The current FRB host galaxy data seem to be consistent with this picture (Li & Zhang 2020). It is still unknown whether there are any FRBs generated by catastrophic events, such as binary neutron star mergers, but the joint detection of an FRB and a compact binary coalescence would unambiguously establish the category of genuinely catastrophic FRBs; although we have none so far, non-detections can also place stringent constraints on such scenarios (Wang et al. 2020).

1.4.4 The Host Galaxy Connection

It is worth noting the environments and host galaxies these transients usually occur in. Long GRBs (LGRBs) are generally found in dwarf, star-forming galaxies with low metallicity (Fruchter et al. 2006; Levesque 2014; Levesque et al. 2010a; Pontzen et al. 2010), but may still sample the general star-forming galaxy population (Palla et al. 2019; Taggart & Perley 2019). SLSN hosts differ depending on whether hydrogen is detected in the spectrum: hydrogen-rich SLSNe (SLSNe-II) come from a broad range of host galaxies with different morphologies, masses, metallicities, and star formation histories (Angus et al. 2016; Perley et al. 2016; Schulze et al. 2018), while hydrogen-poor SLSNe (SLSNe-I) tend to be found in dwarf, star-forming galaxies with low metallicity (Modjaz et al. 2008; Neill et al. 2011; Vreeswijk et al. 2014) which have shown significant signs of interaction (Ørum et al. 2020), suggesting the progenitors may have formed from a recent burst of star formation. The differences in SLSNe-I and SLSNe-II environments are due to the different mechanisms by which they obtain their luminosity. Many early papers pointed out the similarities in host galaxies between LGRBs and SLSNe-I (Japelj et al. 2016; Lunnan et al. 2014; Modjaz et al. 2008), but subsequent studies found that SLSNe-I prefer less massive, more compact, more metal-poor hosts than LGRBs (Angus et al. 2016; Gal-Yam 2019; Leloudas et al. 2015b; Lyman et al. 2017; Schulze et al. 2018). The host galaxy of FRB 121102 is a low-metallicity dwarf galaxy with prominent emission lines (Chatterjee et al. 2017; Marcote et al. 2017; Tendulkar et al. 2017), similar to SLSNe, and since the radio counterpart was found in an intense star bursting region within the galaxy (Bassa et al. 2017), it is likely that there is a link between stellar death and FRBs. However, localization of further FRBs to more massive spiral galaxies (Bannister et al. 2019; Bhandari et al. 2020; Law et al. 2020; Macquart et al. 2020; Marcote et al. 2020; Prochaska et al. 2019; Ravi et al. 2019) cast doubt on that connection, although the idea that different populations of FRBs may originate from different progenitors remains debated (Caleb et al. 2018a; Cui et al. 2020; Palaniswamy et al. 2018; Petroff et al. 2019; Ravi 2019). Overall, FRB-host galaxies show a continuous, broad range of colour, stellar mass, and star formation rate, which span the full parameter space occupied by $z < 0.5$ galaxies (Heintz et al. 2020). Based on their analysis, Heintz et al. (2020) rule out the hypothesis that FRBs strictly track stellar mass in galaxies and rule out galaxies hosting LGRBs as common hosts for FRBs, but note that other transient channels (SGRBs, core-collapse supernovae (CCSNe), and SNe-Ia) host galaxy properties and offsets consistent with the FRB distribution.

1.5 Alternative Models for SLSNe-I

Focussing for a bit on SLSNe-I, there are three main competing models with the pulsar-driven model: ejecta-CSM interaction, pair instability and pulsational pair instability, and fallback accretion. Like the pular-driven model, each of these models have their own strengths and weaknesses, which is why there is still no consensus on the power source of these SNe. Current observations are so far within the allowed theoretical range for the energetics of each model (Sukhbold & Woosley 2016). These models are also not necessarily mutually exclusive - some SLSNe have been interpreted as pulsar-driven with ejecta-CSM interaction to explain late-time undulations in the light curve (Inserra et al. 2017; Yan et al. 2017). Such hybrid models seem inevitable - pulsar-driven SNe likely produce some ^{56}Ni, most massive stars are surrounded by some CSM, pulsational pair-instabililty can lead to ejecta-CSM interaction, fallback can exist within the pulsar-driven model, etc., and these models can fit more observations due to their inherent parametric flexibility, but this flexibility makes hybrid models philosophically weaker in comparison to single-source models (Gal-Yam 2019). These hybrid models should ideally only be used for SLSNe-I that can not be reasonably explained by any single-source models, and should be tested for the unique signatures of both individual models, or perhaps a signature unique to the hybrid model itself. There are several other, more exotic, ideas for the power source of a SLSN-I - for example, the latent heat from a phase transition from neutron stars to quark stars (Ouyed et al. 2012) - but those will not be covered here.

1.5.1 Ejecta-CSM Interaction

Before the supernova explosion, the progenitors of SNe are surrounded by the material shells or circumstellar winds ejected just prior to the explosion. Once the supernova explodes, if the ejecta expand into a low density medium, the interaction only becomes important at the SNR stage a few tens to thousands of years after the SN explosion (Reynolds 2017). In the case of a dense CSM, the interaction already occurs during the SN phase (e.g., Chandra 2018)), and the SN becomes more luminous than normal. CSM interaction is most likely responsible for powering SNe-IIn, SNe-Ibn, rare luminous SN-Ia explosions (Ia-CSM), and even some SNe-Ic (Gal-Yam 2019). If the surrounding material is massive enough and concentrated close to the exploding star, the interaction starts in the early supernova evolution and most of the kinetic energy can be converted to radiation within the first months and produce a SLSN (Moriya et al. 2018b). This CSM may result from binary interaction or mergers, thick stellar winds, or stellar eruption similar to luminous blue variable (LBV) stars (Smith 2014).

Interaction of the expanding ejecta with the surrounding circumstellar material can convert kinetic energy into radiation efficiently via strong shocks. When the ejecta collides with the CSM, forward and reverse shocks are generated, these shocks accelerate electrons, these electrons emit X-ray and gamma-ray photons, and most of these photons soften into IR-optical-UV photons (Wang et al. 2019a). From simple analytical calculations (Moriya et al. 2018b), the shock/photospheric radius for an ejecta-CSM powered SLSN should be $R_{\rm ph} \sim 4 \times 10^{15}$ cm, about an order of magnitude larger than $R_{\rm ph}$ for a standard supernova near peak luminosity. Simple hydrodynamic models get a similar value for the CSM radius (Ginzburg & Balberg 2012) and also state that effective conversion of kinetic energy into radiation requires comparable masses for the ejecta and CSM, while analytical calculations suggest a smaller ejecta-to-CSM mass ratio is more efficient (Moriya et al. 2018b). Due to the large system size, the shock breakout lasts much longer for a SLSN than a standard SN-Ib/c: a standard SN will have a breakout timescale of a few minutes, while the CSM-interacting SLSN will have breakout timescale of a few months. This shock heating mechanism can easily reproduce the blue colour of SLSNe near peak luminosity (Tolstov et al. 2017b).

Chatzopoulos et al. (2012) provided a semi-analytic formula used to simulate interaction-powered light curves, which has been fit to numerous SLSNe. The model is simple and has many degrees of freedom, since it depends on the properties of both the CSM and SN, but can fit light curves as well as the pulsar-driven model. However, this model assumes the heating source is in the centre of the SN, instead of moving outwards as the shock progresses. It also takes the radiation from the reverse and forward shocks into account separately, when it may be almost impossible to seperate the emission form the two shocks if the shocked gas cools quickly; this CSM configuration is inconsistent with numerical simulations (Moriya et al. 2013; Sorokina et al. 2016). A follow-up paper (Chatzopoulos et al. 2013) tried to find a CSM configuration from the semi-analytic model more consistent with numerical simulations, which is important due to the difficulty of numerically modelling this scenario. Numerical codes need to be able to resolve optically thick shocks, which has lead to a lack of published interaction models. The first numerical models of ejecta interation with a dense extended CSM were done by Falk & Arnett (1977); Grassberg et al. (1971); and Grasberg & Nadyozhin (1987), with more recent radiation hydrodynamics studies done by Blinnikov et al. (1998, 2006).

Most SLSN-II show signals of ejecta-CSM interactions similar to those found in SNe-IIn (strong emission lines), so it is natural to assume these SLSNe are powered by a collision of the ejecta with massive CSM (Gal-Yam 2019). However, evidence for ejecta interaction with hydrogen-free CSM without strong emission lines (Ben-Ami et al. 2014) prompts consideration of this model for SLSNe-I as well. Several SLSNe-I, including SN2010gx and PTF12dam, have been argued to be interaction-powered from semi-analytic or simple hydrodynamic light curve modelling (Ginzburg & Balberg 2012; Nicholl et al. 2014; Tolstov et al. 2017a). In numerical modelling of SLSNe-I, the chemical composition of the ejecta and CSM is an important parameter, unlike in hydrogen-rich event. Both observations and modelling prefer a CO composition, since the presence of helium leads to the light curve rising much longer than observed due to its opacity (Sorokina et al. 2016). Narrow, fast evolving events are best reproduced by a C to O ratio of 0.7 and a $\sim 10\ M_{\odot}$ CSM envelope while broad, slowly evolving events are best reproduced by a C to O ratio of 0.9 and a CSM envelope of a few tens of $M_{\odot}$; only the widest light curves are problematic for this model (Moriya et al. 2018b; Sorokina et al. 2016).

The origin of the pre-peak luminosity bump can be qualitatively explained in this model by heating of a detached CSM envelope (Moriya & Maeda 2012). The origin of post-peak undulations observed in several slowly-declining SLSNe-I can also be naturally explained by the collision of the ejecta with multiple layers of CSM (Inserra et al. 2017). An ejecta-CSM interaction model involving multiple interactions between the ejecta and different winds/shells was recently constructed to fit the light curves of iPTF13dcc and iPTF15esb (Liu et al. 2018; Wang et al. 2019a). In most SLSNe-I with undulating light curves, light-time spectroscopy reveals the emergence of emission lines of hydrogen (Yan et al. 2017) or other elements (Lunnan et al. 2018b), suggesting that their progenitors may have been surrounded by a dense CSM shell.

For all its flexibility, there are some problems with modelling SLSNe-I using the ejecta-CSM interaction. There are currently no published models that fit observed SLSN-I spectra assuming pure CSM interaction power. Ubiquitous early bumps in SLSN-I light curves, although possible, are surprising for interaction-powered models if they have similar properties, since shock breakout is expected to occur in widely varying locations within a complex structured CSM, although further observations suggest that early bumps may be more diverse than initially thought (Anderson et al. 2018; Gal-Yam 2019; Vreeswijk et al. 2017). About one month from maximum, the photospheric velocities are much higher (10 000 - 20 000 km/s) than predicted by existing interaction models. The amount of mass lost by the SLSN progenitor to explain the brightness and duration of the SLSN is at least a few solar masses during the last few months before the explosion. Although this is not impossible, there is neither strong theoretical nor observational understanding of the last stages of stellar life, and the required CSM mass is only comparable to observed mass-loss rates from outbursts from luminous blue variables (LBVs) (Smith et al. 2011).

1.5.2 Pair-Instability and Pulsational Pair-Instability

Most core-collapse supernova light curves are powered by the radioactive decay of ^{56}Ni, which is produced in quantities of about 0.1 $M_{\odot}$ in a typical CCSN (Drout et al. 2011). To power most superluminous supernova light curves, more than 5 $M_{\odot}$ of ^{56}Ni would need to be generated, but the ^{56}Ni yields of CCSNe can not exceed 5 $M_{\odot}$ without an extremely large explosion energy (Umeda & Nomoto 2008). The only way to generate more nickel is to invoke a pair instability in the stellar core, giving rise to a pair instability supernova (PISN) (Barkat et al. 1967; Fraley 1968; Rakavy & Shaviv 1967).

At the high-density core of very massive stars, pair production and annihilation occur rapidly. Gamma-rays are held in thermal equilibrium with electron-positron pairs, ensuring that the core remains stable. If some fluctuation suddenly heats or compresses the core, gamma-rays energetic enough to be converted into a cascade of electron-positron pairs can be created. These cascades temporaily reduce the radiation pressure supporting the stellar core against collapse. If the collapse stops, the positron-electron pairs can be reconverted into gamma-rays, driving the radiation pressure back up. The positron population provides a reservoir of new gamma rays as the expanding star's core pressure drops. As the core temperature and gamma-ray energies increase, more and more gamma-ray energy is absorbed into pair creation, and the star contracts, which compresses and heats the core, leading to further increases in core temperature and gamma-ray energy. Once the increased pair creation reduces the radiation pressure to the point that gravitational pressure completely overwhelms it and further pair annihilation is insufficient to halt further contraction of the core, the core begins a runaway rapid (on a timescale of a few seconds (Fryer et al. 2001)) contraction. This contraction bring the adiabatic index of the core below 4/3, which triggers explosive carbon and oxygen burning (Moriya et al. 2018b). This greatly accelerated burning causes a thermonuclear explosion which completely disrupts and unbinds the star, leaving no compact remnant behind (Fraley 1968; Gal-Yam 2019).

PISNe can only happen in stars with a mass range of around 130-250 $M_{\odot}$ and low to moderate metallicity, which have helium cores of 65-135 $M_{\odot}$ (Heger & Woosley 2002). Very massive high-metallicity stars (above $Z_{\odot}/3$ (Langer et al. 2007)) tend to shed mass during the formation process, leading to insufficient core masses; however, if these stars have magnetic fields which can suppress their mass loss, they may exist even in a solar-metallicity environment (Georgy et al. 2017). If the massive star rotates rapidly, the zero-age main sequence (ZAMS) mass can be as low as 65 $M_{\odot}$ for a PISN progenitor (Chatzopoulos & Wheeler 2012; Yusof et al. 2013); this rotation also helps the star remove its hydrogen through quasi-chemically homogeneous evolution (Yoon et al. 2012). For stars larger than 250 $M_{\odot}$, photodisintegration follows the initial pair-instability collapse and absorbs the excess energy from the earlier stages before runaway burning can cause an explosion, leading to a complete collapse into a black hole (Fryer et al. 2001; Heger et al. 2003). Slow-rotating stars with ZAMS masses lower than 100 $M_{\odot}$ do not have gamma-rays energetic enough to produce electron-positron pairs, and stars with masses of 100-130 $M_{\odot}$ will shed mass through a pulsational pair-instability (PPISN - to be discussed later) and drop below 100 $M_{\odot}$, leading to a lack of pair production (Heger et al. 2003).

PISN are expected to produce very large amount of ^{56}Ni (up to 50 $M_{\odot}$ - amount strongly dependent on the core mass of the progenitor (Heger & Woosley 2002; Takahashi et al. 2016)), leading to an extremely luminous supernova with a rise time of $>$ 100 days (Kasen et al. 2011). Light curve studies of some SLSNe-II (SN2006gy (Agnoletto et al. 2009) and CSS121015 (Inserra et al. 2013)) and faster-evolving SLSNe-I (Quimby et al. 2011), which constitute a major fraction of SLSNe-I (Wang et al. 2019a), show the PISN model is inconsistent with these objects. Predicted early light curves of PISNe (e.g. Chatzopoulos et al. 2015; Dessart et al. 2013; Kasen et al. 2011; Kozyreva et al. 2014; Scannapieco et al. 2005; Whalen et al. 2014) are roughly consistent with those of slowly-declining SLSNe I, and several candidate PISNe have been suggested from this group. Early candidates included SN2006gy, which perhaps had 40 $M_{\odot}$ (almost the entire mass of the stellar core) ejected as ^{56}Ni (Smith et al. 2007), SN2007bi (Gal-Yam et al. 2009), and high redshift SNe SN2213-1745 and SN1000+0216 (Cooke et al. 2012). However, studies soon challenged these assertions (Nicholl et al. 2013). Inserra et al. (2017) found that the declined rates of the light curves 150 days post-peak of four slow-evolving SLSNe I (SN 2007bi, PTF12dam, SN 2015bn, and LSQ14an) are inconsistent with that of light curves reproduced by ^{56}Co (the decay product of ^{56}Ni). The production of a large amount of ^{56}Ni should lead to a large amount of Fe-group elements in the ejecta, which should result in a very red spectrum (e.g. Dessart et al. 2012; Jerkstrand et al. 2016); this is inconsistent with observations in both the early phase (Dessart et al. 2012) and nebular phase (Jerkstrand et al. 2017). Still, there are some slow-rising and slow-declining SLSNe-I would could be PISNe, such as PS1-14bj (Lunnan et al. 2016), PTF10nmn (De Cia et al. 2018; Kozyreva & Blinnikov 2015), and OGLE14-073 (Kozyreva et al. 2018), and the discovery of similar events by the next generation of massive all-sky transient surveys is an interesting prospect. Newer models of 200-250 $M_{\odot}$ progenitors at $Z = 0.001$ do not retain hydrogen in the outer layers of the star and produce relatively fast evolving PISNe, which might be suitable to explain some SLSNe (Kozyreva et al. 2017). The internal mixing of PISNe could reduce their rise times as well (Kozyreva & Blinnikov 2015), but multidimensional simulations of PISNe do not find strong mixing (Chen et al. 2014; Gilmer et al. 2017; Joggerst & Whalen 2011).

When the carbon burning core begins to contract and heat up in a 100-130 $M_{\odot}$ progenitor due to a lack of radiation pressure, the oxygen in the core can ignite in a runaway thermal reaction and exert a pulse outwards, which can eject several solar masses from the stellar envelope - this is known as the pulsational pair-instability and can help reduce the amount of hydrogen in the star (Moriya & Langer 2015). Unlike in PISNe, the oxygen can then stabilize, preventing the thermonuclear supernova. Once the progenitor is brought to 100 $M_{\odot}$, the pair-instability will stop and the star will evolve and undergo a normal CCSN. The final core masses from these objects converges to roughly 35-50 $M_{\odot}$, and the light curves may or may not be superluminous (Woosley 2017). The pre-supernova outbursts may be detectable on their own and mistaken for a supernova, leading to the possibility of multiple supernovae detected from the same progentitor; the great 1843 eruption from Eta Carinae has been suggested as a PPISN (Smith et al. 2018), and the hydrogen-rich supernova iPTF14hls was observed to have five peaks over 600 days (Arcavi et al. 2017), and had an eruption previously detected 60 years prior (Minkowski & Abell 1963). The only convincing superluminous PPISN candidate is SLSN-I iPTF16eh. Lunnan et al. (2018a) presented spectroscopic observations which are naturally explained by a resonance scattering light echo from a circumstellar shell. Models of their observations matched theoretical predictions of shell ejections from PPISNe and imply the progenitor had a helium core mass of about 50-55 $M_{\odot}$ and corresponding to an initial mass of about 115 $M_{\odot}$

(Lunnan et al. 2018a).

1.5.3 Fallback Accretion

The fallback accretion model for was first used to explain how relativistic jets are launched during GRBs (MacFadyen & Woosley 1999; Woosley 1993). In these systems, the iron core collapses into a black hole and the inner mantle material, which has high angular momentum, falls back and forms an accretion disk. The accretion is short term, and can power both the jet, which punches a hole in the stripped progenitor and produces gamma-ray emission, and the accompanying hypernova ((Barnes et al. 2018; Hayakawa & Maeda 2018; Woosley 1993). In this context, the model is generally given the name "collapsar".

In a system where not much inner mantle material immediately falls back, a part of the SN ejecta without enough kinetic energy to escape will eventually fall back (Chevalier 1989; Michel 1988) and accrete onto the compact object (either a neutron star or black hole (Dexter & Kasen 2013; Metzger et al. 2018)) over a longer timescale. This may produce a jet or outflow that does not penetrate the ejecta and has its energy deposited and thermalized within the ejected material. This desposited energy can significantly change the optical light curves, and for a large energy deposition, can power a peak luminosity of $\gtrsim 10^{44}$ erg s^{-1} and reproduce the light curves of SLSNe (Dexter & Kasen 2013; Moriya et al. 2018c). Moriya et al. (2018a) used the fallback model to fit 37 SLSNe-I and found that the fallback powered light curves can be consistent with observed light curves for SLSNe-I with relatively short rising timescales ($\lesssim$ 40 days). This study adopted an energy conversion efficiency of 10^{-3} (Dexter & Kasen 2013) and inferred the mass of the accretion disk to be 2-700 $M_{\odot}$, which is much larger than the estimated 10 $M_{\odot}$ possible for a progenitor with a large core (Aguilera-Dena et al. 2018), but when adopting an energy conversion efficiency of 10^{-1}, which could be reasonable if the major source of the outflow is a jet launched at the inner edge of the accretion disk (Gilkis et al. 2016; Kumar et al. 2008; McKinney 2005), they find that most SLSN light curves can be reproduced while accreting $< 10\ M_{\odot}$.

The fallback model does explain some things more naturally than the pulsar-driven model. Unstable mass accretion (as is often the case in AGN) can explain light curve undulations on various timescales (Gal-Yam 2019), and fallback events can also drive a shock breakout flare, which can explain the observed initial bumps (Kasen et al. 2016). The energy budget of accretion models can also be substantially larger than pulsar-driven models, due to the large reservior of fallback mass and high possible mass-to-energy conversion, which makes them attractive to explain very energetic events with large intergrated luminosity (Gal-Yam 2019). However, light curves from the fallback model and pulsar-driven model can be very difficult to distinguish (Moriya et al. 2018a; Wang et al. 2019a), and no smoking gun signal has yet been proposed, so there is not yet any way to test this model observationally.

1.6 Thesis Overview

The combination of extreme gravity, magnetism, and density make neutron stars a unique laboratory to probe theories like general relativity, quantum electrodynamics, and nuclear physics, so it is important to understand their formation, life cycle, and diversity. Yet, the youngest pulsar astronomers know about is the Kes 75 pulsar, which is around 700 years old (Gotthelf et al. 2000). A central engine, like a fast spinning newborn pulsar or a black hole accretion disk, is thought to power many transients across the electromagnetic spectrum, including SLSNe, HNe, and GRBs. We aim to elucidate the connection between pulsars and transients by predicting the detectability of multiple types of non-thermal signals unique to the pulsar engine and doing follow-up observations on promising candidates to verify or refute these predictions and further our understanding of both compact objects and the luminous transients they may cause. We also want to detect and study newborn pulsars, only a few years after their birth, as new insights in nuclear physics, condensed matter, plasma physics, quantum mechanics, and general relativity could come from identifying, modelling, and observing nascent neutron stars.

1.6.1 Chapter 2 - Broadband Pulsar Wind Nebula Modelling and Low Frequency Predictions

There have been previous arguments that Type-I SLSNe are powered by central engines which inject energy for a long period of time after the core-collapse of the progenitor star. A popular hypothesis is that the engine is a rapidly-rotating pulsar with a magnetic field between $10^{13} - 10^{15}$ G, but quasi-thermal optical emission can not differentiate this from other possible engines. Murase et al. (2016) proposed that radio/submillimetre emission from non-thermal positron-electron pairs in the newborn PWN can be used to identify and characterize pulsars in the supernovae they power. In Chapter 2, we present our models for SLSNe-I early optical quasi-thermal emission and late radio non-thermal emission and use them to calculate the PWN emission from six bright newborn SLSN-I remnants, assuming that they are pulsar-driven, and examine the constraints placed by radio and submillimetre emission. We find that the Atacama Large Millimeter/submillimetre Array (ALMA) or NOrthern Extended Millimeter Array (NOEMA) can detect the submillimetre PWN emission from most of them in a few years after the explosion, while the Karl G. Jansky Very Large Array (VLA) can detect the radio PWN emission from a few of them in a few decades. Follow-up observations could help solve the parameter degeneracy problem in the pulsar-powered SN model and could give clues about young neutron stars scenarios for SLSNe-I and FRBs.

The PWN models used in this chapter, which were based on a simpler PWN model presented by Kotera et al. (2013), were developed previously in Murase et al. (2015, 2016) and Kashiyama et al. (2016), before my involvement with the project. Radio light curves were calculated previously in Murase et al. (2016), and optical light curves in Kashiyama et al. (2016), although this was not the focus of these studies. These studies calculated curves over a range of parameters, however, they never related these light curves back to supernova data. What we do differently in this work is to relate both the optical and radio curves to real supernovae, thus showing the applicability and possible predictive capability of these models as well as establishing the idea of fitting early optical data to predict later radio data. My contribution to this project was to do the optical fitting and plotting of all data, as well as writing of the manuscript - I did not do the calculations for radio light curves in this chapter due to time constraints (we wanted to finish the paper prior to the ALMA proposal deadline, and the code takes some training to pick up) - it was instead done by my collaborators.

Even though this model is broadband and can generate X-ray or gamma-ray light curves, we do not show them in this section for three reasons. The first is that Murase et al. (2015) and Murase et al. (2016) focused more on high-energy photon emission, presenting X-ray and gamma-ray light curves and comparing them to the detectability limits of various telescopes; Metzger et al. (2014) also presented X-ray light curves for pulsar wind nebulae due to ionization breakout. A second, and more important, reason is that the timescale for X-ray emission is usually around 3-6 months, which is much smaller than then timescale for radio and millimetre emission. With radio/millimetre emission, the timescale is long enough for specific supernovae to be targetted in an observational proposal without target-of-opportunity (ToO) observations, so the ability to model specific supernovae and predict their emission is very valuable. For X-ray emission, the timescale is short enough where ToO observations are necessary, so modeling individual supernovae is less valuable than understanding general trends to get an idea of which sources are better for triggering, and this understanding was provided by previous studies. The final reason is that X-ray luminosity is extremely sensitive to the ionization state of the ejecta, especially in the soft X-ray band. While our model has been used to make estimates of hard X-ray and gamma-ray emission, these results are not as robust and require more complicated radiation transfer simulations to give flux predictions with much confidence.

1.6.2 Chapter 3 - Searching Young Superluminous Supernovae Remnants for Late-Time Radio Emission and Fast Radio Bursts

In Chapter 3, we present our VLA observations of ten older SLSNe-I at 3 GHz. We both search fast-sampled visibilities for FRBs and performed a deep imaging search for late-time radio emission predicted in Chapter 2. No FRBs were found, and no emission was detected from nine of the ten sources. However, one SLSN-I, PTF10hgi, is detected in deep imaging with a luminosity of 1.2×10^{28} erg s^{-1}. This detection, along with the recent 6 GHz detection of PTF10hgi in Eftekhari et al. (2019), supports the interpretation that this SLSN-I is powered by a young, fast-spinning ($\sim$ ms spin period) magnetar with $\sim 15\ M_\odot$ of partially ionized ejecta. Our observations are broadly consistent with SLSNe-I being powered by pulsars with fast spin periods, although our non-detections suggest most require more free-free absorption than is inferred for PTF10hgi. We predict that radio observations in the near future or at higher frequencies should be able to detect these systems and constrain properties of the young pulsars and their birth environments.

These observations were the first systematic radio observations of older SLSNe-I remnants, and provided the largest sample (prior to Chapter 4) and deepest constraint on possible PWN emission and FRBs. This was also the first study to directly compare model radio light curves to real late-time radio data, giving us the first test of the pulsar-driven model in this context. The modeling done in this chapter is a direct extension of that done in Chapter 2, using the exact same methodology - this is not the case in Chapter 4. The observations and radio analysis were done by my collaborators, and the introduction and observations section, and part of the conclusions, of the original paper was also written by them (I use a modified version of these sections in this chapter). I did the modeling, both in optical and radio, and wrote the discussion section and part of the conclusions. Section 3.2 was not included in the paper and was written solely for this thesis.

1.6.3 Chapter 4 - Extending the Sample of Radio Constraints

Chapter 4 presents a larger, deeper sample of observations at both radio and submillimetre wavelengths to try to detect additional sources and help further constrain the model. This chapter uses a Markov chain Monte Carlo (MCMC) method with a different magnetar model to fit optical light curves and a modified version of the previously introduced pulsar wind nebula model to calculate radio and millimeter light curves. No new sources are detected, but these observations exclude the model for seven sources and constrain ten others. Further observations of PTF10hgi do broadly support the pulsar-driven model, although a specific parameter set that fits all available data has not yet been found. These observations highlight the need for more sophisticated models and better methods for excluding regions of parameter space, and the underlying difficulty of trying to exclude a scenario with many free parameters.

These observations were the second large set of systematic radio observations, done by a different group, and at two different frequencies. This sample almost triples the dataset from Chapter 3, and provides stronger constraints on most supernovae due to the higher observing frequency. These are also the first late-time millimetre observations of SLSNe-I remnants, which was a key prediction from Chapter 2. The fitting process and optical model is completely different than the process and model from previous chapters, and the radio model used had its physics adjusted to be more consistent with this optical model. This work is the first to highlight the differences between these models, both widely in use, and the difficulty in trying to reconcile them. This is also the first work to try and model the 0.6-100 GHz emission from PTF10hgi, which has now had wideband detections, and put constraints on the parameters. The observations and analysis were again mostly done by my collaborators, and the only section of the original paper I wrote was the PWN section of the discussion. However, due to the large scope of the original paper and my desire to focus this thesis on PWN emission, Chapter 4 was written originally for this thesis instead of using a modified version of the source publication.

1.6.4 Chapter 5 - Dust Formation and Re-Emission of Pulsar Wind Nebula Emission

After discussing the direct detectability of PWN emission in previous chapters, Chapter 5 introduces a method of detecting pulsar wind nebulae through their effect of the surrounding ejecta via the detection of reprocessed PWN emission from dust grains in the supernova ejecta. Dust emission has been observed in many supernova remnants that also have a central neutron star, and we investigate the effect of their nebulae on dust formation and evolution in the supernova ejecta. We study the dependence of dust formation time and dust size on the properties of the ejecta and central pulsar and find that a pulsar can either accelerate or delay dust formation, with timescales of a few months to over 15 years, and reduce the average size of dust by a factor of ~ 10 or more compared to the non-pulsar case. We also find that infrared dust emission may be detectable in typical superluminous supernovae out to $\sim$ 100-1000 Mpc in 2-5 years after the explosion, although this depends sensitively on the low-energy spectral index of the nebula, which is still not well known, but which determines how bright the PWN is in infrared and therefore whether PWN emission or dust re-emission will dominate. We also discuss implications on previous supernova observations and caveats of this approach.

Although studies have been done previously on dust formation in SN remnants, but these studies have neglected the effect of a PWN, and studies of dust sublimation have always been about previously formed dust. This study is the first to account for the pulsar, and to study how it effects dust formation, destruction and emission. The model we use for dust formation were developed by Nozawa & Kozasa (2013) and the formalism for sublimation was developed by Waxman & Draine (2000), but the rest of the chapter is original work. I wrote the code for the model, performed the calculations, plotted the figures, and wrote the original manuscript as well as this chapter.

1.6.5 Chapter 6 - Conclusions and Future Prospects

Finally, in Chapter 6, we give concluding remarks on the outlook of the SLSN and pulsar-driven SN community, summarizing the implications of this research and discuss interesting possibilities for future studies.

Chapter 2

Broadband Pulsar Wind Nebula Modelling and Low Frequency Predictions

There have been previous arguments that Type-I SLSNe are powered by central engines which inject energy for a long time after the core-collapse of the progenitor star. A popular hypothesis is that the engine is a rapidly-rotating pulsar with a magnetic field between $10^{13} - 10^{15}$ G, but quasi-thermal optical emission can not differentiate this from other possible engines. Murase et al. (2016) proposed that radio/submillimetre radiation from non-thermal positron-electron pairs within the newborn PWN can be used to identify and characterize pulsars in the supernovae they power. Here, we present two models, a simple one that can predict the early-time quasi-thermal optical emission and a more detailed one that can characterize the broadband emission from the PWN at late times, and apply them to six bright newborn SLSN-I remnants. We use the optical model to constrain the parameters of the central pulsar and ejecta and then examine the range of possible emission in radio and submillimetre. We find that ALMA or NOEMA can detect the submillimetre PWN emission from most of them in a few years post-explosion, while the VLA can detect the radio PWN emission in a few decades post-explosion. These models and predictions serve as the basis for the VLA and ALMA observations presented in Chapters 3 and 4.

This chapter is based on Omand et al. (2018), and the work was done in collaboration with Kazumi Kashiyama and Kohta Murase.

2.1 Introduction

SLSNe are very rare, but are the brightest UV/optical transients associated with the deaths of massive stars (e.g., Gal-Yam 2012). They are divided into two broad groups based on whether hydrogen is detected in the observed spectra. The ones with hydrogen (Type-II) are likely powered by the ejecta-CSM interaction (Section 1.5.1), while the ones devoid of hydrogen (Type-I) are thought to originate from massive Wolf-Rayet progenitors and be driven by some kind of central engine, usually considered to be either a rapidly-rotating pulsar (e.g., Kasen & Bildsten 2010; Woosley 2010) or an accreting black hole (Dexter & Kasen 2013).

The pulsar-driven model is useful for explaining the diversity of explosions associated with the death of a massive star (see Section 1.4). Models have used pulsars with millisecond periods and strong magnetic fields to power GRBs, HNe, and broad-line Type-Ib or Ic SNe (e.g., Thompson et al. 2004). The GRB-SN was extended to more luminous SN types after a SLSN-like optical counterpart to an ultra-long GRB was discovered (Greiner et al. 2015; Metzger et al. 2015). Stripped-envelope SNe, including ordinary Type-Ibc SNe, may also be powered by pulsars with high magnetic fields. The formation rate of magnetars is estimated to be $\sim$ 10% of the rate of core-collapse SNe (Keane & Kramer 2008), and observed Galactic magnetars that currently possess slow rotation periods is consistent with them forming with relatively low initial spin periods of $\lesssim$ 10 ms (Kashiyama et al. 2016) and losing this energy via spin-down. In order for us to better understand how rapidly-rotating pulsars and magnetars are formed, we must important to understand all dfferent types of of stripped-envelope and Type-I SNe (HNe, SLSNe, and Type-Ibc SNe).

SNe can generally be powered by the decay of radioactive nuclei, but this leads to a parameter degeneracy when only using optical/UV light curve information. Thus, non-thermal emission could be useful to find hidden compact objects, and Galactic PWNe are known to efficiently accelerate positrons and electrons (e.g., Gaensler & Slane 2006; Tanaka & Takahara 2010), which makes non-thermal PWN emission a smoking gun for detection of a nascent neutron star.

If the rotational energy of the NS is efficiently converted into radiation, as the pulsar-powered SN model requires, then the nebula should be luminous in gamma-rays and X-rays. The model predicts sychrotron X-rays from electrons/positrons accelerated by the PWN provide a promising signal, with both hard X-ray (Kashiyama et al. 2016) and soft X-ray (Metzger et al. 2014) emission being detectable by current X-ray satellites such as *NuSTAR* and *Swift*. Some tentative candidates have been proposed based on previous X-ray searches (Margutti et al. 2017; Perna et al. 2008; Perna & Stella 2004), however, the detectability of the X-ray emission, especially in soft X-rays, depends on the properties of the plasma with the SN ejecta, and current X-ray measurements are not very constraining. Higher energy gamma-rays, which are produced via inverse-Compton scattering with thermal supernova photons (Kotera et al. 2013; Murase et al. 2015), are a more direct probe of a central pulsar, but detection of these signals will be more challenging.

Radio radiation can also probe particle acceleration within young PWNe. Murase et al. (2016) did calculations of synchrotron emission from young PWNe and various types of radio and high-energy attenuation, while also considering the connection to FRBs. They showed that persistent radio/millimetre radiation from PWNe embedded in SN remnants should be detectable with current interferometers such as VLA and ALMA. Since young neutron stars are also thought to be candidate progenitors of FRBs, follow-up observations searching for persistent radio/submillimetre counterparts of FRBs were proposed to investigate a possible link. Observations of FRB 121102, the first repeating FRB, were able to localize both its host galaxy and its position within the galaxy as well as discover a persistent counterpart in radio, which was seen by both the European Very Long Baseline Interferometry (VLBI) Network and VLA (Chatterjee et al. 2017; Marcote et al. 2017; Tendulkar et al. 2017).

The host galaxy of FRB 121102 is a low-metallicity, dwarf, star-forming galaxy, which is similar to the observed host galaxies of SLSN-I (Chatterjee et al. 2017; Metzger et al. 2017; Tendulkar et al. 2017). The flux of the persistent FRB 121102 radio counterpart is also broadly consistent with PWN radiation from a decades old pulsar-driven SN (Kashiyama & Murase 2017; Metzger et al. 2017; Murase et al. 2016). These similarities motivate follow-up radio observations of pulsar-driven SN candidates to attempt detection of PWN emission, with SLSN-I being among the most interesting types of objects.

The source of energy injected into the SN ejecta in the pulsar-driven/magnetar-driven model is the rotational energy from the newborn pulsar, which manifests as a strongly magnetized relativisitic wind. The injected wind drives reverse and forward shocks, and the reverse shocked region is often referred to as a PWN. In the PWN, the wind dissipates and leptons (mostly electrons and positrons) can be accelerated to ultra-relativistic energies. Non-thermal radiation from these electrons and positrons, as well as heavier leptons, has been the subject of studies for many years (e.g., Gaensler & Slane 2006; Tanaka & Takahara 2010). Modeling Galactic PWNe has shown that most of the rotational energy of the neutron star is used to accelerate particles, and accelerated positrons and electrons lose energy via non-radiative adiabatic cooling as well as sychrotron emission and inverse Compton scattering, which gives rise to a broadband spectrum from radio to gamma-rays (Section 1.3.2).

A natural assumption is that the pulsar wind dissipation and the particle acceleration that results can occur in the early evolution of the PWN. However, early-time non-thermal radiation is completely absorbed or down-scattered in the dense SN ejecta, and diffuses out of the ejecta as quasi-thermal optical supernova emission (Kasen & Bildsten 2010; Woosley 2010). The magnetic field strength and initial spin period of the pulsar can be inferred by fitting the optical light curve near supernova peak luminosity (e.g., Inserra et al. 2013; Nicholl et al. 2013; Pastorello et al. 2010). Once the density, and thus the broadband opacity, decreases due to expansion of the ejecta, non-thermal radiation can escape from the supernova ejecta without being absorbed or scattered. Emission in the radio band can only escape both the PWN and dense SN ejecta without being severely attenuated after a significant amount of time; this escape timescale depends on photon energy, and can vary from months to decades.

This stuation is shown schematically in Figure 2.1. We use two different models to describe the two situations: the model for quasi-thermal optical emission (Section 2.2) works well in the early phases and is computationally inexpensive, but is not reliable at later times, while the model for non-thermal emission (Section 2.4) reliably and self-consistently calculates non-thermal emission for decades after the explosion, but is much more computationally expensive. The quasi-thermal model was developed in Kashiyama et al. (2016) while the non-thermal model was developed in Murase et al. (2015).

In this chapter, we calculate the expected radio/millimetre emission from newborn SLSN-I remnants for the first few decades post-explosion. First, we present the pulsar-driven model for quasi-thermal optical emission (Section 2.2) and apply it to a few of the brightest known SLSN-I to fit the quasi-thermal optical light curves (Section 2.3). Then, we present the model for late-time non-thermal emission (Section 2.4) and, using the parameters obtained from optical fits (initial NS magnetic field strength, initial NS rotation period, and supernova ejecta mass), we calculate radio and millimetre emission from the PWN (Section 2.5). We compare this PWN emission with the detection limits of ALMA and VLA and discuss possible constraints that observations could place on the pulsar-driven model.

2.2 Modelling Quasi-Thermal Optical Emission

2.2.1 Spin-Down

The time evolution of the rotational energy of the newborn pulsar is calculated via (Ostriker & Gunn 1969)

$$-\frac{dE_{\rm rot}}{dt} = L_{\rm em} + L_{\rm gw}, \tag{2.1}$$

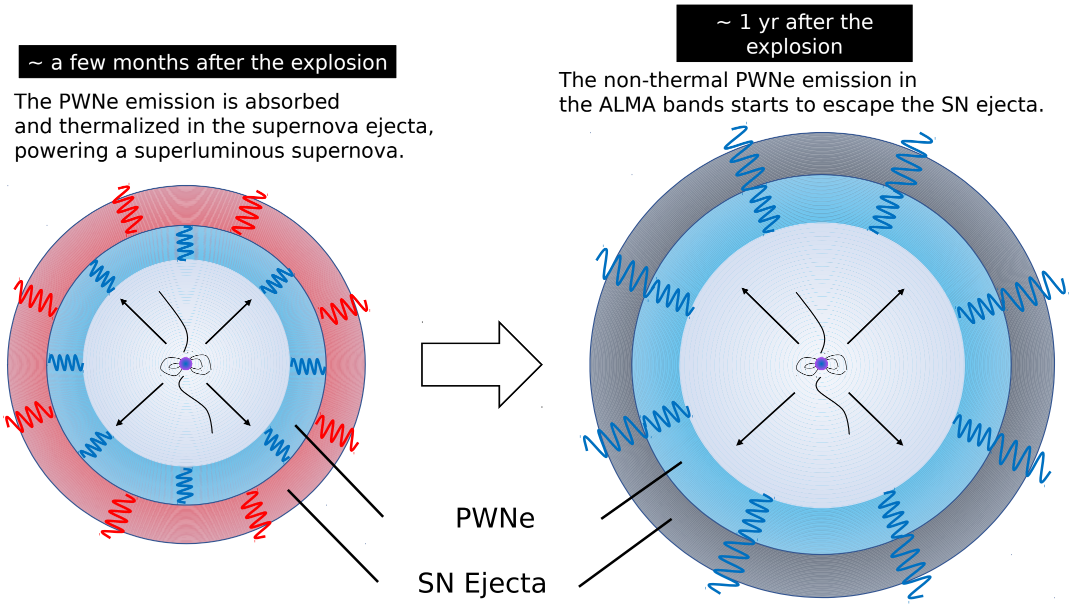

FIGURE 2.1: Schematic picture of the rapidly-rotating pulsar model for SLSNe. In a PWN, electrons and positrons from a newborn pulsar or magnetar are efficiently accelerated to very high energies. Non-thermal emission is converted into thermal radiation while the ejecta is dense enough, but at later times, the system becomes transparent to broadband non-thermal emission. The timescale for photon escape depends on photon energy - while the time for submillimetre AMLA emission to escape is $\sim$ 1 year after the explosion, the timescale for VLA band emission to escape is $\sim$ 10 years. The situation on the left is described by the model in Section 2.2 and the situation on the right is described by the model in Section 2.4.

where the electromagnetic and graviational wave luminosities are given by

$$L_{\rm em} = \frac{\mu^2 \Omega^4}{c^3}(1 + C\sin^2\chi_\mu) \text{ and} \tag{2.2}$$

$$L_{\rm gw} = \frac{2}{5}\frac{G(\epsilon_G I)^2 \Omega_{\rm pat}^6}{c^5}(1 + 15\sin^2\chi_{\epsilon_G})\sin^2\chi_{\epsilon_G} \tag{2.3}$$

respectively. $\mu = B_{\rm dip}R^3/2$ is the magnetic moment, Ω is the rotational angular frequency, χ_μ is the angle between the magnetic and rotational axes, $C \sim 1$ is a prefactor, $\epsilon_G \equiv \Delta I/I$ is the deformation rate (we assume magnetically deformed rotation (Cutler 2002; Dall'Osso et al. 2009; Stella et al. 2005)), $\Omega_{\rm pat}$ is the pattern angular frequency, and χ_{ϵ_G} is the angle between the deformation and rotational axes (Cutler & Jones 2001). Equation 2.2 is motivated by numerical simulations (Gruzinov 2005; Spitkovsky 2006; Tchekhovskoy et al. 2013) and is a factor $3(1 + C\sin^2\chi_\mu)/2\sin^2\chi_\mu \sim 5$ larger than Equation 1.15.

We assume an isotropic magnetized wind for simplicity. This assumption, and thus this model, fails if the explosion becomes sufficiently non-spherical due to the formation of a jet. Although jet formation is still uncertain, the timescale for the prompt emission from an LGRB is around $100 - 1000$ s, which cooresponds to the spin-down timescale of a NS with $B_{\rm dip} \sim 10^{15}$ G and $P \sim 1$ ms. If this timescale is comparable to the cooling or Kelvin-Helmholtz timescale ($\tau_{\rm KH} \sim GM_{\rm NS}^2/L_{\rm neutrino}R_{\rm NS} \lesssim 100$ s) (Thompson et al. 2004) of the proto-NS, which is the diffusion timescale for neutrinos generated by the core-collapse to escape the proto-NS, then the baryons that are ablated from the proto-NS surface due to a neutrino-driven wind can be loaded into the dipolar magnetic field as it is amplified shortly after collapse. If this happens, the highly-magnetized relativistic jet could punch a hole in the progenitor star (Bucciantini et al. 2007, 2008) and the GRB prompt emission can escape. Therefore, in order to avoid jet formation during pulsar spin down, we only consider spin-down timescales $\gg 100$ s and $B_{\rm dip} < 10^{15}$ G.

We also assume magnetically deformed rotation of the neutron star (Cutler 2002; Dall'Osso et al. 2009; Stella et al. 2005); once its inner toroidal magnetic fields are amplified and become comparable to the magnetar value, it deforms and becomes oblate due to a magnetic pinch (Cutler 2002; Gualtieri et al. 2011; Kiuchi & Yoshida 2008). The deformation rate is

$$\epsilon_G = \frac{15}{4}\frac{\mathcal{E}_B}{|W|} \sim 2.5 \times 10^{-4}\left(\frac{B_t}{10^{16}\,{\rm G}}\right)^2, \tag{2.4}$$

where $|W| \approx M_{ns}c^2 \times 0.6\mathcal{C}/(1 - 0.5\mathcal{C}) \sim 4.4 \times 10^{53}$ erg is the gravitational binding energy for a NS with a compactness parameter $\mathcal{C} = GM_{ns}/R_{ns}c^2 \sim 0.17$ (Lattimer & Prakash 2001). Its deformation axis does not generally coincide with its rotation axis, which causes the NS to precess around its rotation axis (Mestel & Takhar 1972) and eventually evolve into a more prolate shape, which is a plausible configuration for emisson of gravitational waves ($\chi_\mu = \chi_{\epsilon_G} = \pi/2, \Omega = \Omega_{\rm pat}$). The gravitational wave emission only occurs when the viscous damping timescale of the neutron star is shorter than its magnetic braking timescale, which can equivalently be stated as (Dall'Osso et al. 2009)

$$B_t < 2.4 \times 10^{16}\,{\rm G}\left(\frac{P_i}{\rm ms}\right)^{-1}\left(\ln\left[320\left(\frac{P_i}{\rm ms}\right)^2\left(\frac{B_{\rm dip}}{10^{14}\,{\rm G}}\right)^{-2} + 1\right]\right)^{1/2}. \tag{2.5}$$

2.2.2 Ejecta Dynamics

We assume that the density profile of the supernova ejecta is

$$\rho_{\mathrm{ej}} \approx \frac{3-\delta}{4\pi}\frac{M_{\mathrm{ej}}}{R_{\mathrm{ej}}^3}\left(\frac{R}{R_{\mathrm{ej}}}\right)^{-\delta}, \tag{2.6}$$

with $\delta = 1$ for the index, so most of the mass is around $\mathrm{R} \approx \mathrm{R}_{\mathrm{ej}}$. This index is motivated by 1D simulations by Kasen & Bildsten (2010), but more recent multi-dimensional simulations suggest that the index may be higher at later times (Suzuki & Maeda 2017, 2019). The ejecta radius evolves as

$$\frac{dR_{\mathrm{ej}}}{dt} = V_{\mathrm{ej}}. \tag{2.7}$$

Without energy ejection post-explosion, the velocity of the ejecta is almost constant up to the Sedov radius, but when a newborn pulsar exists, a magnetized wind accelerates the ejecta with

$$\frac{dE_{\mathrm{K}}}{dt} = \frac{E_{\mathrm{int}}}{t_{\mathrm{dyn}}}, \tag{2.8}$$

where $E_{\mathrm{K}} \approx M_{\mathrm{ej}}V_{\mathrm{ej}}^2/2$ is the ejecta kinetic energy, E_{int} is the total internal energy of the ejecta, and $t_{\mathrm{dyn}} = R_{\mathrm{ej}}/V_{\mathrm{ej}}$ is the ejecta dynamical timescale. The energy injection from the PWN occurs at the shock between the pulsar wind and supernova ejecta. The radius of the shocked wind region increases as

$$\frac{dR_{\mathrm{w}}}{dt} = V_{\mathrm{nb}} + \frac{R_{\mathrm{w}}}{t}, \tag{2.9}$$

where V_{nb} is obtained from pressure equilibrium:

$$V_{\mathrm{nb}} \approx \sqrt{\frac{7}{6(3-\delta)}\frac{\int L_{\mathrm{em}} \times \min[1, \tau_{\mathrm{T}}^{\mathrm{nb}}V_{\mathrm{nb}}/c]dt}{M_{\mathrm{ej}}}\left(\frac{R_{\mathrm{ej}}}{R_{\mathrm{w}}}\right)^{3-\delta}}, \tag{2.10}$$

where $\min[1, \tau_{\mathrm{T}}^{\mathrm{nb}}V_{\mathrm{nb}}/c]$ represents the fraction of spin-down luminosity that is deposited into the SN ejecta and $\tau_{\mathrm{T}}^{\mathrm{nb}} = (R_w/R_{\mathrm{ej}})\tau_{\mathrm{T}}^{\mathrm{ej}}$, where Equation 2.14 gives a formulation for $\tau_{\mathrm{T}}^{\mathrm{ej}}$. If $R_{\mathrm{w}} \geq R_{\mathrm{ej}}$ in the calculation, we take $R_{\mathrm{w}} \approx R_{\mathrm{ej}}$.

2.2.3 Electromagnetic Emission

The time dependency of the total internal energy E_{int} is

$$\frac{dE_{\mathrm{int}}}{dt} = -L_{\mathrm{sn}} - \frac{E_{\mathrm{int}}}{t_{\mathrm{dyn}}} + f_{\mathrm{dep,em}}L_{\mathrm{em}} + f_{\mathrm{dep,^{56}Ni}}L_{^{56}\mathrm{Ni}} + f_{\mathrm{dep,^{56}Co}}L_{^{56}\mathrm{Co}}. \tag{2.11}$$

The terms on the right-hand side of the equation represent the loss of energy via quasithermal supernova emission, the loss of energy via adiabatic expansion, the injection of energy from the pulsar wind, the decay of ^{56}Ni, and the decay of ^{56}Co respectively. L_{sn} can be given as

$$L_{\mathrm{sn}} \approx \frac{E_{\mathrm{int}}}{t_{\mathrm{esc}}^{\mathrm{ej}}}, \tag{2.12}$$

where $t_{\rm esc}^{\rm ej}$ represents the thermal escape time of photons from the ejecta (also called the diffusion time $t_{\rm dif}$),

$$t_{\rm esc}^{\rm ej} = \frac{\tau_{\rm T}^{\rm ej} R_{\rm ej}}{c}, \tag{2.13}$$

where $\tau_{\rm T}^{\rm ej}$ represents the optical depth of the ejecta ($c/\tau_{\rm T}^{\rm ej}$ is called the diffusion velocity), and

$$\tau_{\rm T}^{\rm ej} = \frac{(3-\delta)\kappa M_{\rm ej}}{4\pi R_{\rm ej}^2}, \tag{2.14}$$

where κ is the Thompson opacity. κ generally depends on temperature, composition, and ionization state, which can all change in time, but we set it constant at 0.1 $\rm g^{-1}$ $\rm cm^2$, which is a typical value near the optical peak of a SLSN; this is further justified in Section 2.3. The emission temperature can be estimated as

$$T_{\rm sn} = \left(\frac{E_{\rm int}}{a\mathcal{V}_{\rm ej}}\right)^{1/4}, \tag{2.15}$$

where $\mathcal{V}_{\rm ej}$ is the spherical ejecta volume and a here is the radiation constant. The method of calculating supernova emission shown here is equivalent to using the Arnett model with a uniform ejecta temperature, instead of having the temperature depend on position as in the original model (Arnett 1982; Chatzopoulos et al. 2012).

There are several absorption and scattering processes which cause non-thermal photons across the entire spectrum to be thermalized or down-scattered as they propagate through the supernova ejecta. The dominant type of interaction is dependent on the photon energy: Bethe-Heitler (BH) pair production above 10 MeV, where a gamma-ray photon interacts with a virtual photon from an electron to produce an electron-positron pair; Compton scattering in the 10 keV $\lesssim h\nu \lesssim$ 10 MeV range; photoelectric (bound-free) absorption in the 10 eV $\lesssim h\nu \lesssim$ 10 keV range; and free-free and bound-bound absorption at lower energies. We calculate the deposition fraction of photon energy to be

$$f_{\rm dep} = \max[1, f_{\rm dep,sc} + f_{\rm dep,\,ab}] \tag{2.16}$$

with the contributions for scattering and absorption estimated to be

$$f_{\rm dep,\,sc} = 1 - (1 - K_{\rm comp})^{\max[\tau_{\rm comp}, \tau_{\rm comp}^2]} \text{ and} \tag{2.17}$$

$$f_{\rm dep,\,ab} = 1 - \exp(-\tau_{\rm BH} - \tau_{\rm pe}), \tag{2.18}$$

where $K_{\rm comp}$ represents the inelasticity of Compton scattering, $\tau_{\rm comp}$ represents the optical depth for Compton scattering, $\tau_{\rm BH}$ represents the optical depth for Bethe-Heitler pair production, and $\tau_{\rm pe}$ represents the optical depth of photoelectric absorption (Murase et al. 2015). The optical depth for photoelectric absorption is

$$\tau_{\rm pe} = \frac{(3-\delta) K_{\rm pe} M_{\rm ej}}{4\pi R_{\rm ej}^2}, \tag{2.19}$$

where

$$K_{\rm pe} = 5\zeta \left(\frac{E_\gamma}{10\ \rm keV}\right)^{-3} \rm g^{-1}\ cm^2 \tag{2.20}$$

is the opacity for oxygen dominated ejecta. $0 \leq \zeta \leq 1$ is a scaling factor that is time-dependent and can be calculated from the effective ionization fraction; it increases as the ejecta becomes less ionized since there are more bound electrons to absorb the photons. This value is still very uncertain, and to solve for it would require full radiation hydrodynamics simulations which account for ionization in the ejecta. Since these simulations are difficult and have not yet been done in the case of pulsar-driven supernovae, we set ζ to the midpoint 0.5 for simplicity. It is worth noting that the energy in soft X-rays is always subdominant, and the SN light curve is not sensitive to photoelectric absorption until $\gtrsim 100$ days after the explosion.

Highly relativistic electrons are injected at the interface between the strongly magnetized pulsar wind and the supernova ejecta and further accelerated by magnetic turbulence or Fermi acceleration across the shock; these electrons then cool rapidly via sychrotron radiation and inverse Compton scattering. The inverse Compton scattered photons have enough energy to produce a positron/electron pair by two photon annihilation, which can lead to an electromagnetic cascade. This effect can be calculated by assuming an electron injection spectrum of (Murase et al. 2015)

$$E_e \frac{d\dot{e}^{\rm inj}_{E_e}}{d\gamma_e} \propto \begin{cases} (\gamma_e/\gamma_b)^{-q_1} & (\gamma_e < \gamma_{e,b}), \\ (\gamma_e/\gamma_b)^{-q_2} & (\gamma_b < \gamma_e < \gamma_{\rm M}), \end{cases} \tag{2.21}$$

where q_1 = 1-1.5, q_2 = 2.5-3, and $\gamma_b \sim 10^{4.5-6}$; these are motivated by observations of young Galactic PWNe (Tanaka & Takahara 2010). By equating the acceleration timescale $t_{\rm acc} = \eta\gamma_e m_e c/eB$, where $\eta \geq 1$ is a pre-factor that accounts for acceleration efficiency, and the sychrotron cooling timescale $t_{\rm syn} = 3m_e c/4\sigma_T U_B \gamma_e$, where U_B is the magnetic energy density calculated in Equation 2.26, the maximum electron energy can be estimated as $\gamma_{\rm M} \approx (6\pi e/\eta\sigma_T B)^{1/2}$. The electron/positron pair multiplicity $\mu_\pm$ (the number of pairs which can be produced by each lepton accelerated by the PWN (Timokhin & Harding 2015)) and break Lorentz factor γ_b can be related using

$$\mu_\pm \sim 10^9 \epsilon_e \gamma_{b,5}^{-1} \left(\frac{\gamma_b}{100}\right)^{q_1-1} \left[\frac{(2-q_1)(q_2-2)}{(q_1-1)(q_2-q_1)}\right] B_{\rm dip,14} P_{-2.5}^{-2}, \tag{2.22}$$

where ϵ_e is fraction of energy that goes into particles.

The factor for total energy deposited by the magnetized pulsar wind is

$$f_{\rm dep,em} = \frac{\int f_{\rm dep}(E_\gamma) E_\gamma \frac{dN_\gamma}{dE_\gamma} dE_\gamma}{\int E_\gamma \frac{dN_\gamma}{dE_\gamma} dE_\gamma} \tag{2.23}$$

where $f_{\rm dep}(E_\gamma)$ is the energy deposition fraction for photons of energy E_γ, and dN_γ/dE_γ is the wind nebula spectrum due to the injected electrons in Equation 2.21, which can also be approximated as a broken power law (Murase et al. 2015)

$$E_\gamma \frac{dN_\gamma}{dE_\gamma} = \frac{\epsilon_e L_{\rm em}}{\mathcal{R}_b E^b_{\rm syn}} \begin{cases} (E_\gamma/E^b_{\rm syn})^{-q_1/2} & (E_\gamma < E^b_{\rm syn}), \\ (E_\gamma/E^b_{\rm syn})^{-1} & (E^b_{\rm syn} < E_\gamma < \epsilon_{\gamma,\rm max}) \end{cases} \tag{2.24}$$

with $\mathcal{R}_b \sim 2/(2-q_1) + \ln(\epsilon_{\gamma,\rm max}/E_\gamma/E^b_{\rm syn})$, $\epsilon_e = 1 - \epsilon_B \approx 1$, and the break photon energy

$$E^b_{\rm syn} = \frac{3}{2}\hbar\gamma_b^2 \frac{eB}{m_e c} \tag{2.25}$$

We take the early PWN magnetic field energy density to be

$$U_B = \epsilon_B \frac{3\int L_{\rm em} dt}{4\pi R_w^3}, \tag{2.26}$$

where the fraction of energy that enters the magnetic field $\epsilon_B = 10^{-3} - 10^{-2}$ (e.g., Atoyan & Aharonian 1996; de Jager et al. 1996; Kennel & Coroniti 1984; Tanaka & Takahara 2010). The PWN magnetic field B is estimated as

$$B = 36\,\mathrm{G}\,P_{i,-2.5}^{-1}\epsilon_{B,-2}^{1/2}\left(\frac{V_{\mathrm{ej}}}{5000\ \mathrm{km\ s^{-1}}}\right)^{-3/2} t_7^{-3/2}\left[1-(1+t/t_{\mathrm{SD}})^{-1}\right]^{1/2}, \qquad (2.27)$$

the t_{SD} is the pulsar spin-down time (Equation 1.21).

The luminosity from ^{56}Ni decay is

$$L_{^{56}\mathrm{Ni}} = M_{^{56}\mathrm{Ni}}\epsilon_{^{56}\mathrm{Ni}}\exp\left(-\frac{t}{t_{^{56}\mathrm{Ni}}}\right), \qquad (2.28)$$

$$L_{^{56}\mathrm{Co}} = M_{^{56}\mathrm{Ni}}(\epsilon_{^{56}\mathrm{Co}} - \epsilon_{^{56}\mathrm{Ni}})\exp\left(-\frac{t}{t_{^{56}\mathrm{Co}}}\right), \qquad (2.29)$$

where $M_{^{56}\mathrm{Ni}}$ is the ^{56}Ni mass, $\epsilon_{^{56}\mathrm{Ni}}$ = 3.9 × 10^{10} erg s^{-1} g^{-1}, $\epsilon_{^{56}\mathrm{Co}}$ = 6.8 × 10^{9} erg s^{-1} g^{-1}, $t_{^{56}\mathrm{Ni}}$ = 8.8 days, and $t_{^{56}\mathrm{Co}}$ = 111.3 days. We estimate the deposition fraction from gamma rays as

$$f_{\mathrm{dep},\,^{56}\mathrm{Ni(Co)}} = \frac{\sum_i f_{\mathrm{dep}}(\epsilon_{^{56}\mathrm{Ni(Co)},\,i})\mathcal{P}_{^{56}\mathrm{Ni(Co)},\,i}\epsilon_{^{56}\mathrm{Ni(Co)},\,i}}{\sum_i \mathcal{P}_{^{56}\mathrm{Ni(Co)},\,i}\epsilon_{^{56}\mathrm{Ni(Co)},\,i}}, \qquad (2.30)$$

where $\epsilon_{^{56}\mathrm{Ni(Co)},\,i}$ $\mathcal{P}_{^{56}\mathrm{Ni(Co)},\,i}$ are the mean decay energy and decay probability. We consider the 6 ^{56}Ni channels and 11 ^{56}Co from (Nadyozhin 1994) and we assume that all the energy from positron emission is thermalized.

2.2.4 Peak Time and Luminosity

The peak of the SLSN will occur around when the velocity of photon diffusion through the ejecta becomes equal to the ejecta velocity, and it follows that the peak time equivalent to both the diffusion time and dynamical time under this condition. Using Equation 2.13 here gives

$$t_{\mathrm{dif}} = \frac{\tau_{\mathrm{T}}^{\mathrm{ej}} R_{\mathrm{ej}}}{c} = \frac{R_{\mathrm{ej}}}{V_{\mathrm{ej}}}, \qquad (2.31)$$

where using Equation 2.14 gives the ejecta velocity

$$V_{\mathrm{ej}} = \frac{4\pi c R_{\mathrm{ej}}^2}{(3-\delta)\kappa M_{\mathrm{ej}}}, \qquad (2.32)$$

Solving for R_{ej} here gives

$$R_{\mathrm{ej}} = \sqrt{\frac{(3-\delta)\kappa M_{\mathrm{ej}}}{4\pi c V_{\mathrm{ej}}}}. \qquad (2.33)$$

However, since the ejecta kinetic energy comes almost entirely from the rotational energy of the central pulsar, then the velocity can also be written

$$V_{\mathrm{ej}} \approx \sqrt{\frac{2E_{\mathrm{rot}}}{M_{\mathrm{ej}}}} = \sqrt{\frac{I}{M_{\mathrm{ej}}}}\frac{2\pi}{P}. \qquad (2.34)$$

using Equation 1.14. Using Equations 2.31, 2.33, and 2.34, we can calculate the peak time

$$t_{\text{peak}} \approx \frac{P^{1/2} M_{\text{ej}}^{3/4} \kappa^{1/2}}{\pi I^{1/4} c^{1/2}} \sqrt{\frac{3-\delta}{8}}. \tag{2.35}$$

$$\approx 25 \text{ days} \left(\frac{P}{1 \text{ ms}}\right)^{1/2} \left(\frac{M_{\text{ej}}}{5M_{\odot}}\right)^{3/4}. \tag{2.36}$$

It is worth noting that the peak width is roughly comparable to the peak time.

The luminosity at the peak time is around

$$L_{\text{peak}} \approx \frac{E_{\text{int}}}{t_{\text{dif}}}, \tag{2.37}$$

where E_{int} can be approximated as

$$E_{\text{int}} \approx E_{\text{rot}} \left(\frac{t_{\text{dif}}}{t_{\text{SD}}}\right)^{\pm 1}, \tag{2.38}$$

where the index is positive if $t_{\text{dif}} \leq t_{\text{SD}}$ and negative if $t_{\text{dif}} \geq t_{\text{SD}}$.

If $t_{\text{dif}} \leq t_{\text{SD}}$, then the peak luminosity is just the spin-down power of the pulsar from Equation 1.15 (Equation 2.2 in our model). Equation 1.15 can also be written to depend on P and B_{char}

$$L_{\text{peak}} \approx 2.9 \times 10^{45} \text{ erg s}^{-1} \left(\frac{P}{1 \text{ ms}}\right)^{-4} \left(\frac{B_{\text{char}}}{10^{13} \text{ G}}\right)^{2}. \tag{2.39}$$

If $t_{\text{dif}} \geq t_{\text{SD}}$, then L_{peak} becomes

$$L_{\text{peak}} \approx \frac{12\pi^2 I^{5/2} c^4}{R_{\text{NS}} \kappa (3-\delta)} B_{\text{char}}^{-2} P^{-1} M_{\text{ej}}^{-3/2}, \tag{2.40}$$

$$\approx 5.6 \times 10^{46} \text{ erg s}^{-1} \left(\frac{P}{1 \text{ ms}}\right)^{-1} \left(\frac{B_{\text{char}}}{10^{13} \text{ G}}\right)^{-2} \left(\frac{M_{\text{ej}}}{5M_{\odot}}\right)^{-3/2}. \tag{2.41}$$

2.2.5 Summary

This model has six input parameters overall: the initial pulsar spin period P, the initial pulsar toroidal/poloidal magnetic field B, the supernova ejecta mass M_{ej}, the ejected nickel mass M_{Ni}, the initial explosion energy from the neutrino mechanism E_{SN}, and the Thompson opacity κ. The model outputs optical light curves in bands that can be modified by the user, allowing us to produce model curves in $UBVR$ and $ugriz$ filters, as well as any custom filters.

The main assumption that is unreliable at later times is the assumption of the photon spectrum in the wind nebula - Equation 2.24. To solve this self-consistently, we should calculate from the electron injection spectrum using a more complicated energy transport model within the PWN, which includes a more complicated treatment of pair cascades. The early quasi-thermal emission is not sensitive to the spectral shape, since all the photons are absorbed and re-emitted, so this treatment is justified for modelling that emission, but not for non-thermal emission once it escapes the ejecta.

Name	RA	Dec	z	D_L (Gpc)	Band	References
iPTF13ajg	16:39:03.95	+37:01:38.4	0.7403	4.6736	R	Vreeswijk et al. (2014)
SN2012il	09:46:12.91	+19:50:28.7	0.175	0.8686	r	Inserra et al. (2013)
SN2013dg	13:18:41.35	-07:04:43.0	0.1918	0.9615	r	Nicholl et al. (2014)
SN2010gx	11:25:46.71	-08:49:41.4	0.2297	1.1766	r′	Pastorello et al. (2010)
SN2011ke	13:50:57.77	+26:16:42.8	0.1428	0.6950	V	Inserra et al. (2013)
SN2015bn	11:33:41.57	+00:43:32.2	0.1136	0.5427	V	Nicholl et al. (2016b)

TABLE 2.1: Properties of SLSNe-Ic that were selected for this study.

2.3 Fitting SLSNe Optical Light Curves

2.3.1 Supernova Sample

We use optical photometric data from the Open Supernova Catalog [1] (Guillochon et al. 2017) using the search criteria "SLSN-Ic". Since we effectively need to fit the peak luminosity and diffusion time, we select sample SNe which have observed data both before and after peak luminosity in a single band. There are only six SLSNe that fit the aformentioned criteria and can be used in this study; we summarize their properties in Table 2.1 and show their light curves in Figure 2.2.

2.3.2 Applying the Model to Data

We vary three model parameters: the initial spin period P of the NS, the initial magnetic field $B_{13} = B/(10^{13}\ \mathrm{G})$ of the neutron star, and the supernova ejecta mass M_{ej}. Other parameters in the model, which we fix for this study, are the nickel mass M_{Ni}, the supernova explosion energy E_{SN}, and the ejecta opacity κ; we set them to 0.1 $M_{\odot}$, 10^{51} erg, and 0.1 g cm^{-2} respectively. Varying the nickel mass makes almost no difference to the light curve luminosity unless $M_{\mathrm{Ni}} \gtrsim 1\ M_{\odot}$, since the luminosity of the system is mostly generated by the spin-down energy of the pulsar, and 0.1 $M_{\odot}$ is more usual for CCSNe (see, e.g., Drout et al. 2011); the initial explosion energy is typical for ordinary supernovae, but irrelevant in this case, since the energy deposition into the ejecta will be dominated by the rotational energy of the pulsar, which will inject $\gtrsim 10^{52}$ erg within a few weeks of the explosion; and the ejecta opacity is uncertain, but line opacity values imply that the ejecta opacity is between 0.01-0.2 g cm^{-2} at all times, so our value will never be off by a factor of more than a few at any time in the supernova evolution (Inserra et al. 2013; Kleiser & Kasen 2014). We fit the light curves to the model by eye without the aid of any software or statistical measurement. The model does not correct for extinction; this can be justified for this sample because the known $E(B-V)$ values are $\lesssim 0.04$ (Guillochon et al. 2017) for every supernova in our sample and the host galaxy extinction is expected to be low, since most SLSN reside in dwarf, low metallicity galaxies (Lunnan et al. 2014). The expected change in luminosity would be at most 0.15 mag, which does not significantly affect the inferred parameters. We fit only the brightest 1.5 magnitudes of the light curve due to the low reliability of the model at later times (see Section 2.2 for details).

We investigate the parameter range of $P \geq 1.0$ ms and $M_{\mathrm{ej}} \geq 1.0\ M_{\odot}$. The period condition cooresponds to the neutron star mass-shedding limit (Watts et al. 2016) while the mass condition is a reasonable limit for core collapse supernovae, with the notable exception of ultra-stripped supernovae (Tauris et al. 2015). We found that all

---

[1] https://sne.space/

Name	B_{13} at 1 ms	$M_{\rm ej}$ ($M_{\odot}$) at 1 ms	$P_{\rm max}$ (ms)	B_{13} at $P_{\rm max}$	$M_{\rm ej}$ ($M_{\odot}$) at $P_{\rm max}$
iPTF13ajg	1.6	5.0	1.1	1.3	3.5
SN2012il	8.0	7.0	2.4	3.0	1.0
SN2013dg	13.0	14.0	4.1	4.0	1.4
SN2010gx	4.5	10.0	1.6	3.5	3.5
SN2011ke	7.5	9.5	2.4	2.9	1.3
SN2015bn	2.1	17.0	1.4	1.0	5.0

TABLE 2.2: Model parameters for each SN found to fit the optical light curve data. Rotation periods were investigated from 1.0 ms to $P_{\rm max}$, with any period above $P_{\rm max}$ either having too slow a decline, not having enough luminosity, or having a shape inconsistent with the observed data - likely due to having a low ejecta mass. Data and cooresponding fit for P = 1.0 ms are shown in Figure 2.2.

SLSNe in our sample can be fit by a P = 1.0 ms model, as shown in Figure 2.2. Cooresponding $(B_{13}, M_{\rm ej})$ are given in Table 2.2, and they span the range from $B_{13} \sim 1 - 15$ and $M_{\rm ej} \sim 5 - 15$ M$_{\odot}$.

However, since there is a parameter degeneracy between $(P, B_{13}, M_{\rm ej})$ due to the fitting essentially just the diffusion time and peak luminosity, the SLSN data can also be fit by models with slower initial pulsar spin periods. The pulsar spin-down luminosity is sensitive to the initial pulsar rotation period; since the supernova peak luminosity is determined by the spin-down luminosity at the diffusion time, with $L_{\rm SN} \propto P^{-1}B^{-2}M_{\rm ej}^{-3/2}$ if $t_{\rm dif} \geq t_{\rm SD}$ and $L_{\rm SN} \propto P^{-4}B^{2}$ if $t_{\rm dif} \leq t_{\rm SD}$ (See Equations 2.39 and 2.41), a slower period results in a dimmer SN in both cases. A slower spin also suppresses acceleration of the ejecta and results in a longer diffusion time, with $t_{\rm dif} \propto P^{1/2}M_{\rm ej}^{3/4}$, thus leading to the peak time of the supernova being longer. These effects, resulting from an increased spin period, can be compensated for by changing the pulsar magnetic field and supernova ejecta mass.

In Table 2.2, we also show the model with the slowest spin $P_{\rm max}$ that fits each optical light curve. The longest spin periods that can give a reasonable fit to the light curves range from 1.1-4.1 ms depending on SNe; a slower spin period for any of these would either give the luminosity too low, or bring the magnetic field or ejecta mass low enough that the light curve shape would become inconsistent with the data (Figure 2.3).

The parameters found for SN2010gx, SN2011ke, and SN2012il are different from those found in Inserra et al. (2013). They have best-fit models with a larger magnetic field B by a factor of ~ 10 and with a larger spin period P by a factor of $\sim$ a few. One reason for this discrepancy is that Inserra et al. (2013) uses the classical dipole spin-down formula and we use a formula motivated by numerical simulations (Equation 2.2). The numerically inspiring spin-down has a factor $3(1 + C\sin^2\chi_{\mu})/2\sin^2\chi_{\mu} \sim 5$ larger spin-down luminosity than the classical dipole formula for fixed (P, B) (see Kashiyama et al. (2016) and Section 2.2 for a discussion). Another reason is that our model ejecta has an optical depth smaller than theirs by a ~ 1.5 factor for the same $M_{\rm ej}$, κ, and ejecta radius, due to a different assumption of the supernova ejecta profile; they use ejecta with a homogeneous core which is surrounded by a homologous envelope with density profile $\rho \propto v_{\rm ej}^{-10}$, with $v_{\rm ej}$ here being the local velocity of the ejecta, and we only consider a homologous core having a density profile $\rho \propto v_{\rm ej}^{-1}$ (see, e.g., Kasen & Bildsten 2010). These differences between models and model parameters are an inherent uncertainty in the pulsar-driven model.

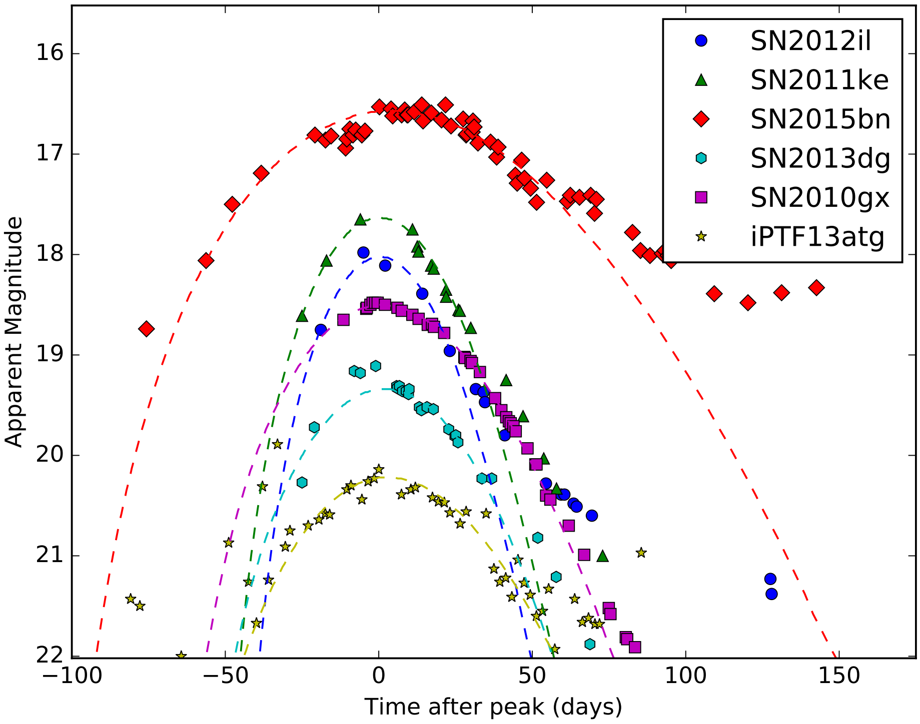

FIGURE 2.2: Supernova data (points) and modeled light curve (dashed lines) for each supernova, using their $P = 1$ ms parameter sets as shown in Table 2.2.

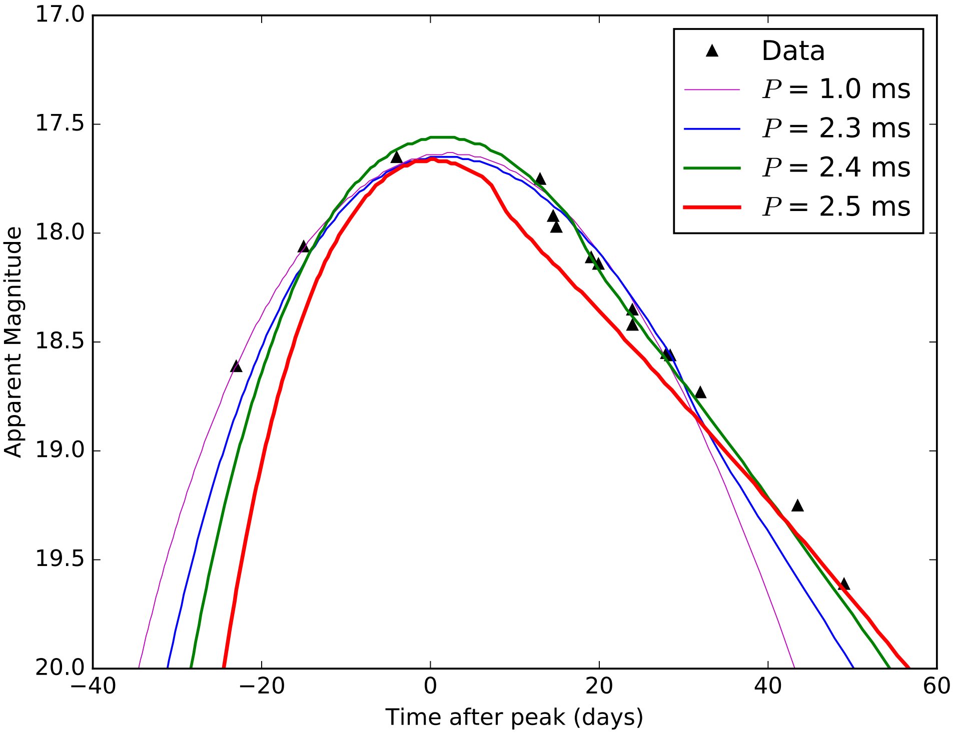

FIGURE 2.3: Supernova data (black triangles) and modeled light curves for SN2011ke, using (P, B_{13}, $M_{\rm ej}$) = (1.0 ms, 7.5, 9.5 $M_\odot$), (2.3 ms, 3.7, 2 $M_\odot$), (2.4 ms, 2.9, 1.3 $M_\odot$), and (2.5 ms, 2.1, 0.8 $M_\odot$). The models with P = 1.0, 2.3, and 2.4 ms are considered good fits near the light curve peak, while the P = 2.5 ms model is not wide enough at the peak, declines too slowly, and has a small post-peak drop not seen in the data - this is likely due to the reduction in ejecta mass needed to keep the peak luminosity consistent with the data. There are no parameter sets with P = 2.5 ms that generate a model that can fit the data, so 2.4 ms is what we consider to be $P_{\rm max}$.

Since the early optical light curve of these SLSNe could be produced by multiple different energy sources, or some combination of these sources, confirming the pulsar-driven model through only fitting optical/UV light curves is impossible. We do not investigate this problem any further here; we instead calculate non-thermal radio and millimetre emission consistently within our framework to examine possible constraints imposed by multi-wavelength observations.

2.4 Modelling Non-Thermal Emission

This model gives a full treatment of electron and photon energy transport, and will thus produce reliable results for later non-thermal emission. Producing reliable results for low frequency emission still requires self-consistent modeling over the entire electromagnetic and electron energy spectrum, since high-energy processes such as pair creation/annihilation can affect the number and energy of low energy electrons that produce radio synchrotron emission. The neutron star spin-down and ejecta dynamics are treated the same as in the early-time optical model, so Equations 2.1-2.10 and Equation 2.26 are still valid in this model. We use the notation $Q = 10^x Q_x$ in CGS units unless noted otherwise.

2.4.1 Leptonic Emission from Embryonic PWNe - Overview and Analytical Estimates

The electron injection spectrum from Equation 2.21 is also assumed in this model, with the same parameters q_1, q_2, and γ_b and with most of the energy $\epsilon_e \sim 1$ being carried by electrons and positrons (Tanaka & Takahara 2010, 2013).

The timescale for radiative cooling is given by $t_{\rm rad}^{-1} = t_{\rm syn}^{-1} + t_{\rm IC}^{-1} = t_{\rm syn}^{-1}(1+Y)$, where $t_{\rm syn} = 3m_e c/4\sigma_T U_B \gamma_e$ and $Y = t_{\rm syn}/t_{\rm IC}$ is the Compton Y parameter. When $t \gg t_{\rm SD}$, the cooling Lorentz factor of the leptons can be estimated to be

$$\gamma_c = 1.9 \times 10^{-2} P_{i,-2.5}^2 \epsilon_{B,-2}^{-1} \left(\frac{V_{\rm ej}}{5000\ {\rm km\ s^{-1}}}\right)^3 t_7^2 (1+Y)^{-1}, \tag{2.42}$$

where $t_{\rm rad} = t_{\rm dyn} = R_{\rm ej}/V_{\rm ej}$. Since γ_e can not physically be less than unity, a γ_c value less than unity implies that relativistic electrons will radiate almost all of their energy within $t_{\rm dyn}$. In the low-energy (Thomson) limit, the Y parameter is around

$$Y \approx \frac{-1 + \frac{L_{\rm SN} t V_{\rm ej}}{\epsilon_B \mathcal{E}_{\rm em} c} + \sqrt{\left(1 + \frac{L_{\rm SN} t V_{\rm ej}}{\epsilon_B \mathcal{E}_{\rm em} c}\right)^2 + \frac{4\epsilon_e L_{\rm SN} t V_{\rm ej}}{\epsilon_B \mathcal{E}_{\rm em} c}}}{2}. \tag{2.43}$$

The energy distribution of electron/positron pairs is mostly in the fast cooling regime. In this case, and with constant Y, the steady-state electron distribution $d\mathcal{N}_e/d\gamma_e$ is $\propto \gamma_e^{-2}$ for $1 \lesssim \gamma_e \lesssim \gamma_c$, $\gamma_e^{-q_1-1}$ for $\gamma_c \lesssim \gamma_e \leq \gamma_b$, and $\gamma_e^{-q_2-1}$ for $\gamma_b \leq \gamma_e \leq \gamma_M$, with the decrease in power-law index resulting from higher energy electrons radiating their energy away faster. γ_M is calculated by equating the total radiative timescale $t_{\rm rad}$ and the acceleration timescale $t_{\rm acc} = \eta \gamma_e m_e c/eB$, which gives

$$\gamma_M \approx \sqrt{\frac{6\pi e}{\eta \sigma_T B(1+Y_M)}} \simeq 1.9 \times 10^7 P_{i,-2.5}^{1/2} \eta^{-1/2} \epsilon_{B,-2}^{-1/4} \left(\frac{V_{\rm ej}}{5000\ {\rm km\ s^{-1}}}\right)^{3/4} t_7^{3/4} (1+Y_M)^{-1/2}, \tag{2.44}$$

where $Y_M \equiv Y(\gamma_M)$. This means that gamma-ray energies should be less than

$$E_\gamma^M \approx \gamma_M m_e c^2 \simeq 9.9 \text{ TeV } P_{i,-2.5}^{1/2} \eta^{-1/2} \epsilon_{B,-2}^{-1/4} \left(\frac{V_{\rm ej}}{5000 \text{ km s}^{-1}}\right)^{3/4} t_7^{3/4} (1+Y_M)^{-1/2}, \tag{2.45}$$

which implies that $\gtrsim$ 10-100 TeV gamma-rays should not be expected in early stages of PWN evolution.

In the fast cooling regime, the photon spectrum from synchrotron radiation is

$$E_\gamma L_{E_\gamma}^{\rm syn} \sim \frac{\epsilon_e L_{\rm em}}{2(1+Y)\mathcal{R}_b} \begin{cases} (E_\gamma / E_{\rm syn}^b)^{(2-q_1)/2} & (E_\gamma \le E_{\rm syn}^b), \\ (E_\gamma / E_{\rm syn}^b)^{(2-q_2)/2} & (E_{\rm syn}^b \le E_\gamma) \end{cases}, \tag{2.46}$$

with $\mathcal{R}_b \sim (2-q_1)^{-1} + (q_2-2)^{-1}$, and a characteristic synchrotron energy which is given in Equation 2.25. The spectra is expected to peak in the X-ray range for similar microphysical parameters as Galactic PWNe. It is worth noting that the maximum synchotron energy

$$E_{\rm syn}^M \equiv E_{\rm syn}^b(\gamma_b = \gamma_M) = 240 \text{ MeV } \eta^{-1}(1+Y_M)^{-1} \tag{2.47}$$

is almost completely parameter independent.

The expected IC luminosity in the fast cooling regime is very roughly $L_{\rm IC} \sim Y(1+Y)^{-1} L_{\rm em}$. We first assume a seed photon spectrum with $E_\gamma L_{E_\gamma} \propto E_\gamma^{2-\beta}$, where $\beta \le 1 + q_1/2$. One should note that, in the fast cooling regime, the synchrotron self-Compton (SSC) emission spectrum corresponds to $\beta = 1 + q_1/2$. Thus, in the low-energy Thomson limit, the inverse Compton photon spectrum is

$$E_\gamma L_{E_\gamma}^{\rm IC} \propto \begin{cases} E_\gamma^{(2-q_1)/2} & (E_\gamma \le E_{\rm IC}^b), \\ E_\gamma^{(2-q_2)/2} & (E_{\rm IC}^b < E_\gamma) \end{cases}, \tag{2.48}$$

This can be obtained by noting that $L_{E_\gamma}^{\rm IC} \sim \int d\gamma_e (d\tau_{\rm IC}/d\gamma_e) L_E^{\rm seed}(\gamma_e, E)$, where $\tau_{\rm IC}$ is the inverse Compton optical depth. A similar spectrum can be expected if the seed spectrum is thermal. In the SSC case, the typical inverse Compton photon energy is

$$E_{\rm SSC}^b \approx 2\gamma_b^2 E_{\rm syn}^b \simeq 130 \text{ TeV } \gamma_{b,5}^4 P_{i,-2.5}^{-1} \epsilon_{B,-2}^{1/2} \left(\frac{V_{\rm ej}}{5000 \text{ km s}^{-1}}\right)^{-3/2} t_7^{-3/2}, \tag{2.49}$$

although such energies can be difficult to achieve in the early PWN evolution due to the implications of Equation 2.45. On timescales of weeks to months, when optical supernova emission is prominent, thermal photons, via the external inverse Compton (EIC) process, are upscattered by relativistic electrons and positrons. The energy flux of the seed photons has its peak at $E_{\rm SN} \approx 3.92 k T_{\rm SN}$ with a typical IC energy being

$$E_{\rm EIC}^b \approx 2\gamma_b^2 E_{\rm SN} \simeq 78 \text{ GeV } \gamma_{b,5}^2 \left(\frac{k_B T_{\rm SN}}{1 \text{ eV}}\right). \tag{2.50}$$

In fact, the Klein-Nishina (KN) effect (Klein & Nishina 1929) becomes increasingly important at higher energies. We introduce two energy scales (Murase et al. 2011),

$$E_{\rm KN}^{\rm typ} \approx m_e^2 c^4 / (2 E_{\rm typ}), \tag{2.51}$$

$$E_{\rm KN}^b \approx \gamma_b m_e c^2, \tag{2.52}$$

where E_{typ} represents the typical energy of target photons. $E_{\mathrm{KN}}^{\mathrm{typ}}$ is the typical energy of an electron affected by the KN effect while E_{KN}^{b} cooresponds to when the effect becomes more pronounced; these energies also correspond to breaks in the IC spectrum when the Klein-Nishina effect is relevant, as we shall show shortly. The KN cross-section is

$$\sigma_{\mathrm{KN}} = \frac{3}{4}\left[\frac{1+x}{x^3}\left(\frac{2x(1+x)}{1+2x} - \ln(1+2x)\right)\right] + \frac{1}{2x}\ln(1+2x) - \frac{1+3x}{(1+2x)}, \tag{2.53}$$

where $x \equiv \frac{E_\gamma}{m_e c^2}$. We expect $E_{\mathrm{typ}} \approx E_{\mathrm{syn}}^{b}$ for the SSC case and $E_{\mathrm{typ}} \approx E_{\mathrm{SN}}$ for the EIC case. At these energies the KN effect makes the IC spectra more complicated, so we end up solving these equations numerically. However, some analytical expressions can be useful to estimate energy scale and spectral indices.

First, the seed photon spectrum has $E_\gamma L_{E_\gamma} \propto E_\gamma^{2-\beta}$ with $E_{\mathrm{KN},1}$ as the first break energy because of the KN effect. For $E_{\mathrm{KN},1} > E_{\mathrm{IC}}^{b}$, we get (e.g., Murase et al. 2011, 2010)

$$E_\gamma L_{E_\gamma}^{\mathrm{IC}} \propto \begin{cases} E_\gamma^{(2-q_1)/2} & (E_\gamma \le E_{\mathrm{IC}}^{b}) \\ E_\gamma^{(2-q_2)/2} & (E_{\mathrm{IC}}^{b} < E_\gamma \le E_{\mathrm{KN},1}) \\ E_\gamma^{\beta-q_2} & (E_{\mathrm{KN},1} \le E_\gamma), \end{cases} \tag{2.54}$$

where

$$E_{\mathrm{KN},1} = E_{\mathrm{KN}}^{\mathrm{typ}} \simeq 33\ \mathrm{GeV}\left(\frac{E_{\mathrm{typ}}}{4\ \mathrm{eV}}\right)^{-1}. \tag{2.55}$$

The inverse Compton emission at $E_\gamma > E_{\mathrm{KN},1}$ is mostly due to Thomson scattering between electron/positron pairs with $\gamma_e \sim E_\gamma/(m_e c^2)$ and seed photons with $E \sim m_e^2 c^4/(2E_\gamma)$. If $E_{\mathrm{KN},1} < E_{\mathrm{IC}}^{b}$, then

$$E_\gamma L_{E_\gamma}^{\mathrm{IC}} \propto \begin{cases} E_\gamma^{(2-q_1)/2} & (E_\gamma \le E_{\mathrm{KN},1}) \\ E_\gamma^{\beta-q_1} & (E_{\mathrm{KN},1} < E_\gamma \le E_{\mathrm{KN},2}) \\ E_\gamma^{\beta-q_2} & (E_{\mathrm{KN},2} \le E_\gamma), \end{cases} \tag{2.56}$$

where Equation 2.55 still holds for the first KN break and

$$E_{\mathrm{KN},2} = E_{\mathrm{KN}}^{b} \simeq 51\ \mathrm{GeV}\ \gamma_{b,5} \tag{2.57}$$

is the energy of the second KN break. If $\beta = 1 + q_1/2$, as would be expected from the SSC case, then

$$E_\gamma L_{E_\gamma}^{\mathrm{IC}} \propto \begin{cases} E_\gamma^{(2-q_1)/2} & (E_\gamma \le E_{\mathrm{KN},2}) \\ E_\gamma^{\beta-q_2} & (E_{\mathrm{KN},2} \le E_\gamma). \end{cases} \tag{2.58}$$

The above spectrum could be realized in the PWN SSC emission, but the break is smeared out due to photons with E_{typ} which are upscattered by leptons, and these photons not contributing above $E_{\mathrm{KN}}^{\mathrm{typ}}$.

Because the Rayleigh-Jeans spectrum is harder than the synchrotron spectrum, the KN cross section becomes more relevant when the spectrum of the seed photons is thermal. For $E_{\mathrm{KN},1} > E_{\mathrm{IC}}^{b}$, we expect

$$E_\gamma L^{\rm IC}_{E_\gamma} \propto \begin{cases} E_\gamma^{(2-q_1)/2} & (E_\gamma \leq E^b_{\rm IC}) \\ E_\gamma^{(2-q_2)/2} & (E^b_{\rm IC} < E_\gamma \leq E_{\rm KN,1}) \\ E_\gamma^{\beta_{\rm KN}-q_2} & (E_{\rm KN,1} \leq E_\gamma), \end{cases} \tag{2.59}$$

where $\beta_{\rm KN}$ shows the logarithmic energy dependence of the KN cross section. In the EIC case, one expects roughly $E_\gamma^{\beta_{\rm KN}} \propto \ln[2E_\gamma E_{\rm SN}/(m_e^2c^4)]$. If $E_{\rm KN,1} \leq E^b_{\rm IC}$, then

$$E_\gamma L^{\rm IC}_{E_\gamma} \propto \begin{cases} E_\gamma^{(2-q_1)/2} & (E_\gamma \leq E_{\rm KN,1}) \\ E_\gamma^{\beta_{\rm KN}-q_1} & (E_{\rm KN,1} < E_\gamma \leq E_{\rm KN,2}) \\ E_\gamma^{\beta_{\rm KN}-q_2} & (E_{\rm KN,2} \leq E_\gamma). \end{cases} \tag{2.60}$$

These are the typical spectra anticipated for EIC emission from the PWN in the early phase.

2.4.2 Leptonic Emission from Embryonic PWNe - Numerical Calculation

While we have given some analytical estimates, we solve the necessary equations numerically not only because of the KN effect, but also because high-energy gamma rays might produce electron/positron pairs within the PWN. Becase of this, detailed numerical spectra will deviate from the analytical estimates given above. For the intrinsic PWN emission, we solve the kinetic equations:

$$\frac{\partial n^e_{E_e}}{\partial t} = \frac{\partial n^{(\gamma\gamma)}_{E_e}}{\partial t} - \frac{\partial}{\partial E}\left[\left(\frac{E_e}{t_{\rm IC}} + \frac{E_e}{t_{\rm syn}} + \frac{E_e}{t_{\rm dyn}}\right) n^e_{E_e}\right] + \dot{n}^{\rm inj}_{E_e}, \tag{2.61}$$

$$\frac{\partial n^\gamma_{E_\gamma}}{\partial t} = -\frac{n^\gamma_{E_\gamma}}{t_{\gamma\gamma}} - \frac{n^\gamma_{E_\gamma}}{t^{\rm nb}_{\rm esc}} + \frac{\partial n^{\rm (IC)}_{E_\gamma}}{\partial t} + \frac{\partial n^{\rm (syn)}_{E_\gamma}}{\partial t}, \tag{2.62}$$

where

$$\begin{aligned} t^{-1}_{\gamma\gamma} &= \int dE_\gamma n^\gamma_{E_\gamma} \int \frac{d\cos\theta}{2} \tilde{c}\sigma_{\gamma\gamma}, \\ \frac{\partial n^{\rm (IC)}_{E_\gamma}}{\partial t} &= \int dE_e n^e_{E_e} \int dE_\gamma n^\gamma_{E_\gamma} \int \frac{d\cos\theta}{2} \tilde{c}\frac{d\sigma_{\rm KN}}{dE_\gamma}, \\ \frac{\partial n^{(\gamma\gamma)}_{E_e}}{\partial t} &= \frac{1}{2}\int dE_\gamma n^\gamma_{E_\gamma} \int dE'_\gamma n^\gamma_{E'_\gamma} \int \frac{d\cos\theta}{2} \tilde{c}\frac{d\sigma_{\gamma\gamma}}{dE_e}, \\ \sigma_{\gamma\gamma} &= \frac{3}{16}\sigma_T(1-\beta^2_{\rm cm})\left(2\beta_{\rm cm}(\beta^2_{\rm cm}-2) + (3-\beta^4_{\rm cm})\ln\left[(1+\beta_{\rm cm})/(1-\beta_{\rm cm})\right]\right), \end{aligned}$$

$\tilde{c} = (1-\cos\theta)c$ (where θ is the angle between the velocity of two particles), $t_{\gamma\gamma}$ is the photon-photon annihilation timescale, $\sigma_{\gamma\gamma}$ is the photon-photon annihilation cross section, $t^{\rm nb}_{\rm esc} = R_w/c$ is the escape time or photons from the PWN, $\beta_{\rm cm} = \sqrt{1-4m_e^2c^4/S_m}$, and S_m is the Mandelstam variable (Mandelstam 1958). We use the continuous energy-loss approximation for inverse Compton scattering to save time, and we assume $E_e = (E_\gamma + E'_\gamma)/2$ for pairs produced by photon-photon annihilation. We solve these above equations using a constant electron injection with $\dot{n}^{\rm inj}_{E_e}$ determined from Equation 2.21. We also consistantly calculate the energy spectrum and emission from previously injected "relic" electrons. To simplify our calculations, we use a one-zone model.

For initial conditions, we set $n^e_{E_e} = 0$ and $n^\gamma_{E_\gamma}$ to a thermal spectrum cooresponding to $T_{\rm SN}$. Higher-energy photons are produced from non-thermal electrons injected into the PWN. The calculation is performed over a dynamical time $t_{\rm dyn}$, giving us a quasi-steady-state spectrum. The differential pre-attenuation luminosity, which is a function of $n^\gamma_{E_\gamma}$, is

$$E_\gamma L_{E_\gamma} = \frac{(E_\gamma^2 n^\gamma_{E_\gamma})\mathcal{V}_w}{t^{\rm nb}_{\rm esc}} \tag{2.63}$$

which is consistent with observed X-ray and gamma-ray fluxes. $\mathcal{V}_w = (4/3)\pi R_w^3$ here is the volume of the PWN.

2.4.3 Photon-photon Annihilation in Embryonic PWNe

Quasi-thermal and synchrotron emission can both prevent high enery photons from exiting the PWN due to two-photon annihilation, so we must take into account both gamma-ray attenuation and its subsequent regeneration via pair creation. For a black-body photon spectrum with the supernova photon density $n_\gamma^{\rm SN} = 2\zeta(3)(k_B T_{\rm SN})^3/(\pi^2\hbar^3c^3)$, the pair-production optical depth is

$$\tau^{\rm ej}_{\gamma\gamma_{\rm SN}} \approx \frac{3}{16}\sigma_T n_\gamma^{\rm SN} R_{\rm ej}\mathcal{G}\left(x = \frac{m_e^2c^4}{E_\gamma k_B T_{\rm SN}}\right) \simeq 2.0\times 10^4 \left(\frac{k_B T_{\rm SN}}{1\ {\rm eV}}\right)^3 \left(\frac{V_{\rm ej}}{5000\ {\rm km\ s^{-1}}}\right) t_7, \tag{2.64}$$

where $\mathcal{G}(x) \equiv \mathcal{F}(x)/\zeta(3)$ and $\mathcal{F}(x)$ is as defined in Dermer et al. (2012). In this expression, $\mathcal{G}(x)$ peaks at around at

$$E^{\rm typ}_{\gamma\gamma} \approx \frac{m_e^2c^4}{2k_B T_{\rm SN}} \simeq 130\ {\rm GeV}\left(\frac{k_B T_{\rm SN}}{1\ {\rm eV}}\right)^{-1}. \tag{2.65}$$

When the target photons have a power-law spectrum from synchrotron emission with $n_E^{\rm syn} \propto E^{-\beta}$, the optical depth for pair production in the PWN can be estimated as

$$\tau^{\rm nb}_{\gamma\gamma_{\rm syn}} \approx 0.2\sigma_T(E_\gamma n_E^{\rm syn})R_w, \tag{2.66}$$

$$\simeq 3.1\times 10^{-3}\gamma_{b,5}^{-2}P_{i,-2.5}B^{-2}_{{\rm dip},14}\epsilon_{B,-2}^{-1/2}\epsilon_e\left(\frac{V_{\rm ej}}{5000\ {\rm km\ s^{-1}}}\right)^{1/2}\frac{t_7^{-3/2}}{(1+Y)}\left(\frac{E_\gamma}{E^{\rm typ}_{\gamma\gamma}}\right)^{\beta-1}, \tag{2.67}$$

where we use $R_w \approx R_{\rm ej} = V_{\rm ej}t$ for analytical estimates. The typical two-photon energy $E^{\rm typ}_{\gamma\gamma}$ is

$$E^{\rm typ}_{\gamma\gamma} \approx \frac{m_e^2c^4}{E^b_{\rm syn}} \simeq 41\ {\rm MeV}\ \gamma_{b,5}^{-2}P_{i,-2.5}\epsilon_{B,-2}^{-1/2}\left(\frac{V_{\rm ej}}{5000\ {\rm km\ s^{-1}}}\right)^{3/2} t_7^{3/2}. \tag{2.68}$$

We calculate electromagnetic cascades for radiation generated within the PWN, and we take also into account attenuation by supernova photon fields by multiplying by $e^{-(\tau^{\rm ej}_{\gamma\gamma}+\tau^{\rm nb}_{\gamma\gamma})}$.

TeV gamma rays can not leave the PWN in the early phase due to SN photons in the optical or infrared bands, but are expected to be able to escape in a few years. GeV photons can escape much earlier but are still strongly attenuated for around the first 30 days.

2.4.4 Photon Attenuation by Matter in the Supernova Ejecta

Photons that escape from the PWN can also be significantly attenuated in the ejecta, which we account for by doing post-process calculations. At energies lower than $\sim$ 10 keV, photoelectric absorption dominates; in soft X-rays, emission from ionization breakout may be able to provide an interesting signal (Metzger et al. 2014); and at high energies, Bethe-Heitler (BH) pair production and Compton scattering dominate. The total optical depth is $\tau = \tau_{\rm pe} + \tau_{\rm BH} + \tau_{\rm comp}$, where the three optical depths are for photoelectric absorption, BH pair production, and Compton scattering respectively. With a coefficient κ for mass attenuation, τ is generally given by $\kappa\rho R$, where ρ is the density and R is the photon path length. The bound-free opacity $\kappa_{\rm bf} \simeq 2.37$ cm^2 g^{-1} $(Z/6)^3(E_\gamma/10\ {\rm keV})^{-3}$ can be used to give conservative estimates for the flux of X-ray emission.

The Compton optical depth within the supernova ejecta is

$$\tau_{\rm comp}^{\rm ej} \approx \kappa_{\rm comp}\rho_{\rm ej}R_{\rm ej} = \frac{(3-\delta)M_{\rm ej}\sigma_{\rm comp}}{4\pi\mu_e m_u R_{\rm ej}^2}, \tag{2.69}$$

where $\kappa_{\rm comp} = \sigma_{\rm comp}/(\mu_e m_u)$. The mass-energy transfer coefficient is

$$\begin{aligned} K_{\rm comp}\sigma_{\rm comp} = \frac{3}{4}\sigma_T \Bigg[& \frac{2(1+x)^2}{x^2(1+2x)} - \frac{1+3x}{(1+2x)^2} - \frac{(1+x)(2x^2-2x-1)}{x^2(1+2x)^2} \\ & - \frac{4x^2}{3(1+2x)^3} - \left(\frac{1+x}{x^3} - \frac{1}{2x} + \frac{1}{2x^3}\right)\ln(1+2x)\Bigg], \end{aligned} \tag{2.70}$$

where $x \equiv E_\gamma/(m_e c^2)$ and $K_{\rm comp}$ is the gamma-ray inelasticity. This formula is obtained from kinematics using the known KN cross section.

For a nucleus with atomic number Z and mass number A, the cross-section for the BH process on a nuclear scale is $\sigma_{\rm BH} = Z^2\sigma_{\rm BH}^{(p)}$. Taking contributions from both nuclei and leptons into account, with $\mu_e \approx 2$,

$$\tau_{\rm BH}^{\rm ej} \approx \frac{(3-\delta)M_{\rm ej}(Z_{\rm eff}+1)\sigma_{\rm BH}^{(p)}}{8\pi m_u R_{\rm ej}^2}, \tag{2.71}$$

where $Z_{\rm eff}$ represents an effective atomic number that depends on the chemical composition of the supernova ejecta. For a hydrogen rich composition with $X_{\rm H}$ = 0.6, $X_{\rm He}$ = 0.3, $X_{\rm C}$ = 0.1, we get $Z_{\rm eff} \approx 2.5$, while $Z_{\rm eff} \approx 7$ for the type-Ic composition with $X_{\rm CO}$ = 1. The coefficient for mass-energy transfer at high energies is roughly

$$K_{\rm BH}\sigma_{\rm BH} = \frac{x-2}{x}\sigma_{\rm BH}, \tag{2.72}$$

although this neglects contributions from pair annihilation. This model uses a cross section which is derived from the Born approximation (Chodorowski et al. 1992), but a simpler formula, useful for analytical estimates, is

$$\sigma_{\rm BH}^{(p)} \approx \frac{3\alpha_{\rm em}}{8\pi}\sigma_T\left(\frac{28}{9}\ln(2x) - \frac{218}{27}\right), \tag{2.73}$$

which gives $\sigma_{\rm BH} \sim Z^2 10^{-26}$ cm^2 at GeV energies. Note that $\sigma_{\rm BH}^{(p)} \sim \alpha_{\rm em}\sigma_T$, where $\alpha_{\rm em} \simeq 1/137$ is the fine-structure constant. At GeV energies, $\tau_{\rm BH}^{\rm ej}$ is estimated as

$$\tau_{\rm BH}^{\rm ej} \simeq 0.57 \left(\frac{Z_{\rm eff}+1}{3}\right) \left(\frac{M_{\rm ej}}{5M_\odot}\right) \left(\frac{V_{\rm ej}}{5000\ {\rm km\ s^{-1}}}\right)^{-2} t_7^{-2} \tag{2.74}$$

which implies significant BH attenuation at early times.

In the small-inelasticity limit, particles lose K_γ for every interaction, which gives a survival fraction of $(1 - K_\gamma)^{\max[\tau,\tau^2]}$, where $\max[\tau,\tau^2]$ is the total number of scatterings. In the large-inelasticity limit, which is more commmon for the attenuation case, the survival fraction is simply given by $e^{-\tau}$. Combining these two limits gives a hard X-ray/gamma ray escape fraction of

$$f_{\rm esc} = e^{-\tau} + (1 - e^{-\tau})(1 - K_\gamma)^{\max[\tau,\tau^2]} \tag{2.75}$$

Gamma rays with GeV and higher energies can not escape the ejecta until a few months post-explosion. The GeV gamma-ray escape timescale is

$$t_{\gamma,\,{\rm esc}} \simeq 88\ {\rm days} \left(\frac{Z_{\rm eff}+1}{3}\right)^{1/2} \left(\frac{M_{\rm ej}}{5M_\odot}\right)^{1/2} \left(\frac{V_{\rm ej}}{5000\ {\rm km\ s^{-1}}}\right)^{-1}. \tag{2.76}$$

In the low-energy Thomson limit, the flux of gamma rays at $E_{\rm IC}^b$ for $t \gtrsim t_{\rm SD}$ is approximately

$$\begin{aligned} F_{\rm IC}^b \sim\ & 3.7\times 10^{-8}\ {\rm GeV\ cm^{-2}\ s^{-1}} B_{\rm dip,14}^{-2} \epsilon_e \frac{Y}{1+Y} \left(\frac{Z_{\rm eff}+1}{3}\right)^{-1} \\ & \times \left(\frac{M_{\rm ej}}{5M_\odot}\right)^{-1} \left(\frac{V_{\rm ej}}{5000\ {\rm km\ s^{-1}}}\right)^{2} \left(\frac{d}{16.5\ {\rm Mpc}}\right)^{-2} \left(\frac{t}{t_{\gamma,\,{\rm esc}}}\right)^{-2} \end{aligned} \tag{2.77}$$

The supernova ejecta becomes optically thin to Thomson scattering on a timescale of

$$t_{\rm HX,\,esc} \simeq 420\ {\rm days} \left(\frac{2}{\mu_e}\right)^{1/2} \left(\frac{M_{\rm ej}}{5M_\odot}\right)^{1/2} \left(\frac{V_{\rm ej}}{5000\ {\rm km\ s^{-1}}}\right)^{-1} \tag{2.78}$$

The synchrotron flux at the break energy at late times can be estimated as

$$\begin{aligned} F_{\rm syn}^b \sim\ & 2.6\times 10^{-12}\ {\rm erg\ cm^{-2}\ s^{-1}} B_{\rm dip,14}^{-2} (1+Y)^{-1} \left(\frac{2}{\mu_e}\right)^{-1} \\ & \times \left(\frac{M_{\rm ej}}{5M_\odot}\right)^{-1} \left(\frac{V_{\rm ej}}{5000\ {\rm km\ s^{-1}}}\right)^{2} \left(\frac{d}{16.5\ {\rm Mpc}}\right)^{-2} \left(\frac{t}{t_{\rm HX,\,esc}}\right)^{-2} \end{aligned} \tag{2.79}$$

It is worth noting that low-energy photons that experience multiple scatterings with low K_γ can escape earlier.

In the radio band, where we have synchrotron radiation, the important attenuation or suppression processes are the Razin effect, free-free absorption, and synchrotron self-absorption. The Razin effect (or Tsytovich-Razin effect) is a low-energy cut-off of synchtron emission due to the suppression of relativistic beaming (Razin 1957, 1960; Tsytovich 1951). In a medium, the critical angle for the beaming effect is

$$\theta_b \sim \sqrt{1 - n_r^2\beta^2} \tag{2.80}$$

where n_r is the refractive index within the medium and β is v_e/c (Rybicki & Lightman 1979). If n_r is close to unity, then θ_b depends mostly on β, which is the vacuum case. If n_r deviates strongly from unity, then

$$\theta_b \sim \sqrt{1-n_r^2} = \frac{\Omega_p}{\Omega}, \tag{2.81}$$

where the plasma frequency of the medium is given by

$$\Omega_p = \sqrt{\frac{4\pi n_e e^2}{m_e}}. \tag{2.82}$$

The Razin frequency, where this effect becomes prevalent, is (Ginzburg & Syrovatskii 1965; Murase et al. 2014)

$$\Omega_{\rm R} = \frac{4\pi e c n_e}{B}. \tag{2.83}$$

At higher frequencies, θ_b decreases until it becomes $1/\gamma$, the vacuum value. At lower frequencies, the synchrotron spectrum will experience a quasi-exponential cutoff due to the increase in θ_b (Boischot & Clavelier 1967).

Synchrotron emission can be reabsorbed by neighboring electrons within the PWN, causing the nebula to become optically thick to its own radiation at low frequencies; this is called self-absorption (Yang et al. 2016). This can be expressed as the brightness temperature

$$T_b = \frac{I_\nu c^2}{2k_B\nu^2}, \tag{2.84}$$

where I_ν is the specific synchrotron intensity, approaching the electron temperature

$$T_e = \left(\frac{2\pi m_e c\nu}{eB}\right)^{1/2}\frac{m_e c^2}{3k_B} = 1.18\times10^6\ \mathrm{K}\left(\frac{\nu}{\mathrm{Hz}}\right)^{1/2}\left(\frac{B}{\mathrm{G}}\right)^{-1/2}. \tag{2.85}$$

Setting them equal gives the spectral index for self-absorbed radiation,

$$I_\nu = \frac{2k_B T_e\nu^2}{c^2} \propto \nu^{5/2}B^{-1/2}. \tag{2.86}$$

In general, the self-absorption optical depth is (Murase et al. 2016)

$$\tau_{\rm sa}^{\rm nb} = R_w\int d\gamma_e\frac{dn_e^{\rm nb}}{d\gamma_e}\sigma_{\rm sa}(\nu,\gamma_e), \tag{2.87}$$

where the cross-section for self-absorption is (Ghisellini & Svensson 1991)

$$\sigma_{\rm sa}(\nu,\gamma_e) = \frac{1}{2m_e\nu^2\gamma_e p_e}\frac{\partial}{\partial\gamma_e}[\gamma_e p_e j_{\rm syn}(\nu,\gamma_e)], \tag{2.88}$$

where p_e is the momentum of the electron and $j_{\rm syn}$ is the synchrotron emissivity.

Photons can be absorbed by electrons in the presence of an ion in an inverse process of bremsstrahlung, known as free-free absorption. From Kirchhoff's law, $j_\nu = 4\pi\kappa_\nu^{\rm abs}B_\nu(T)$, we get

$$\kappa_\nu^{\rm abs} \propto \rho T^{-1/2}\nu^{-3}(1-e^{-h\nu/k_BT}), \tag{2.89}$$

where the factor $T^{-1/2}$ appears because a larger ion thermal velocity will lead to a higher chance of absorption (Ostlie & Carroll 1996). A more complete calculation, accounting for stimulated emission, gives (Shu 1991)

$$\rho\kappa_{\nu,ff} = \sum_i n_{Z_i} n_e \left(\frac{2m_e}{3\pi k_B T}\right)^{1/2} \left(\frac{4\pi Z_i^2 e^6}{2m_e^2 ch\nu^3}\right) g_{ff}(\nu)(1 - e^{-h\nu/k_B T}), \tag{2.90}$$

where $g_{ff}(\nu)$ is a quantum-mechanical correction known as the Gaunt factor (Gaunt 1930). This clearly depends on chemical composition, so we use X, the mass fraction of hydrogen, and Z, the mass fraction of all elements heavier than helium (usually called the metallicity). A numerical fit of the frequency integral of Equation 2.90 yields Kramer's Law (Kramers 1923; Shu 1991) in the form

$$\kappa_{ff} = 4 \times 10^{22}\ \mathrm{cm}^2\ \mathrm{g}^{-1}\ g_{ff}(1 - Z)(1 + X) \left(\frac{\rho}{\mathrm{g\ cm}^{-3}}\right)^{1/2} \left(\frac{T}{\mathrm{K}}\right)^{-7/2}. \tag{2.91}$$

The resulting optical depth is (Murase et al. 2017b)

$$\tau_{ff} = 8.4 \times 10^{-28} T_{e,4}^{-1.35} \nu_{10}^{-2.1} \int dr n_e n_i \bar{Z}^2. \tag{2.92}$$

where $\bar{Z}$ is the effective charge of the ejecta. Using (Murase et al. 2017a)

$$n_i = n_e = \frac{3M_{\mathrm{ej}}}{4\pi R_{\mathrm{ej}}^3 \bar{A} m_H}, \tag{2.93}$$

where $\bar{A}$ is the mean nuclear number of the ejecta, and setting τ_{ff} = 1 gives the radio escape time

$$t_{\mathrm{rad,\,esc}} \sim 30\ \mathrm{yr}\ T_{e,4}^{-0.27} \nu_{10}^{-0.42} \left(\frac{M_{\mathrm{ej}}}{5M_\odot}\right)^{2/5} \left(\frac{V_{\mathrm{ej}}}{5000\ \mathrm{km\ s}^{-1}}\right)^{-1} \left(\frac{\bar{Z}}{4.5}\right)^{2/5} \left(\frac{\bar{A}}{16}\right)^{-1/5}. \tag{2.94}$$

2.5 Radio and Millimetre Emission Predictions

We calculate radio and millimetre band synchrotron emission from pulsar-driven SLSNe using the parameters found in Section 2.3. We calculate PWN emission in Section 2.5.1 and discuss emission from the supernova forward shock in Section 2.5.2. Radio PWN emission has been calculated previously (e.g., Gaensler & Slane 2006; Tanaka & Takahara 2010), but we take dynamics of the PWN and SN as well as pair cascades and attenuation in the both PWN and SN into account (See Section 2.4).

2.5.1 Radio/Millimetre Emission from Embryonic Nebulae

As the supernova expands, non-thermal emission begins to escape the supernova ejecta. The timescale for escape depends heavily on photon energy because the opacity and absorption processes within the ejecta depend on energy, (Section 2.4.4).

The PWN spectrum depend on both the lepton injection history into the PWN and the ejecta ionization state, neither of which are well constrained for young pulsar-powered SNe. Our model of the injection spectrum is based on Galactic PWNe, most notably the Crab PWNe (e.g., Tanaka & Takahara 2010), which can be modelled using a broken power law spectrum with spectral indices of $q_1 = 1.5$ and $q_2 = 2.5$ and a peak electron Lorentz factor of $\gamma_{\mathrm{e}^\pm,\mathrm{b}} = 10^5$ (See Equation 2.21).

The spectrum lies within the fast cooling regime, where electrons and positrons with $\gamma_{\mathrm{e}^\pm,\mathrm{b}}$ cool on a much shorter timescale than the dynamical time, so our results are not very sensitive to the spectral indices, especially q_2. The equipartition parameter for magnetic field energy ϵ_B is assumed to be 0.01, with the rest of the spin-down energy assumed to accelerate pairs (i.e., $\epsilon_{\mathrm{e}} = 0.99$); these assumptions are based on detailed modeling of Galactic PWNe (Tanaka & Takahara 2010, 2013). To take into account free-free absorption within the SN ejecta we assume a pure oxygen ejecta where each atom is singly-ionized and the ejecta has electron temperature $T_{\mathrm{e}} = 10^4$ K, giving a mean mass number $\bar{A} = 16$, and effective atomic number (which takes charge shielding into account) $\bar{Z} = 4.5$ (See Equations 2.92 and 2.94), ; the assumed metal abundance is based on the findings of previous nucleosynthesis studies (e.g., Maeda et al. 2002). Although the effect is very difficult to calculate self-consistently, the ionization state of the ejecta can be maintained by X-ray radiation from the PWN. Although observations of PS1-14bj found a strong [OIII] signal in the nebular spectra at $t \sim 0.5$ yr (Lunnan et al. 2016), which suggests a doubly-ionized state, the doubly-ionized state may not be present over the entire ejecta, and free electron recombination may proceed efficiently in the ejecta for $t \gtrsim 1$ yr. Because of this, the single-ionization assumption probably overestimates free-free absorption, which will give a conservative estimate of the radio emission.

The spin-down of the pulsar and dynamics of the ejecta and PWN are done as shown in Section 2.2, while other effects are calculated as shown in Section 2.4. After calculating spin-down and ejecta and PWN dynamics, we solve a kinetic equation for electrons, positrons, and photons in the PWN which takes synchrotron radiation, inverse Compton scattering, adiabatic cooling, and pair cascades into account.

Multiwavelength spectra from SN2011ke with $P = 1$ ms at $10^{0.5}$, 10, and $10^{1.5}$ years post-explosion are shown in Figure 2.4. The spectrum has two components: a roughly broken power-law spectrum up to $\nu \lesssim 10^{14}$ GHz due to synchrotron emission, and the higher frequency bump which comes from the inverse Compton scattering of blackbody photons in the supernova ejecta. The peak νF_ν spectral frequency is the synchrotron frequency of positrons or electrons with $\gamma_{\mathrm{e}^\pm,\mathrm{b}}$. As time increases, the spectrum softens and flux decreases because of the decline of energy injection as well as adiabatic energy loss from the PWN. The low frequency cutoff also moves to lower frequencies as time increases due to the decreasing radio/submillimetre opacity. Each PWN spectrum is qualitatively similar, so we use SN2011ke as an example.

From now, we focus on radio PWNe which radiate synchrotron emission from relativistic positrons and electrons accelerated by the PWN. The synchrotron cooling time of the high-energy particles is much shorter at early times compared to the PWN dynamical time. At later times, low-energy positrons and electrons start to accumulate in the PWN because they have a longer cooling timescale and can not lose all their energy. These "relic" particles injected previously can also contribute to radio emission, which is calculated self-consistently in our model.

Figure 2.5 shows the intrinsic light curves of SN2011ke in the 1 GHz (blue) and 100 GHz (red) band. The solid lines show models which include absorption processes in the SN ejecta while the dashed lines show the emission without absorption in the ejecta - synchrotron-self absorption is included though. The time of the unabsorbed light curve wthout ejecta absorption peak cooresponds to when the radio frequency and synchrotron self-absorption frequency become comparable, while the time of the

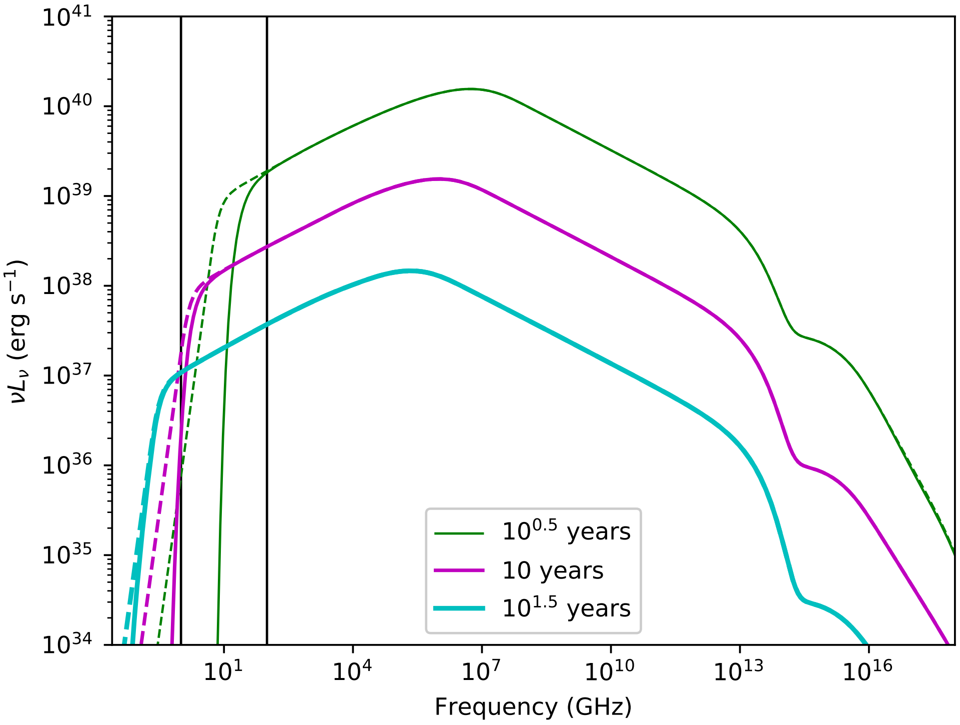

FIGURE 2.4: Multiwavelength PWN spectra for SN2011ke with $P =$ 1 ms at $10^{0.5}$ (green), 10 (magenta), and $10^{1.5}$ (cyan) years post-explosion. The solid coloured lines show calculations that account for the free-free absorption of radio waves while the dashed lines show calculations that do not. The solid black lines indicate 1 and 100 GHz, which are the main frequencies we examine in this study.

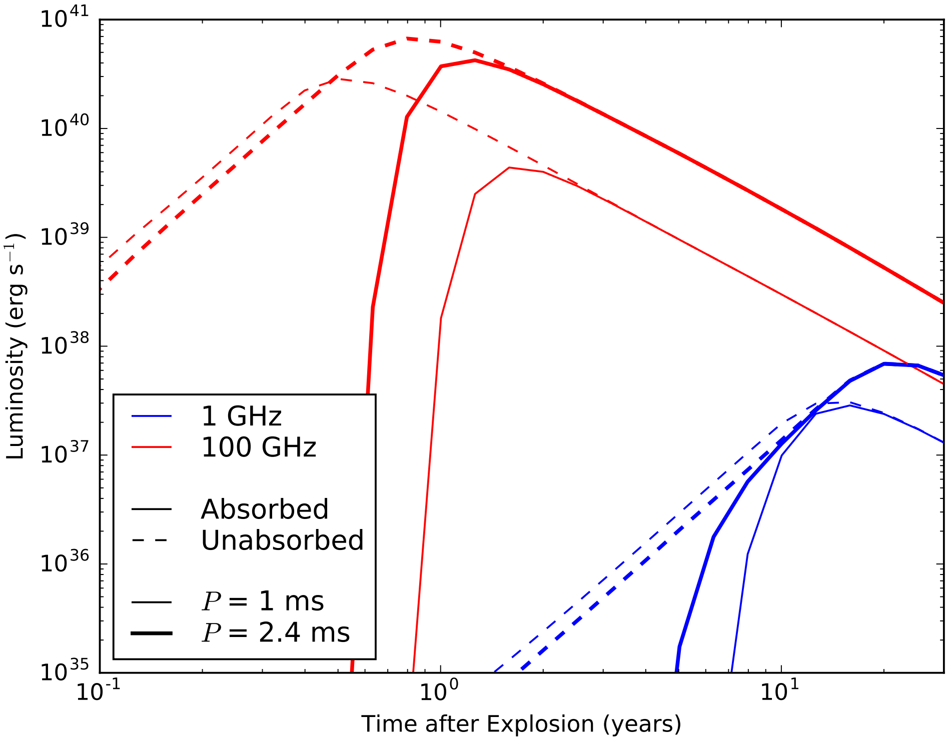

FIGURE 2.5: Intrinsic radio and submillimetre light curves from the PWN of SN2011ke at 1 GHz (blue) and 100 GHz (red). The thick and thin lines represent the $P = 1$ ms and $P = P_{\max} = 2.4$ ms cases, respectively. Solid lines include absorption processes in the supernova ejecta, while dashed lines show the unabsorbed light curves.

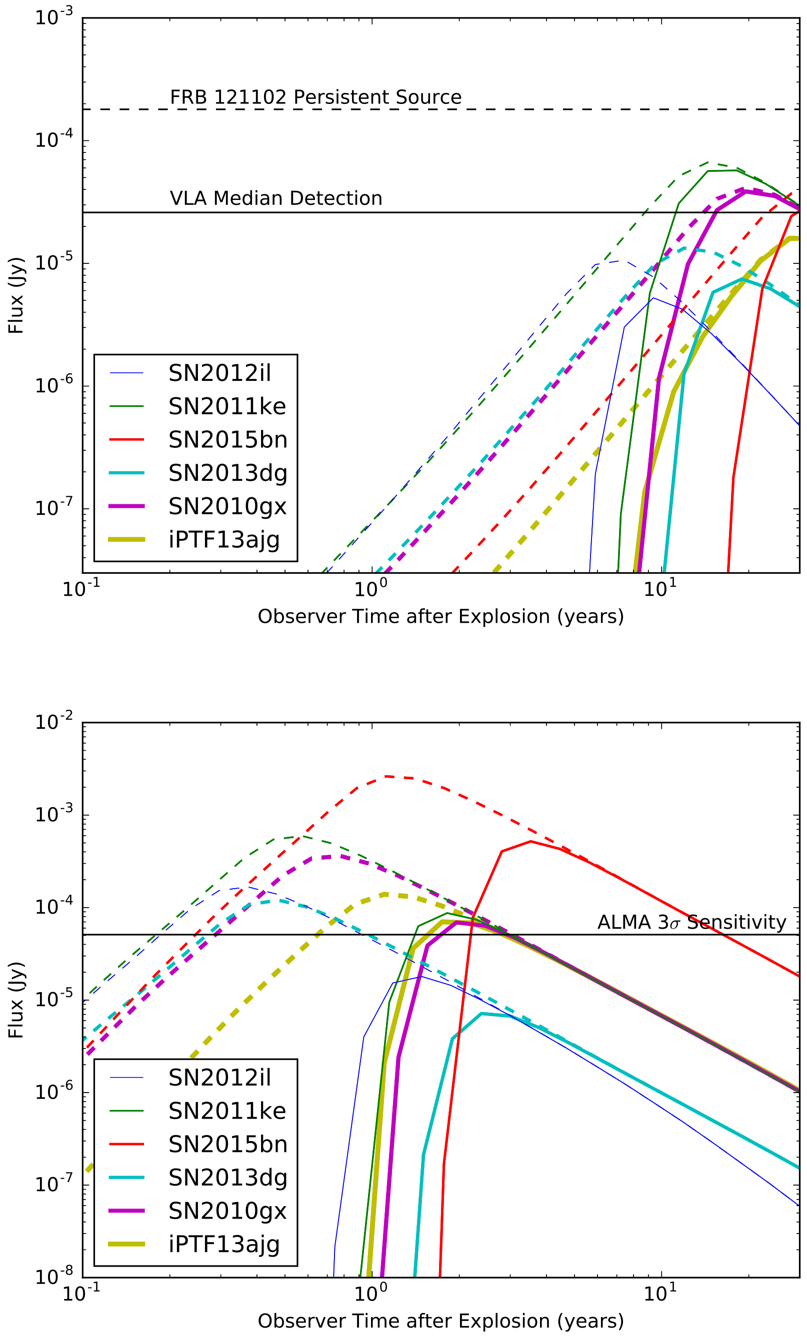

FIGURE 2.6: Predicted observable light curves from the PWN of each SLSN at 1 GHz (above) and 100 GHz (below) using the $P = 1$ ms parameter sets. The solid lines indicate the flux with absorption in the SN ejecta and the dashed lines indicate the flux with no absorption. The solid black horizontal lines indicate the median VLA detection of 26 μJy (top) and the 3σ detection limit of 51 μJy from ALMA (bottom) taken from (Chatterjee et al. 2017), although these fluxes were at 3 GHz and 230 GHz respectively. The dashed black line shows the 180 μJy flux of the persistent radio source of FRB 121102 at $D_{\rm L} = 972$ Mpc.

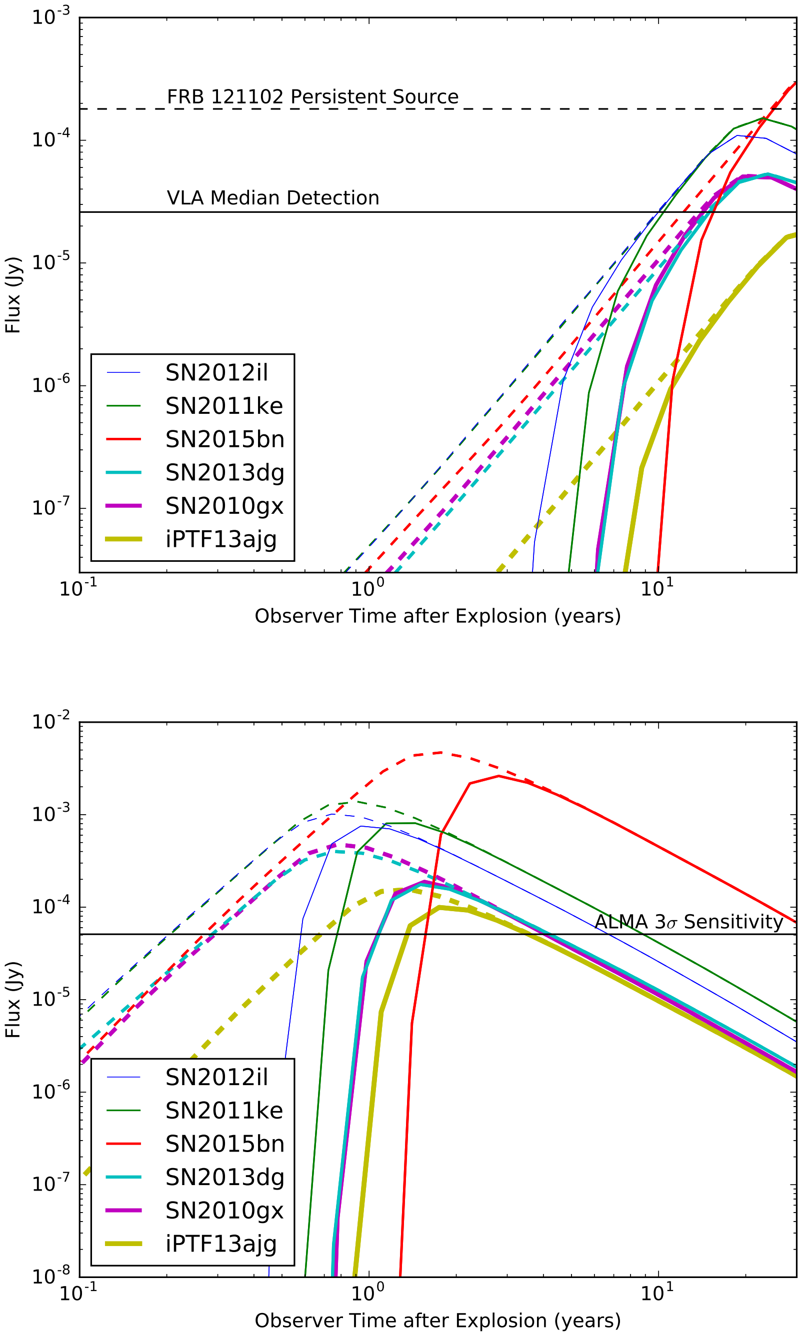

FIGURE 2.7: The same as Figure 2.6, but for the $P_{\max}$ parameters from Table 2.2.

light curve peak with ejecta absorption is determined by free-free absorption. Absorption processes become irrelevant $\sim$ 10 and $\sim$ 1 yrs after the explosion for the $\sim$ 1 and $\sim$ 100 GHz band, respectively, as little radiation is absorbed post-peak and the decline essentially is just from the spin-down of the central pulsar.

Figure 2.5 also shows the dependence of the radio PWN emission on model parameters. The thick and thin solid lines represent the shortest ($P = 1$ ms) and longest ($P = P_{\rm max} = 2.4$ ms) spin period models found for SN2011ke, respectively. Looking at Table 2.2, we see that the $P_{\rm max}$ set requires a smaller pulsar initial magnetic field, which increases the spin-down time, which keeps the spin-down luminosity high for a longer period of time. The long-period case also requires less ejecta mass, which makes the PWN and ejecta become transparent earlier. Consequently, the peak luminosity of the long-period parameter set is higher than the short-period parameter set by a factor of $\lesssim 10$.

The light curves for all six SLSNe, as they would be observed from Earth, are shown in Figure 2.6 for both the 1 GHz and 100 GHz bands using the P = 1 ms parameters. At 1 GHz, we show the 26 μJy median flux density from $\sim$ 70 background sources observed by VLA around the persistent source of FRB 121102, and at 100 GHz we show the ALMA 51 μJy 3σ detection limit[2]. The 1 GHz radio emission from some of the SLSNe reach the sensitivity of the VLA within 10-20 years and will remain detectable until at least 30 years after the explosion. The signal may be detectable earlier if absorption can be suppressed an effect such as mass-shedding due to Rayleigh-Taylor instabilities or if the ejecta is significantly less ionized than our assumption. At 100 GHz with ejecta absorption, several SLSNe have their peak flux just above the detection limit for ALMA, and the peak of SN2015bn is brighter than the limit by afull order of magnitude, although it peaks later than the other supernovae due to its higher ejecta mass. If emission at the peak time is observed due to the suppression of absorption, millimetre emission could be detectable from $\sim$ 2-7 months until $\sim$ 1-2 years post-explosion, except for SN2015bn, which can be detected until around 15 years post-explosion. Motivated by the possible connection between magnetar-powered SNe and FRBs (Murase et al. 2016), we show the 180 μJy flux from the persistent counterpart of FRB 121102 with a dashed black line in the VLA band (Chatterjee et al. 2017).

Figure 2.7 shows radio and submillimetre light curves for each SLSN in our sample, using their $P_{\rm max}$ parameters from Table 2.2. In the 1 GHz band, all of our sample SNe have their peak flux on a timescale of $\sim$ 20-30 years (not heavily affected by absorption), which is later than in the P = 1 ms case. Even including absorption in the ejecta, only iPTFajg is not detectable by VLA. The peak flux of SN2015bn is well above the flux from the FRB 121102 persistent source and the peak flux of SN2011ke is only slightly below, at $\sim$ 445 and 152 μJy respectively. Unfortunately, our calculations only go to 10^9 s ($\sim$ 30 years), so we can't give a precise timescale for how long the emission will be detectable; however, it becomes detectable at $\sim$ 10-20 years depending on the supernova and in the case of SN2015bn, is still increasing at 30 years. Given this, 1 GHz emission from SN2015bn may be detectable for 70-100 years or longer after the explosion. In the 100 GHz band, all the sample SLSNe are detectable even with ejecta absorption. With absorption, the emission should be detectable from $\sim$ 1-2 years until $\sim$ 3-30 years post-explosion, and with no absorption, they become detectable from 2-7 months depending on the supernova. Regardless of absorption, SN2015bn has the highest peak flux, while iPTF13ajg has the lowest.

---

[2] These limits actually come from the VLA 3 GHz band and ALMA 230 GHz band respectively.

2.5.2 Radio Emission Predictions from Ejecta Forward Shocks

We have so far only considered non-thermal emission from PWNe which are associated with pulsar-powered SLSNe. But, we can also expect synchrotron emission radiated by electrons accelerated by the supernova forward shock. We estimate the flux of this emission here using a standard model (e.g., Chevalier 1998; Nakar & Piran 2011).

Using the model parameter sets from Table 2.2, the central pulsar loses it energy on a timescale of a few months post-explosion. A large fraction of the initial rotational energy is converted into ejecta kinetic energy $E_{\rm K} \sim 2 \times 10^{52}$ erg $(P/1~{\rm ms})^{-2}$ (See Equation 1.14). The typical velocity of the ejecta is $v_{\rm ej} \approx (2E_{\rm K}/M_{\rm ej})^{1/2} \sim 0.06c~(P/1~{\rm ms})^{-1}$ $(M_{\rm ej}/5~M_{\odot})^{-1/2}$. Here, the radio light curve peak for $\nu \gtrsim$ GHz cooresponds to the SN ejecta deceleration time, $t_{\rm dec} \sim 100$ yr $(n/1~{\rm cm}^{-3})^{-1/3}(M_{\rm ej}/5~M_{\odot})^{1/3}$, where n is the number density of the ISM (See Equation 1.7). Thus, the peak flux is estimated to be around 65 μJy $(\nu/1.5~{\rm GHz})^{-3/4}$ at a luminosity distance of $D_{\rm L} = 300$ Mpc. In this estimate, we assume the accelerated electrons have a power-law index of $p = 2.5$, the amplification efficiency of magnetic field is $\epsilon_{\rm B} = 0.1$, and the efficiency of electron acceleration is $\epsilon_{\rm e} = 0.1$; the flux becomes lower as $\epsilon_{\rm B}$ and $\epsilon_{\rm e}$ decrease. Before the peak, the flux is $\propto t^3$. The parameter set for this estimate is optimistic; for example, the kinetic energy would be smaller for a slower rotating pulsar. If we compare the forward shock emission to the PWN emission (Figures 2.6 and 2.7), we can conclude that PWN emission will likely dominate the forward shock emission until at least a few decades after the explosion.

It is worth noting that radio emission from the supernova forward shock is much more important if the progenitor is surrounded by dense CSM. Interaction-powered supernovae, such as SLSNe-II, are expected to be particularly strong radio sources on timescales of 1-10 years (Murase et al. 2014; Petropoulou et al. 2016).

2.6 Discussion and Summary

In this chapter, we presented a model for quasi-thermal early-time optical emission from pulsar-driven SLSNe and used it to constrain the pulsar and ejecta parameters from six recent SLSNe, and we presented a model for broadband late-time PWN emission and used it to investigate non-thermal radio and submillimetre emission from those SLSNe within a few decades post-explosion. Our calculations show that PWNe emission will likely dominate the ejecta forward shock emission. Additionally, we find that follow-up observations of SLSNe-I with ALMA (and NOEMA, which has similar sensitivity) at $\sim$ 100 GHz and VLA at 1 GHz on $\sim$ 1 and $\sim$ 10 year post-explosion timescales respectively are promising for events at $D_{\rm L} \lesssim 1$ Gpc. A detection of this emission would lend support the pulsar-driven model for SLSNe-I and help solve the parameter degeneracy intrinsic to the model, while a non-detection would help constrain the magnetar paradigm for different types of stripped-envelope SNe.

We assumed a simplified one-dimensional evolution of the PWN and SN ejecta. External absorption is taken into account, assuming an oxygen-rich ejecta in a singly-ionized state. We should note that the uncertainties of these predictions are non-negligible. Synchrotron self-absorption and the Razin effect are relevant at lower frequencies, and this is accounted for in our calculations. Radio emission can also be attenuated by free-free absorption in the supernova ejecta. The strength of these processes is sensitive to the ejecta ionization state, where the ionization is caused by X-rays emitted from the PWNe and the reverse shock induced by the interaction of the supernova ejecta with circumstellar material. Our nominal microphysical and compositional parameters could overestimate radio absorption, thusly underestimate the observable flux. For example, neutralization of the supernova ejecta may be able to proceed efficiently before the ionization state becomes decoupled from the ejecta evolution after a few years post-explosion (e.g., Hamilton & Sarazin 1984). Also, the inner edge of the ejecta being pushed by the strongly magnetized pulsar wind could lead to a Rayleigh-Taylor instability, which would make ejecta more patchy and clumpy (e.g., Arons 2003; Blondin et al. 2001; Chen et al. 2016; Chevalier 2005; Chevalier & Fransson 1992; Suzuki & Maeda 2017), as opposed to the spherically symmetric ejecta in our model. Because of this, some lines of sight may more easily observed the PWN due to the reduced optical depths of a rarefied ejecta, even if the ionization degree of the ejecta is still high on average. If the wind bubble, surrounded by the nebula and mixed with reverse shocked ejecta, is largely blown out, the PWN radius can increase rapidly, and the resulting spectra will become similar to the spectra of Galactic PWNe.

Searching for millimetre and radio non-thermal emission from SLSNe is also of interest to try and verify the possible connection between FRBs and young pulsars. Here, our calculations show that the radio emission from an embryonic SLSN-I remnant that is about a few decades old is broadly consistent with the flux of the persistent radio source from FRB 121102. It is also worth noting the pulsar-driven scenario for SNe and FRBs was able to predict the existence of quasi-steady bright radio emission before the FRB 121102 host galaxy was detected and localized (Murase et al. 2016).

The energy for the nebular emission does not necessarily have to be extracted from the rotational energy of the pulsar. Beloborodov (2017) argued that the nebular emission can instead be powered by the magnetic activity of a an FRB-associated magnetar. Although this is different from our model, if the time-integrated injected energy is similar, both models will exhibit similar nebular emission (although they are stll distinguishable by a long-term follow-up observations with VLA and ALMA from ~ 1 to 10 years), which can keep the consistency with the SLSN-FRB connection.

Chapter 3

Searching Young Superluminous Supernovae Remnants for Late-Time Radio Emission and Fast Radio Bursts

Now that the expected timescales and fluxes for radio emission from a pulsar-driven supernova have been calculated, and the oldest type-I superluminous supernovae (SLSNe-I) are around the age where their emission may be detectable, we conducted radio observations of 10 older SLSNe-I using the Karl G. Jansky Very Large Array (VLA) at 3 GHz. We searched highly time resolved data for FRBs and used the integrated data for a deep imaging search, trying to detect late-time radio emission expected from models of pulsar-driven supernovae. We detected no FRBs. One SLSN-I, PTF10hgi, is detected by deep imaging with a luminosity of 1.2×10^{28} erg s^{-1}. This luminosity, in conjunction with the recent PTF10hgi detection at 6 GHz by Eftekhari et al. (2019), supports the interpretation that the supernova and radio emission are powered by a young, rapidly-rotating ($\sim$ ms spin period) magnetar with $\sim 15\ M_\odot$ of partially ionized ejecta. Our observations are broadly consistent with magnetars with faster spin periods powering SLSNe-I, although most of them require more free-free absorption than we infer for PTF10hgi. Our calculations predict that radio observations in the near future or at higher frequencies will be able to detect these systems and we can begin constraining properties of newborn pulsars and their birth environments.

This chapter is based on Law et al. (2019), and the work was done in collaboration with Casey Law, Kazumi Kashiyama, Kohta Murase, Geoffrey Bower, Kshitij Aggarwal, Sarah Burke-Spolaor, Bryan Butler, Paul Demorest, Joseph Lazio, Justin Linford, Shriharsh Tendulkar, and Michael Rupen.

3.1 Introduction

The development of wide-field time domain surveys has led to new, rare classes of astrophysical transients being discovered and characterized. Optical surveys have identified am extremely luminous transient class that we call superluminous supernovae (SLSNe; Gal-Yam 2012). The energy source of hydrogen-poor SLSNe ("type-I") is inconsistent with an interaction with the surrounding circumstellar medium. This suggests that their power source is internal, such as an accreting black hole (Woosley & Bloom 2006) or rapidly-rotating magnetar (Metzger et al. 2017; Murase et al. 2016).

Centimetre-wavelength radio surveys have discovered Fast Radio Bursts (FRBs; Cordes & Chatterjee 2019; Petroff et al. 2019), which are coherent, millisecond-duration transients. The association of FRB 121102 with a galaxy at $z = 0.1927$ was able to confirm that these bursts are extremely bright and luminous (Chatterjee et al. 2017; Tendulkar et al. 2017), which motivates new models for their origin (Kashiyama & Murase 2017). A new suite of origin models for FRBs was immediately published (Metzger et al. 2019). However, only one model was able to successfully *predicted* the properties of the persistent counterpart of FRB 121102: young magnetars (Murase et al. 2016).

The pulsar-driven model has emerged as a strong candidate for the production of many of luminous transients (e.g. Kashiyama et al. 2016; Maeda et al. 2007; Margalit et al. 2018; Metzger et al. 2015; Nicholl et al. 2015b). Object classes such as FRBs, SLSNe-I, and even ultralong gamma-ray bursts (GRBs) have severely high energetic requirements that can be quickly met by tapping into the rotational energy of a magnetar with a rotation period around the neutron star mass shedding limit. The millisecond-magnetar scenario also presents a testable hypothesis: SLSNe-I should have an association with luminous pulsar wind nebulae (PWNe) on timescales of around a decade (Metzger et al. 2017; Murase et al. 2016, Chapter 2). It may also be possible that SLSNe-I can leave compact remnants that emit transient coherent radio emission which would be detectable as FRBs. The coherent radio emission of pulsars is well characterized observationally, and due to the beaming of this coherent emission, the fraction of detectable sources where the coherent emission can be detected is around 10% (Tauris & Manchester 1998).

Observations from Eftekhari et al. (2019) provided the first evidence for the pulsar-driven supernova model with their detection of ~ 7 years post-explosion radio emission coincident with PTF10hgi, a SLSN-I. The source is in a dwarf galaxy, which is similar to what has been seen for most SLSNe-I (Lunnan et al. 2014; Vreeswijk et al. 2014), but the radio emission could potentially also be associated with an active galactic nucleus (AGN) from the host galaxy, or an off-axis GRB jet afterglow. New radio observations of PTF10hgi would help constrain the spectral and temporal evolution of the source an would help distinguish between these different types of object. Late-time radio emission has been a powerful observational tool for studying short gamma-ray bursts (Metzger & Bower 2014), long gamma-ray bursts (Soderberg et al. 2004), and tidal disruption events (Bower et al. 2013).

In this chapter, we present multifaceted radio observations to search for signatures of the pulsar-driven model for SLSNe-I. We observe the young remnants of known SLSNe-I with the Karl G. Jansky Very Large Array (VLA) and search for both FRBs at 3 GHz commensally through millisecond imaging using the real-time transient search system known as *realfast* (Law et al. 2018b) as well as late-time radio emission. In Section 3.2, we present an overview of the VLA, its hardware and the capabilities and limits of the telescope, as well as the *realfast* and Common Astronomy Software Applications (CASA) software used in the analysis of the data. In Section 3.3, we decribe the observations and our analysis method. In Section 3.4, we discuss the implications of our observations by comparing them to models like those from Chapter 2. Finally, we offer concluding remarks in Section 3.5.

3.2 Hardware and Software

3.2.1 The Karl G. Jansky Very Large Array (VLA)

The VLA[1] is a radio interferometer with 27 active dishes (and 1 spare) located in the desert northwest of Socorro, New Mexico, USA; this location is ideal for its low humidity, resulting in less interference and distortion from water molecules, and its position in a valley ringed by mountains, which limits radio interference from surrounding cities. Construction began in April 1973 with the first interferometric observation taking place on Feb. 18, 1976. Each dish is 25 meters in diameter with 10 supercooled receivers inside and mounted on an altitude-azimuth mount. The antennae are configured in a "Y" shape with 9 dishes in each arm, and the dishes can be moved by truck between 4 different configurations with longest baselines from 36.4 km (A configuration) to 1.0 km (D configuration) and shortest baselines from 0.68 km (A configuration) to 0.035 km (D configuration). An atomic clock is used to timestamp incoming data, and this timing signal is amplified with the radio waves before being digitized for their travel down the fiber-optic cables to the supercomputer. This supercomputer, known as the Wideband Interferometric Digital ARchitecture (WIDAR) correlator, can perform 10^{16} operations per second. Additional correlation analysis is done in a commodity compute clusterknown as the correlator backend (CBE) (Perley et al. 2011).

The VLA can observe in 10 bands, ranging from 73 MHz to 50 GHz, and can determine the position of an object to within 2 milliarcseconds (mas) in ideal conditions. The resolution is usually diffraction limited, and thus set by the antennae baselines and observing frequency. The VLA is sensitive to emission on angular scales between the diffraction limit (the smallest angular scale detectable) and a "Largest Angular Scale" θ_{LAS}. For emitting structures smaller than the diffraction limit, the VLA image is smoothed to the resolution of the array, as if the array was a single dish instrument; for emitting structures larger than θ_{LAS}, the VLA is completely blind to their emission - a unique limitation of interferometers. The synthesized FWHM beamwidth θ_{HPBW} ranges from 24″ at low frequency to 0.043″ at high frequency in A configuration and 850″ at low frequency to 1.5″ at high frequency in D configuration while θ_{LAS} ranges from 800″ at low frequency to 1.2″ at high frequency in A configuration and 20 000″ at low frequency to 32″ at high frequency in D configuration.

In theory, the thermal noise of an image using a natural weighting of visibility data is

$$\Delta I_m = \frac{SEFD}{\eta_c \sqrt{n_{\mathrm{pol}} N(N-1) t_{\mathrm{int}} \Delta\nu}} \tag{3.1}$$

where

- $SEFD$ is the system equivalent flux density (Jy), which is defined as the flux density of a radio source that doubles the temperature of the system - lower $SEFD$ values indicate more sensitive performance. Each antenna has $SEFD = 5.62 T_{\mathrm{sys}}/\eta_A$, where T_{sys} is the total system temperature ($T_{\mathrm{receiver}} + T_{\mathrm{antenna}} + T_{\mathrm{sky}}$) and η_A is the efficiency of the antenna aperture, which depends on which band is used. In D-configuration, the $SEFD$ is 2790 Jy at low frequency and 1300 Jy at high frequency, with a minimum of 250 Jy at 10 GHz.

- η_c is the correlator efficiency (~0.93 using 8-bit samplers).

---

[1] https://public.nrao.edu/telescopes/vla/ and https://science.nrao.edu/facilities/vla

- n_{pol} is the number of polarization products in the image; $n_{\text{pol}} = 2$ for images in Stokes I, Q, U, and V, and $n_{\text{pol}} = 1$ for images in right- or left-circular polarization.
- N is the number of antennae.
- t_{int} is the total on-source integration time (in seconds).
- $\Delta\nu$ is the bandwidth in Hz.

Equation 3.1 gives the best limit possible, but factors such as intermediacy between pure natural and pure uniform weightings, confusion (either within the sythesized beam or the sidelobes of the primary beam (Condon et al. 2012)), weather, and losses from the 3-bit samplers will increase the noise compared to this theoretical limit. The beam-averaged brightness temperature (T_b, in Kelvin), which depends on the synthesized beam, is related to flux density by

$$T_b = \frac{S\lambda^2}{2k\Omega} = FS \tag{3.2}$$

where S is the flux density in mJy per beam, Ω is the beam solid angle, and F is a parameter that depends on array configuration, and takes approximate values $F = 190, 18, 1.7, 0.16$ for A, B, C, and D configurations respectively. The brightness temperature sensitively is obtained by substituting ΔI_m for S. For HI in galaxies, the sensitivity of the observation to HI mass is given by (van Gorkom et al. 1986)

$$M_{\text{HI}} = (2.36 \times 10^5 M_\odot) D^2 \sum S\Delta V \tag{3.3}$$

where D is the distance of the galaxy in Mpc and $S\Delta V$ is the HI line area in Jy km/s.

The default integration times vary between 2-5 s depending on the band and antenna configuration, but can be lowered to $\sim$ 50 ms when using the 8-bit samplers instead of the 3-bit (wideband) samplers. The minimum integration time recommended for any observations is 10 ms. In order to search the data for $\lesssim$ 10 ms FRBs, we use the *realfast* search system to scan the data in real time; this system will be explained in Section 3.2.2.

When synthesizing visibilities from a finite bandwidth as if they are monochromatic, the images will be smeared due to chromatic aberration, an effect that is worse for sources farther from the delay-tracking centre. The integrated flux density of a point source will remain constant, but the peak response will be reduced and the apparent radial width will be increased, leading to radial degradation in the resolution and sensitivity of the array. This can be parameterized by the product of the fractional bandwith $(\Delta\nu/\nu_0)$ and the source offset in synthesized beamwidths $(\theta_0/\theta_{\text{HPBW}})$, and the peak response drops to 0.50 as this product increases to 2.0.

For objects not at the phase-tracking centre, the sampled coherence function is time-variable, so averaging these samples in time will cause a loss of amplitude. This is not easily parameterizable for observation with declinations $\delta \neq 90°$, and approximate analysis methods must be employed (Perley et al. 1989). For 1% amplitude loss, the averaging time is 2.1 s in the A configuration and 68.0 s in the D configuration, while for 10% amplitude loss, the averaging time is 6.7 s in the A configuration and 210.0 s in the D configuration.

Within $\sim$ a decade, the VLA will begin to be upgraded to the next-generation VLA (ngVLA), which will include (Di Francesco et al. 2019)

- A Main Array of 214 18 m clustered in mostly New Mexico, but also some in west Texas, southern Arizona, and northern Mexico, which will provide 10-1000 km baselines.
- A Short Baseline Array of 19 6 m antennae at the current VLA site to allow low surface brightness imaging.
- A Long Baseline Array of 30 18 m antennae located in 10 clusters across North America, including Hawaii, the U.S. Virgin Islands, and western Canada, which will allow very high angular resolution imaging.

and has five main science goals (Di Francesco et al. 2019; McKinnon et al. 2019)

1. Unveiling the Formation of Solar System Analogues on Terrestrial Scales (Wilner & ngVLA Key Science Goal 1 Science Team 2020)
2. Probing the Initial Conditions for Planetary Systems and Life with Astrochemistry (Isella 2020)
3. Charting the Assembly, Structure, and Evolution of Galaxies from the First Billion Years to the Present (Dale & ngVLA Key Science Goal 3 Team 2020)
4. Using Pulsars in the Galactic Center to Make a Fundamental Test of Gravity (Bower et al. 2018)
5. Understanding the Formation and Evolution of Stellar and Supermassive Black Holes and Compact Objects in the Era of Multi-Messenger Astronomy (Lazio & ngVLA Key Science Case 5 Science Team 2020)

The ngVLA will be able to observe from 1.2-116 GHz, execpt at 50-70 GHz due to atmospheric opacity. The array should achieve point-source sensitivities of 0.07 μJy/beam at 30 GHz with 8 hours of integration, 0.5 μJy/beam at 100 GHz with 2 hours of integration, and 0.23 μJy/beam at 10 GHz with 1 hour of integration. The spectral sensitivity should be $\sim$ 30 μJy/beam/km/s with a 10-hour integration. The angular resolution will be $\sim$ 5 mas at 30-100 GHz and 0.6 mas at 10 GHz. The array will be able to recover emission on scales up to 20" $\times$ (100 GHz/ν) (Di Francesco et al. 2019; McKinnon et al. 2019). The final design of the array should be completed by late 2024, with construction starting in 2025 and the array seeing first light in 2034.

3.2.2 *realfast*

Realfast[2] is a commensal, fast transient search system at the VLA consisting of an integrated 160-GPU computing cluster for in situ analysis that searches images generated on millisecond to minute timescales (Law et al. 2018b). By analyzing in situ, the system can trigger recording of a parallel stream for future analysis, and announce candidates for multiwavelength follow-up observations. By using this system, each VLA observation can simultaneously function as a fast transient survey encompassing of thousands of hours per year with a 10σ sensitivity of $\lesssim$ 1 Jy ms.

The *realfast* system receives a copy of the visibility data from the CBE sampled between 5-20 ms, while the original data is integrated to the $\sim$ second timescale for the primary observation. Once the system receives the data, it removes radio-frequency

---

[2] http://realfast.io

interference, applies calibration, and grids and images each time for a range of fiducial dispersion measure (DM) values; this is all done in real time at a rate of 1.4 GB s^{-1} (Law et al. 2018b). The idea was first demonstrated with the first blind interferometric localization of a transient neutron star (Law et al. 2012), and this system was used in the first localization of a repeating FRB (Chatterjee et al. 2017). All *realfast* results are available to the public.

3.2.3 CASA

The CASA toolkit[3] is used in the reduction and analysis of radio and submillimetre data, both single-dish and interferometric (Jaeger 2008), and use an iPython user interface. The kit features a number of tools, which are flexible and more functional but can be tedious to use, and tasks, which are more user friendly Python scripts which are intended to be used for commonly performed data analysis tasks (Jaeger 2008). The kit can import ALMA and EVLA data, or any generic UVFITS data, and data can be flagged either automatically, manually through a task, or interactively through plotter/viewer GUIs (Jaeger 2008).

Calibrating with CASA is a multi-step process, but several tasks make the process much easier. The relationship between the observed and ideal visibilities on the baseline between antennas i and j is given by the Hamaker-Bregman-Sault (HBS) Measurement Equation (Hamaker et al. 1996; Sault et al. 1996)

$$\vec{V}_{ij} = J_{ij}\vec{V}_{ij}^{\mathrm{IDEAL}} \tag{3.4}$$

where $\vec{V}_{ij}$ is the observed visibility, which is a complex number that represents the amplitude and phase of the correlated data from antennas i and j in each sample time; $\vec{V}_{ij}^{\mathrm{IDEAL}}$ is the corresponding ideal visibilities; and J_{ij} represents the accumulation of every corruption affecting the baseline from antenna i to j. Since the visibilities are given as vectors spanning the four correlation combinations which one can form from dual-polarization signals, and these correlations are related to the four Stokes polarization parameter which completely decribe the radiation, the J_{ij} is thus a 4×4 matrix which can be factored into a sequence of different corrupting effects

$$J_{ij} = M_{ij}B_{ij}G_{ij}D_{ij}E_{ij}P_{ij}T_{ij} \tag{3.5}$$

where:

- M_{ij} is the baseline-based correlator errors. These are not factorable into antenna-based parts by definition.

- B_{ij} is the frequency-dependent bandpass response, including that introduced by spectral filters in the electronic transmission system.

- G_{ij} is the polarization-dependent electronic gain response due to components in the signal path between the feed and the correlator. This complex term includes the scale factor for absolute flux density calibration.

- D_{ij} is the instrumental polarization response, which describes the polarization leakage between feeds.

- E_{ij} includes properties of the optical components of the telescopes, such as the dependence of collecting area on elevation.

---

[3] http://casa.nrao.edu/

- P_{ij} is the parallactic angle, which describes the orientation of the polarization coordinates on the plane of the sky. This term can vary with the type of the antenna mount.
- T_{ij} is the polarization-independent effects introduced by the atmosphere, such as opacity and path-length variation.

The steps to calibrate, which mostly involve finding the various terms of Equation 3.5, are as follows [4]:

1. Calibrator Model Visibility Specification: Model visibilities must be set for calibration sources, which can be either point source visibilities if the flux density or structure of the calibrator is unknown (although they are usually approximately point-like), or the visiblities can be derived from a piori images or or standard flux density values. The *setjy* task is used for calibrator flux densities and models.
2. Prior Calibration: Pre-apply previously known calibration quantities, such antenna gain-elevation curves, atmospheric models, delays, and antenna position offsets. The *gencal* task is used for antenna position offsets, gaincurves, antenna efficiencies, opacity, and other prior calibrations.
3. Bandpass Calibration: Solve for the relative gain of the system over the frequency channels. The *bandpass* task is used.
4. Gain Calibration: Solve for the gain variations of the system as a function of time. The *gaincal* task is used.
5. Polarization Calibration: Solve for polarization leakage terms and linear polarization position angle. The *polcal* task is used.
6. Establish Flux Density Scale (if only some calibrators have known flux densities): Rescale gain solutions and derive flux densities of unknown secondary calibrators. The *fluxscale* task is used.
7. Smooth: If necessary, the *smoothcal* task will smooth the calibration table.
8. Examine Calibration: At any point, the *plotcal* or *listcal* tasks can be used to look at the calibration tables that have been created.
9. Apply Calibration to the Data: The corrected data can be formed using the *applycal* task and undone using *clearcal* task.
10. Post-Calibration Activities: These include determinating and subtracting the continuum signal from line data (*uvcontsub*); splitting data-sets into subsets (*split*, *mstransform*); and other operations, such as simple model-fitting: *uvmodelfit*).

Once the data has been calibrated, images can be reconstructed using stages of Fourier transforming the visibilities and image-based deconvolution (Jaeger 2008). Imaging reconstruction involves solving a linear system of equations

$$\vec{V} = [A]\vec{I} \tag{3.6}$$

---

[4] https://casa.nrao.edu/casadocs/casa-5.6.0

where $\vec{V}$ represents the visibilities that have been calibrated for direction independent effects, $\vec{I}$ is the parameters that model the sky brightness distribution, and $[A]$ is a measurement operator which encodes the process of how visibilities are generated when the telescope observes sky brightness $\vec{I}$. $[A]$ is usually given by $[S_{dd}][F]$ where $[F]$ is a 2D Fourier transform, and $[S_{dd}]$ is a 2D spatial frequency sampling function that includes direction-dependent instrumental effects. For an interferometer with a finite number of array elements, $[A]$ is non-invertible because there an unsampled regions in the UV plane. This system of equations must therefore be solved iteratively, with constraints applied from choices of image parameterization and instrumental model.

The algorithm CASA uses to reconstruct images consists of a series of outer loops, which transform between data and image spaces using Fourier transforms, and a series of inner loops, which occur purely in the image space (Clark 1980; Högbom 1974; Schwab 1984; Taylor et al. 1999). The iteration begins with a guess of the image model, then the major cycles predict model visibilities, calculate residual visiblities, and construct a residual image via inverse Fourier transform. This residual image is a convolution of the true sky image and point spread function, and the minor cycle deconvolves the image to produce a model for the true sky image. Different reconstruction algorithms operating on the minor cycle can allow the parameterization of sky brightness to be more flexible. Once this deconvolution is done, the image is Fourier transformed back to the visibility space and the major cycle loops again. The data to image transform can sometimes ignore direction dependent effects, especially baseline, frequency or time-dependent ones; while the minor loops are not accurate over the entire image due to using PSF patches; but the image to data transform must be as accurate as possible so model components include all instrumental effects when converting back to visiblities.

3.3 Data and Analysis

3.3.1 Observations

We observed ten SLSNe-I at 3 GHz using the VLA. Because of the long expected timescale for the radio emission to emerge, we chose the ten oldest SLSN-I from the first large sample that has well-characterized host galaxies (Lunnan et al. 2014). All SNe in this sample have rest-frame ages older than 5 years, but the sample excludes SCP06F6, which is predicted to be too faint to be detectable within a reasonable amount of time. Table 3.1 lists the SLSN-I in order of their rest-frame age in late 2017, the time of observation. We designed the VLA observations for two purposes: to search for FRBs and to search for late-time radio emission. For the FRB search, we wanted to observe frequencies $\lesssim$ 3 GHz, which is where most previous FRBs have been detected. The VLA also has a larger field of view at lower frequencies, which improves the odds of us being able to detect an FRB unassociated with the SLSN-I in our sample. The late radio emission from pulsar-driven supernovae should fade as t^{-2}, but is subject to free-free absorption within the supernova ejecta before the radio emission peaks (e.g. Kashiyama & Murase 2017). Balancing these two effects favours observations on timescales of 5-20 years at 2-10 GHz frequencies.

We observed using the S band as a compromise between our FRB and late-time emission detection goals. There are 8 spectral windows which cover the frequency range between 2.5–3.5 GHz using 32 channels per window with a 4 MHz width per channel. We recorded the visibility data with a 5 ms cadence (this is comparable to an typical FRB pulse width; Petroff et al. 2016) which allows real-time searching for FRBs

TABLE 3.1: SLSN-I Sample.
[a] Late-time radio limit at 1.4 GHz by Schulze et al. (2018).
[b] Late-time radio limit at 3 GHz by Hatsukade et al. (2018).
[c] Late-time radio detection at 6 GHz by Eftekhari et al. (2019).

Name	Redshift	R.A. (J2000)	Decl. (J2000)	Age (yr)
SN 2005ap[a]	0.283	13:01:14:83	+27:43:32.3	9.9
SN 2007bi	0.127	13:19:20.14	+08:55:43.7	9.4
SN 2006oz	0.396	22:08:53.56	+00:53:50.4	8.0
PTF10hgi[c]	0.098	16:37:47.04	+06:12:32.3	6.8
PTF09cnd	0.258	16:12:08.94	+51:29:16.1	6.6
SN 2010kd	0.101	12:08:00.89	+49:13:32.9	6.4
SN 2010gx[b]	0.23	11:25:46.71	-08:49:41.4	6.2
PTF09cwl	0.349	14:49:10.08	+29:25:11.4	6.1
SN 2011ke	0.143	13:50:57.77	+26:16:42.8	5.7
PTF09atu	0.501	16:30:24.55	+23:38:25.0	5.5

with *realfast*. During the observation, the antennas were in the "B" configuration, for which the baseline lengths are up to 10 km and the synthesized beam size is $\sim 3''$ at 3 GHz. Thus, the collected data are sensitive to FRBs anywhere within the primary beam, which has a FWHM size of 14′ .

Table 3.2 describes our observations of each SLSN-I in the sample. The targets were scheduled into four groups, which were each observed in two epochs between late 2017 to early 2018. The duration we observed for each epoch was set to be able to detect a source with a power around 10 times lower than the persistent radio counterpart of FRB 121102 (3σ power sensitivity of $L_{3\mathrm{GHz}} = 3 \times 10^{28}$ erg s^{-1} Hz^{-1}).

For three of the days we observed (MJD 58128, 58130, and 58131), the correlator was unable to write data fast enough, which means some of the data were lost. About $\sim 20\%$ of our data were affected by these correlator issues, interference, or bad calibrations; in some of our later observations, up to 50% of our data were lost.

3.3.2 Searching for FRBs

After each observation, the *rfpipe* pipeline (Law 2017) was used to search the 5 ms data for fast transients. This was run offline by using CPUs in the spare nodes of the VLA correlator cluster. The search applied calibrations which were calculated in real-time by *telcal*, the VLA observing system. Bad channels and integrations were flagged by using a sigma clipping algorithm, while the visibility variance over different baselines was used to flag near-field interference for some specific channel-integration-polarization bins.

We used this to search for FRBs with pulse widths up to 40 milliseconds and dispersion measures up to 3000 pc cm^{-3}. The maximum distance within our SLSN-I sample is $z \sim 0.5$, which would imply an intergalactic medium DM contribution of roughly 400 pc cm^{-3} (Prochaska & Zheng 2019). The Milky Way DM contribution is expected to be smaller than the extragalactic DM contribution in all cases (Cordes & Lazio 2002). The host galaxy and FRB environment DM contribution is expected to be much less than 3000 pc cm^{-3} (Kulkarni et al. 2014); this component contributed $<$ 225 pc cm^{-3} to the total DM for FRB 121102 (Tendulkar et al. 2017).

All candidate bursts which were above 8σ were inspected by looking at the 5 ms image and dedispersed burst spectra associated with the event, and none of the candidates were found to be FRBs. Our typical observations had 26 antennas and 1.5 GHz of clean bandwidth, which means the sensitivity would be about 4 mJy per 5 ms snapshot.

Our nominal sensitivity is idealized, and we need to correct it for the primary beam attenuation and dedispersion effects. *rfpipe* uses a brute-force dedispersion algorithm that loses sensitivity when pulses have DM between the DM search grid (Keane & Petroff 2015). The size of the DM search grid was set so that we wuld lose at most 5% of our nominal sensitivity from intra-DM sensitivity losses, so the 8σ limit becomes 34 mJy for 5 ms snapshots at the primary beam centre. Our deep imaging search was also sensitive to FRBs throughout the primary beam, which has a full-width-at-half-power size of 14′ at 3 GHz. The primary beam FRB search was complete down to a limiting flux of 68 mJy per 5 ms interval. This sensitivity is better defined as a fluence limit which is averaged over the entire 2.5–3.5 GHz band, so sensitivity to spectrally or temporally narrow emission structure is likely worse than what we state here (Gajjar et al. 2018; Law et al. 2017).

3.3.3 Deep imaging

We integrated the 5-ms-resolved snapshots to 1 s and analyzed the time-integrated sets with the standard CASA calibration pipeline (McMullin et al. 2007). Any of our 1 s integrations was fully flagged if it had more than 30% of its subintegrations flagged.

Three observing blocks (which included seven of the targets) used a standard flux calibrator (which was either 3C48 or 3C286). These were calibrated using the VLA CASA calibration pipeline (version 5.4.0). One observing block, which included PTF09cnd, PTF09atu, and PTF10hgi, used 3C295 as a flux calibrator - this source is not supported by the latest CASA pipeline, so we used the VLA scripted pipeline (version 1.4.0) instead for this block. The calibration quality was validated in all cases by checking the standard pipeline output, which includes gain solutions, calibrator images, and visibility plots.

tclean, part of the CASA pipeline, was used to image both epochs of all ten fields. For each field, the first thing we did was produce a sky model through a light clean of sources with mJy-brightness using natural weighting. For some fields, that simple model was sufficient to self-calibrate for both epochs using a single solution per antenna and spectral window. Afterwords, we created the final map for each field by combining both epochs to create a deep-cleaned image. When images had artifacts from nearby sources, we used a robust weighting of 0.5. The cleaner image from either natural or robust weighting for each SLSN was used to estimate noise and search for persistent radio emission.

The sensitivity measured from the deep image made for each SLSN is listed in Table 3.2. Only one target, PTF10hgi, was detected with significance greater than 3σ. Three of the other fields (PTF09cnd, SN2007bi, SN2006oz) also had a detection a radio source within 1′ of the sample SLSN, but all of these sources have an offset more than 10″ - this is far larger than the astrometric uncertainty. This makes these sources very unlikely to be associated with either our sample SLSNe or the host galaxies (host galaxy images are at Lunnan et al. 2014). Stacking all of the images by inverse noise squared produces an image that contains no significant source at the SLSN-I location with a 3σ limit of 0.8 μJy.

TABLE 3.2: Observations of SLSN-I
[a] Detected with a peak flux density of 47 μJy.

Name	Epochs (MJD)	Obs. Time (min; total)	Sensitivity (μJy beam^{-1}; 1σ)
SN 2005ap	58060, 58131	57	10
SN 2007bi	58074, 58128	34	22
SN 2006oz	58036, 58124	60	8
PTF10hgi[a]	58045, 58130	26	14
PTF09cnd	58045, 58130	46	11
SN 2010kd	58074, 58128	27	14
SN 2010gx	58074, 58128	41	11
PTF09cwl	58060, 58131	73	9
SN 2011ke	58060, 58131	35	12
PTF09atu	58045, 58130	109	8

Figure 3.1 shows the 3 GHz detection of a compact source coincident with a 6 GHz counterpart to PTF10hgi (Eftekhari et al. 2019). The source is detected in both observed epochs and its existence is robust to a range of self-calibration and imaging parameter assumptions. We modelled the region using the CASA *imfit* tool which defined a 2-dimensional Gaussian with its width fixed to the synthesized beam shape. The best fit source has a flux density peak of 47 ± 14 μJy (3.3 σ) at (RA, Dec) (J2000) = (16:37:47.04, 6:12:31.4) with a centroid uncertainty of $0.7'' \times 0.4''$. This means the detected 3 GHz radio emission is spacially coincident with the 6 GHz emission found at (16:37:47.071, 6:12:31.88). A 3σ significance has a false alarm rate of 10^{-3}, which means a 1% probability of detection within a ten source sample. Using the noise properties in the observed 3 GHz PTF10hgi image, we estimate that the chance of false association with this source is smaller than 1%.

The source at 6 GHz is consistent with the optical position of PTF10hgi (Lunnan et al. 2014), however, the 3 GHz source is offset slightly at $1''$ from the optical position. We attribute the discrepancy to small phase calibration errors, which affect localizations smaller than the synthesized beam size of $3''$. Uncertainties in referencing the radio and optical frames may also contribute. Henceforth, we shall make the assumption that the 6 GHz and 3 GHz sources are coincident with both the SLSN-I and each other.

The PTF10hgi 3 GHz flux density corresponds to a luminosity $L_\nu = 1.2 \pm 0.4 \times 10^{28}$ erg s^{-1} Hz^{-1}. The 3 and 6 GHz observations of PTF10hgi were made within three months of each other, which makes them effectively simultaneous in the synchrotron emission model context (see Section 3.4). Comparing the 3 GHz and 6 GHz flux densities implies a spectral index $\alpha = 0.0 \pm 0.6$ ($F_\nu \propto \nu^\alpha$). This measurement of the spectral index is consistent with, and slightly more precise than, the one from Eftekhari et al. (2019).

3.4 Discussion

These observations comprise the first search for FRBs and late-time radio emission from a sample of SLSNe-I. The non-detections of FRB do much strongly constrain the rates of FRBs from these sources, especially since several repeating FRB sources have been shown to have quiescent and active phases (Cruces et al. 2020; Tavani et al. 2020b). There are only three SLSN-I with previous observational constraints on radio

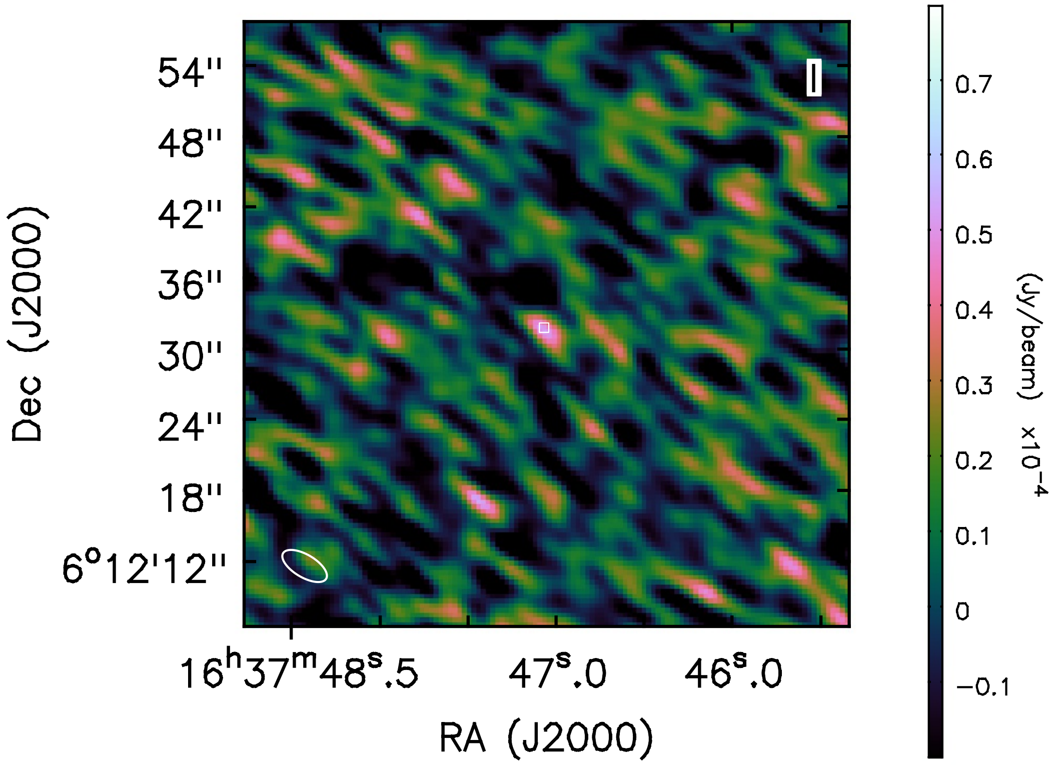

FIGURE 3.1: 3 GHz radio VLA image of PTF10hgi. The location of a 6 GHz source also associated with PTF10hgi (Eftekhari et al. 2019) is represented by the white square, and the beam size is shown on the bottom left.

emission at > 5 years. Schulze et al. (2018) present an upper limit of $F_{1.4\ \mathrm{GHz}} < 75\ \mu$Jy ($3\sigma$) for SN2005ap around 10 years post-explosion, Hatsukade et al. (2018) give 3 GHz upper limits for 8 SLSNe (of which 5 were SLSNe-I, one of these - SN2010gx - is included in our sample), and Eftekhari et al. (2019) detected PTF10hgi with a $F_{6\ \mathrm{GHz}} = 47.3 \pm 7.1\ \mu$Jy flux around 7 years post-explosion.

3.4.1 Modelling

In a pulsar-driven supernova, the luminosity of the persistent radio source is derived from the magnetar-driven wind interacting with the supernova ejecta surrounding it (Metzger et al. 2017; Murase et al. 2016). The birth properties of the pulsar (especially initial magnetic field strength and spin period) are inferred from the early quasi-thermal optical light curve. The optical data we use was taken from the Open Supernova Catalog [5] (Guillochon et al. 2017) and fit by eye with a three-parameter model (Kashiyama et al. 2016): the initial magnetic field $B_{13} = B/(10^{13}\ \mathrm{G})$ and spin period P of the neutron star, and the mass M_{ej} of the supernova ejecta. With this method, we can infer the parameters to within around 5-10%. Since the pulsar-driven model has parameter degeneracies, we define one parameter set with P = 1 ms (P_{min}), close to the neutron star mass-shedding limit (Watts et al. 2016) and another with the

---

[5] https://sne.space/

largest spin period still consistent with the early optical light curve (P_{max}). In Chapter 2 we found that P_{max} can vary between SLSNe, but typically remains < 5 ms.

There are a few different approaches to modeling early optical light curves for SLSNe-I (e.g., Inserra et al. 2013; Liu et al. 2017b; Nicholl et al. 2017b; Prajs et al. 2017) and they can derive different pulsar and ejecta parameters for the same sources. Previous studies tended to assume a simple, classical dipole spin-down, while our model uses a formula based on numerical simulations (Gruzinov 2005; Spitkovsky 2006; Tchekhovskoy et al. 2013). The numerically-inspired spin-down requires much smaller P and B_{13} for the same spin-down luminosity (Kashiyama et al. 2016). Our model also accounts for ejecta acceleration via interaction with the PWN, which couples the spin-down luminosity to the dynamics of the ejecta; a more realistic ejecta profile (a homologous core; Kasen & Bildsten 2010); and self-consistently treats both optical and radio signatures to break degeneracies which are inherent to inferences from the optical data alone.

These studies derive a single set of best-fit parameters, usually via a Markov chain Monte Carlo mechanism, which completely ignores the degeneracy in the parameters, and thus the diversity of possible radio curves that can arise; this is a major reason why calculate radio curves for both the P_{min} and P_{max} cases.

Once the pulsar and ejecta parameters for both parameter sets have been determined, we use the model from Chapter 2 to calculate the radio light curve from the PWN based on the optically-derived parameters. This PWN emission is calculated as it was in previous studies (see Gaensler & Slane 2006; Tanaka & Takahara 2010, and references therein). We model not only the SN and PWN dynamics as we do in our three-parameter early optical model, but we also self-consistently calculate Compton and inverse Compton scattering, adiabatic cooling, pair cascades and both external and internal attenuation by solving the Boltzmann equation for photons, electrons, and positrons in the PWN over the full range of photon frequencies and electron energies (Murase et al. 2015, 2016). We assume a lepton injection spectrum motivated by models of Galactic PWNe, especially the Crab Nebula (e.g., Tanaka & Takahara 2010, 2013), which takes the form of a broken power law spectrum with spectral indices $q_1 = 1.5$ and $q_2 = 2.5$ and a peak Lorentz factor of $\gamma_b = 10^5$. Free-free absorption is calculated by assuming a singly-ionized pure oxygen ejecta, and we do not account for absorption or scattering outside the ejecta (e.g. interstellar dust or gas).

3.4.2 PTF10hgi

Given the more precise new measurement of spectral index, we discuss the viability of different astrophysical progenitors for the observed radio emission coincident with PTF10hgi. Eftekhari et al. (2019) noted that there are three viable models for this radio emission: an off-axis GRB jet, an AGN, and a PWN. The off-axis GRB model predicts emission well above the limits placed on other SLSNe at earlier times (Coppejans et al. 2018; Eftekhari et al. 2019), and also predicts a spectral index $\alpha \sim -1$, which is inconsistent with our observations. Our observed spectral index is, however, consistent with a radio-loud AGN (Chatterjee et al. 2017; Elvis et al. 1994), although the AGN scenario is disfavoured (Eftekhari et al. 2019) because either the black hole must have an unexpectedly large mass compared to a typical radio-quiet AGN (5% of the host galaxy, while dwarf galaxy black holes are usually $\lesssim 0.1\%$ of the galaxy total mass (Merloni et al. 2003; Reines et al. 2013)) or the host galaxy must be peculiar, considering the prevalence of radio-loud AGN found in dwarf galaxies is $\lesssim 1\%$ (Reines et al. 2013).

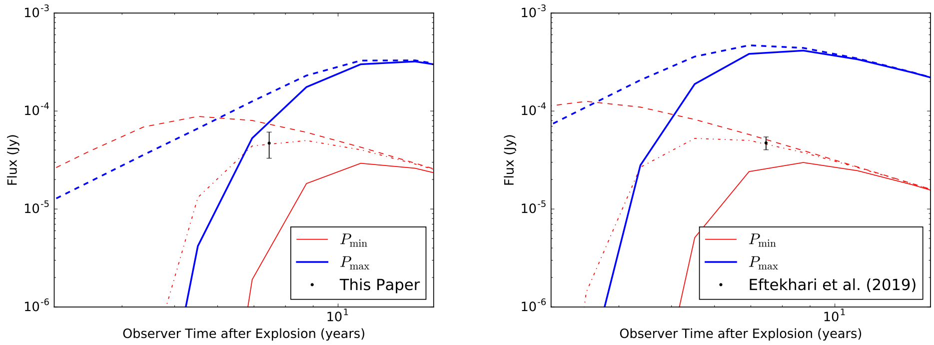

FIGURE 3.2: The detected 3 GHz (left panel; this paper) and 6 GHz (right panel; Eftekhari et al. 2019) flux densities for PTF10hgi with 1σ uncertainties shown in black. The $P_{\rm min}$ and $P_{\rm max}$ models from Table 3.3 are shown in red and blue respectively, with solid lines indicating the light curve with ejecta absorption and dashed lines indicating the curve without ejecta absorption. We find that a $P_{\rm min}$ model where 30-50% of the ejecta is singly ionized and the rest is neutral can reproduce the observed data; the dash-dotted red line indicates a $P_{\rm min}$ model where 40% of the ejecta is singly ionized.

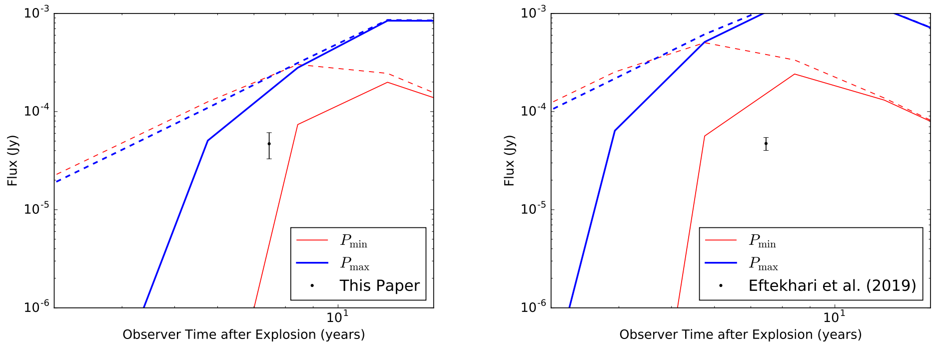

FIGURE 3.3: The same as Figure 3.2, but with $\gamma_b = 10^2$ instead of 10^5 and with no models that have partially ionized ejecta.

In Figure 3.2, we show the radio predictions from the pulsar-driven model for the $P_{\rm min}$ and $P_{\rm max}$ parameter sets, along with the observational data at 3 and 6 GHz. The $P_{\rm max}$ set only slightly overpredicts the 3 GHz data, but severely overpredicts the data at 6 GHz, while the $P_{\rm min}$ set slightly underpredicts both frequencies with ejecta absorption, but is fairly close to fitting both data points with little or no absorption. We find that using the $P_{\rm min}$ parameters and using an ejecta where 30-50% of the ejecta is singly ionized and the rest is neutral can produce a light curve consistent with the observed data; a model with 40% of the ejecta ionized is shown in Figure 3.2. The low ionization fraction may be expected for a the ejecta mass that usually accompanies $P_{\rm min}$ parameter sets, or the lack of absorption could be because that the ejecta are more clumped in regions away from line of sight and more diffuse along line of sight. The $P_{\rm min}$ model does not favour a Wolf-Rayet progenitor, since the expected ejecta mass from these progenitors is smaller than that of the model.

It is also possible to constrain the lepton injection spectrum with this detection. Since optical observations are only sensitive to the total energy injected, they can not constrain the injection Lorentz factor γ_b, which determines the frequency of the spectral break, which is the frequency where most of the energy is injected - γ_b could

Name	B_{13} at 1 ms (G)	$M_{\rm ej}$ at 1 ms ($M_\odot$)	$P_{\rm max}$ (ms)	B_{13} at $P_{\rm max}$ (G)	$M_{\rm ej}$ at $P_{\rm max}$ ($M_\odot$)	Data Reference
SN2005ap	3.0	7	1.4	2.0	2.0	Quimby et al. (2007)
SN2007bi	4.0	25	2.2	2.0	5.5	Gal-Yam et al. (2009)
SN2006oz	5.0	12.5	2.0	2.0	2.5	Leloudas et al. (2012)
PTF09cnd	2.0	14	1.0	2.0	14	Quimby et al. (2011)
PTF10hgi	14	15	4.2	4.0	2.0	Inserra et al. (2013)
SN2010kd	4.7	25	2.4	2.0	4.0	Vinko et al. (2012)
SN2010gx	4.5	10.0	1.6	3.5	3.5	Pastorello et al. (2010)
PTF09cwl	2.0	12	1.5	1.7	3.5	Brown et al. (2014)
SN2011ke	7.5	9.5	2.4	2.9	1.3	Inserra et al. (2013)
PTF09atu	3.0	14	1.6	2.0	4.5	Yaron & Gal-Yam (2012)

TABLE 3.3: Model parameters from early-time optical light curve fits for the SLSNe-I in our sample. Pulsar spin periods were investigated from 1.0 ms to $P_{\rm max}$, with any period above $P_{\rm max}$ either having too slow a decline, not having enough luminosity, or having a light curve shape inconsistent with the observed data (likely due to the decrease in ejecta mass). The parameter uncertainty from these fits is $\sim$ 5-10% each.

take values from $10^2 - 10^6$. Figure 3.2 showed models with $\gamma_b = 10^5$, which is also the assumption in Chapter 2; this makes the synchrotron νF_ν spectrum peak at UV/X-ray energies. Figure 3.3 shows the late-time radio emission for the same parameters, but instead using $\gamma_b = 10^2$, which gives a spectrum with a peak at microwave/infrared energies - emission models for the persistent counterpart of FRB 121102 usually have their spectra peak in that range (Margalit & Metzger 2018). We see that the emission at the radio light curve peak is much more luminous, completely excluding all models at 6 GHz, even though the light curve has reached peak brightness yet. From this result, we find that these observations favour higher γ_b values and exclude those with $\gamma_b \lesssim 10^4$.

Overall, the fluxes observed in both bands are broadly consistent with the pulsar-driven model, but further observations at future epochs with more frequencies will be necessary to confirm the properties of the system with any level of certainty. Models that involve fast cooling emission tend to predict strong evolution of the spectral index through peak luminosity until there is a consistent, negative spectral index. Models that involve relic cooling emission predict a weaker evolution of the spectral index, which remains almost flat even post-peak (e.g. Margalit & Metzger 2018, Chapter 2). The flat measured spectral index suggests that PTF10hgi may be close to peak luminosity and disfavours a detection early in the rise of the radio emission, while there is still a strong absorption signature. However, only further observations will be able to fully differentiate between the two scenarios.

3.4.3 Non-detections

The 3σ luminosity upper limit is shown in Figure 3.4 for the higher sensitivity observation for each undetected SLSN shown in Table 3.2 as well as the radio light curves predicted for each source. Table 3.3 lists the ejecta and pulsar parameters that were used to fit the quasi-thermal early optical light curves and are used in the models of radio emission.

The constraints our observations placed on these models, summarized in Table 3.4, are as follows:

- PTF09atu: Most likely because PTF09atu is the youngest and furthest SLSN-I in our sample, none of our models were excluded, even those without ejecta absorption.
- SN2007bi, PTF09cnd, SN2010kd, and PTF09cwl: Models that include free-free absorption are consistent with observations, but models without free-free absorption are excluded. The absorption amount needed for the model to be consistent with the data varies by supernova; PTF09cnd and PTF09cwl both require only a small amount of absorption, while SN2007bi and SN2010kd both need more. All of these supernovae have data consistent with a $P_{\rm min}$ model with 40% ionized ejecta, similar to PTF10hgi.
- SN2010gx and SN2011ke: Both of these SLSNe-I exclude models without absorption as well, and the $P_{\rm min}$ model would require a large amount of absorption in order to be consistent with observations, more than the best fit model for PTF10hgi. The $P_{\rm max}$ model is also completely excluded for these two supernovae, so a faster spinning pulsar with larger magnetic field and ejecta mass is required to be consistent.
- SN2006oz: Because of the age of this SLSN, free-free absorption for SN2006oz is predicted to be small, regardless of the pulsar parameters. The $P_{\rm max}$ model is excluded by these observations, while the $P_{\rm min}$ model is still viable, even though the emission is predicted to be at or after the peak. Only a small reduction in period from the $P_{\rm max}$ model would be required to make the model viable, however, since the predicted emission has almost the same flux as our 3σ limit.
- SN2005ap: We find that all of our models are excluded based on our observations, as they all overpredict the expected emission. There are three likely reasons for this: this SLSN-I is not magnetar-driven; the electron injection spectrum is not broad and Crab-like (e.g. Tanaka & Takahara 2010, 2013), but sharply peaked at higher energies; or the ejecta are more heavily ionized than predicted. Margalit et al. (2018) predicts at most singly ionized species, but assumes 10 $M_\odot$ of ejecta. However, SN2005ap is best modeled with 2–7 $M_\odot$ of ejecta and Milisavljevic et al. (2018) finds evidence for higher oxygen lines in SN2012au, a putative magnetar-driven supernova. Given these points, the ejecta may become more ionized on a timescale of ~ 5 years. Free-free absorption outside the ejecta could also suppress the emission further.

3.5 Conclusions

In this chapter, we presented new VLA observations that test the hypothesis that SLSNe-I are powered by newborn magnetars or pulsars. We detect one of the ten SLSNe-I observed, PTF10hgi, which supports a previous result and the idea that it is a pulsar-driven supernova (Eftekhari et al. 2019). The two PTF10hgi detections are most consistent with the lowest-period pulsar model with a high mass of partially-ionized ejecta and microphysical parameters similar to those inferred for Galactic PWNe (Murase et al. 2016, Chapter 2). The detections are also not consistent with models using a lower electron-injection Lorentz factor, which is typical for models of the persistent radio counterpart of FRB 121102. This may imply that either these two radio sources have different electron acceleration mechanisms, or that the mechanism changes or becomes less powerful over time, considering that the central pulsar of FRB 121102 is projected to be older than the one in PTF10hgi.

Name	$P_{\min}$ abs	$P_{\min}$ unabs	$P_{\max}$ abs	$P_{\max}$ unabs	$P_{\min}$ w/ PTF10hgi-like abs
SN2005ap	Unviable	Unviable	Unviable	Unviable	Unviable
SN2007bi	Consistent	Unviable	Consistent	Unviable	Consistent
SN2006oz	Consistent	Consistent	Unviable	Unviable	Consistent
PTF09cnd	Consistent	Unviable	Consistent	Unviable	Consistent
SN2010kd	Consistent	Unviable	Consistent	Unviable	Consistent
SN2010gx	Consistent	Unviable	Unviable	Unviable	Unviable
PTF09cwl	Consistent	Unviable	Consistent	Unviable	Consistent
SN2011ke	Consistent	Unviable	Unviable	Unviable	Unviable
PTF09atu	Consistent	Consistent	Consistent	Consistent	Consistent

TABLE 3.4: The viability of different parameter sets for radio emission calculations. Sets of models were made for $P_{\min}$ and $P_{\max}$ and with and without free-free absorption, as well as for a PTF10hgi-like ionization state in the ejecta.

We place constraints on the luminosity of the radio emission from the other nine SLSNe-I in our sample. These limits broadly favour models with faster rotating pulsars, larger ejecta mass, higher magnetic fields, and significant free-free absorption. This contrasts with the most consistent model for PTF10hgi.

Although there are multiple mechanisms that can power the early optical emission from SLSNe-I, the pulsar-driven model predicts an increase in radio flux for all SLSNe-I in this sample (Chapter 2). Repeating these observations with similar sensitivity in 5-10 years would allow stronger constraints on pulsar/ejecta parameters because six of these SLSNe-I (SN2005ap, PTF09cnd, PTF09cwl, SN2010kd, SN2010gx, and SN2011ke) are predicted to be detectable on that timescale for a range of scenarios. Observations today with more sensitive instruments (e.g. MeerKAT or SKA1) or at higher frequencies would also be more likely to be either detect or better constrain the nature of the supernova power source.

The persistent radio counterpart FRB 121102 and the radio source associated with PTF10hgi may be the first observed examples of $<$ 100 yr old pulsars (c.f., De Luca 2017; Gotthelf et al. 2000). Observations of SN1986J in radio also imply the existence of some kind of compact object, but the nature of that object is still unknown (Bietenholz & Bartel 2017a,b,c). Aside from their extreme brightness, the former two radio sources are are observed to possess relatively flat radio spectra at $<$ 10 GHz. A new set of FRB 121102 observations would test whether the persistent radio source evolves in a similarly to PTF10hgi as predicted by our models, both spectrally and temporally. Also, broader spectral PTF10hgi observations would test whether the emission has a spectral break similar to FRB 121102 (Chatterjee et al. 2017).

If other supernovae or transients can be shown to also be pulsar-driven, radio observations can be performed to study both the birth properties of pulsars as well as their progenitors. Radio measurements of PTF10hgi suggest that it was driven by a pulsar which was born with a rotational period close to the 1 ms mass-shedding limit. Meanwhile, Kashiyama & Murase (2017) used the properties of FRB 121102 to estimate a source age of 10-100 years and an initial spin period of $\lesssim$ a few ms. However, initial spin period estimates are somewhat degenerate with photon absorption processes, pulsar magnetic field, and more. Radio observations of known SLSNe-I allow us to use the known age and optical light curve in our models, which help us place stronger constraints on the system properties. Ultimately, we may find ourselves able to connect the FRB phenomenon to these young pulsars, which allows many observational constraints, such as age, ejecta mass, and pulsar spin period (Piro 2016).

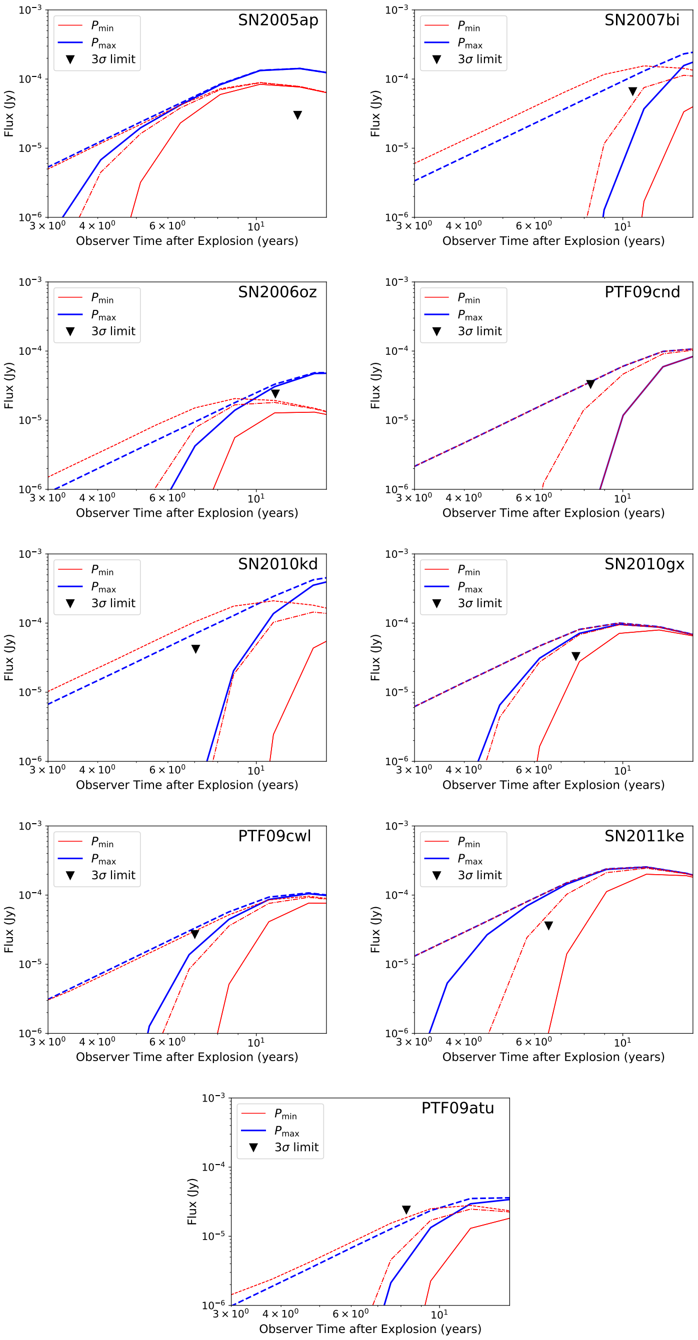

FIGURE 3.4: Comparison of observed flux limits at 3 GHz and the expected flux from a range of magnetar-powered models which are constrained by early optical emission. Each panel represents a specific SLSNe-I and, ordered from left to right, starting at top: SN2005ap, SN2007bi, SN2006oz, PTF09cnd, SN2010kd, SN2010gx, PTF09cwl, SN2011ke, and PTF09atu. The black triangle cooresponds to the 3σ flux limit, while the red and blue lines show the models assuming $P_{\rm min}$ and $P_{\rm max}$ parameters, respectively. The solid lines indicate the modeled radio flux assuming ejecta absorption, the dashed lines indicate the curve without ejecta absorption, and the dash-dotted $P_{\rm min}$ line indicates a PTF10hgi-like model with 40% ionization.

Chapter 4

Extending the Sample of Radio Constraints

Now that we have shown some radio observations, we present a larger, deeper sample at radio and submillimetre wavelengths to help further constrain the model or try to detect additional sources. We use an MCMC method with a different magnetar model to fit optical light curves here, and use parameters from this model and a modified version of our radio model to calculate radio and millimeter light curves. No new radio sources are detected, but these observations exclude this model for seven sources and constrain ten others. Further observations of PTF10hgi do support the magnetar-driven model, but not any particular parameter set that we have been able to find so far. These observations highlight the need for more sophisticated models and better methods for excluding regions of parameter space, and the underlying difficulty of trying to exclude a scenario with many free parameters.

This chapter is based of parts of Eftekhari et al. (2020), and was done in collaboration with Tarraneh Eftehkari, Kate Alexander, Edo Berger, Peter Blanchard, Shami Chatterjee, Deanne Coppejans, James Cordes, Paul Demorest, Sebastian Gomez, Griffin Hosseinzadeh, Brian Hsu, Kazumi Kashiyama, Ben Margalit, Raffaella Margutti, Brian Metzger, Kohta Murase, Matt Nicholl, Ashley Villar, Peter Williams, and Yao Yin. Eftekhari et al. (2020) also contains discussion of obscured star formation, off-axis jets, forward shocks, and ion-electron nebulae; these are omitted here to focus on electron-positron pulsar wind nebulae, which was my contribution to the paper.

4.1 Introduction

Recent wide-field untargeted optical surveys have led to the discovery of a variety of transients, including superluminous supernovae (SLSNe), a rare subclass of core-collapse supernovae (SNe) with luminosities up to 100 times larger than ordinary SNe (Chomiuk et al. 2011; Gal-Yam 2012; Quimby et al. 2011). The hydrogen rich Type II events seem to be simply a more luminous extension of normal Type IIn SLSNe, powered by a collision between the supernova ejecta and circumstellar medium, but the energy source of Type I SLSNe (for simplicity we refer to the hydrogen poor (Type I) events as just SLSNe for the rest of this chapter) is still a topic of debate. Ideas range from pair-instability explosions (Gal-Yam et al. 2009), to interaction with a dense hydrogen-poor circumstellar medium (Chevalier & Irwin 2011), to the injection of energy from a central engine - either the spin-down of a millisecond magnetar central engine (Kasen & Bildsten 2010; Woosley 2010) or fallback onto an accreting black hole (Dexter & Kasen 2013). Recently, a growing line of evidence has emerged to favour the central engine explanation, from the spectroscopic detection of forbidden ionization lines at several years post explosion (Milisavljevic et al. 2018), to spectropolarimetric detection of non-sphericity in two SLSNe (Bose et al. 2018; Inserra et al. 2016a; Saito et al. 2020), to the radio observations presented in Chapter 3, Eftekhari et al. (2019), and Mondal et al. (2020). The early light curve evolution of these SLSNe is well-characterized by the dipole spin-down of rapidly-rotating strongly magnetized neutron stars with large magnetic fields of $\sim 10^{13} - 10^{15}$ G and initial spin periods of $\sim 1 - 10$ ms (Blanchard et al. 2020; Inserra et al. 2013; Kashiyama et al. 2016; Nicholl et al. 2017b, 2014).

Some similarities have also been noted between these SLSNe and long duration gamma-ray bursts (LGRBs). Both arise from massive stripped-envelope stars, show a preference for low metallicity host galaxies (e.g., Levesque et al. 2010b; Lunnan et al. 2014; Modjaz et al. 2008), share ejecta properties as evidenced by nebular-phase spectra (Jerkstrand et al. 2017; Nicholl et al. 2016b), and seem to be powered by central engines, although in the case of LGRBs the engines have generally been assumed to be black holes (e.g., MacFadyen & Woosley 1999; MacFadyen et al. 2001), although some may be powered by magnetars as well (Greiner et al. 2015; Metzger et al. 2011, 2015).

Another possible connection to SLSNe has been suggested by the localization of repeating fast radio burst FRB121102 (Spitler et al. 2014, 2016) to a low metallicity star forming galaxy (Chatterjee et al. 2017; Tendulkar et al. 2017) and an associated parsec-scale persistent radio source (Marcote et al. 2017) with emission broadly consistent with PWN emission from a decades old pulsar-driven SLSN (Kashiyama & Murase 2017; Metzger et al. 2017; Murase et al. 2016) and large and variable rotation measure indicating a highly magnetized and dynamic environment (Michilli et al. 2018). These similarities suggest that FRB production may be associated with the birth of young, millisecond magnetars in SLSN and/or LGRB explosions (Kashiyama & Murase 2017; Margalit & Metzger 2018; Margalit et al. 2018; Metzger et al. 2017; Murase et al. 2016; Nicholl et al. 2017b; Piro 2016).

More recently, the localization of seven apparently non-repeating FRBs by the Australian Square Kilometre Array (SKA) and VLA (Bannister et al. 2019; Bhandari et al. 2020; Law et al. 2020; Macquart et al. 2020; Prochaska et al. 2019; Ravi et al. 2019) and one repeating FRB (Marcote et al. 2020) to more massive galaxies with varying star formation rates suggests that some FRBs may be produced by pulsars or magnetars formed from older progenitor populations, including from binary neutron star (BNS) mergers or the accretion-induced collapse (AIC) of white dwarfs (Margalit et al. 2019). The recent discovery of a luminous, millisecond-duration radio burst from Galactic magnetar SGR 1935+2154 (Bochenek et al. 2020b; Scholz & CHIME/FRB Collaboration 2020) also suggests a connection between magnetars and FRBs (Margalit et al. 2020a); and some portion, although not all, of the FRB population may be emitted from within young SLSN remnants.

Late-time radio and millimetre emission from SLSNe may be key to probe FRB 121102-like systems, but has largely not be explored to date. Early radio follow-up ($\lesssim$ 1-5 years) has yielded only non-detections (e.g., Coppejans et al. 2018; Hatsukade et al. 2018), but follow-up of the SLSN PTF10hgi on a timescale of 8-10 years post-explosion has led to a number of radio detections (Chapter 3; Eftekhari et al. 2019; Mondal et al. 2020). While a magnetar origin has not been completely confirmed for this source, the available data are consistent with emission powered by a magnetar-powered nebula.

In this chapter we present more deep late-time radio and millimeter observations of SLSNe searching for non-thermal synchrotron emission from these sources, which will hopefully shed light on their central engines, possible connection to FRBs, and their host galaxies. This study provides the largest and deepest sample of late-time radio and millimeter observations of SLSNe to date, and we use this data to futher refine constraints on the pulsar-driven model. In Section 4.2, we overview ALMA, which was used to do observations at 100 GHz. In Section 4.3, we present our SLSN sample and overview the observations. In Section 4.4 we overview `MOSFiT`, which is software that can generate many optical light curves and uses an MCMC algorithm to find the best fit magnetar parameters - we use this software here instead of the model from Chapter 2 and our previous χ-by-eye fitting method. In Section 4.5 we overview the radio light curves generated using a `MOSFiT`-tuned model and how they constrain the pulsar-driven model, and finally we conclude in Section 4.6. Throughout the chapter, we use the latest Planck cosmological parameters, $H_0 = 67.8$ km s^{-1} Mpc^{-1}, $\Omega_m = 0.308$, and $\Omega_\Lambda = 0.692$ (Planck Collaboration et al. 2016).

4.2 The Atacama Large Millimeter/submillimeter Array (ALMA)

ALMA[1] is a millimetre and submillimetre interferometer with 66 active dishes on the Chajnantor Plateau in northern Chile; this location was chosen because it is located at 5000 metres in the Atacama Desert, making it one of the highest and driest observing locations on Earth - since most submillimetre emission is absorbed by water molecules in the Earth's atmosphere, this kind of location is required to perform observations. The first prototype antennae underwent evaluation at the VLA from 2003, and the antennae were manufacured in the USA, Europe, and Japan and delivered between 2008 and 2011. Initial testing observations were conducted with 16 antennae in 2011, with the Array officially inaugurated on March 13, 2013. The Main Array consists of 50 antennae 12 metres in diameter that can be arranged with maximum baselines from 0.16 to 16.2 kilometres. The Atacama Compact Array (ACA) or Morita Array sits at the centre of the Main Array and consists of twelve 7-m antennae and four 12-m antennae with baselines up to 30 metres. The data gathered by ALMA is processed in two correlators: the 64-input Correlator (also known as the Baseline Correlator or BLC), which processes data from the Main Array, and the ACA Correlator, which processes data from the compact array. Both of these correlators run simultaneously and independently. Once the signal is through the correlators it is transfered to ALMA offices in Santiago, then distributed to ALMA Regional Centres in North America, Europe, and East Asia. Data analysis is done using CASA, as with the VLA - see Section 3.2.3 for an overview.

ALMA can observe in 8 bands, ranging from 84 to 950 GHz, although this will be extended down to 35 GHz in the future. ALMA has an angular resolution of $\sim 0.2''$ $\times$ (300/ν GHz) $\times$ (1 km/maximum baseline) (Schieven 2020). Because of the ACA, ALMA can image sources of several degrees across while sill maintaining arcsecond resolution. The primary beamwidth $\theta_{\rm HPBW}$ ranges from $\sim$60″ at low frequency to $\sim$7″ at high frequency while $\theta_{\rm LAS}$ ranges from 34″ at low frequency to 3.6″ at high frequency in the most compact configuration and $\sim$1.5″ at low frequency to $\sim$0.3″ at high frequency in the most extended configuration. The continuum sensitivity ranges from 0.08 mJy/beam at low frequency to 3.2 mJy/beam at high frequency while the spectral sensitivity $\Delta T_{\rm line}$ ranges from 0.08 K at low frequency to 4.3 K at high frequency in the most compact configuration and 96 K at low frequency to 1150 K at high frequency in the most extended configuration (Remijan et al. 2020; Schieven

---

[1] https://alma-telescope.jp/en/ and https://www.eso.org/public/teles-instr/alma/

2020). The interferometer has spectral resolution of < 1 km/s at 300 GHz with 3840 channels per baseband, while also able to do dual polarization measurements.

4.3 Sample and Observations

The SLSNe observed with the Karl G. Jansky Very Large Array (VLA) form a (as of February 2017) complete volume-limited sample out to twice the distance of FRB 121102 ($z \leq 0.35$) within 5 years of the supernova explosion. Of these, three were observed at early times: PTF09cnd (Chandra et al. 2009, 2010), SN2012il (Chomiuk et al. 2012), and SN2015bn (Nicholl et al. 2016b) - none were detected, which placed constraints on possible shock interaction powered SNe. The Atacama Large Millimeter/submillimeter Array (ALMA) observations were done in two observing campaigns. The first covered all sources observable with ALMA as of March 2017 (with one exception due to a scheduling error) within 3 years of the supernova explosion, and the second consisted of all events with Decl. $< 30^\circ$ and $z < 0.4$. Not all supernovae have enough optical data to properly constrain a light curve fit, so we only analyse those that do; this sample is shown in Table 4.1, the total integration times and observed fluxes/limits are given in Table 4.2, and calibration sources and beam sizes/angles are given in Table 4.3.

C-band (6 GHz) VLA observations were performed in configurations A and B with an intergration time of ≈ 40 minutes on each target. 2017 observations utilized the 8-bit samplers with ~ 2 GHz bandwidth, while 2019 observations utilized the 3-bit samplers, providing the full 4 GHz of bandwidth. Bandpass and flux density calibration was done using 3C286 and 3C48, with individual sources listed in Table 4.3. Data processing was done with the Common Astronomy Software Application (CASA) software package (McMullin et al. 2007), as in Chapter 3. Imaging was done using 2048×2048 pixel fields at 0.07 - 0.2 arcsec per pixel using multi-frequency synthesis (MFS, Sault & Wieringa 1994) and w-projection with 128 planes (Cornwell et al. 2008). Flux densities and image rms values were extracted using *imtool* (Williams et al. 2017).

In addition to the detection of PTF10hgi (Eftekhari et al. 2019), radio emission was also detected near the location of PTF12dam in two epochs with constant flux density $F_\nu = 117 \pm 12$ μJy. However, the emission is offset from the SN position by ~ 1 arcsecond; traces the optical emission of the galaxy; and is resolved out in the second, A-configuration, observation (indictive of an extended source); we thus conclde that this emission is most likely related to star formation. There is also a marginal 3.6σ ($F_\nu = 23.3 \pm 6.4$ μJy) detection $1.6 \pm 0.3''$ from the position of SN2009jh, but this is likely unrelated to the SN. No clear radio emission was detected from any other sources, with typical rms values of 5-10 μJy.

Band 3 (100 GHz) VLA observations were performed with an intergration time of ≈ 20 minutes on each target. Data processing was also done in CASA using standard imaging techniques, with each field imaged using MFS, a standard gridding convolution function, and Briggs weighting with a robust parameter of 0.5. The image scales span 0.04-0.2 arcsec per pixel with field sizes of around 1500×1500 pixels. Flux densities and image rms values were also extracted using *imtool*.

The only detection at 100 GHz was a marginal 3.0σ ($F_\nu = 55.3 \pm 18.8$ μJy) detection near SN2007bi, but after using achival images we find that the source is offset $1.0 \pm 0.6''$ from the SN and $1.5 \pm 0.6''$ from the host galaxy, making it unlikely to be related to either. No other sources were detected, with typical rms values of ~ 20 μJy.

Supernova	R.A. (J2000)	Decl. (J2000)	Redshift	Observed Frequencies (GHz)
SN2005ap	13:01:14.84	+27:43:31.4	0.283	3,6
SN2006oz	22:08:53.56	+00:53:50.4	0.396	3,6,100
SN2007bi	13:19:20.19	+08:55:44.3	0.127	3,6,100
SN2009jh	14:49:10.08	+29:25:11.4	0.350	3,6
PTF09cnd	16:12:08.94	+51:29:16.1	0.258	3,6
PTF10hgi	16:37:47:04	+06:12:32:3	0.098	3,6,100
SN2010gx	11:25:46.71	-08:49:41.4	0.230	3,6,100
SN2010kd	12:08:01.11	+49:13:31.1	0.1	6
SN2011ke	13:50:57.77	+26:16:42.8	0.143	3,6
SN2011kf	14:36:57.53	+16:30:56.6	0.245	6,100
SN2011kg	01:39:45.51	+29:55:27.0	0.192	6
SN2012il	09:46:12.91	+19:50:28.7	0.175	6,100
PTF12dam	14:24:46.20	+46:13:48.3	0.107	6
LSQ12dlf	01:50:29.80	-21:48:45.4	0.255	6,100
SSS120810	23:18:01.80	-56:09:25.6	0.156	100
SN2013dg	13:18:41.35	-07:04:43.0	0.265	100
LSQ14bdq	10:01:41.60	-12:22:13.4	0.345	100
LSQ14mo	10:22:41.53	-16:55:14.4	0.253	100
SN2015bn	11:33:41.57	+00:43:32.2	0.114	100
OGLE15sd	01:42:21.46	-71:47:15.6	0.57	100
SN2016ard	14:10:44.55	-10:09:35.4	0.203	100
iPTF16bad	17:16:40	+22:04:52.47	0.24	100
SN2016els	20:30:13.92	-10:57:01.81	0.22	100
SN2017gci	06:46:45.026	-27:14:55.86	0.09	100
SN2017jan	03:07:22.570	-64:23:01.00	0.40	100
SN2018lfe	09:33:29.556	+00:03:08.39	0.35	100
SN2018hti	03:40:53.750	+11:46:37.29	0.06	100
SN2018ibb	04:38:56.960	-20:39:44.01	0.16	100

TABLE 4.1: The SLSNe observed by the VLA (6 GHz) and ALMA (100 GHz) with enough optical data to constrain pulsar parameters through light curve fitting. The 3 GHz observations were presented in Chapter 3, and the data will be presented again here for re-analysis.

Supernova	6 GHz			100 GHz		
	δt (years)	$t_{\rm int}$ (min)	F_ν (μJy)	δt (years)	$t_{\rm int}$ (min)	F_ν (μJy)
SN2005ap	9.94, 11.32	19.75, 45.63	<34.17, <6.71			
SN2006oz	7.93	37.55	<20.22	8.11	21.67	<52.83
SN2007bi	9.73	19.75	<36.42	10.00	22.68	<53.10
SN2009jh	6.26	43.15	<19.5			
PTF09cnd	6.74	42.15	<18.54			
PTF10hgi	6.91	40.5	47.3 ± 7.1	6.98	22.18	<44
SN2010gx	6.23	38.55	<16.92	6.41	21.17	<57.12
SN2010kd	6.92	37.55	<14.29			
SN2011ke	5.85	41.15	<14.91			
SN2011kf	4.77, 6.17	41.10, 44.27	<16.68, <13.86	4.89	23.69	<50.1
SN2011kg	4.82	40.80	<18.9			
SN2012il	4.88, 6.53	40.5, 45.60	<15.99, <15.96	5.09	26.21	<57.21
PTF12dam	5.14, 6.69	43.15, 45.63	117.2 ± 11.6			
LSQ12dlf	4.13	40.80	<29.76	4.36	20.66	<51.18
SSS120810				4.71	22.68	<51.87
SN2013dg				3.70	21.17	<61.89
LSQ14bdq				2.82	21.17	<55.5
LSQ14mo				3.21	20.66	<60.66
SN2015bn				2.75	21.67	<54.66
OGLE15sd				1.43	53.42	<36.24
SN2016ard				1.62	21.17	<59.79
iPTF16bad				2.89	69.55	<42.18
SN2016els				2.77	18.44	<60.48
SN2017gci				2.24	18.14	<46.17
SN2017jan				1.68	21.17	<64.38
SN2018lfe				0.86	18.65	<62.04
SN2018hti				1.10	20.16	<51.81
SN2018ibb				1.02	18.14	<57.57

TABLE 4.2: The time between explosion and observation δt (in the explosion rest frame), integration time $t_{\rm int}$, and flux density F_ν for the 6 GHz VLA observations and the 100 GHz ALMA observations. The detection of PTF10hgi was first presented in Eftekhari et al. (2019), and the detection of PTF12dam, where the emission is offset from the SN position by $\sim 1''$, did not change in time and is likely due to star formation in the host galaxy. Flux density upper limits are 3σ.

Supernova	6 GHz BP Cal.	Phase Cal.	B. Size (arcsec)	B. Angle (deg)	100 GHz BP Cal.	Phase Cal.	B. Size (arcsec)	B. Angle (deg)
SN2005ap	3C286	J1310+3220	0.96 × 0.95	-66.36				
	3C286	J1310+3220	0.33 × 0.30	83.64				
SN2006oz	3C48	J2212+0152	1.17 × 0.92	11.13	J2148+0657	J2156-0037	0.41 × 0.31	-85.96
SN2007bi	3C286	J1309+1154	1.18 × 1.04	85.43	J1229+0203	J1254+1141	1.19 × 1.153	-57.23
SN2009jh	3C286	J1443+2501	0.89 × 0.86	22.65				
PTF09cnd	3C286	J1549+5038	0.94 × 0.75	22.25				
PTF10hgi	3C286	J1658+0741	1.07 × 0.90	-41.48	J1550+0527	J1658+0741	0.48 × 0.37	73.44
SN2010gx	3C286	J1131-0500	1.88 × 0.90	-42.57	J1058+0133	J1135-0428	0.53 × 0.39	61.30
SN2010kd	3C286	J1219+4829	1.09 × 0.88	76.33				
SN2011ke	3C286	J1407+2827	1.05 × 0.90	-54.68				
SN2011kf	3C286	J1446+1721	1.09 × 0.90	-45.20	J1550+0527	J1446+1721	0.72 × 0.63	5.17
	3C286	J1446+1721	0.33 × 0.30	37.63				
SN2011kg	3C48	J0151+2744	1.36 × 0.96	-79.72				
SN2012il	3C48	J0954+1743	1.12 × 0.99	-50.17	J0854+2006	J0940+2603	0.48 × 0.37	70.72
	3C286	J0954+1743	0.31 × 0.27	-1.32				
PTF12dam	3C286	J1417+4607	0.95 × 0.74	17.84				
	3C286	J1417+4607	0.39 × 0.28	-63.41				
LSQ12dlf	3C48	J0135-2008	1.15 × 1.04	-32.01	J0006-0623	J0151-1732	0.40 × 0.29	-76.78
SSS120810					J2357-5311	J2336-5236	0.38 × 0.36	-12.61
SN2013dg					J1256-0547	J1312-0424	0.67 × 0.58	80.41
LSQ14bdq					J1037-2934	J0957-1350	0.46 × 0.32	71.07
LSQ14mo					J1037-2934	J0957-1350	0.47 × 0.32	72.08
SN2015bn					J1058+0133	J1135-0428	0.57 × 0.39	55.43
OGLE15sd					J2357-5311	J0112-6634	0.45 × 0.36	-22.87
SN2016ard					J1337-1257	J1406-0848	0.82 × 0.58	-86.36
iPTF16bad					J1924-2914	J1722+2815	3.58 × 2.77	-6.69
SN2016els					J1924-2914	J2025-0735	1.49 × 0.95	87.45
SN2017gci					J0538-4405	J0632-2614	2.70 × 2.28	88.54
SN2017jan					J0334-4008	J0303-6211	3.31 × 2.68	-42.71
SN2018lfe					J0750+1231	J0930+0034	3.55 × 2.52	73.94
SN2018hti					J0423-0120	J0334+0800	2.89 × 2.66	-41.55
SN2018ibb					J0423-0120	J0416-1851	3.03 × 2.39	-71.73

TABLE 4.3: Bandpass calibrators, phase calibrators, beam sizes, and beam angles for each supernova in our sample.

4.4 `MOSFiT` (the Modular Open-Source Fitter for Transients)

In this chapter, we shall use optical supernova data fits previously done using `MOSFiT` (Guillochon et al. 2018) instead of the model introduced in Chapter 2 and fitting by eye. We shall first introduce `MOSFiT` and explain what it is, and then explain the differences between it and our previous model.

4.4.1 What is `MOSFiT`?

`MOSFiT` is a Python-based package that can take multi-band transient data from open catalogs and generate Monte Carlo ensembles of semi-analytic light curve fits to the data as well as generating Bayesian parameter posteriors (Guillochon et al. 2018). The goal of `MOSFiT` is to be easy, adaptable, fast, accurate, transparent, and community-driven. To this end, the code is open-source and modular, making it easy for new users to add new types of transient models within the already existing architecture.

`MOSFiT` models are constructed out of smaller modules, with the model file defining how the modules interact with each other. Each module defines a class that preforms a particular function, and are grouped together depending on their purpose. The groupings are (Guillochon et al. 2018):

- Arrays: Data structures for storing vectors and matrices used by other modules. An example is an array used to store observation times.
- Constraints: A penalizing factor applied to a model with some parameter or combination of parameters enters a disallowed portion of parameter space. An example constraint is when the kinetic energy of the supernova exceeds the total energy previously input.
- Data: Modules to import data from external sources.
- Energetics: Used to calculate needed parameters from the energetics of the supernova, for example, the ejecta velocity or temperature.
- Engines: The physical process that injects energy into a supernova. Examples include the decay of radioactive nickel and cobalt, the fallback of debris onto a black hole, and the spin-down of a rapidly rotating magnetar.
- Objectives: Used to score the performance of a model fit with respect to an observational dataset - typically the likelihood of the model (how probable is the dataset given the predition of the model) as a function of model parameters.
- Observables: Mock observations predicted by a model to be matched against observed data, such as photometry and spectra.
- Outputs: Modules that process model outputs to return to the user or write to disk.
- Parameters: Defines fixed parameters, free parameters, their ranges, and their priors.
- Photospheres: Describes the surface of the transient, where the optical depth drops below unity, and thus photons can escape the transient and be observed.

- SEDs: Spectral energy distributions produced by different components. Usually assumed to be a blackbody, but modified blackbodies or SEDs from template spectra can be used. Also includes extinction corrections from the host galaxy and Milky Way.
- Transforms: Transformations by some component of the transient (e.g. the central engine or ejecta) of some function of time. An example is the reprocessing of input luminosity via photon diffusion.
- Utilities: Other modules that don't belong to other catagories. Examples include arthmetic operators that act upon outputs of multiple modules, such as summing up the energtic components from multiple input engines.

The default models built upon these modules include nickel and cobalt decay (Nadyozhin 1994), ejecta-CSM interaction (Chatzopoulos et al. 2013; Villar et al. 2017a), interaction + NiCo decay, exponential rise or power law decay, NiCo decay with I-band features or synchrotron emission, magnetar engine with or without NiCo decay or other constraints (Nicholl et al. 2017b), single- or multi-component r-process decay (Metzger 2017; Villar et al. 2017a,b), or tidal disruption events (TDEs) (Mockler et al. 2019). These models can fit many classes of supernova inclding IIn, Ia, Ic, SLSN-I and -II, and PISN; as well as kilonovae, TDEs, and other transients (Guillochon et al. 2018).

`MOSFiT` employs a Markov Chain Monte Carlo (MCMC) method to calculate the best fit parameters and their uncertainty. The calculation (see Figure 5 in Guillochon et al. (2018)) is based on an affine-invariance algorithm (Goodman & Weare 2010), an ensemble sampler implemented by the code *emcee* (Foreman-Mackey et al. 2013). This code takes an extremely long time to converge if the number of parameters is $\mathcal{O}(10)$ or higher (Huijser et al. 2015), so before the MCMC walker burns in, `MOSFiT` uses a modified version of *emcee* with a Gibbs sampler-like stretch move which varies a random number of dimensions, making it less likely that the walker gets stuck in a poor local minimum. During this pre-burn phase, walkers are randomly selected for optimization before being substituted back into the walker emsemble. Once this process has occured a pre-determined number of times, the calculation reverts to the basic affine-invariance algorithm. Convergence is checked continuously using the Gelman-Rubin statistic (PSRF, Gelman & Rubin (1992)), and once the statistic is satified a series of uncorrelated samples are collected, where this sampling frequency is determined by the autocorrelation time.

`MOSFiT` has several ways of calculating the goodness-of-fit of a particular model. The simplest one is the reduced chi-square metric $\chi^2_{\rm red} \equiv \chi^2/N_{\rm dof}$, where

$$\chi^2 = \sum_{i=1}^{o} \frac{x_i^2}{\sigma_i^2}, \tag{4.1}$$

where $x_i \equiv O_i - M_i$ is the difference between the ith observation O_i and the model prediction $M_i(\theta)$ (θ is the free parameter vector), σ_i is the Gaussian error for the ith observation, and $N_{\rm dof} = o - m$ is the number of degrees of freedom, where o is the number of observations and m is the number of free parameters within the model. This metric, however assumes that errors are given by Gaussian distributions of uncorrelated noise, which is not likely for either astronomical observation nor model errors. Using this method may also give physically different models with $\chi^2_{\rm red} \leq 1$ since this metric selects regions of parameter space with highest posterior probability density instead of probabalistic mass.

Instead of finding a single best fit, it is best to map all parameter combinations which closely fit the data, which is done using Bayesian analysis, which gives all parameter combinations a posterior probability $p(\theta|O) \approx p(O|\theta)p(\theta)$, where $p(\theta)$ is the prior. Using an additional variance σ^2 added to errors to simulate white noise, the log likelihood is

$$p(O|\theta) = \sum_{i+1}^{n} P(O_i|\theta), \tag{4.2}$$

and the likelihood of a single datum is

$$\log p(O|\theta) = -\frac{1}{2}\sum_{i+1}^{n}\left[\frac{x_i^2}{\sigma^2+\sigma_i^2} + \log 2\pi(\sigma^2+\sigma_i^2)\right], \tag{4.3}$$

with σ^2 incorporated into the parameters θ. This metric, however, asumes uncorrelated errors, which is unlikely for astronomical observations, which are dominated by correlated systematic errors.

The default error model used in `MOSFiT` are Gaussian processes (Rasmussen & Williams 2006). These processes describe the error with a covariance matrix $\boldsymbol{K}$ which has entries K_{ij} given by evaluating a kernal function (in this case, a squared exponential) for every pair of observaed input coordinates i and j. The likelihood calculated from this is

$$\log p(O|\theta) = -\frac{1}{2}\mathbf{x}^T K_{ij}^{-1}\mathbf{x} - \frac{1}{2}\log|K_{ij}| - \frac{n}{2}\log 2\pi, \tag{4.4}$$

where $\mathbf{x}$ is the vector of differences between observations and the model predictions.

Evaluating the total evidence for a model with m free parameters requires an m-dimensional integral performed over the full parameter space, which is usually impossible to perform analytically and prohibitively expensive to perform numerically with economical sampling, such as nested sampling (Skilling 2004), and approximations, such as variation inference (Roberts et al. 2013). Since MCMC models may not explore regions of parameter space with low posterior density, taking the sum of individual walker locations can not be used to determine evidence for a model. A heuristic metric, or information criteria, which relates the distribution of likelihood scores or the fractional volume of parameter space occupied by the walker ensemble to the overall edivdence for a model, can be used to evaluate the model. The one implemented by `MOSFiT` is the Watanabe-Akaike Information Criteria (WAIC) (Gelman et al. 2014; Watanabe & Opper 2010)

$$\mathrm{WAIC} = \log \overline{p(O|\theta)} - \mathrm{var}[\log p(O|\theta)] \tag{4.5}$$

where $p(\overline{O}|\theta)$ is the posterior sample mean of the likelihood and $\mathrm{var}[\log p(O|\theta)]$ is the posterior sample variance of the log likelihood.

4.4.2 The `MOSFiT` Magnetar Model

`MOSFiT` uses a simple model for spin-down luminosity which only accounts for magnetic dipole radiation

$$L_{\mathrm{SD}} = \frac{E_{\mathrm{rot}}}{t_{\mathrm{SD}}}\frac{1}{(1+t/t_{\mathrm{SD}})^2}, \tag{4.6}$$

with $E_{\rm rot}$ and $t_{\rm SD}$ being defined in Equations 1.14 and 1.21 (the values are slightly different due to a slightly different assumption about the neutron star moment of inertia), instead of our spin-down Equation 2.1, which accounts for both gravitational waves and magnetic dipole radiation, and uses a numerical spin-down formula which gives ~ 5 larger spin-down luminosity for fixed (P, B). The diffusion module allows the output luminosity to written analytically as

$$L_{\rm out}(t) = e^{-(t/t_{\rm dif})^2}(1 - e^{-At^2}) \int_0^t 2L_{\rm SD}(t') \frac{t'}{t_{\rm dif}} e^{(t'/t_{\rm dif})^2} \frac{dt'}{t_{\rm dif}} \tag{4.7}$$

with $t_{\rm dif}$ being defined in Equation 2.31 and $A = \tau_{\rm T}^{\rm ej}/t^2$ where $\tau_{\rm T}^{\rm ej}$ was defined in Equation 2.14.

`MOSFiT` ignores feedback between the PWN and ejecta, assuming the ejecta expands at a constant velocity. This assumption decouples the luminosity of the pulsar from the dynamics of the ejecta, necessitating the use of an additional parameter $v_{\rm phot}$, which `MOSFiT` assumes is equal to $v_{\rm ej}$ until a certain plateau temperature T_f is reached, at which point the photosphere recedes into the ejecta. The photospheric temperature and radius have the form

$$T_{\rm phot}(t) = \begin{cases} \left(\frac{L_{\rm out}(t)}{4\pi\sigma v_{\rm phot}^2 t^2}\right)^{1/4} & (\left(\frac{L_{\rm out}(t)}{4\pi\sigma v_{\rm phot}^2 t^2}\right)^{1/4} > T_f), \\ T_f & (\left(\frac{L_{\rm out}(t)}{4\pi\sigma v_{\rm phot}^2 t^2}\right)^{1/4} \leq T_f), \end{cases} \tag{4.8}$$

$$R_{\rm phot}(t) = \begin{cases} v_{\rm phot} t & (\left(\frac{L_{\rm out}(t)}{4\pi\sigma v_{\rm phot}^2 t^2}\right)^{1/4} > T_f), \\ \left(\frac{L_{\rm out}(t)}{4\pi\sigma T_f^4}\right)^{1/4} & (\left(\frac{L_{\rm out}(t)}{4\pi\sigma v_{\rm phot}^2 t^2}\right)^{1/4} \leq T_f). \end{cases} \tag{4.9}$$

The inclusion of the plateau temperature allows `MOSFiT` to extend fits to later times, and has little effect on the posterior of more important physical parameters (Nicholl et al. 2017b). `MOSFiT` assumes that the ejecta emits as a blackbody with a linear flux suppression above a certain cutoff wavelength to mimic the absoption found in UV observations (Chomiuk et al. 2011; Nicholl et al. 2017a; Prajs et al. 2017). The model is constrained so that energy is conserved and the SN does not reach the nebular phase too early, so

$$t_{\rm neb} = (3\kappa M_{\rm ej}/4\pi v_{\rm ej}^2)^{1/2} \tag{4.10}$$

is constrained to be below 100 days, since no SLSN has exhibited a spectrum with a strong nebular component prior to 100 days post explosion (Nicholl et al. 2017b). `MOSFiT` also applies extinction corrections to the light curves for both the host galaxy, where R_V is assumed to be 3.1 and A_V is left as a free parameter, and for the Milky Way, which uses dust maps from Schlafly & Finkbeiner (2011) and a reddening curve from O'Donnell (1994), which is a modified version of the curve from Cardelli et al. (1989).

`MOSFiT` fits for 11 total parameters: 9 physical parameters (P, $B_\perp$, $M_{\rm ej}$, $\langle \nu_{\rm phot} \rangle$, κ, κ_γ, $M_{\rm NS}$, $T_{\rm f}$, and A_V) and two additional parameters (the explosion time and the variance). The priors for each parameter are given in Table 4.4. This is much different than our previous model, which only fit for 4 parameters (P, $B_\perp$, $M_{\rm ej}$, explosion time); fixed κ, κ_γ, and $M_{\rm NS}$; does not include an ad hoc plateau temperature, which does not allow the previous model to fit the light curve well long after the peak; and does

Parameter	Prior	Min	Max	Mean	Std. Dev.
P (ms)	Flat	0.7	20		
$B_\perp$ (10^{13} G)	Log-flat	0.1	100		
$M_{\rm ej}$ ($M_\odot$)	Log-flat	0.1	100		
$v_{\rm phot}$ (10^9 cm s^{-1})	Gaussian	0.1	2.0	1.47	4.3
κ (g cm^{-2})	Flat	0.05	0.2		
κ_γ (g cm^{-2})	Log-flat	0.01	100		
T_f	Gaussian	3.0	10.0	6.0	1.0
A_V (mag)	Flat	0	0.5		
Explosion time (days)	Flat	-100	0		
Variance	Log-flat	10^{-3}	100		

TABLE 4.4: The free parameters fit by `MOSFiT` and their priors. The mean $v_{\rm phot}$ is the mean spectroscopic velocity at 15 days post maximum based on Liu et al. (2017c), and the value for any particular SLSNe was taken directly from their paper if it was in their sample.

not consider extinction, due to most SLSNe being in dwarf galaxies and having low exinction (See Chapter 2 for a quantitative discussion).

4.4.3 Sample Parameters and Model Differences

The best-fit parameters found by `MOSFiT` for our supernova sample are given in Tables 4.5, which shows the key parameters that we used to help calculate the radio model, and 4.6, which shows the less important nuisance parameters, error parameters, WAIC (that could be used to compare the magnetar model to another model), and data references. A full parameter posterior for SN2015bn is shown in Nicholl et al. (2017b) Figure 4. The parameter values span a wide range, with some supernovae showing $P_{\rm min}$-like parameters and some showing $P_{\rm max}$-like parameters. The neutron star masses found are also higher than the previously assumed value of 1.4 $M_\odot$; we previously used $M_{\rm NS}$ = 1.4 $M_\odot$ because it is typical for those found in double pulsar systems, which is where most mass determinations of pulsars have taken place, but $M_{\rm NS} > 1.7$ $M_\odot$, which is what is found by `MOSFiT`, may be typical for slow and bursting neutron stars (Özel & Freire 2016), which may be a better analog for the neutron stars in these systems.

`MOSFiT` has many differences from our previous model, including the spin-down luminosity, lack of ejecta feedback, marginalization over nuisance parameters, and MCMC based multiband fitting, and thus can derive different parameters than ones previously found. To demonstrate this, Figure 4.1 shows V-band light curves of SN2005ap, SN2007bi, and SN2011ke for several models; we show the data taken from the Open Supernova Catalog (Guillochon et al. 2017), the light curves generated by `MOSFiT`, and the light curves generated by a modified version of the previous model using `MOSFiT` derived parameters with the spin-down luminosity and neutron star masses changed to be consistent with those derived by `MOSFiT` and ejecta feedback/acceleration either turned off, so the ejecta velocities are consistent with those of `MOSFiT`, or with ejecta feedback left on. What we find is that the presence or absence of ejecta feedback does not always have the same impact on the light curve; sometimes making it brighter and thinner, and sometimes dimmer and wider. This is likely due feedback coupling the ejecta dynamics to the spin-down of the pulsar, meaning that different pulsars will affect the dynamics differently. We also find that even with feedback turned off, the previous model is still not consistent with `MOSFiT`,

Supernova	P (ms)	$B_\perp$ (10^{14} G)	$\mathrm{M_{ej}}$ ($\mathrm{M_\odot}$)	$\langle v_{\mathrm{phot}} \rangle$ (10^8 cm s^{-1})	$\mathrm{M_{NS}}$ ($\mathrm{M_\odot}$)
SN2005ap	$1.28^{+0.57}_{-0.39}$	$1.71^{+0.75}_{-0.63}$	$3.57^{+3.04}_{-1.23}$	$15.22^{+2.51}_{-2.20}$	$1.89^{+0.16}_{-0.35}$
SN2006oz	$2.70^{+0.74}_{-0.75}$	$0.32^{+0.24}_{-0.19}$	$2.97^{+2.58}_{-1.08}$	$9.46^{+0.69}_{-0.75}$	$1.80^{+0.28}_{-0.23}$
SN2007bi	$3.92^{+0.53}_{-0.50}$	$0.35^{+0.13}_{-0.08}$	$3.80^{+1.52}_{-1.09}$	$7.90^{+0.95}_{-1.41}$	$1.81^{+0.26}_{-0.24}$
SN2009jh	$1.74^{+0.66}_{-0.76}$	$0.27^{+0.59}_{-0.22}$	$6.98^{+9.32}_{-2.78}$	$9.11^{+4.14}_{-2.08}$	$1.86^{+0.27}_{-0.32}$
PTF09cnd	$1.46^{+0.38}_{-0.48}$	$0.10^{+0.09}_{-0.06}$	$5.16^{+2.41}_{-1.64}$	$8.56^{+1.53}_{-1.41}$	$1.82^{+0.23}_{-0.22}$
PTF10hgi	$4.78^{+0.89}_{-0.77}$	$2.03^{+0.45}_{-0.45}$	$2.19^{+1.80}_{-0.80}$	$5.12^{+0.36}_{-0.31}$	$1.85^{+0.22}_{-0.30}$
SN2010gx	$3.66^{+0.60}_{-0.54}$	$0.59^{+0.28}_{-0.15}$	$2.39^{+0.61}_{-0.58}$	$12.6^{+0.55}_{-0.63}$	$1.79^{+0.28}_{-0.24}$
SN2010kd	$3.51^{+0.32}_{-0.41}$	$0.57^{+0.15}_{-0.13}$	$10.51^{+1.44}_{-1.34}$	$5.90^{+0.37}_{-0.32}$	$1.9^{+0.22}_{-0.30}$
SN2011ke	$0.78^{+0.09}_{-0.06}$	$3.88^{+0.32}_{-0.64}$	$7.64^{+6.96}_{-1.89}$	$8.15^{+0.23}_{-0.32}$	$2.05^{+0.10}_{-0.19}$
SN2011kf	$1.48^{+1.16}_{-0.66}$	$0.70^{+0.56}_{-0.33}$	$4.57^{+17.85}_{-2.66}$	$11.46^{+1.15}_{-1.45}$	$1.85^{+0.26}_{-0.30}$
SN2011kg	$2.07^{+2.77}_{-0.95}$	$2.88^{+1.22}_{-2.13}$	$6.54^{+4.08}_{-4.57}$	$12.11^{+1.81}_{-1.89}$	$1.87^{+0.22}_{-0.30}$
SN2012il	$2.35^{+0.51}_{-0.46}$	$2.24^{+0.33}_{-0.57}$	$3.14^{+0.97}_{-0.58}$	$7.93^{+0.57}_{-0.75}$	$1.90^{+0.19}_{-0.34}$
PTF12dam	$2.28^{+0.32}_{-0.30}$	$0.18^{+0.04}_{-0.05}$	$6.27^{+1.23}_{-0.95}$	$7.01^{+0.31}_{-0.25}$	$1.83^{+0.26}_{-0.27}$
LSQ12dlf	$2.82^{+0.55}_{-0.58}$	$1.20^{+0.31}_{-0.26}$	$3.68^{+2.28}_{-0.96}$	$8.28^{+0.25}_{-0.24}$	$1.77^{+0.31}_{-0.25}$
SSS120810	$3.00^{+0.90}_{-1.11}$	$1.93^{+0.45}_{-0.48}$	$2.22^{+1.25}_{-0.66}$	$11.13^{+0.93}_{-0.88}$	$1.88^{+0.22}_{-0.35}$
SN2013dg	$3.50^{+0.60}_{-0.59}$	$1.56^{+0.41}_{-0.32}$	$2.75^{+1.63}_{-0.99}$	$8.38^{+0.44}_{-0.51}$	$1.80^{+0.22}_{-0.21}$
LSQ14bdq	$0.98^{+0.20}_{-0.15}$	$0.49^{+0.13}_{-0.12}$	$33.71^{+6.16}_{-6.56}$	$8.71^{+0.61}_{-0.66}$	$1.80^{+0.27}_{-0.20}$
LSQ14mo	$4.97^{+0.65}_{-0.71}$	$1.01^{+0.27}_{-0.30}$	$2.10^{+0.42}_{-0.36}$	$10.74^{+0.52}_{-0.41}$	$1.85^{+0.22}_{-0.27}$
SN2015bn	$2.16^{+0.29}_{-0.17}$	$0.31^{+0.07}_{-0.05}$	$11.73^{+0.83}_{-1.34}$	$5.46^{+0.16}_{-0.14}$	$1.78^{+0.28}_{-0.23}$
OGLE15sd	$2.16^{+0.75}_{-0.83}$	$1.74^{+0.71}_{-0.74}$	$7.27^{+5.92}_{-2.69}$	$9.33^{+1.51}_{-1.12}$	$1.91^{+0.21}_{-0.30}$
SN2016ard	$0.93^{+0.17}_{-0.18}$	$1.55^{+1.26}_{-0.78}$	$16.6^{+1.23}_{-0.87}$	$14.2^{+0.74}_{-1.45}$	$1.81^{+0.26}_{-0.31}$
iPTF16bad	$3.73^{+0.65}_{-0.70}$	$2.62^{+0.55}_{-0.49}$	$2.22^{+1.05}_{-0.98}$	$7.11^{+0.71}_{-0.59}$	$1.79^{+0.23}_{-0.24}$
SN2016els	$0.92^{+0.30}_{-0.16}$	$5.38^{+1.03}_{-1.27}$	$11.83^{+6.54}_{-3.29}$	$15.43^{+1.75}_{-1.71}$	$1.95^{+0.18}_{-0.30}$
SN2017gci	$1.26^{+0.56}_{-0.37}$	$3.46^{+0.68}_{-0.78}$	$11.74^{+8.11}_{-4.52}$	$1.35^{+1.65}_{-7.83}$	$1.92^{+0.20}_{-0.30}$
SN2017jan	$3.08^{+0.30}_{-0.38}$	$0.34^{+0.10}_{-0.09}$	$7.14^{+1.75}_{-1.58}$	$8.03^{+1.18}_{-0.97}$	$1.90^{+0.31}_{-0.31}$
SN2018lfe	$2.85^{+0.50}_{-0.69}$	$2.20^{+1.38}_{-0.67}$	$3.80^{+1.29}_{-1.26}$	$10.05^{+0.92}_{-0.95}$	$1.90^{+0.21}_{-0.41}$
SN2018hti	$1.25^{+0.42}_{-0.30}$	$2.59^{+0.51}_{-0.58}$	$31.04^{+16.96}_{-10.03}$	$6.06^{+1.24}_{-1.18}$	$1.89^{+0.22}_{-0.29}$
SN2018ibb	$0.74^{+0.07}_{-0.03}$	$0.16^{+0.09}_{-0.05}$	$43.47^{+13.79}_{-10.82}$	$10.27^{+1.42}_{-1.22}$	$2.10^{+0.07}_{-0.14}$

TABLE 4.5: Key `MOSFiT` parameters for each SLSN used to help calculate the radio model. First presented in Nicholl et al. (2017b) except for SN2016ard, which was presented in Blanchard et al. (2018).

Supernova	κ ($\mathrm{cm}^2\ \mathrm{g}^{-1}$)	κ_γ ($\mathrm{cm}^2\ \mathrm{g}^{-1}$)	T_f (10^3 K)	A_V (mag)	σ (mag)	WAIC	Data References
SN2005ap	$0.15^{+0.03}_{-0.06}$	$0.09^{+5.05}_{-0.08}$	$5.77^{+0.89}_{-0.95}$	$0.25^{+0.15}_{-0.16}$	$0.01^{+0.01}_{-0.00}$	57.05	Quimby et al. (2007)
SN2006oz	$0.13^{+0.06}_{-0.04}$	$0.39^{+13.20}_{-0.35}$	$5.93^{+0.72}_{-1.05}$	$0.11^{+0.15}_{-0.08}$	$0.01^{+0.02}_{-0.01}$	76.58	Leloudas et al. (2012)
SN2007bi	$0.16^{+0.03}_{-0.05}$	$0.06^{+0.03}_{-0.02}$	$8.38^{+0.42}_{-0.36}$	$0.07^{+0.11}_{-0.06}$	$0.13^{+0.01}_{-0.01}$	169.22	Gal-Yam et al. (2009)
SN2009jh	$0.17^{+0.02}_{-0.06}$	$0.03^{+2.05}_{-0.02}$	$3.91^{+0.32}_{-0.26}$	$0.32^{+0.11}_{-0.19}$	$0.06^{+0.22}_{-0.06}$	-8.21	Quimby et al. (2011)
PTF09cnd	$0.16^{+0.03}_{-0.05}$	$0.01^{+0.01}_{-0.00}$	$4.44^{+0.36}_{-0.41}$	$0.17^{+0.18}_{-0.12}$	$0.13^{+0.01}_{-0.02}$	58.03	Quimby et al. (2011)
PTF10hgi	$0.10^{+0.06}_{-0.04}$	$0.06^{+0.03}_{-0.03}$	$6.58^{+0.23}_{-0.20}$	$0.11^{+0.11}_{-0.07}$	$0.12^{+0.01}_{-0.01}$	96.83	Inserra et al. (2013)
SN2010gx	$0.18^{+0.02}_{-0.03}$	$0.02^{+0.02}_{-0.01}$	$3.99^{+0.11}_{-0.12}$	$0.02^{+0.02}_{-0.01}$	$0.14^{+0.01}_{-0.01}$	248.46	Pastorello et al. (2010) Quimby et al. (2011)
SN2010kd							Vinko et al. (2012)
SN2011ke	$0.13^{+0.04}_{-0.06}$	$4.75^{+47.75}_{-4.24}$	$5.52^{+0.20}_{-0.17}$	$0.06^{+0.08}_{-0.05}$	$0.19^{+0.02}_{-0.02}$	129.84	Inserra et al. (2013)
SN2011kf	$0.16^{+0.03}_{-0.05}$	$0.04^{+0.04}_{-0.02}$	$5.86^{+0.26}_{-0.25}$	$0.23^{+0.20}_{-0.18}$	$0.06^{+0.02}_{-0.03}$	66.53	Inserra et al. (2013)
SN2011kg	$0.16^{+0.03}_{-0.05}$	$0.25^{+20.23}_{-0.23}$	$8.28^{+0.45}_{-0.59}$	$0.42^{+0.06}_{-0.07}$	$0.29^{+0.02}_{-0.03}$	44.94	Inserra et al. (2013)
SN2012il	$0.08^{+0.03}_{-0.01}$	$3.18^{+31.64}_{-2.89}$	$6.27^{+0.24}_{-0.15}$	$0.12^{+0.10}_{-0.08}$	$0.11^{+0.02}_{-0.01}$	56.56	Inserra et al. (2013)
PTF12dam	$0.16^{+0.02}_{-0.04}$	$0.01^{+0.00}_{-0.00}$	$6.48^{+0.28}_{-0.21}$	$0.16^{+0.09}_{-0.10}$	$0.22^{+0.01}_{-0.02}$	109.39	Nicholl et al. (2013) Chen et al. (2015) Vreeswijk et al. (2017)
LSQ12dlf	$0.11^{+0.04}_{-0.04}$	$2.36^{+18.09}_{-2.00}$	$3.77^{+0.14}_{-0.14}$	$0.29^{+0.14}_{-0.11}$	$0.08^{+0.01}_{-0.01}$	141.34	Nicholl et al. (2014)
SSS120810	$0.14^{+0.04}_{-0.06}$	$0.22^{+3.00}_{-0.12}$	$3.80^{+0.12}_{-0.19}$	$0.33^{+0.12}_{-0.19}$	$0.20^{+0.03}_{-0.03}$	31.00	Nicholl et al. (2014)
SN2013dg	$0.12^{+0.06}_{-0.04}$	$0.04^{+0.02}_{-0.02}$	$5.07^{+0.23}_{-0.31}$	$0.07^{+0.10}_{-0.06}$	$0.01^{+0.02}_{-0.01}$	125.80	Nicholl et al. (2014)
LSQ14bdq	$0.19^{+0.01}_{-0.02}$	$0.01^{+0.00}_{-0.00}$	$6.78^{+0.49}_{-0.29}$	$0.37^{+0.09}_{-0.14}$	$0.12^{+0.02}_{-0.02}$	53.51	Nicholl et al. (2015a)
LSQ14mo	$0.17^{+0.03}_{-0.02}$	$0.02^{+0.01}_{-0.00}$	$4.97^{+0.17}_{-0.16}$	$0.08^{+0.10}_{-0.06}$	$0.00^{+0.01}_{-0.00}$	128.35	Chen et al. (2017b)
SN2015bn	$0.19^{+0.01}_{-0.02}$	$0.01^{+0.00}_{-0.00}$	$8.32^{+0.32}_{-0.16}$	$0.08^{+0.09}_{-0.04}$	$0.18^{+0.01}_{-0.01}$	587.65	Nicholl et al. (2016b) Nicholl et al. (2016a)
OGLE15sd							Wyrzykowski et al. (2015)
SN2016ard	$0.16^{+0.02}_{-0.03}$	$5.75^{+30.55}_{-5.24}$	$6.06^{+0.25}_{-0.95}$	$0.55^{+0.13}_{-0.11}$	$0.15^{+0.01}_{-0.02}$		Chornock et al. (2016)
iPTF16bad							Yan et al. (2017)
SN2016els							Mattila et al. (2016)
SN2017gci							Delgado et al. (2017)
SN2017jan							Wyrzykowski & Gromadzki (2017)
SN2018lfe							Chambers et al. (2019)
SN2018hti							Tonry et al. (2018a)
SN2018ibb							Tonry et al. (2018b)

TABLE 4.6: Other `MOSFiT` parameters, and the WAIC, for each SLSN, which are not used by the radio model. First presented in Nicholl et al. (2017b) except for SN2016ard, which was presented in Blanchard et al. (2018).

likely due to the way that energy transport and ejecta temperature is calculated in the model, or the other differences mentioned previously.

Chapters 2 and 3 also only fit three parameters (P, $B_\perp$, $M_{\rm ej}$) to the the peak of the supernova light curve in one band by eye, which leads to larger uncertainty on parameters and no way to marginalize nuisance parameters or generate posteriors. This may lead to systematic differences in parameters, like the neutron star masses mentioned above. $E_{\rm SN}$ is also fixed to 10^{51} erg in the previous model due to the dynamics being governed mostly by the spin-down luminosity of the pulsar, and this value is close to the maximum ($\sim 2 \times 10^{51}$ erg) that can be deposited by neutrinos due to their small cross-section (Janka 2012; Müller 2017; Terreran et al. 2017). Due to the non-mathematical determination of goodness of fit (χ-by-eye fitting, the previous model is not able to determine a "best-fit" parameter set, but rather take two extreme examples, one with a pulsar spinning close to the mass-shedding limit (Watts et al. 2016), and one with the pulsar spinning as slow as possible while still able to fit the light curve - these two parameter sets generate very different radio curves, effectively giving an upper and lower bound an the expected radio emission. This may be possible to accomplish with `MOSFiT` as well, by marginalizing over other parameters while keeping one fixed (like P or $M_{\rm ej}$), thus generating a series of parameter sets that can reproduce the optical emission well and thus give an idea of the variety of possible radio light curves; this is beyond the scope of what we are trying to present now, and will be saved for a future study.

4.5 Results and Discussion

We calculate broadband spectra and radio/millimetre light light using a modified version of the PWN model presented in Chapter 2. We modify the spin-down formula and neutron star masses, and ignore the effects of ejecta feedback for consistency with the `MOSFiT` models. The radio models solve the Boltzmann equation for photons and electron/positrons in the PWN over all photon frequencies and electron energies (Murase et al. 2015, 2016), allowing for a self-consistent calculation of pair cascades, Compton and inverse Compton scattering, adiabatic cooling and both internal and external attenuation. The electron-positron injection spectrum is assumed to be a broken power law with injection spectral indices of $q_1 = 1.5$ and $q_2 = 2.5$ and a peak Lorentz factor of $\gamma_b = 10^5$ as in Chapters 2 and 3, which is consistent with Galactic PWNe (e.g., Tanaka & Takahara 2010, 2013) such as the Crab PWN, as well as the inferred nebula for PTF10hgi with $q_1 = 1.3 \pm 0.1$ (Mondal et al. 2020). Free-free absorption in the ejecta is calculated assuming a singly-ionized oxygen ejecta, and we do not consider absorption outside the ejecta, as in Chapters 2 and 3. This version of the code also has an updated implicit solver, which will cause faster convergence with low time resolution. This will cause the radio curves to be lower than in previous chapters, which will change our interpretation of PTF10hgi.

The results of the models are shown in Figure 4.2, where we plot the predicted light curves at 3, 6, and 100 GHz for the SLSNe in our sample, as well as those from Chapter 3. A general feature of the models is that they predict emission which peaks in the millimeter with a high flux density on timescales of $\sim$ 1000 days and cascades to lower frequencies and lower flux densities at later times (See Chapter 2). In this context, our ALMA observations lead to less constraining limits as they do not probe the peak of the emission, which is expected on earlier timescales.

For many of our sources, we find that our non-detections are consistent with the predicted radio modelling. At 3 and 6 GHz, a number of sources are expected to

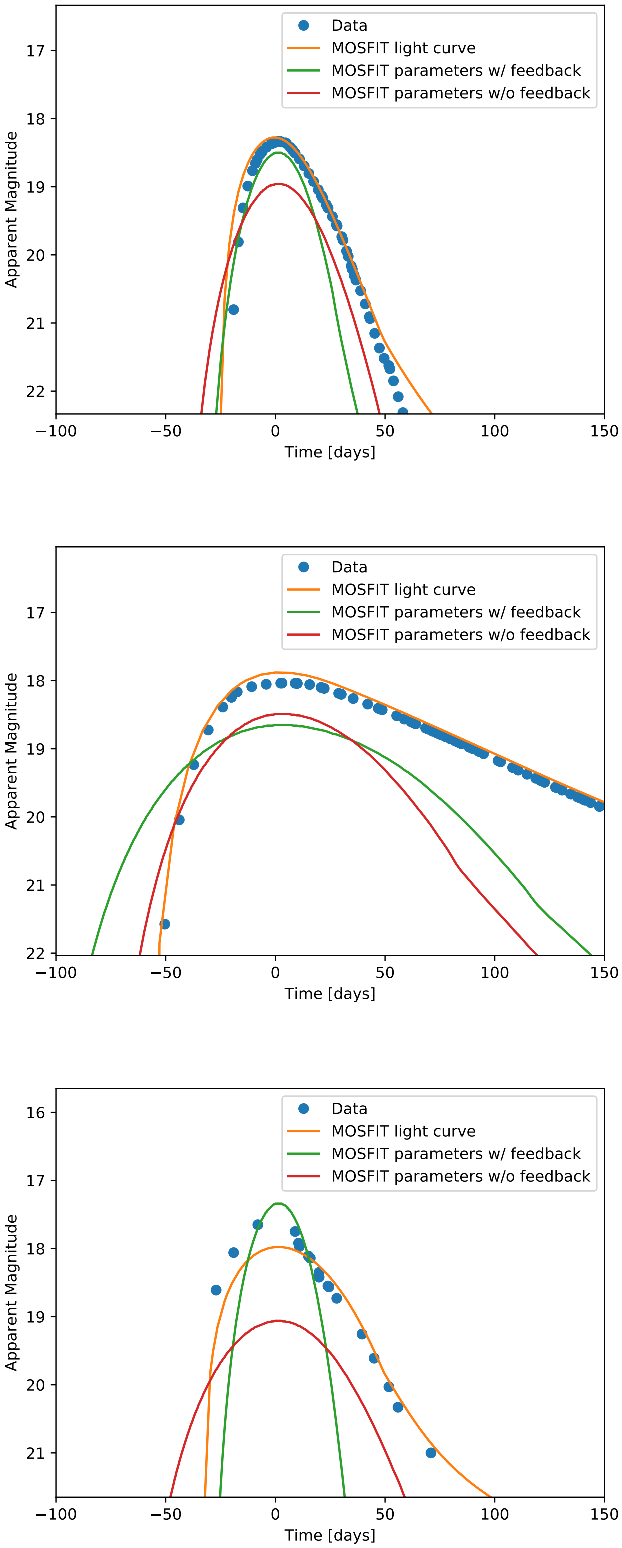

FIGURE 4.1: V-band light curves for SN2005ap (top), SN2007bi (middle), and SN2011ke (bottom). The blue dots represent observational data taken from the Open Supernova Catalog (Guillochon et al. 2017), the orange lines are the best-fit light curves generated by `MOSFiT` (Nicholl et al. 2017b), and the green and red lines are generated from the Chapter 2 model using `MOSFiT`-derived parameters with modified spin-down luminosities and neutron star masses and ejecta feedback turned on and off respectively.

peak at later times than those we observed, and therefore may be detected with future observations. However, seven sources exhibit predicted emission at or above the level of our 3σ upper limits at the time of our observations. These are SN2005ap, SN2006oz, SN2009jh, PTF09cnd, and SN2011kf at 6 GHz, SN2010gx at 3 and 6 GHz, and SN2007bi at 3, 6, and 100 GHz. For ten additional sources (SN2006oz at 3GHz; SN2010kd, SN2011ke, SN2011kg, SN2012il, and PTF12dam at 6 GHz; SN2015bn, SN2017jan, SN2018hti, and SN2018ibb at 100 GHz), the limits exclude models without absorption but not models with absorption. These non-detections might indicate some serious flaws with the magnetar-driven model for SLSNe, but due to the uncertainty in the model itself, the parameter degeneracies not taken account by `MOSFiT`, and the lack of constraints on parameters pertaining to the injection spectrum, its not clear if these observations invalidate the model for these sources or if the true magnetar parameters simply lie in an unexplored region of parameter space.

In Figure 4.3 we plot the predicted radio emission for PTF10hgi and observations of the SLSN presented in Chapter 3, Eftekhari et al. (2019), and Mondal et al. (2020) over the range $0.6 - 100$ GHz. We show two models here, the model based on `MOSFiT` parameters with modified dynamics, as in the rest of this section, and the $P_{\rm min}$ model from Chapter 3 that was found to fit the 6-7 year 3 and 6 GHz data with 30-50% ionized ejecta, but re-calculated with the updated implicit solver. We find that neither of these models accurately predict the spectrum obtained by Mondal et al. (2020), as both of them underestimate the radio emission in all bands, with only the unabsorbed 6 GHz emission from the `MOSFiT` parameters consistent with any the data.

In Figure 4.4 we plot the same data and models, but with $\gamma_b = 10^4$ here instead of 10^5; we find these models are much more consistent with the data. The `MOSFiT`-tuned model is below the non-detection upper limits at 0.6 and 100 GHz, is consistent with the 3 GHz observations assuming no absorption, is consistent with the 6 GHz observations assuming partial absorption at 6 years and almost maximal absorption at 8 years, and is consistent with the 15 GHz observation regardless of absorption (the ejecta is predicted to be optically thin for free-free absorption at 15 GHz by this time); these differences are negligible in light of systematic uncertainties in the models. However, the `MOSFiT`-tuned model vastly underpredicts the 1.2 GHz observation due to having a much later rise time.

Conversely, while the $P_{\rm min}$ model is also below the non-detection upper limits at 0.6 and 100 GHz and mostly consistent with the 1.2, 3, and 6 GHz observations, slightly underpredicting all of the later observations when assuming no absorption, it vastly underpredicts the 15 GHz observation due to having a much earlier rise time. Lowering γ_b even more here would likely fit the data better, as the unabsorbed curves at 8 years would be brighter and pushed closer to the data, and the absorbed curves would need to be increased by more than a factor of two before overestimating any of the data. One interesting physical implication of this is that the pair multiplicity in PTF10hgi (See Equation 2.22) is significantly higher than that of the Crab pulsar or other Galactic PWNe, which may indicate that the pair formation or acceleration processes in the nebulae of supernovae driven by highly magnetic millisecond pulsars are qualitatively different then those of Galactic PWNe - whether this is unique to SLSN nebulae due to the luminosity of the nebula and strength of the pulsar field or the SLSN nebula will eventually evolve to have a lower multiplicity is an interesting question that arises from this. Still, finding a consistent model with these parameters, only adjusting γ_b, seems unlikely.

Since the `MOSFiT`-tuned model has high spin period and low ejecta mass compared to the $P_{\rm min}$ model, we can infer that the true pulsar parameters likely lie in between those of the two models (e.g., $P \approx 2 - 4$ ms, $M_{\rm ej} \approx 6 - 9\ M_\odot$) - this can have to be tested at a later time by creating a series of optically-consistent models and comparing them to these radio observations. The flat shape of the spectrum between $1 - 15$ GHz may also indicate a steeper injection spectrum, so we may have to adjust parameters that do not affect the optical observations - this parameter study is outside the scope of the current work. Continued broadband radio monitoring will test both of these scenarios, as well as the vaildity of the pulsar-driven model as a whole.

4.6 Conclusions

In this chapter we presented the largest sample of radio and millimeter SLSNe observations to date. Using the VLA and ALMA, these observations probed non-thermal synchrotron emission from these SLSNe on timescales of $\sim$ 1-12 years after the explosion. Combined with existing observations from the literature and earlier chapters, we placed constraints on the central engines and explored possible connections to FRBs.

We overviewed a new method of finding magnetar parameters via the software `MOSFiT`, which has some differences with the optical model presented in Chapter 2 and finds different parameters than that model. We used those parameters and a modified version of the radio model also presented in Chapter 2 to calculate radio light curves and use our observations to place constraints on those systems. We find that the `MOSFiT`-tuned model is completely excluded for seven of the sources and limits are placed on absorption for ten more for microphysical parameters similar to those of Galactic pulsar wind nebulae (Murase et al. 2016, Chapter 2). These constraints are much stronger than those placed in Chapter 3 due to the higher frequency, and exclude the model for many more supernovae. However, because this study only uses one set of magnetar parameters and ignores the degeneracy of those parameters, the model exclusions are less meaningful than those from previous chapters. Without a full exploration of both the degenerate magnetar parameters (P, B, and $M_{\rm ej}$) and the PWN parameters (spectral indices and γ_b), it is impossible to say with any confidence that any particular SLSN is not magnetar-driven. While the magnetar parameters can be explored with software like `MOSFiT` by restricting the number of parameters marginalized over, it was be nearly impossible to test the PWN parameters without developing a simpler, quicker model to generate radio curves.

Observations of PTF10hgi, both those presented in this document and by others, seem to favour the magnetar-driven model, but finding consistent parameters for all observations is still a challenge. Models using a lower electron injection index, by about a factor of ten compared to Galactic pulsar wind nebulae, are needed to achieve consistency with the data. Parameter sets with high spin periods and low ejecta masses have late rise times that are inconsistent with low frequency observations, and parameter sets with low spin periods and high ejecta masses have early rise times that are inconsistent with high frequency observations, so the true parameters are likely in between, but the true PWN parameters are likely also different than those we have assumed, so a more thorough examination of different light curves with the same magnetar parameters will be needed. Although we found in Chapter 3 that a very low electron-injection Lorentz factor is inconsistent, there are much smaller variations to the factor, as well as the spectral indices, that need to be investigated.

Ultimately, more observations will need to be performed and better, faster models will need to be developed. Many of the sources that were not constrained by low frequency observations in this chapter can be tested with similar observations at a later date, since the predicted rise time is later than we performed our observations. Also, millimeter follow-up of younger sources than those examined here can test the model in that regime, since many of our sources (with the notable exception of SN2015bn, which is a perfect candidate for another set of millimeter observations) were past the peak of the predicted millimeter light curves. Combining these radio observations with other multiwavelength follow-up will be key to identifying and characterizing interesting sources in the future. Other models of SLSNe, such as fallback accretion, also need their possible "smoking gun" signatures tested, since there may be multiple channels for SLSN explosions.

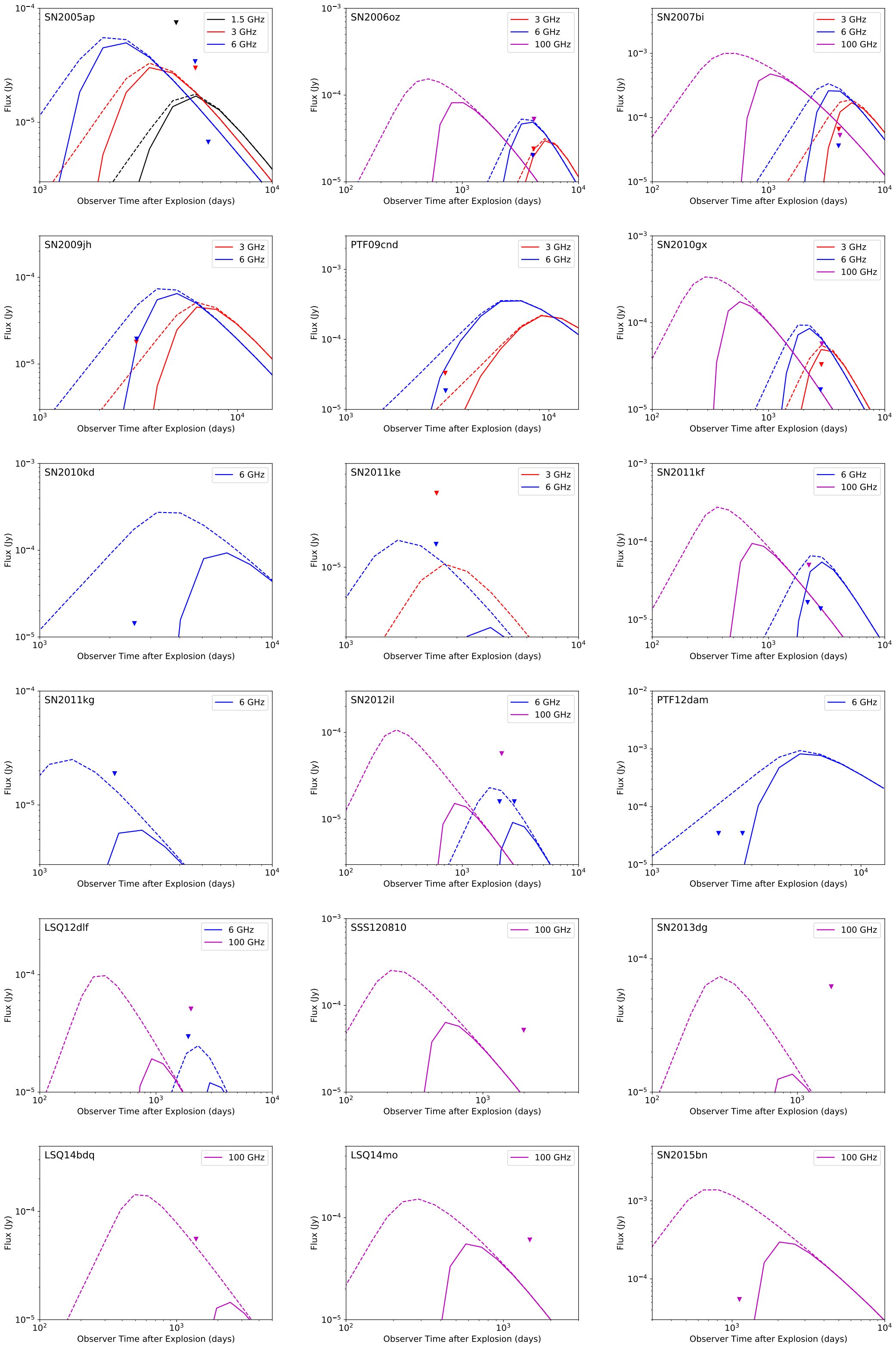

FIGURE 4.2: Comparison of observed 3, 6, and 100 GHz flux limits and expected flux from pulsar-driven models constrained by the early-phase optical emission from the SLSNe. Each panel shows a specific SLSNe-I. The red, blue, and purple triangles show the 3σ 3, 6, and 100 GHz flux limits, respectively; the red, blue, and purple lines show the models for those bands, respectively; and the solid lines indicate the modeled radio flux assuming absorption, the dashed lines indicate the curve with no absorption. SN2005ap also shows 1.5 GHz data from Schulze et al. (2018), and we generate a 1.5 GHz light curve for comparison.

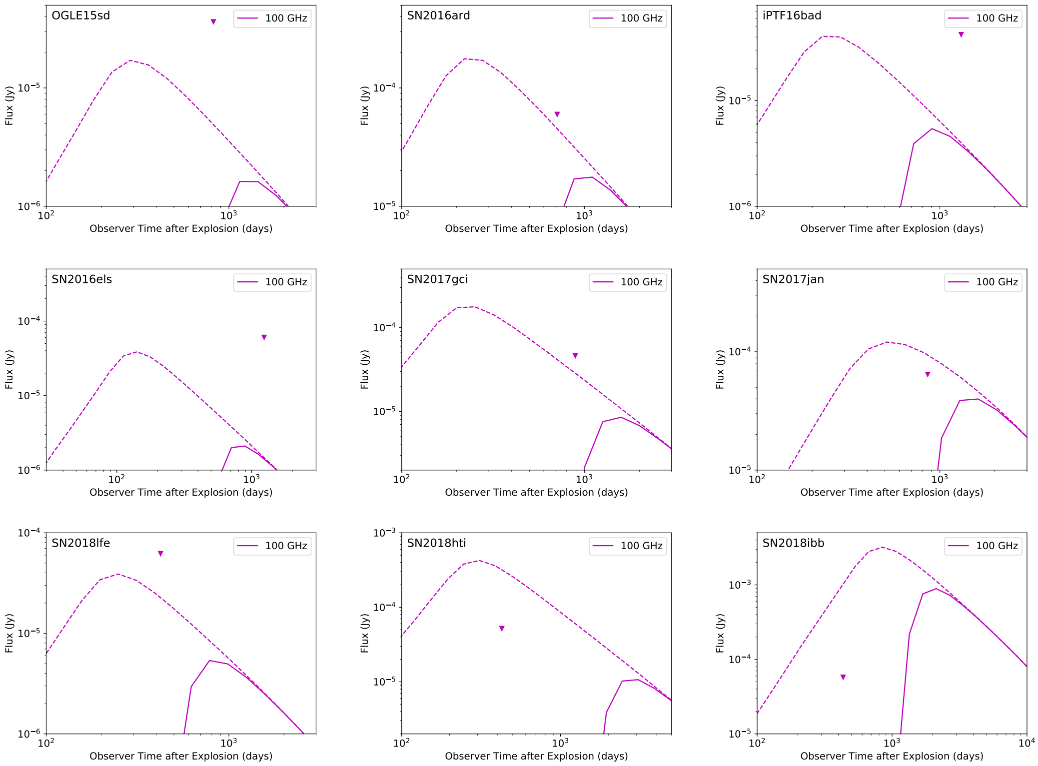

FIGURE 4.2: (cont.)

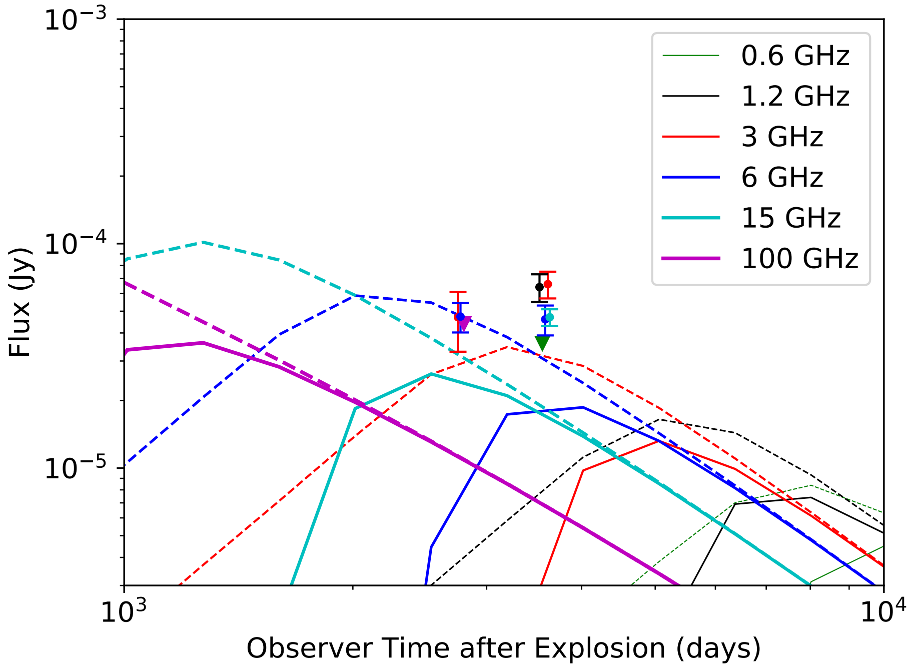

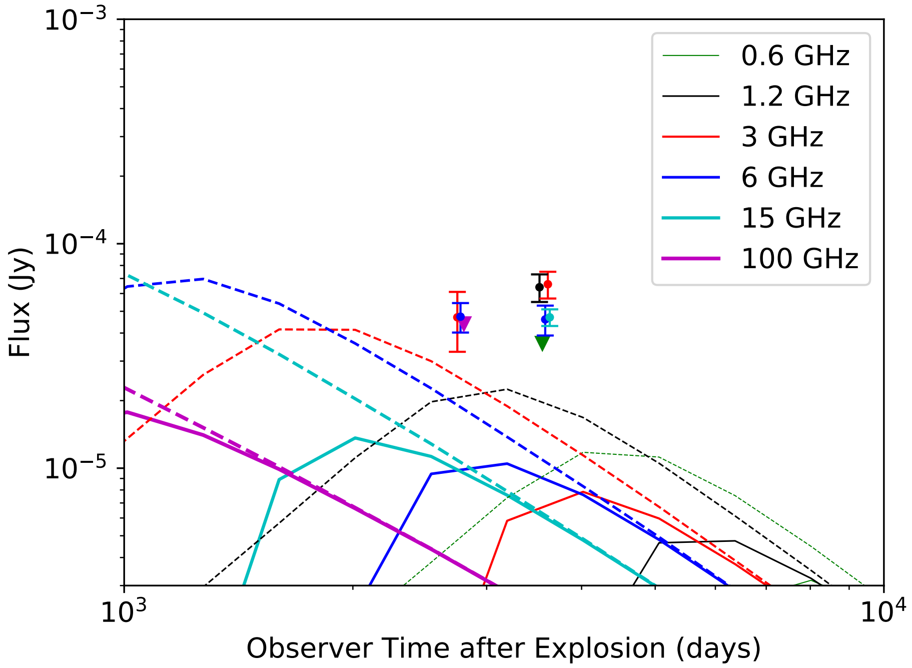

FIGURE 4.3: 0.6 – 100 GHz Wideband spectral data and 3σ for PTF10hgi from Chapter 3, Eftekhari et al. (2019), and Mondal et al. (2020), and models based on the `MOSFiT` parameters (top) and $P_{\min}$ parameters (bottom). Solid lines indicate the modeled radio flux assuming absorption, the dashed lines indicate the curve with no absorption.

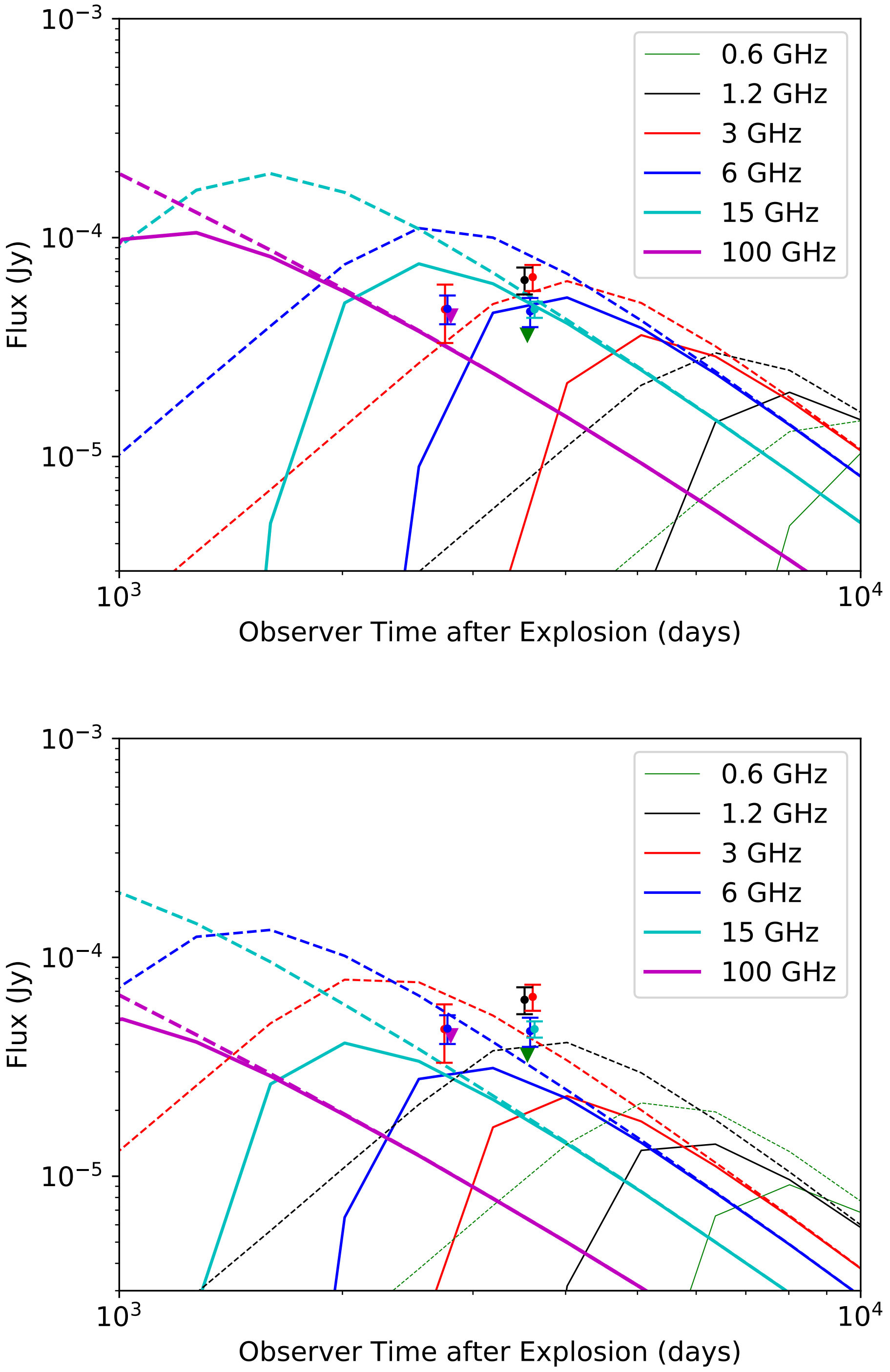

FIGURE 4.4: Same as Figure 4.3, but with $\gamma_b = 10^4$ here instead of 10^5.

Chapter 5

Dust Formation and Re-Emission of Pulsar Wind Nebula Emission

We studied the direct detectability of PWN emission in previous chapters, and now we introduce and discuss a method of detecting pulsar wind nebulae through their effect on the surrounding ejecta via the detection of reprocessed PWN emission from dust grains in the supernova ejecta. Many supernova remnants with neutron star compact remnants have also had dust emission observed in them, and here we investigate the effect of the emission from these PWNe on dust formation, growth, destruction, and emission. The influence of a pulsar might be able to explain discrepancies between dust formation models and observations of nearby supernova remnants, such as the formation time for dust in SN1987A or the dust size in the Crab Nebula. Knowledge of the timescale, luminosity, and frequency of dust re-emission will be helpful to understanding future ALMA observations of SLSNe-I. We investigate the dependence of dust formation timescale and average dust size on the properties of the central pulsar and supernova ejecta. Our studies show that a pulsar can either delay or accelerate dust formation, giving a range of timescales from a few months to over 15 years, and can reduce the average dust size of by a factor of $\gtrsim 10$ compared to the case without PWN emission. We find that re-radiation from dust may be detectable in infrared for typical superluminous supernovae out to distances of $\sim$ 100-1000 Mpc on timescales of 2-5 years post-explosion, although this is very sensitive to the emission properties of the PWN. We discuss implications on previous supernova observations.

This chapter is based on Omand et al. (2019), and the work was done in collaboration with Kazumi Kashiyama and Kohta Murase.

5.1 Introduction

Within the expanding ejecta of supernovae, cooling metal-rich gas condenses to form dust grains. These grains are subsequently injected into the ISM, where they cause diffuse infrared emission and interstellar extinction, catalyze H_2 formation, and function as building blocks for planets, moons, asteroids, and other rocky bodies.

The origin of dust has been hotly debated since the discovery of a large amount of dust at $z \gtrsim 5$ (Gall et al. 2011). CCSNe from massive stars are likely to be the dust dominant source in the early universe (Dwek et al. 2007). Submillimeter and infrared observations of SN1987A (Dwek & Arendt 2015; Indebetouw et al. 2014; Lakićević et al. 2012; Matsuura et al. 2011, 2015), SNR G54.1+0.3 (Temim et al. 2017), Cas A (Barlow et al. 2010; Sibthorpe et al. 2010), and the Crab Nebula (Gomez et al. 2012); and optical observations looking at emission-line asymmetry in SN 1980K, SN1993, and Cas A (Bevan et al. 2017); have reported the presence of $< 1\ M_\odot$ of cool dust in the ejecta of the supernovae which has yet to be destroyed by the hot gas from the reverse shock (Micelotta et al. 2016). The amount of dust that survives the shock depends on the post-formation dust size (e.g., Nozawa et al. 2006, 2007), so understanding both the size and mass of dust produced in supernovae is necessary.

Previous studies of dust formation in supernovae have usually neglected the effect of the PWN, even though some models and data have been inconsistent in several SNR where nebulae and dust have been detected together. For example, the dust detected in the Crab Nebula was smaller than models predicted (Kozasa et al. 2009; Temim et al. 2012b); this may have been because of early PWN energy injection. The formation of dust in SN1987A also occurred slower than most condensation models predicted (Kozasa et al. 1991; Sarangi & Cherchneff 2015; Wooden et al. 1993), which may have been because of PWN emission, even though a PWN has yet to be detected. It is not known whether a PWN could be both energetic enough to delay the formaion of dust and be weak enough to remain undetected.

The idea has recently emerged to try and test the millisecond-magnetar model for energetic SNe by detecting early PWN radiation from hypernovae and SLSNe-I (Kotera et al. 2013; Metzger et al. 2014; Murase et al. 2016), which are both hypothesized to be magnetar-powered (e.g., Dai et al. 2016b; Inserra et al. 2013; Metzger et al. 2015; Nicholl et al. 2014, 2016b; Pastorello et al. 2010; Quimby et al. 2011; Wang et al. 2015). These studies have suggested X-rays and gamma rays (Kashiyama et al. 2016; Metzger et al. 2014; Murase et al. 2016), radio waves (Murase et al. 2016, Chapter 2), submillimetre emission (Murase et al. 2016, Chapter 2), and even neutrinos (Kashiyama et al. 2016) to be "smoking gun" signals of a central magnetar. X-ray studies have produced tentative candidates (Margutti et al. 2017; Perna et al. 2008; Perna & Stella 2004), but have not yet placed strong constraints, while detecting gamma-ray signals is more challenging and has yet to produce any candidates (Kotera et al. 2013; Murase et al. 2015). Radio observations could be promising, but the ejecta can attenuate emission at this wavelength until about 10 years post-explosion (Murase et al. 2016, Chapter 2), which roughly matches the age of our oldest SLSN candidates, so only the oldest sources can be well constrained. Millimetre observations are also promising, as the ejecta only attenuates signals at this wavelength until about 1 year post-explosion (Murase et al. 2016, Chapter 2). However, ALMA has also been used to investigate dust in supernova remnants (e.g., Indebetouw et al. 2014), and dust re-emission in SLSN remnants may contaminate the PWN emission signal. Therefore, comparing the spectra of dust emission in SLSNe to PWNe spectra would allow us to check if hot dust will interfere with ALMA observations; be detectable at another wavelength, such as infrared; or be less luminous than the PWN emission in all cases.

We use a steady-state formation model, which we elucidate in Section 5.2, to investigate dust formation, destruction, and emission in pulsar-powered supernovae. So far, only sublimation of already formed dust has been investigated (e.g., Kobayashi et al. 2011; Waxman & Draine 2000). PWN emission may be able to delay the formation of dust via additional energy injection and can sublimate dust as it forms, leading to even longer formation timescales and the possible non-production of dust at all. Higher energy PWN emission can also ionize the gas in the ejecta prior to dust formation, leading to increased temperature and electrostatic repulsion between ions, which can prevent dust from forming altogether. However, once dust grains have formed, they can absorb radiation in the optical/UV band, greatly increasing the dust temperature compared to the non-pulsar case. These radiation heated grains will re-emit, likely in the infrared, and this might be detectable with telescopes like Herschel, Spitzer, or the James Webb Space Telescope (JWST). This gives a method of indirectly detecting emission from the PWN through its effects on the ejecta, which compliments the direct radio detection discussed in previous chapters.

We present our model for dust formation, sublimation, and emission, as well as other theoretical concerns, in Section 5.2. We present the results of our calculations in Section 5.3, discuss those results in Section 5.4, and then summarize in Section 5.5.

5.2 Theory

In the late phase after a pulsar-driven supernova explosion, dust particles can form by the nucleation of gas molecules into a mesoscopic grain and grow via the further accretion of un-nucleated gas. Without an external energy source, this dust will quickly cool and its emission will not be detectable. However, in the presence of pulsar wind nebula emission, dust that is not sublimated can emit at a higher blackbody temperature, perhaps at a detectable flux. The thermodynamics-based model we use for dust nucleation and accretion was developed by Nozawa & Kozasa (2013) for a supernova with a simple power law temperature and concentration evolution, but can be used with our more complicated evolution; we present this model in Section 5.2.1. We discuss the composition of the ejecta and of the dust grains we will study in Section 5.2.2. The criteria for sublimation was developed by Waxman & Draine (2000) for use in a gamma ray burst, but can also be used in a spherical explosion; we present this criteria in Section 5.2.3. The dust emission is thermal and we derived the formulas based on simple optical depth and blackbody considerations; we present these in Section 5.2.4. Finally, we discuss the ionization of gaseous atoms by PWN radiation in Section 5.2.5.

The simplified model we use for the PWN-ejecta system is shown schematically in Figure 5.1, and we study it from the time of supernova explosion until the reverse shock. The loss of rotational energy of the neutron star generates a PWN which presses against and injects energy into the supernova ejecta at $R_{\rm w}$. We use a one-zone thin-shell approximation, where the entire ejecta is contained between $R_{\rm w}$ and $R_{\rm ej}$ and is at a constant density. The innermost region of the ejecta can be either a sublimation region out to radius R_c, if the optical/UV radiation is luminous enough to heat the dust above the critical temperature T_c for supersaturation/sublimation, or an ionization region of radius R_s, if higher-energy emission can ionize the gas in that region. Both of these mechanisms can prevent dust from forming in the inner region; we explain the conditions governing the boundaries of these regions in Sections 5.2.3 and 5.2.5. Outside of this region, there will be a thin ejecta layer where most of the optical/UV radiation is absorbed by dust and re-radiated at lower energies; the thickness of the absorption region is given by $\tau_{\rm opt/UV} \sim 1$. Outside the absoption region, stretching to the edge of the ejecta, is the cold, dusty region, where dust is not heated by PWN emission and cools by both adiabatic and radiative cooling; we neglect emission from this region, since the dust temperature is expected to be much lower than in the absorption region. If R_c or R_s is $> R_{\rm ej}$, then no dust forms at all, and all the ejecta will be in an ionization/sublimation region with no absorption or cold, dusty regions.

We use the same dynamics and PWN spectrum as the model presented in Section 2.2, and we take the nickel mass $M_{\rm Ni}$, SN energy $E_{\rm SN}$, and opacity κ to be 0.1 $M_\odot$, 10^{51} erg, and 0.1 g cm^{-2} respectively, as in Chapter 2.

5.2.1 Dust Formation

The formation of dust in supernova ejecta has been mainly studied using classical nucleation theory and its extensions (Bianchi & Schneider 2007; Kozasa et al. 1989,

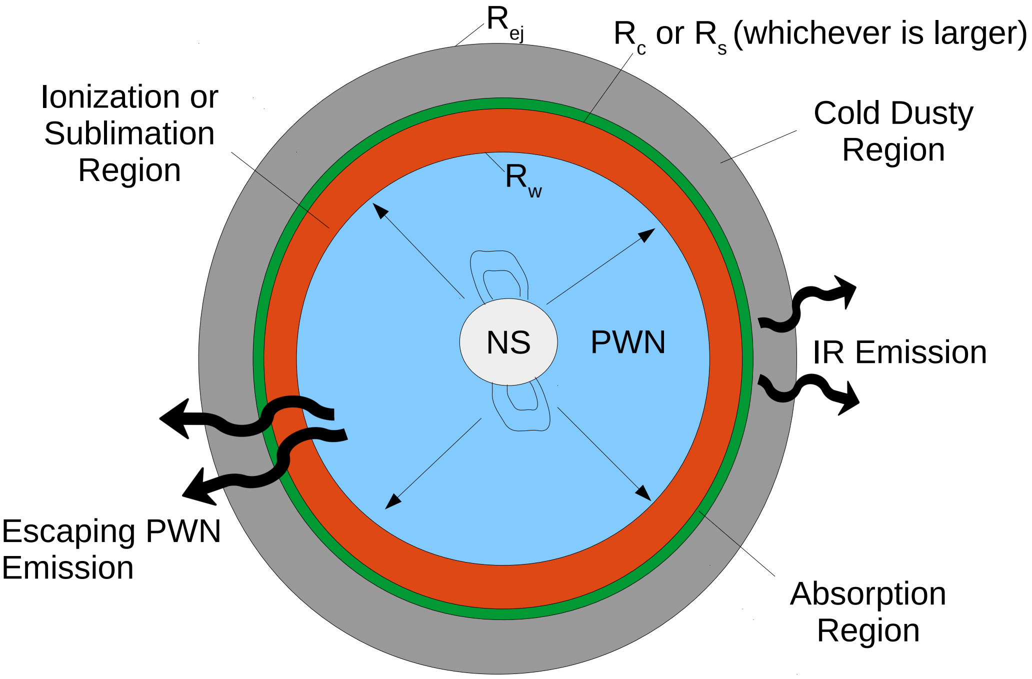

FIGURE 5.1: A schematic of the system we examine - not to scale. The nebula formed by the central pulsar presses on and injects energy into the supernova ejecta at $R_{\rm w}$. We consider the ejecta as having three layers: the ionization or sublimation region on the inside, where dust can not form due to non-thermal emission from the PWN; the absorption region, which has thickness $\ll R_{\rm ej}$ and is located at the edge of the sublimation/ionization region, where optical and UV photons are absorbed and infrared (IR) photons are re-emitted; and the cold, dusty region on the outside, where dust is optically thin to infrared emission and not heated by PWN radiation. All three regions do not always appear, depending on parameters and time evolution.

1991; Nozawa et al. 2010, 2003, 2011, 2008; Todini & Ferrara 2001). Within this framework, the condensation of dust can be described by stable seed nuclei formation and growth, where the rate of grain formation is derived by assuming a steady-state nucleation current (Nozawa & Kozasa 2013). This theory has allowed predictions of the size and mass of different condensing grain species, which can nicely explain the mass of dust in SN1987A (Kozasa et al. 1991) and the formation and evolution of dust in Cas A (Nozawa et al. 2010).

We also use a steady-state model for dust formation, specifically, the model first developed by Kozasa & Hasegawa (1987) which introduces the concept of a key molecule or key species - the one with the lowest collisonal frequency among the different gaseous reactants (the rate-limiting species, in a sense) - and then generalized by Nozawa & Kozasa (2013), whose formulation we use. In this formulation, the reaction kinetics are controlled by collisions between gaseous key species atoms/molecules and clusters of n key molecules, which we call n-mers.

Dust Formation Basics

As the ejecta gas cools, the condensation of dust proceeds via the formation of small clusters and further attachment of key molecules to those clusters. The concentration of key gas atoms c_1 (the concentration of n-mers is denoted $c(n,t) = c_n$) is

$$c_1 = \frac{M_{\mathrm{ej}} f_{\mathrm{KM}} (1 - f_{\mathrm{con}})}{V_{\mathrm{ej}} m_1} \tag{5.1}$$

where $V_{\mathrm{ej}} = (4/3)\pi(R_{\mathrm{ej}}^3 - R_{\mathrm{w}}^3)$ is the volume of the ejecta from R_{w} to R_{ej}, f_{KM} is the initial mass fraction of the key species within the ejecta, f_{con} is the condensation efficiency (the fraction of key gas atoms that are already part of dust grains), and m_1 is the mass of the key atom.

The time evolution of the concentration of n-mers is given by detailed balance

$$\frac{dc_n}{dt} = J_n(t) - J_{n+1}(t) \text{ for } 2 \leq n \leq n_*, \tag{5.2}$$

where $J_n(t)$ is the net current density from $(n-1)$-mer to n-mer. In this model, any cluster composed of more than n_* key molecules is treated as a macroscopic dust grain.

The growth rate of the grains, which we assume are spherical, is

$$\frac{da}{dt} = s\Omega_0 \left(\frac{k_B T_{\mathrm{gas}}}{2\pi m_1}\right)^{\frac{1}{2}} c_1 \left(1 - \frac{1}{S}\right), \tag{5.3}$$

where a is the radius of the grain, s is the sticking probability of the key atom onto grains, Ω_0 is the volume of condensate per each key atom, k_B is the Boltzmann constant, T_{gas} is the gas temperature, and S is the supersaturation ratio

$$\begin{aligned} \ln S =& \frac{1}{k_B T_{\mathrm{gas}}}(\mathring{g}_c - \Delta\mathring{g}_{\mathrm{gas}}) + \ln\left(\frac{p_1}{p_s}\right) + \ln \Xi & (5.4) \\ =& \frac{A}{T_{\mathrm{gas}}} - B + \ln\left(\frac{c_1 k_B T_{\mathrm{gas}}}{p_s}\right) + \ln \Xi, & (5.5) \end{aligned}$$

where A and B are thermodynamic constants that were given in Nozawa et al. (2003), p_s is the standard thermodynamic pressure 1 bar = 10^6 Ba = 10^6 erg cm^{-3}, $\mathring{g}_c$ and $\Delta\mathring{g}_{\text{gas}}$ are defined later, and

$$\Xi = \frac{\prod_{k=1}^{i}(p_k^{\mathcal{A}}/p_s)^{\nu_k}}{\prod_{k=1}^{j}(p_k^{\mathcal{B}}/p_s)^{\eta_k}}, \tag{5.6}$$

where ν_k and η_k are the stoichiometric coefficients and $p_k^{\mathcal{A}}$ and $p_k^{\mathcal{B}}$ ($k = 1$-i and 1-j respectively) are the partial pressures of the gaseous reactants and products, $\mathcal{A}_k$ and $\mathcal{B}_k$, respectively, in the general chemical reaction below.

$$\mathcal{Z}_{n-1} + (\mathcal{X} + \nu_1\mathcal{A}_1 + ... + \nu_i\mathcal{A}_i) \rightleftharpoons \mathcal{Z}_n + (\eta_1\mathcal{B}_1 + ... + \eta_j\mathcal{B}_j), \tag{5.7}$$

where $\mathcal{Z}_n$ is an n-mer cluster formed from the nucleation of n key molecules $\mathcal{X}$. From now, we denote quantities of the reactants and products with superscript A and B, similar to p_k^A and p_k^B in Equation 5.6.

Formation of a Dimer

Since collisions of key atoms/molecules control the kinetics of the formation reaction, the current density for the formation of a dimer, $J_2(t)$, can be expressed

$$J_2 = \alpha_1 c_1^2 - \beta_2 c_2 \left(\frac{\sum_{k=1}^{j}(c_k^B)^{\eta_k}}{\sum_{k=1}^{i}(c_k^A)^{\nu_k}}\right)^2, \tag{5.8}$$

with α and β being the forward and backward reaction coefficients. This form is based on detailed balance, where

$$\frac{\alpha_1}{\beta_2} = K = \mathring{c}_2 \left(\frac{\sum_{k=1}^{j}(\mathring{c}_k^B)^{\eta_k}}{\sum_{k=1}^{i}(\mathring{c}_k^A)^{\nu_k}}\right)^2, \tag{5.9}$$

in chemical equilibrium. This allows the current density to be expressed

$$J_2 = \alpha_1 c_1^2 \left(c_1 - c_2 \frac{c_1}{\mathring{c}_2 b^2}\right), \tag{5.10}$$

where

$$b = \frac{c_1}{\mathring{c}_1} \frac{\sum_{k=1}^{i}(c_k^A/\mathring{c}_k^A)^{\nu_k}}{\sum_{k=1}^{j}(c_k^B/\mathring{c}_k^B)^{\eta_k}} = \frac{p_1}{\mathring{p}_1} \frac{\sum_{k=1}^{i}(p_k^A/\mathring{p}_k^A)^{\nu_k}}{\sum_{k=1}^{j}(p_k^B/\mathring{p}_k^B)^{\eta_k}}, \tag{5.11}$$

where $\mathring{c}_k^A$ and $\mathring{c}_k^B$ ($\mathring{p}_k^A$ and $\mathring{p}_k^B$) are the concentrations (gas pressures) of the kth gaseous reactants and products, respectively, in a gas in thermodynamic equilibrium at temperature T. The factor $c_1/\mathring{c}_2 b^2$ can be rewritten as

$$\frac{p_s}{\mathring{p}_2}\left(\frac{\mathring{p}_1}{p_s}\right)^2 \left(\frac{\sum_{k=1}^{i}(\mathring{p}_k^A/p_s)^{\nu_k}}{\sum_{k=1}^{j}(\mathring{p}_k^B/p_s)^{\eta_k}}\right)^2 = \frac{c_1\Pi}{\mathring{c}_2 b^2}\left(\frac{p_1}{p_s}\Xi\right)^{2-\frac{1}{\omega}}, \tag{5.12}$$

where

$$\Pi = \left(\frac{\prod_{k=1}^{i}(c_k^A/c_1)^{\nu_k}}{\prod_{k=1}^{j}(c_k^B/c_1)^{\eta_k}}\right)^{\frac{1}{\omega}} \tag{5.13}$$

and

$$\omega = 1 + \sum_{k=1}^{i} \nu_k - \sum_{k=1}^{j} \eta_k. \tag{5.14}$$

We apply the law of mass action, which states that the rate of any chemical reaction is proportional to the product of the concentrations of the reactants, to find

$$\frac{p_s}{\mathring{p}_2}\left(\frac{\mathring{p}_1}{p_s}\right)^2 \left(\frac{\sum_{k=1}^{i}(\mathring{p}_k^A/p_s)^{\nu_k}}{\sum_{k=1}^{j}(\mathring{p}_k^B/p_s)^{\eta_k}}\right)^2 = \exp\left(\frac{1}{k_B T_{\text{gas}}}(\mathring{g}_2 - 2\Delta\mathring{g}_{\text{gas}})\right), \tag{5.15}$$

with

$$\Delta\mathring{g}_{\text{gas}} = \mathring{g}_1 + \sum_{k=1}^{i} \nu_k \mathring{g}_k^A - \sum_{k=1}^{j} \eta_k \mathring{g}_k^B, \tag{5.16}$$

where $\mathring{g}_k^A$ and $\mathring{g}_k^B$ are the chemical potentials of kth gaseous reactants and products at a pre-defined standard pressure p_s, respectively. Using this, Equation 5.12 can be rewritten

$$\frac{c_1\Pi}{\mathring{c}_2 b^2} = \exp\left(\frac{1}{k_B T_{\text{gas}}}(\mathring{g}_2 - 2\Delta\mathring{g}_{\text{gas}}) - \left(2 - \frac{1}{\omega}\right)\left[\ln\left(\frac{p_1}{p_s}\right) + \ln\Xi\right]\right) \tag{5.17}$$

$$= \exp(\gamma_2) \tag{5.18}$$

where

$$\gamma_2 = \frac{1}{k_B T_{\text{gas}}}\left[\mathring{g}_2 - \left(2 - \frac{1}{\omega}\right)\mathring{g}_c - \frac{1}{\omega}\Delta\mathring{g}_{\text{gas}}\right] - \left(2 - \frac{1}{\omega}\right)\ln S \tag{5.19}$$

where $\mathring{g}_c$ is the chemical potential of the bulk condensate at p_s. Finally, this allows us to rewrite Equation 5.10 as

$$J_2 = \alpha_1 c_1^2 \left(c_1 - c_2 \frac{1}{\Pi}\exp(\gamma_2)\right), \tag{5.20}$$

Steady State Approximation

For $3 \leq n \leq n_*$, the current density $J_n(t)$ is

$$J_n(t) = \alpha_{n-1} c_{n-1} c_1 - \beta_n c_n \frac{\sum_{k=1}^{j}(c_k^B)^{\eta_k}}{\sum_{k=1}^{i}(c_k^A)^{\nu_k}}, \tag{5.21}$$

$$= \alpha_{n-1} c_1 \left(c_{n-1} - c_n \frac{\mathring{c}_{n-1}}{\mathring{c}_n b}\right). \tag{5.22}$$

Rewriting in a similar way as Equations 5.17 and 5.20 gives

$$\frac{\mathring{c}_{n-1}}{\mathring{c}_n b} = \exp\left[\frac{1}{k_B T_{\text{gas}}}(\mathring{g}_n - \mathring{g}_{n-1} - \Delta\mathring{g}_{\text{gas}}) - \ln\left(\frac{p_1}{p_s}\right) + \ln\Xi\right] \tag{5.23}$$

and

$$J_n = \alpha_{n-1} c_1((c_{n-1} - c_n \exp(\gamma_n)). \tag{5.24}$$

Using the steady-state approximation, the current density J_n becomes independent of n and equal to the steady-state nucleation rate J_s. Using this equivalency, Equations 5.10 and 5.22 lead to the following relations, respectively:

$$\frac{J_s}{\alpha_1 c_1^2} = 1 - \frac{c_2}{\mathring{c}_2 b^2} \tag{5.25}$$

$$\frac{J_s}{\alpha_{n-1} c_1 \mathring{c}_{n-1}} = \frac{c_{n-1}}{\mathring{c}_{n-1}} - \frac{c_n}{\mathring{c}_n b} \text{ for } n \geq 3. \tag{5.26}$$

By summing up these two equations multiplied by $1/b^{n-1}$, J_s can be derived from

$$J_s \left(\frac{1}{\alpha_1 c_1^2} + \sum_{i=2}^{n} \frac{1}{\alpha_i c_1 \mathring{c}_i b^i} \right) = 1 - \frac{c_n}{\mathring{c}_n b^n}. \tag{5.27}$$

Using Equations 5.17 and 5.23, $1/\mathring{c}_n b^n$ can be rewritten

$$\frac{1}{\mathring{c}_n b^n} = \frac{1}{c_1 \Pi} \exp \left[\frac{1}{k_B T_{\text{gas}}} (\mathring{g}_n - n \Delta \mathring{g}_{\text{gas}}) - \left(n - \frac{1}{\omega} \right) \left(\ln \left(\frac{p_1}{p_s} \right) + \ln \Xi \right) \right] \equiv \frac{1}{c_1 \Pi} \exp(\gamma'_n) \tag{5.28}$$

with

$$\gamma'_n = \frac{1}{k_B T_{\text{gas}}} \left[(\mathring{g}_n - \left(n - \frac{1}{\omega} \right) \mathring{g}_c - \frac{1}{\omega} \Delta \mathring{g}_{\text{gas}} \right] - \left(n - \frac{1}{\omega} \right) \ln S. \tag{5.29}$$

Since the right-hand since of Equation 5.27 goes to zero as $n \to \infty$ if $S > 1$, J_s for large n becomes

$$\frac{1}{J_s} = \frac{1}{\alpha_1 c_1^2} + \sum_{i=2}^{\infty} \frac{1}{\alpha_i c_1 \mathring{c}_i b^i} = \frac{1}{\alpha_1 c_1^2} + \sum_{i=2}^{\infty} \frac{1}{\alpha_i c_1^2 \Pi} \exp(\gamma'_i). \tag{5.30}$$

The summation can be replaced by an integration if $1/\alpha c_1^2 \ll 1$, which gives

$$\frac{1}{J_s} \simeq \frac{1}{c_1^2 \Pi} \int_2^{\infty} \frac{1}{\alpha_i} \exp(\gamma'_i) di. \tag{5.31}$$

In principle, the nucleation rate J_s can be calculated once the chemical potentials of the n-mers are given, but unfortunately these potentials are only available for small ($n \lesssim 5$) clusters for a few interesting materials (e.g., Goumans & Bromley 2012). Therefore, we must use the capillary approximation, which allows us to estimate the chemical potential of an n-mer in terms of the chemical potential and surface energy of a monomer in the bulk condensate (Abraham 1974; Blander & Katz 1972). This approximation expresses $\mathring{g}_n$ as

$$\mathring{g}_n = 4\pi a_0^2 \sigma_{\text{ten}} (n-1)^{2/3} + (n-1)\mathring{g}_c + \mathring{g}_1 \tag{5.32}$$

for a single-element grain (e.g., Yasuda & Kozasa 2012), where σ_{ten} represents the surface tension of the bulk condensate and $a_0 = (3\Omega_0/4\pi)^{1/3}$ is the hypothetical grain radius per key atom/molecule, which are both given or calculated in Nozawa et al. (2003). In a multi-element grain, where the factor $1/\omega$ represents the contribution of the key species to the chemical potential change, a slightly more complicated expression arises:

$$\mathring{g}_n = 4\pi a_0^2 \sigma_{\text{ten}} \left(n - \frac{1}{\omega}\right)^{2/3} + \left(n - \frac{1}{\omega}\right) \mathring{g}_c + \frac{1}{\omega} \Delta \mathring{g}_{\text{gas}}. \tag{5.33}$$

Using this approximation, γ'_n from Equation 5.31 can be expressed as

$$\gamma'_n = \mu \left(n - \frac{1}{\omega}\right)^{2/3} - \left(n - \frac{1}{\omega}\right) \ln S, \tag{5.34}$$

where $\mu = 4\pi a_0^2 \sigma_{\text{ten}} / kT_{\text{gas}}$. This has a maximum at n_{crit}, which is given by

$$\left(n_{\text{crit}} - \frac{1}{\omega}\right)^{1/3} = \frac{2}{3} \frac{\mu}{\ln S}. \tag{5.35}$$

Thus, Equation 5.31 can be integrated using the saddle-point method, resulting in a nucleation rate

$$J_s = s_{n_{\text{crit}}} \Omega_0 \left(\frac{2\sigma_{\text{ten}}}{\pi m_{n_{\text{crit}},1}}\right)^{\frac{1}{2}} \frac{n_{\text{crit}}^{2/3}}{(n_{\text{crit}} - 1/\omega)^{2/3}} c_1^2 \Pi \exp\left(-\frac{4}{27} \frac{\mu^3}{(\ln S)^2}\right). \tag{5.36}$$

and, for $n_{\text{crit}} \gg 1$,

$$J_s = s\Omega_0 \left(\frac{2\sigma_{\text{ten}}}{\pi m_1}\right)^{\frac{1}{2}} c_1^2 \Pi \exp\left(-\frac{4}{27} \frac{\mu^3}{(\ln S)^2}\right). \tag{5.37}$$

This steady state nucleation closely approximates the non-steady state model in Nozawa & Kozasa (2013) if

$$\Lambda = \frac{\tau_{\text{sat}}}{\tau_{\text{coll}}} = \left(\frac{d \ln S}{dt}\right)^{-1} \left(s 4\pi a_0^2 \tilde{c}_1 \sqrt{\frac{k_B T_{\text{gas}}}{2\pi m_1}}\right) \tag{5.38}$$

$$\sim \frac{C}{\gamma - 1} \left(\frac{s}{1.0}\right) \left(\frac{\tilde{c}_1}{10^8 \text{ cm}^{-3}}\right) \left(\frac{T_{\text{gas}}}{2000 \text{ K}}\right)^{\frac{3}{2}} \left(\frac{t}{300 \text{ days}}\right) \tag{5.39}$$

is greater than ~ 30 at the time at dust formation onset. Here, C is a constant that depends on grain composition (1.94×10^3 for C grains and 1.15×10^3 for $MgSiO_3$ grains), and $\tilde{c}_1$ is the gas concentration if no dust is formed. This expression assumes a temperature evolution of

$$T_{\text{gas}} = T_{\text{gas},0} \left(\frac{t}{t_0}\right)^{-3(\gamma-1)}, \tag{5.40}$$

but ours is much more complicated due to the pulsar's energy injection. Therefore, we need to approximate γ in this expression. If $\Lambda < 30$, then the steady state model we use predicts earlier formation and smaller overall grain size (see Nozawa & Kozasa (2013) Figures 4 and 5 for examples); this usually happens with lower density ejecta.

Cluster Formation

Dividing by $\tilde{c}_1$ once J_s is calculated gives I_s, which is used to calculate

$$\frac{dK_i}{dt} = \begin{cases} I_s(t) n_*^{\frac{i}{3}} + \frac{i}{a_0}\left(\frac{da}{dt}\right) K_{i-1} & \text{for } i = 1-3 \\ I_s(t) & \text{for } i = 0. \end{cases}$$

Here K_0 is proportional to the number density of dust grains ($K_0 = n_{\text{dust}}/\tilde{c}_1$), and K_3 is the number fraction of key species atoms locked into dust grains. Therefore, the condensation efficiency $f_{\text{con}}(t)$ and average grain radius $a_{\text{ave}}(t)$ are

$$f_{\text{con}} = K_3, \tag{5.41}$$

$$a_{\text{ave}} = a_0 \left(\frac{K_3}{K_0}\right)^{\frac{1}{3}}. \tag{5.42}$$

5.2.2 Ejecta and Dust Composition

We studied dust formation for two ejecta compositions (mass fractions given in Table 5.1), which we refer to as the Ib and Ic compositions, since those are the supernovae they should correspond to. These compositions are based on nucleosynthesis calculations (Yoon et al. 2010) which account for nuclear fusion during the explosion and were used in radiative transfer simulations of various supernova types and various progenitor types (Dessart et al. 2011, 2012, 2015, 2017; Vlasis et al. 2016). The Ib composition is similar to the ejecta from a small (ZAMS mass of 15-25 $M_\odot$), roughly solar metallicity Wolf-Rayet progenitor with a binary companion - around 3-5 $M_\odot$ of ejecta is expected for this case. The Ib composition is also similar to that from an isolated low-metallicity Wolf-Rayet progenitor with a ZAMS mass of around 25 $M_\odot$ - the ejected mass in this case is expected to be $\sim$ 15 $M_\odot$. The Ic composition is most similar to the ejecta from a large isolated solar metallicity Wolf-Rayet star with ZAMS mass $\sim$ 60 $M_\odot$ - around 5-7 $M_\odot$ of ejecta is expected for this case.

The main differences between the two compositions are the lower overall numbers in the Ib composition and the lack of Si in the Ic composition. The Ib composition has lower numbers because most of the gas in the ejecta is either H or He, which does not form dust and can be thus neglected for our purposes. In real type-Ic SNe, the Si mass fraction is not zero - simulations give around a 10 times lower mass fraction for Si than that of Mg in the Ic composition ejecta; this is small enough where much greater quantity of MgO dust would be expected to form than $MgSiO_3$ or Mg_2SiO_4, so we completely neglect Si in the Ic composition. The large fraction of He in the Ib composition means that SNe with this composition would be classified as either Type Ib or IIb, depending on if any H gas was also present, while an observed SNe with the Ic composition would be classified as Type Ic.

We study two different types of dust formation and growth in both compositions. For Ib, we investigate C and $MgSiO_3$ dust, the latter of which is expected to be preferentially formed over Mg_2SiO_4 by around a factor of 3 (Nozawa et al. 2010). For the Ic composition, because there is too little Si to form large quantities of $MgSiO_3$ or Mg_2SiO_4, we investigate C and MgO dust. The growth reactions for the pre-grain n-mers are

$$\mathrm{C}_{n-1} + \mathrm{C} \rightleftharpoons \mathrm{C}_n, \tag{5.43}$$

$$\mathrm{MgSiO}_{3,n-1} + \mathrm{Mg} + \mathrm{SiO} + \mathrm{O} \rightleftharpoons \mathrm{MgSiO}_{3,n}, \tag{5.44}$$

$$\mathrm{MgO}_{n-1} + \mathrm{Mg} + \mathrm{O} \rightleftharpoons \mathrm{MgO}_n. \tag{5.45}$$

Composition	f_C	f_O	f_{Mg}	f_{Si}
Ib	0.1	0.3	0.03	0.03
Ic	0.3	0.6	0.05	0

TABLE 5.1: Initial mass fractions of the different gaseous elements in the ejecta for both compositions.

Grain Type	$C_{(s)}$	$MgSiO_{3(s)}$	$MgO_{(s)}$
Key Species	$C_{(g)}$	$Mg_{(g)}$	$Mg_{(g)}$
$A/10^4$ (K)	8.64726	25.0129	11.9237
B	19.0422	72.0015	33.1593
a_0 (Å)	1.281	2.319	1.646
$\sigma_{\rm ten}$ (erg cm^{-2})	1400	400	1100

TABLE 5.2: The physical properties of the dust grains we investigate. The subscript (s) and (g) represent solids and gases respectively. Mg and Si have the same concentration in the Ib composition, so either one can be used as the key species. Values are originally given in Nozawa et al. (2003).

The physical properties for all dust grains we study are listed in Table 5.2. In the Ib composition, we assume that the Mg and Si gas concentrations remain equal, and we also assume that the number of oxygen atoms in the ejecta remains fixed, since the ejecta is oxygen dominated and even the formation of multiple types of dust grains will not significantly effect the oxygen concentration.

We ignore the formation of carbon monoxide (CO), even though one expects that carbon dust will not be formed in large quantities within oxygen-rich ejecta (both our Ib and Ic compositions are oxygen-dominated) due to the preferential formation of CO molecules. Since we use a one-zone model, including CO formation would greatly suppress carbon dust formation. In more complicated ejecta models, there is both a carbon-rich shell where carbon dust formation dominates and an oxygen-rich shell where silicate- and Mg-molecule-based dust formation dominates (e.g., Nozawa et al. 2010, 2008). For most supernovae, carbon dust formation would only be expected in the carbon-rich shell, which surrounds the oxygen-dominant shell and contains $\sim 50\%$ of the carbon atoms, although in SLSNe, turbulence mixes the gas and homogenizes the ejecta, meaning that carbon dust should not form in significant quantities. Because of this, the formation of each species is treated independently, and we do not account for radiation shielding due to the earlier formation of one dust species.

We take the sticking probability of a colliding key species gas atom s and the minimum number n for an n-mer to be considered a macroscopic dust grain n_* to be 0.8 and 100 respectively; as discussed in Appendix B of Nozawa & Kozasa (2013), the results will not change qualitatively as long as n_* is large enough.

5.2.3 Dust Sublimation

Once the gas temperature is low enough for dust formation to proceed, optical-UV emission from the PWN can still sublimate the dust. The equation for grains of dust in radiative equilibrium between absorption of non-thermal optical/UV PWN emission and thermal re-emission is

$$\frac{L_{\rm opt/UV}}{4\pi\sigma r^2} Q_{\rm opt/UV}\pi a^2 = \langle Q\rangle_T 4\pi a^2 \sigma T_{\rm dust}^4, \tag{5.46}$$

where $L_{\rm opt/UV}$ is the total non-thermal luminosity between 2-6 eV (0.2-0.6 μm), σ is the Stefan-Boltzmann constant, r is the radius of the position of the dust grain, $Q_{\rm opt/UV}$ is the optical/UV absorption efficiency factor, which we assume to be ≈ 1 since the grain radii should be $\gtrsim 10^{-5}$ cm, and finally

$$\langle Q\rangle_T = \frac{B_\nu(T_{\rm dust}) Q_{{\rm abs},\nu} d\nu}{B_\nu(T_{\rm dust}) d\nu} \tag{5.47}$$

$$\approx \frac{D a_{-5}(T_{\rm dust}/2300\ {\rm K})}{1 + D a_{-5}(T_{\rm dust}/2300\ {\rm K})}, \tag{5.48}$$

where $a_{-5} = a/10^{-5}$ and D is a constant which depends on grain composition ($\sim$ 0.3 for C dust grains, $\sim$ 0.03 for silicates and MgO) (Draine & Lee 1984). These emissivities are consistent with previous studies which examine sublimation of already formed dust grains larger than 10^{-5} cm (Waxman & Draine 2000), but is not accurate while dust is growing, or if the dust does not grow to $\sim 10^{-5}$ cm. Draine & Lee (1984) calculated emissivities for both graphite (carbon dust) and silicates by using their dielectric function and found they varied strongly and non-linearly with both grain size and absorption frequency. We discuss the caveats of our approximation further in Section 5.4.

Sublimation will occur if the dust equilibrium temperature is greater than the critical temperature for supersaturation T_c (also known as the sublimation temperature), which is calculated by setting $S = 1$ in Equation 5.5. From Equation 5.46, the dust sublimation critical radius is

$$R_c = \left(\frac{L_{\rm opt/UV}}{16\pi\sigma T_c^4} \frac{Q_{\rm opt/UV}}{\langle Q\rangle_{T_c}}\right)^{\frac{1}{2}}. \tag{5.49}$$

If $R_c < R_{\rm ej}$ (the edge of the ejecta), then no dust can be formed at all due to sublimation from PWN emission. In our calculation, any dust that would have formed is converted back to gas.

5.2.4 Dust Emission

Once dust starts to form without immediately being sublimated, it re-emits thermally. The optical depth in the optical/UV band

$$\tau_{\rm opt/UV} = \int_{R_c}^{R_{\rm ej}} n_{\rm dust}(r)\pi a^2 dr \tag{5.50}$$

is $\gg 1$ in dusty ejecta, so only a thin shell (we call this the absorption region) is heated by PWN emission. This shell is located just outside R_c and will emit at $T \approx T_c$ if R_c is $> R_{\rm w}$, or be located at the inner edge of the ejecta $R_{\rm w}$ and emit at $T_{\rm dust}(R_{\rm w})$, with a blackbody luminosity

$$L_\nu = 4\pi R^2 \langle Q\rangle_T \pi \frac{2h\nu^3}{c^2} \frac{1}{e^{\frac{h\nu}{k_B T}} - 1}. \tag{5.51}$$

Although the remission is can modelled with a greybody (frequency-dependent) emissivity with $L_\nu \propto \nu^{2+\beta}$ for $h\nu < kT$ (e.g., Beckwith & Sargent 1991; Draine et al. 2007;

Schnee et al. 2010), we simply use the frequency-averaged emissivity from Equation 5.48. We are interested only in the peak of the thermal emission spectrum, so the spectral index in the Rayleigh-Jeans limit is not important for our study.

The dust re-emission has a longer wavelength than both the incident PWN emission and the typical dust grain size, so the grains in the cold, dusty region will appear optically thin to the re-radiation, and the blackbody emission at T_c or $T_{\text{dust}}(R_{\text{w}})$ will be directly observable.

5.2.5 Gas Ionization

Ionization of ejecta gas can cause an increase in temperature due to collisons between free electrons, as well as cause increased Coulomb repulsion between charged ions, which may be able to prevent dust formation. However, ion-molecule reactions can proceed more quickly because of ions inducing dipole moments in neutral atoms, which enhances their electrostatic attraction (Stahler & Palla 2005). Although the ionization states in which these effects dominate and the extent to which they compete are not well known, it is important for us to identify the region of the ejecta in which they will be present.

We calculate the maximum radius where gas can be ionized by non-thermal PWN radiation using the formula for the Strömgen radius R_s, although we need to slightly modify it due to the thin-shell structure of the ejecta. The formula becomes

$$R_s = \left(\frac{3}{4\pi} \frac{\Phi}{c_1^2 \beta_2} + R_{\text{w}}^3 \right)^{\frac{1}{3}}, \tag{5.52}$$

where β_2 is the electron temperature and chemical compsition dependent total recombination rate and Φ is the ionizing photons flux from the PWN. Φ can be calculated from the Equation 2.24 broken power-law spectrum to be

$$\Phi = \frac{F_\nu^b}{E_{\text{syn}}^b} \times \begin{cases} \frac{1}{\alpha_1 - 1}[(\frac{E_I}{E_{\text{syn}}^b})^{-(\alpha_1 - 1)} - 1] + \frac{1}{\alpha_2 - 1} & (E_I < E_{\text{syn}}^b), \\ \frac{1}{\alpha_2 - 1} \left(\frac{E_I}{E_{\text{syn}}^b} \right)^{-(\alpha_2 - 1)} & (E_{\text{syn}}^b < E_I) \end{cases} \tag{5.53}$$

where E_I is the gas atom ionization energy, which is dependent on the atom being ionized, but lies between 5-15 eV for all atoms of interest to our study.

We use $\tilde{c}_1$ for gas density, since ionization is not physically relevant to our study after dust begins to form, but we study multiple different species of dust and we want to treat their ionization and formation independently. We do not couple the ionization calculation to our dust formation and sublimation calculation, since it is not well known what the effect of partial ejecta ionization will be on dust formation - to do so would require computationally expensive radiative transfer simulations.

The results produced from this simple formulation are mostly consistent with results by Margalit et al. (2018), who calculate the ionization state of 10 $M_\odot$ of hydrogen- or oxygen-rich ejecta with a $B = 10^{14}$ G and $P = 1$ ms rotating pulsar. They show that the density-averaged ionization fraction increases slowly for hydrogen-rich ejecta and stays almost constant for oxygen-rich ejecta. However, the ejecta profile they use consists of a homogeneous core inside R_{w} and a high-velocity tail outside, instead of a

ID	Composition	$M_{\rm ej}$ $M_\odot$	ϵ_e
Ib5-1	Ib	5	1
Ib5-05	Ib	5	0.5
Ib15-1	Ib	15	1
Ic5-1	Ic	5	1
Ic15-1	Ic	15	1

TABLE 5.3: The five sets parameter sets we study. ϵ_e is a multiplicative factor for the PWNe luminosity.

thin shell at the edge of the PWN like ours, which could change the ionization fraction of the ejecta.

5.3 Results

We study a wide parameter space for the initial magnetic field B and initial pulsar spin period P for the five sets of ejecta parameters shown in Table 5.3. The total PWN luminosity is multiplied by a factor ϵ_e, which could be considered analogous to changing the dust absorption bandwidth or power law spectrum, since only the total optical/UV band luminosity is relevant for dust sublimation and temperature. These parameter sets will give us qualitative information on the effect of changing the ejecta mass, PWN spectrum, and composition while also being case studies for typical binary solar-metallicity Wolf-Rayet progenitors (Ib5-1), isolated low-metallicity Wolf-Rayet progenitors (Ib15-1), large isolated solar-metallicity Wolf-Rayet progenitors (Ic5-1), and magnetar-powered SLSNe-I (Ic15-1). It is interesting to note that Ib15-1 and Ic5-1 also have the same total amount of carbon, so comparing graphite formation in these two gives insight into the effect of significantly changing the supernova dynamics.

5.3.1 Effects of a Pulsar

In Figure 5.2, we examine the time evolution of I_s, $\ln(S)$, $f_{\rm con}$ and $a_{\rm ave}$ for C and MgSIO$_3$ dust with the Ib5-1 parameters both with no pulsar (top) and with a $B = 10^{13}$ G, $P = 2$ ms pulsar (bottom). The pulsar delays the start of formation (which we call the formation timescale) and decreases the timescale from when of dust formation commences until $f_{\rm con} \approx 1$ (which we call the condensation timescale). Due to the effect of the pulsar, the formation timescale increases from ~ 180 to ~ 590 days for C dust and ~ 215 to ~ 800 days for MgSiO$_3$ dust, while the condensation timescale decreases from ~ 5 days to less than 1 day for both species of dust. This is because of gas cooling being slowed due to PWN energy injection and also because of sublimation, which can increase $\ln(S) \gg 1$ when dust formation starts, leading to the nucleation reaction being heavily favoured.

The overall time evolution of these properties is, however, qualitatively similar between the two cases. There is a sharp increase in I_s at the formation timescale cooresponding to the sudden nucleation of dust throughout the absorption and cold, dusty regions, which causes $f_{\rm con}$ to rise to ~ 1 within the condensation timescale. After most of the gas condenses, the supersaturation ratio drops due to the decrease in gas concentration, which causes I_s to fall to ~ 0. As time goes on, the already nucleated dust grows in size via the accretion of free key atoms, which causes the gas concentration to drop even further, although more slowly than during the rapid nucleation phase.

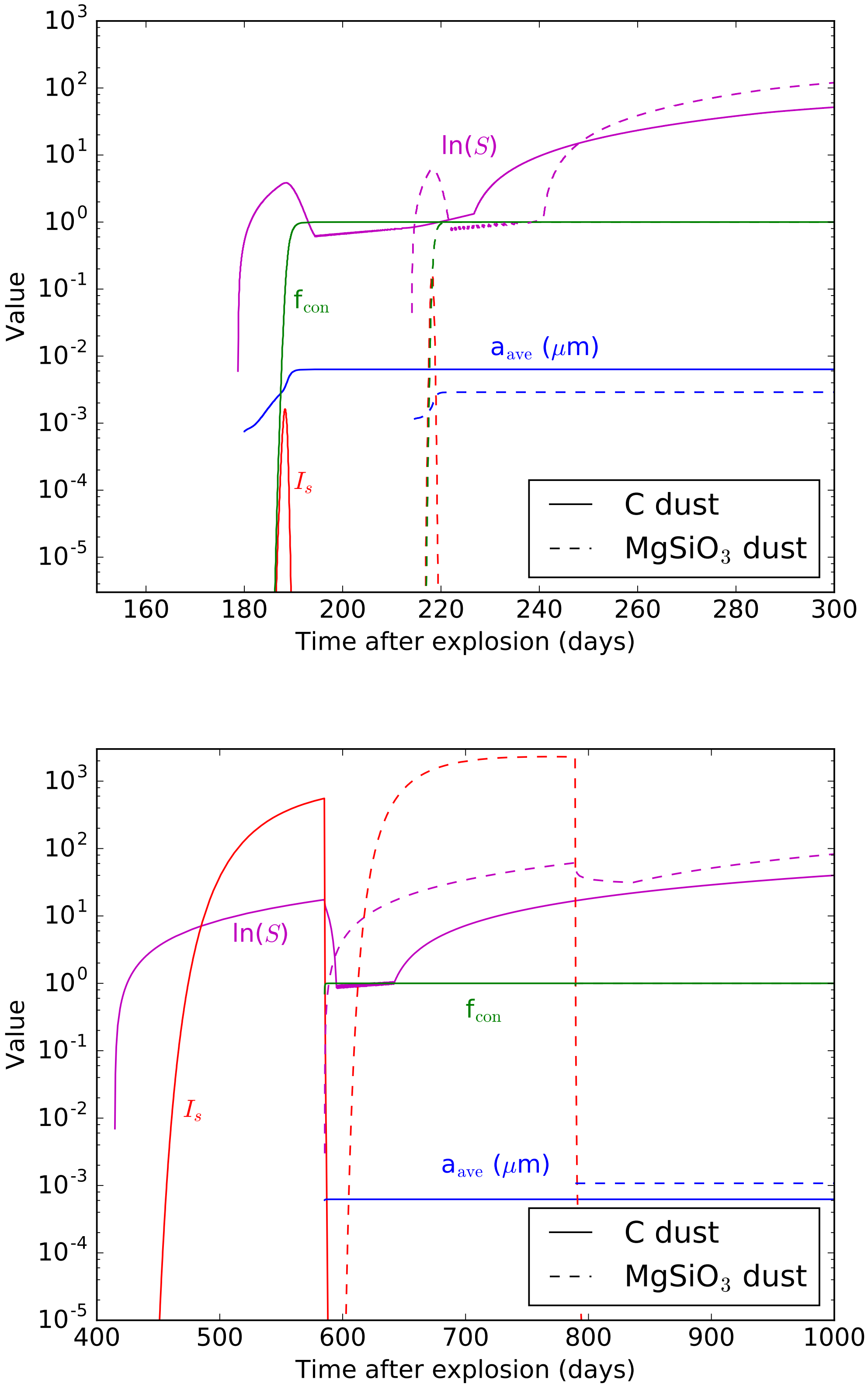

FIGURE 5.2: The time evolution of I_s, $\ln(S)$, f_{con} and a_{ave} for both C and MgSiO$_3$ grains in the Ib5-1 ejecta composition without a pulsar (top) and with a P = 2 ms, $B = 10^{13}$ G pulsar (bottom). The pulsar increases the formation timescale but decreases the condensation timescale, and the evolution is qualitatively similar for both cases.

There is still nucleation of new dust grains after f_{con} reaches ~ 1, but the growth rate is very small and gas concentration evolution is predominantly due to the growth of previously nucleated grains. However, the growth rate of these grains is low after the condensation timescale, as a_{ave} stays almost constant after this timescale. $\ln(S)$ falls, and then rises again on later timescales; this second rise cooresponds to when the grain growth rate falls to ≈ 0. The results are also similar qualitatively to the high density parameter set from Nozawa & Kozasa (2013), where the steady-state model agrees with the more rigorous non-steady-state formulation.

5.3.2 Formation Timescale and Ionization

Figure 5.3 shows the time evolution of the inner R_{w} and outer R_{ej} ejecta radius, the sublimation (critical) radius R_{c} for each species of dust, and ionization (Strömgen) radius R_{s}, for the Ib5-1 ejecta parameters with initial magnetic field $B = 5 \times 10^{12}$ G and initial pulsar spin periods P = 1, 3, and 10 ms. The critical radius begins to be shown when $\ln(S)$ first becomes positive, and thus $T_{\mathrm{gas}} < T_c$, even if $T_{\mathrm{dust}} > T_c$ and dust is sublimated as soon as it begins to form.

The PWN emission becomes more luminous as spin becomes more rapid, and there are multiple effects because of this. The formation timescale for both dust species increases because of the PWN emission heating the ejecta. All the radii increase as the PWN becomes more luminous; R_{w} and R_{ej} increase because of ejecta acceleration from the magnetized wind , and R_{c} and R_{s} both increase due to increased non-thermal luminosity in the optical/UV band and at higher energies, respectively; the increase in R_{w} can also enhance adiabatic cooling, which can, in principle, decrease the formation timescale. The ejecta is also not as compressed, and thus thicker, at high P due to a low amount of ejecta acceleration.

However, R_{s} and R_{c} increase more rapidly than R_{w} as spin period decreases, which gives different qualitative dust formation behaviour. With a P = 10 ms pulsar, the formation dust of begins throughout almost the entire ejecta for both dust species when the supersaturation ratio $S = 1$, since at that point R_{s} is only slightly larger than R_{w}, so only the very inner region will be ionized, while $R_{\mathrm{c,C}} < R_{\mathrm{w}}$ and $R_{\mathrm{c,MgSiO3}} \approx R_{\mathrm{w}}$, meaning no C dust will be sublimated while the very inner region will have $\mathrm{MgSiO_3}$ dust grains sublimated for a few days before they start to form in that region too. For P = 3 ms, the critical radius for both dust species is outside the R_{ej} when $S = 1$, so dust is immediately sublimated once it grows to a size where it can absorb optical/UV radiation - because small grains have lower infrared emissivity than larger ones, the newly formed grains can not efficiently radiate heat and are thus easier to sublimate. At later times, R_{c} drops below R_{ej} and dust formation commences near the outer edge of the ejecta. The dust-forming region will grow larger as the critical radius recedes until $R_{\mathrm{c}} = R_{\mathrm{s}}$, at which point the dust in the outer region will remain unsublimated, although maybe partially ionized, while the gas in the inner region will remain mostly ionized. For P = 1 ms, the entire ejecta is at least partially ionized before $S = 1$, so it is unlikely that a much dust will be able to form at all.

Figure 5.4 shows the dependence of formation timescale of C and $\mathrm{MgSiO_3}$ (Ib composition) or MgO (Ic composition) grains on pulsar spin period and magnetic field for all parameters shown in Table 5.3. The dashed black line represents when sublimation delays dust formation ($T_{\mathrm{dust}} > T_c$ when $S = 1$), and the solid black line represent where the ejecta is completely ionized before dust formation begins, which may completely stop dust formation. Values for the minimum and maximum formation timescales (not accounting for ionization), as well as the formation timescale when there is no pulsar, are given in Table 5.4.

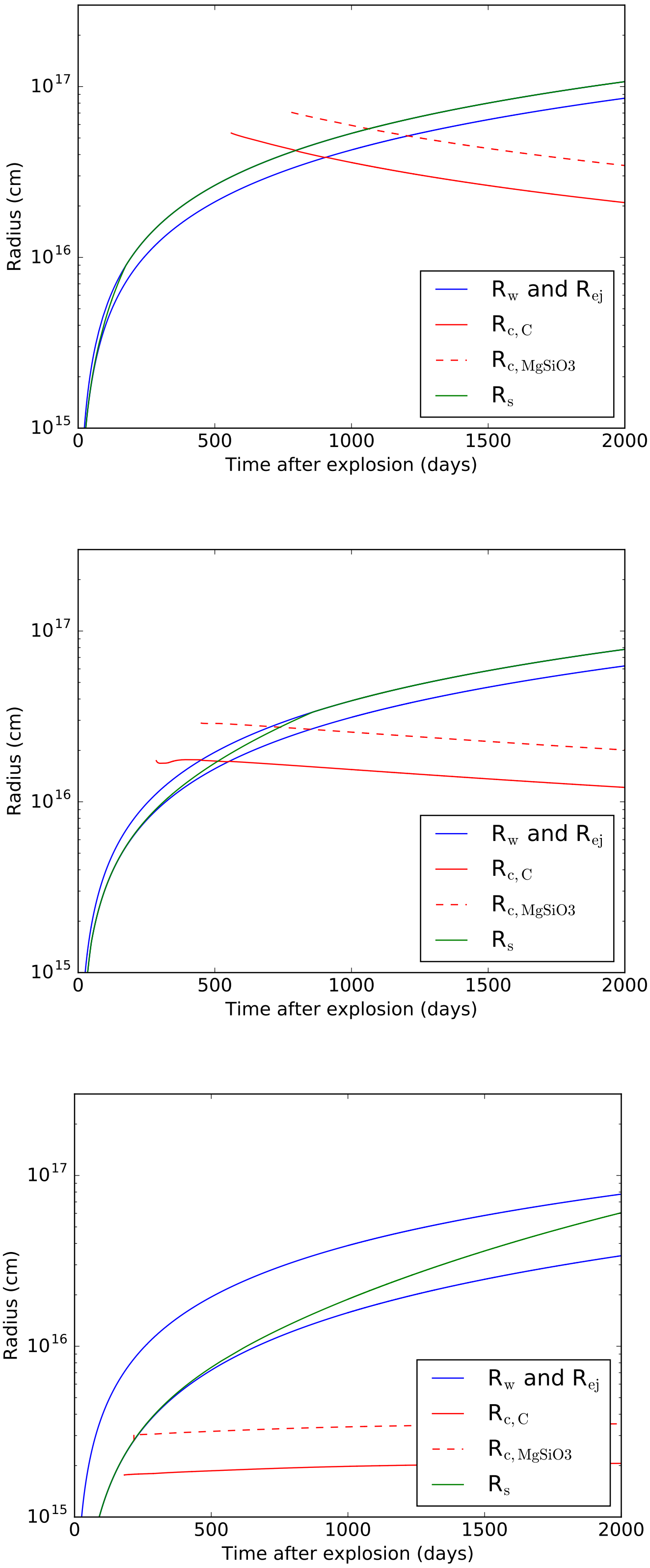

FIGURE 5.3: The time evolution of the inner R_w and outer R_{ej} ejecta radius (blue), sublimation (critical) radius R_c for both C (solid red) and $MgSiO_3$ (dashed red) grains, and ionization (Strömgen) radius R_s (green), for the Ib5-1 parameter set with $P = 1$ (top), 3 (middle), and 10 ms (bottom) and $B = 5 \times 10^{12}$ G. The critical radius is shown from the time where $\ln(S)$ first becomes positive.

Each parameter set has a few qualitative features in common. Dust forms fastest is at high B and low P; this is because the there is a lot of initial energy injected which causes the ejecta to expand rapidly and makes adiabatic cooling more effective, and the short spin-down timescale of the pulsar means the PWN luminosity decreases very quickly, so further ejecta heating is minimal. As B decreases, the slower ejecta expansion and slower decline of PWN luminosity makes dust formation take longer, and sublimation inside the dashed region increase the timescale even more, like in Figure 5.3 (middle). With some parameters, there is a P-B region where the ejecta will be fully ionized prior to the start of dust formation, like in Figure 5.3 (top). For these parameters, the ionization breakout will likely prevent dust formation entirely. However, decreasing B even further will cause the formation timescale to decrease as the effect of PWN emission becomes weaker and eventually negligible. As P increases, the PWN emission will also get weaker, and can cause the ejecta velocity and thus adiabatic cooling to decrease, increasing the formation timescale, or cause heating from the PWN to decrease, decreasing the formation timescale. The formation timescale is determined by the balance between these two effects.

The different dust species are formed on different timescales due to both their thermodynamic properties and the mass fractions of their constituent atoms within the ejecta. The formation timescale for $MgSiO_3$ grains is around 120% that of C dust for pulsar-free or accelerated formation and 140-150% for delayed formation. The parameter space for sublimation delay and for ionization is larger for $MgSiO_3$ compared to C. The factor difference between MgO formation timescale and C formation timescale has more variance than with $MgSiO_3$. For pulsar-free formation, the MgO timescale is similar to $MgSiO_3$ - around 120% of the C dust timescale. For pulsar-accelerated formation, the MgO timescale is about 150% the C timescale with high ejecta mass and around 250% with low ejecta mass - this is due to sublimation delaying formation more by with low ejecta mass. Delayed formation has the highest discrepancy though, with MgO dust taking around 5 times longer to form than C. The parameter space for both ionization and sublimation delay is much larger for MgO than C, with most of the parameter space in our study delayed because of sublimation.

The parameter sets have many quantitative differences because of the effects of PWN luminosity and ejecta mass on energy injection and ejecta expansion. Decreasing the PWN luminosity (comparing Ib5-1 to Ib5-05) decreases the thermal energy injection, ejecta acceleration, and non-thermal sublimation and ionization. This decreases the maximum timescale for formation and increases the minimum timescale, bringing everything closer to the scenario without a pulsar, which is the limit as $\epsilon_e \to 0$. However, though the PWN emission was decreased by 50%, the formation timescales only changed by 20-30% and the parameter space for both sublimation delay and ionization do not decrease very much. Increasing the ejecta mass (comparing Ib5-1 to Ib15-1, and Ic5-1 to Ic15-1) slows expansion, which slows adiabatic cooling and increases energy flux from the nebula, increasing the ejecta temperature. As a result, formation timescales are increased for all species and scenarios, varying from around a 30% increase for delayed formation to 100% for accelerated formation, except for MgO dust, which has its formation timescale increased by only around 20% for accelerated formation.

5.3.3 Dust Size Parameter Dependence

Figure 5.5 shows the dependence of final average dust size for C and $MgSiO_3$ (Ib composition) or MgO (Ic composition) grains on pulsar spin period and magnetic

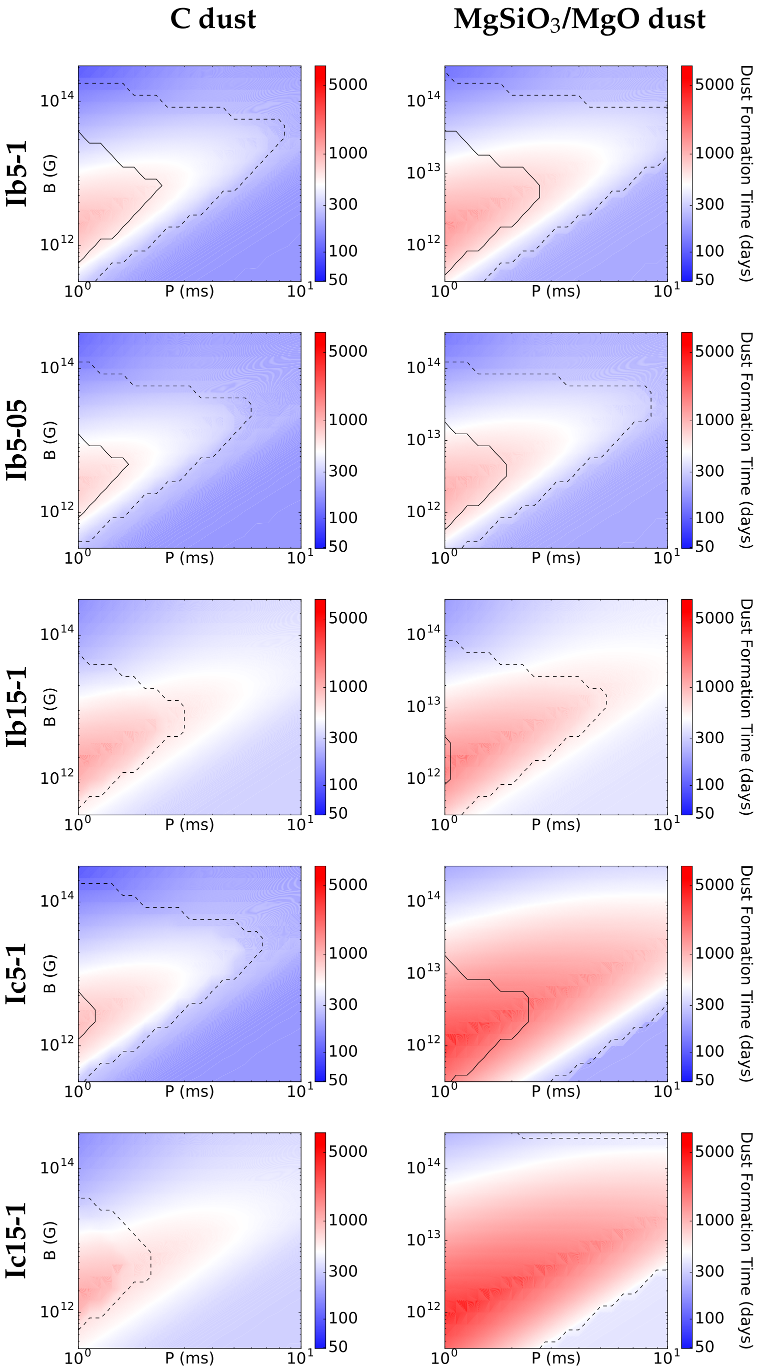

FIGURE 5.4: The dependence of formation timescale of C and $MgSiO_3$ (Ib composition) or MgO (Ic composition) grains on pulsar spin period and magnetic field for all parameters shown in Table 5.3. The dashed black line indicates when sublimation delays dust formation, and the solid black line indicates where the ejecta is ionized before dust formation commences, which could stop dust formation altogether (E.g. Figure 5.3 top). Numerical values for the minimum and maximum formation timescales and the formation time without a PWN are shown in Table 5.4.

	C dust			$MgSiO_3$ dust			MgO dust		
ID	$t_{\max}$	$t_{\min}$	$t_{\text{no pulsar}}$	$t_{\max}$	$t_{\min}$	$t_{\text{no pulsar}}$	$t_{\max}$	$t_{\min}$	$t_{\text{no pulsar}}$
Ib5-1	1118	58	180	1649	73	215			
Ib5-05	883	72	180	1263	88	215			
Ib15-1	1498	120	316	2180	141	376			
Ic5-1	1072	58	177				5030	143	216
Ic15-1	1420	118	311				6657	175	378

TABLE 5.4: The minimum and maximum formation timescales, as well as the formation timescale without a pulsar (all in days), for all parameter sets given in Table 5.3. The dependence of formation timescale on P and B is shown in Figure 5.4.

	C dust		$MgSiO_3$ dust		MgO dust	
ID	$a_{\max}$	$a_{\min}$	$a_{\max}$	$a_{\min}$	$a_{\max}$	$a_{\min}$
Ib5-1	8.4	0.6	3.6	1.1		
Ib5-05	8.7	0.6	3.7	1.1		
Ib15-1	30	0.6	10.0	1.1		
Ic5-1	21	0.6			2.3	0.8
Ic15-1	85	0.7			8.1	0.8

TABLE 5.5: Values for the minimum and maximum average final dust size in nm (10^{-7} cm) for all parameter sets given in Table 5.3. Figure 5.5 shows the size dependence on P and B.

field for all parameters given in Table 5.3, and give numerical values for the minimum and maximum average size in each scenario for each species in Table 5.5. Dust size depends heavily on gas concentration as dust starts to form. Thus, in parameter regions where dust formation is expedited by ejecta acceleration or delayed by sublimation, the average size of dust is significantly smaller. Dust size is largest when the PWN has weak or negligible effect on the ejecta, which is why the small B and large P region produces the largest dust; the spin-down timescale of these pulsars is $> 10^4$ years. Increasing ejecta mass (comparing Ib5-1 to Ib15-1, and Ic5-1 to Ic15-1) or gas concentration (comparing C dust in Ib5-1 to Ic5-1, and Ib15-1 to Ic15-1) also increases dust size.

Numerical simulations (Silvia et al. 2010, 2012) suggest that dust grains smaller than 100 nm will be almost completely destroyed by the supernova reverse shock, and larger ones will have their size reduced via be sputtering (Nozawa et al. 2010). Using this criterion, most dust in our study will be destroyed by the reverse shock in every parameter set, since the average dust radius is always smaller than 100 nm. However, since the dust size distribution found by Nozawa & Kozasa (2013) spans around an order of magnitude, the largest C dust in a Type Ic SN without a pulsar or in a supernova with a large ejecta mass may be able to survive the reverse shock, but the presence of a luminous PWN increases the fraction of dust grains destroyed. Regardless of the properties of the PWN, magnesium silicates should will never survive the reverse shock unless the ejecta mass is higher than we model, and neither will graphite in the Ib5-1 and Ib5-05 compositions. Therefore, it is unlikely that pulsar-driven supernovae will greatly contribute to the overall dust concentration in the ISM.

The average final dust size is almost constant over the entire parameter space

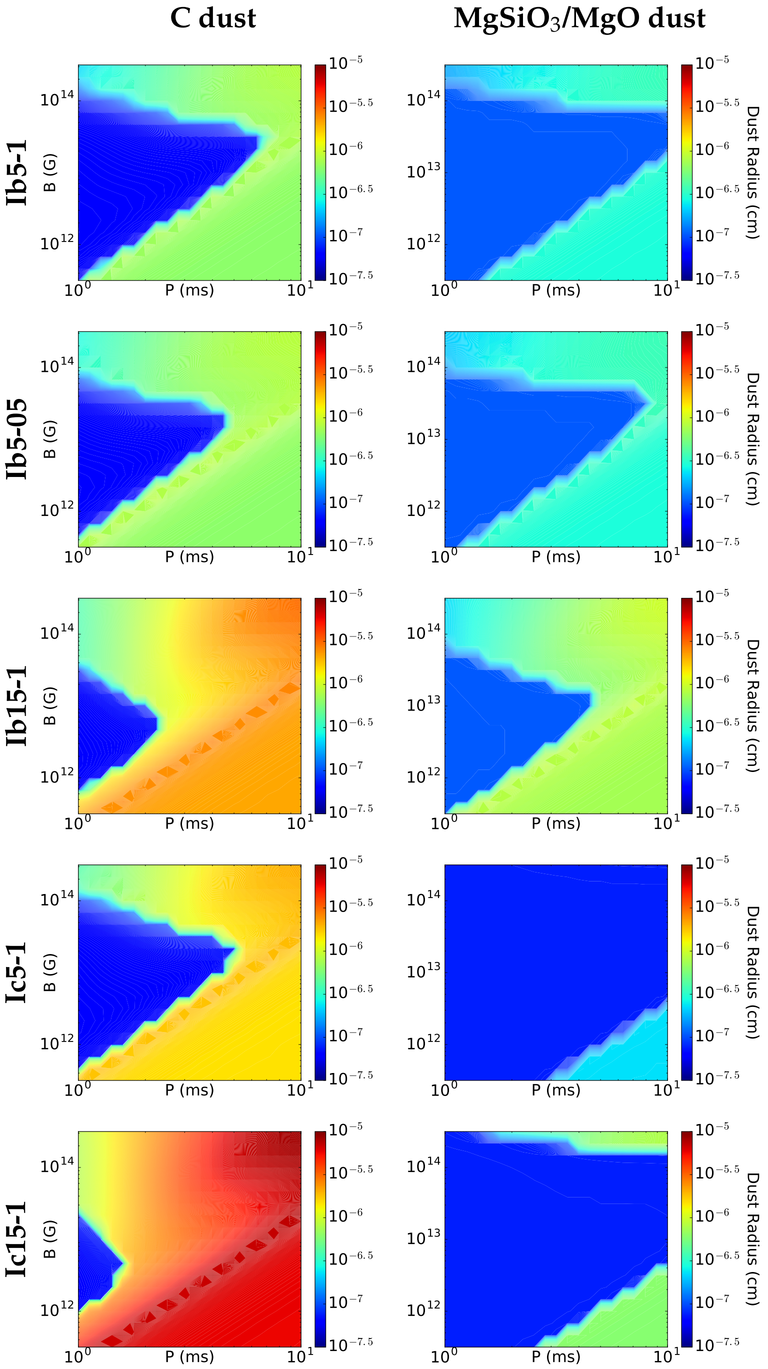

FIGURE 5.5: Dependence of average final size of dust for C and $MgSiO_3$ (Ib composition) or MgO (Ic composition) dust on P and B.

where formation is delayed due to sublimation (compare to the dashed lines in Figure 5.4); this is likely because of our implemention of the steady-state approximation. This size is minimum dust size that can be considered a grain, and this indicates that dust can not grow beyond the point where it can efficiently absorb optical/UV continuum energy, so the final size of this dust will actually depend on detailed microphysics which are beyond the scope of this work.

5.3.4 Dust Emission

Our main interest is the possible detection of dust re-emission in young SLSN-Ic remnants, so we study the re-radiation using the Ic composition for two fiducial parameter sets: the P1 set, with $M_{\rm ej}$ = 15 $M_\odot$, P = 1 ms, and $B = 10^{14}$ G; and the P2 set, with $M_{\rm ej}$ = 5 $M_\odot$, P = 2 ms, and $B = 2 \times 10^{13}$ G. These are chosen to be similar to the typical $P_{\rm min}$ and $M_{\rm max}$ cases from previous chapters.

Figure 5.6 compares the spectra of dust and the PWN for both parameter sets. Since the PWN spectrum is uncertain, we show the region for q_1 (the lower energy spectral index, where $q_1 = 2$ would be flat in νF_ν) between 1.5 and 1.8 - while the possible minimum and maximum spectral index is not well constrained, these values seem like reasonable limits given our knowledge of both Galactic PWNe and particle acceleration mechanisms within PWNe. The dust spectrum we show was calculated with q_1 = 1.8, but will only be lower by a factor of $\lesssim 2$ within the first decade post-explosion if calculated with q_1 = 1.5. The detectability of the dust emission is heavily dependent on the PWN spectral index, ranging from easily detectable after 2 years using both parameter sets if q_1 = 1.5 to completely undetectable if q_1 = 1.8.

If q_1 = 1.8, the dust spectrum approaches the PWN spectrum as time passes due to less absorbed energy decreasing the dust spectrum peak frequency, but dust emission is subdominant for $>$ 20 years in both the P1 and P2 case. For q_1 = 1.5, the dust luminosities within the first few years are above the PWN emission at around $\nu L_\nu \sim 10^{37} - 10^{39}$ erg/s at $10^4 - 10^5$ GHz depending on parameters, which would be detectable within $\sim$ 100-1000 Mpc using 2500 s observations from JWST. Dust also does not emit significantly below 10^3 GHz, so PWN observations with ALMA (100-250 GHz) are not affected by dust.

5.3.5 Applications to Previous SNe

The most well studied supernova so far is SN1987A, partially because of dust formed within its ejecta. The collapse and explosion of Sk-69 202, a $\sim$ 18-20 $M_\odot$ blue supergiant, produced $\sim$ 15 $M_\odot$ of ejecta (Gilmozzi et al. 1987). The ejecta contains a hydrogen envelope of $\sim$ 10 $M_\odot$ and a $\sim$ 5 $M_\odot$ core of heavier elements (Nomoto et al. 2006; Woosley et al. 1988). Mg and Si were produced in almost equal amounts of around 0.1 $M_\odot$, while around 0.15-0.25 $M_\odot$ of C was produced (Matsuura et al. 2011; Thielemann et al. 1990); this gives mass fractions of 0.007 and 0.01-0.02 respectively, which are both a factor of $\sim$ 5 smaller than in our Ib composition. There is evidence that almost all of the carbon gas ended up in dust grains, and about 0.4 $M_\odot$ of $MgSiO_3$ was produced (Dwek & Arendt 2015; Matsuura et al. 2011; Sarangi & Cherchneff 2015). Silicate lines were not detected in early spectra (Wooden et al. 1993), which could have been because those emission lines were absorbed by carbon dust (Dwek & Arendt 2015). There has been no confirmation of a compact remnant yet, although a pulsar with initial spin $P >$ 100 ms and $B \sim 10^{11-12}$ G is still not ruled out (Manchester 2007) and recent studies do support the existence of a neutron star (Cigan et al. 2019; Page et al. 2020). Observation suggest dust grains formed

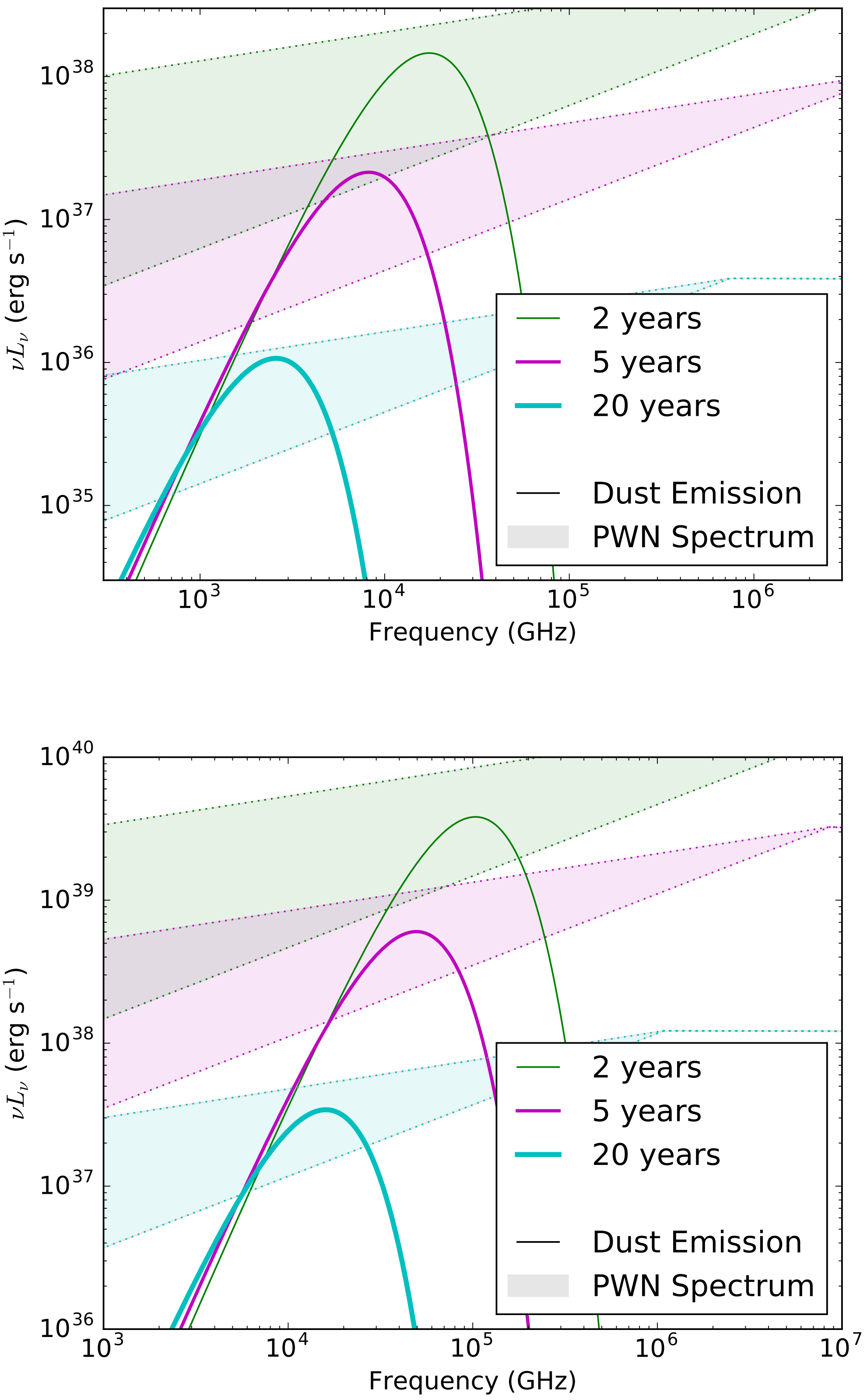

FIGURE 5.6: The PWN (dotted lines and shaded region) non-thermal spectrum and dust (solid) blackbody re-emission spectrum at 2 (green), 5 (magenta), and 20 (cyan) years after the explosion. The P1 case is shown above and the P2 case below. The dotted lines show PWN spectra with $q_1 = 1.5$ and 1.8, with the shaded region in between - the limits on q_1 are not well constrained, but these values are reasonable given our knowledge of both Galactic PWNe and particle acceleration mechanisms within PWNe.

within the ejecta between 415 to 615 days (Wooden et al. 1993) or even at > 1000 days (Sarangi & Cherchneff 2015; Wesson et al. 2015), and this timescale is longer than expected with no pulsar; the C dust concentration is a factor of ~ 5 lower than in our Ib composition, but the Ic composition has a C concentration a factor of 3 higher but only condenses 5 days faster - the ejecta temperature is similar, so dust formation should happen on a similar timescale. Although a difference of a few dozens of days could be due to uncertainties or caveats in our model (see below), a longer timescale could imply that a pulsar delayed the formation of dust, but such a pulsar would have produced detectable non-thermal radiation (McCray & Fransson 2016), and would have increased the dust temperature to over 1000 K, which is hotter than predicted by any model (Matsuura et al. 2011; Wooden et al. 1993).

A few other Galactic supernova remnants have been observed to have both a compact remnant and dust, such as SNR G54.1+0.3 (Lu et al. 2001; Temim et al. 2010), Kes 75 (Gavriil et al. 2008; Temim et al. 2012a), Cas A (Elshamouty et al. 2013; Nozawa et al. 2010), and the Crab Nebula (Temim et al. 2012b). These supernovae produced between 0.01-1 $M_{\odot}$ of dust, and none of them have yet experienced a reverse shock. However, the pulsars in these systems likely have initial spin periods > 10 ms, so PWN emission likely did not have much of an effect on their dust formation histories. However, since the dust found in the Crab Nebula was reported to be smaller than expected (Kozasa et al. 2009; Temim et al. 2012b), which be evidence of the initial pulsar spin period being < 10 ms and suppressing grain growth, although it may only be because dust mass estimates were derived using an inaccurate distance to the Crab (Bailer-Jones et al. 2018; Fraser & Boubert 2019).

5.4 Discussion

5.4.1 Dependence on γ_b

The value of γ_b, which determines the energy of the synchrotron break (see Equation 2.25), has not been well constrained for newborn PWNe (Tanaka & Takahara 2013; Torres et al. 2014; Venter & de Jager 2007). The value we use throughout this chapter, 3 $\times$ 10^5, puts the spectral break between optical and X-ray, depending on timescale, but a $\gamma_b \sim 10^2$ would lower the spectral break energy into the submillimetre or infrared band. We re-calculated the time evolution of I_s, $\ln(S)$, $f_{\rm con}$ and $a_{\rm ave}$ for the same ejecta and pulsar as Figure 5.2 (bottom) with $\gamma_b = 3 \times 10^2$, and show the result in Figure 5.7. The formation timescale is much closer to the case without a pulsar than the $\gamma_b = 3 \times 10^5$ case, with C dust forming at about 210 days and $MgSiO_3$ forming at about 270 days.

The formation of $MgSiO_3$ is qualitatively similar here to the case with $\gamma_b = 3 \times 10^5$. Both $\ln(S)$ and I_s rise to a very high value before dropping at the formation time. The drop-off in I_s and rise in $f_{\rm con}$ happen on a shorter timescale than without a pulsar, which signifies a short condensation timescale. Our interpretation of this is that while C dust is not delayed by sublimation, $MgSiO_3$ dust is, and the more diffuse ejecta combined with the large cluster formation rate show that as soon as the dust temperature drops below the critical temperature, all the Mg and Si gas condenses on a short timescale without the resulting dust having a chance to grow by further accretion of gas particles. This also explains why the final average dust size for $MgSiO_3$ is smaller than the non-pulsar case and similar to the $\gamma_b = 3 \times 10^5$ case, while the average size of C grains is similar to the non-pulsar case.

We also calculated the dependence of both the formation timescale and final average dust size on magnetic field and pulsar spin period for the Ib5-1 parameters,

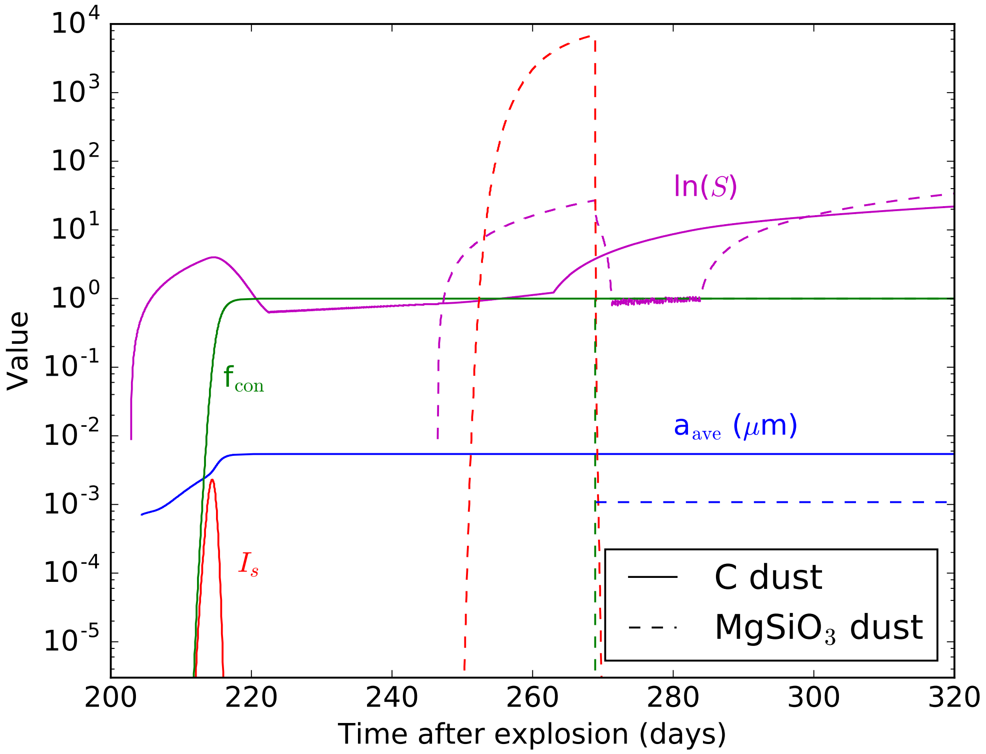

FIGURE 5.7: The same as Figure 5.2 (bottom), but with γ_b = 3 × 10^2 instead of 3 × 10^5.

shown in Figures 5.8 and 5.9. We show that the PWN does not have as large an effect on dust formation, as the maximum formation timescale for C and $MgSiO_3$ is reduced from 1118 to 462 days and 1649 to 626 days respectively, and the minimum formation timescale for C and $MgSiO_3$ is increased from 58 to 92 days and 73 to 109 days respectively. Ionization breakouts no longer occur, and the parameter space for sublimation delay decreases in size. We also find that a millisecond magnetar barely affects dust size, but a millisecond pulsar with $B = 10^{12} - 10^{13}$ G reduces the size down to the model minimum, just like when γ_b = 3 × 10^5.

When γ_b = 3 × 10^2, it would be difficult to detect a signal from the pulsar engine. The PWN effect on the formation timescale is much weaker than when γ_b = 3 × 10^2, and occurs over a smaller parameter space - a noticeable reduction of dust size is confined to a small parameter region as well. Since the spectral break is in the sub-millimetre or infrared, detecting a re-emitted signal is unlikely because the emission from the dust, which will have a lower temperature due to a low flux in optical/UV, will be dominated by the non-thermal radiation close to the spectral peak.

5.4.2 Relic Electrons and Uncertainty in the PWN Spectrum

Although the PWN spectrum we use has only one break, a more realistic one many have many depending on the timescale, ejecta, and pulsar parameters. The indices may also have a wider variation, leading to a more complicated shape that changes over time, and previously cooled electrons (known as relic electrons) can also emit synchrotron emission and change the power law index below the break energy.

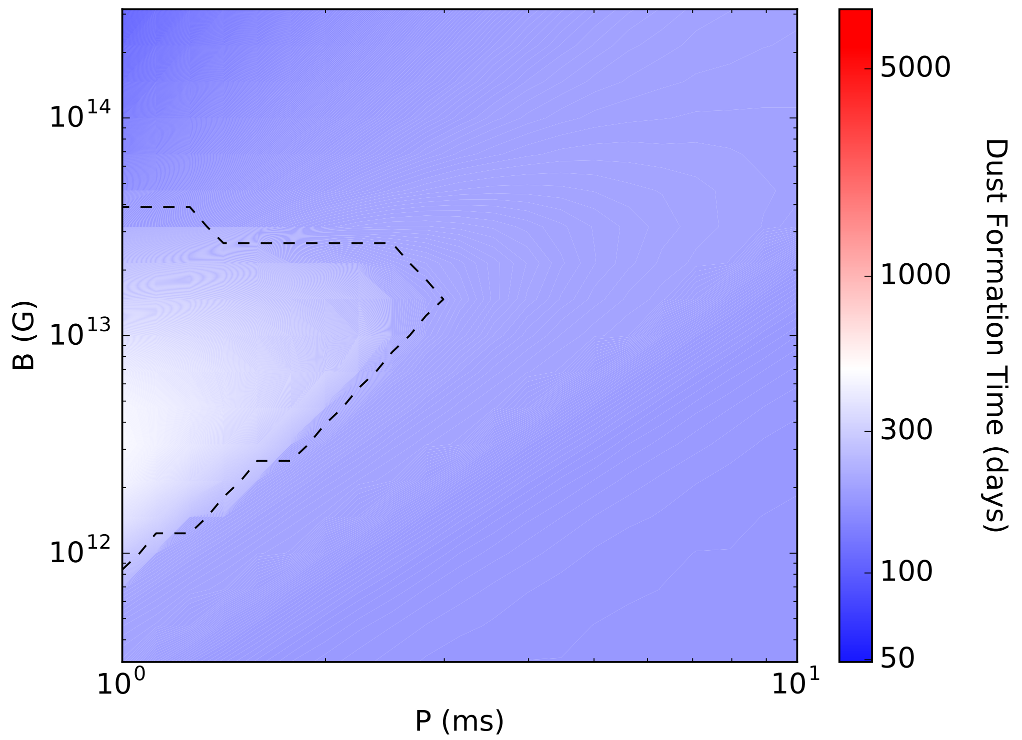

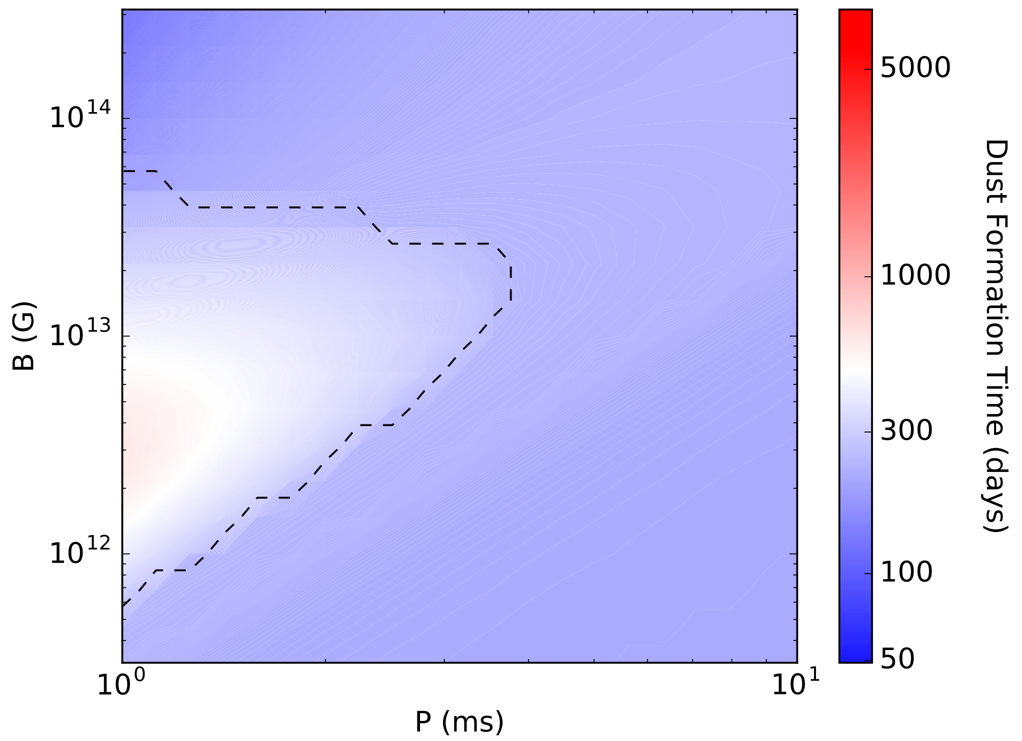

FIGURE 5.8: The formation timescale distribution for C (top) and $MgSiO_3$ (bottom) dust for the Ib5-1 parameter set with $\gamma_b = 3 \times 10^2$.

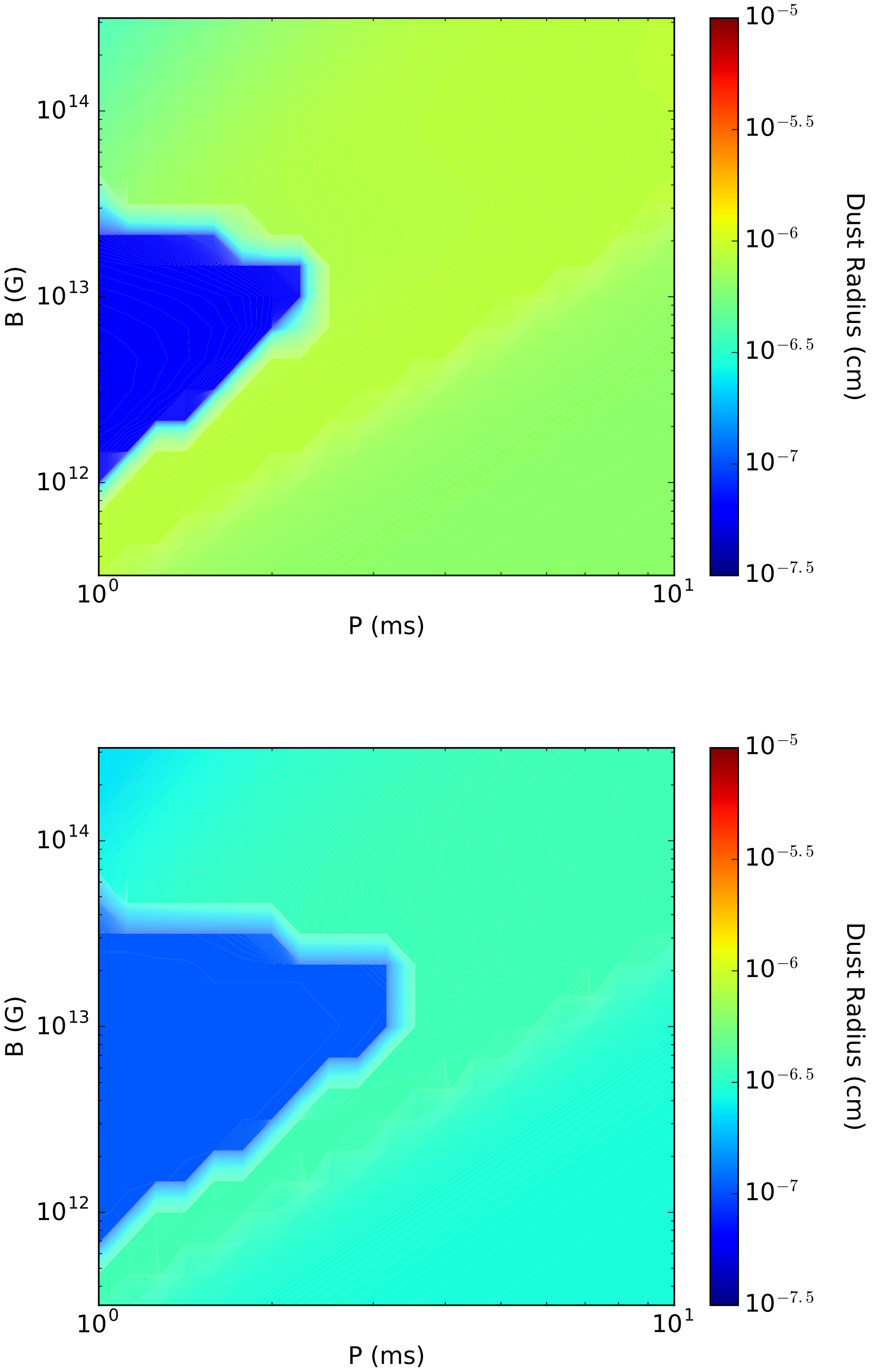

FIGURE 5.9: The average dust size distribution for C (top) and $MgSiO_3$ (bottom) dust for the Ib5-1 parameter set with $\gamma_b = 3 \times 10^2$.

Given that the PWN spectrum used throughout this chapter has $q_1 = 1.8$, our spectrum is more flat than a more realistic spectrum. Due to the uncertainty of q_1, q_2, and γ_b in very young PWN, it is very difficult to tell exactly what this spectrum should look like, most notably where its spectral breaks are. If the spectrum is less flat and the spectral peak is around the optical/UV band, then the effects of sublimation and the re-emitted radiation would be similar, but the effects of ionization would be weakened and the PWN spectrum in the infrared region would be less likely to dominate the dust re-emission, making it possible to detect the re-emission earlier and to a larger distance (see Figure 5.6). If the spectral peak is around the submillimetre/infrared band, then the effects of ionization and sublimation would be decreased and the dust re-emission would be less powerful, making it unlikely to detect the re-emission or infer the effects of the pulsar at all.

5.4.3 Hot Bubble Breakout

It is suggested in Suzuki & Maeda (2017) that once the energy injected by the pulsar becomes comparable to the initial explosion energy, the ejecta will undergo what is called a hot bubble breakout, where the hot material from the PWN forms Rayleigh-Taylor instabilities with the ejecta, causing a convective motion that heats the ejecta and changes the density profile. If this breakout occurs after dust has formed, it could cause the dust to be destroyed via sputtering. We determine the turbulent breakout timescale $t_{\rm br}$ using

$$E_{\rm inj} = E_{\rm SN}, \tag{5.54}$$

$$t_{\rm br} = t_{\rm SD}\left(\frac{E_{\rm SN}}{E_{\rm SD}}\right), \tag{5.55}$$

$$= 0.8 \text{ days } B_{13}^{-2} P_{-3}^{4}, \tag{5.56}$$

and show the timescale in Figure 5.10. Note that if $E_{\rm SD} < E_{\rm SN}$, the turbulent breakout does not occur at all. We find that the turbulent breakout timescale becomes comparable to the formation timescale below $B = 10^{12}$ G for $P = 1$ ms, and has roughly the same slope as the isochronal formation contours in Figure 5.4, meaning that the turbulent breakout occurs before dust formation when the sublimation delay is longest. However, since Suzuki & Maeda (2017) assumes that the ejecta does not radiate, and only expands adiabatically, it may be that the large energy radiated by the ejecta before bubble breakout prevents it from happening at all.

5.4.4 Emissivities

In Section 5.2.3, we mention that our treatment of emissivities is the biggest uncertainty in our model, because the emissivities vary greatly with dust size (e.g., Draine & Lee 1984, Figures 4 and 5). For graphite, the emissivity when $a > 10^{-5}$ cm is ~ 1 at 1-12 eV, and decreases in this band as dust size decreases; however, the emissivity increases at higher energies as dust size decreases. For silicates, the emissivity starts to decrease at $a > 10^{-4}$ cm in optical/UV, but is otherwise fairly similar to that of graphite. Both species of grains absorb almost all incident radiation across around an order of magnitude, and since we use a fairly flat PWN spectrum in νF_ν, the energy absorbed by dust will be comparable for all dust sizes unless $a < 10$ nm, because the emissivity decreases over all bands by a factor of 2-3. Our bandwidth is only around half an order of magnitude, so we likely slightly underestimate the temperature of the

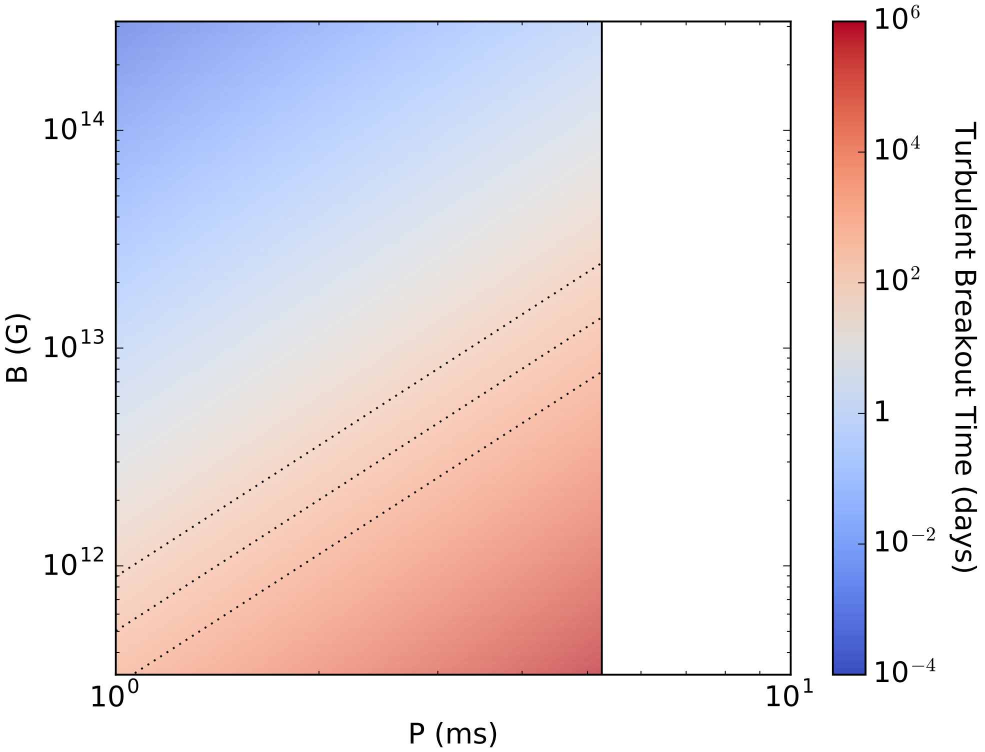

FIGURE 5.10: The timescale for turbulent breakout in the ejecta. The dotted lines indicate a timescale of 10^2, $10^{2.5}$, and 10^3 days from top to bottom.

dust. The energy absorbed by dust should be around twice as high as our model for $a > 10$ nm, which gives a temperature difference of around a factor of 1.2; this causes emission to be more detectable, but also makes sublimation more effective. The formation timescale and average dust size differences will be similar to the differences between the Ib5-05 and Ib5-1 parameters. However, since final grain sizes in many cases were < 10 nm, this bandwidth decreases the energy absorbed by small grains by a factor of $\gtrsim$ 2-3, which leads to less effective sublimation of newly formed grains.

5.4.5 Other Caveats

Our model and formulation also have a few other caveats and uncertainties. We used a steady-state approximation, where the current density J_n from $(n-1)$-mer to n-mer is independent of n and is given by the steady-state nucleation rate J_s from Equation 5.37. Nozawa & Kozasa (2013) show that this approximation is only valid when the saturation timescale $\tau_{\mathrm{sat}} \gtrsim 30\tau_{\mathrm{coll}}$, where τ_{coll} is the collisional timescale, which occurs at higher densities; otherwise, the steady-state model has a shorter condensation timescale and smaller dust than the non-steady-state model.

We assume the ejecta is spherically symmetric, which ignores both non-sphericity of the nebular emission and fluid instabilities as well as the formation of clumps within the ejecta (Dwek & Arendt 2015; Kozasa et al. 1991). Our calculation is a one-zone model with no spacial variance in the density and perfect mixing, which makes the dust formation rate independent of radius; in a real supernova, formation rate should be strongly affected by the density profile and the shell structure of the ejecta. We want to study emission at $\lesssim$ decade timescales, so we assume a reverse shock has not yet propagated through the ejecta; if the supernova is surrounded by dense CSM, the ejecta-CSM interaction can send an early reverse shock through the ejecta and destroy the newly formed dust (McCray & Fransson 2016; Suzuki & Maeda 2018).

We also only consider spherical grains, instead of ellipsoidal (Dwek & Arendt 2015; Matsuura et al. 2015) or more irregularly shaped ones (Min et al. 2003). We calculate where the ejecta is ionized, but we ignore the how increased electron temperature and charge separation effect the rest of the ejecta. We ignore sputtering, which decreases dust size (Draine & Salpeter 1979a,b; Jones et al. 1996), although this effect should not be highly pronounced due to the slow thermal velocity of the dust (Oort & van de Hulst 1946). We neglect the dust size distribution altogether and calculate only the average grain size; even though the emission region is optically thick, not having a size distribution effects dust emission because there should be a range of emissivities, and thus a range of emission temperatures from the absorption region.

5.5 Summary

We use a model of dust formation, sublimation, emission, and gas ionization to calculate the dust abundances, formation timescales, sizes, and re-emission for several supernovae with energetic PWNe. We found that dust formation is qualitatively similar with or without a pulsar, can be accelerated by millisecond magnetars due to the increased effectiveness of adiabatic cooling, or can be delayed by pulsars with subcritical fields or higher spin periods due to thermalized energy injection increasing the ejecta temperature and non-thermal emission causing sublimation, or possibly stopped altogether via an ionization breakout. Graphite forms before silicates, and

$MgSiO_3$ forms on much shorter timescales than MgO when the PWN delays formation, even though they form on similar timescales when the PWN accelerates formation or does not significantly effect ejecta evolution. Increasing ejecta mass and lowering the key species concentration both delay formation as well. The typical formation timescales range from a few months for accelerated formation, to around a year with no significant PWN effect, to around 3-4 years for delayed formation of C or $MgSiO_3$ dust, to over 15 years for delayed formation of MgO dust.

The average size of the grains decreases from the $\gtrsim 10$ nm dust formed when pulsar energy injection is not significant to $\lesssim$ a few nanometers when it is, meaning that grains in pulsar-driven SNe will probably not survive the reverse shock. However, the re-radiation from the PWN-heated dust might be detectable out to $\sim$ 100-1000 Mpc with JWST for typical SLSNe if the low-energy spectral index of the PWN is slightly lower than calculated from previous simulations. These results are not expected to be influenced by a turbulent shock due to the timescale for this shock being smaller than the formation timescale in most parameter regions of interest.

Nothing particularly insightful comes from applying this model to Galactic supernova remnants with both a PWN and dust, as the newborn pulsar in each cases was expected to spin too slowly for the PWN to have significantly affected dust formation, although the small dust size found in the Crab Nebula compared to model predictions could be evidence of an effect from its pulsar. Applying this scenario to SN1987A can explain the slow formation of dust in some models, but the predicted PWN has a non-thermal luminosity greater than previous upper limits.

We find that uncertainties in the early PWN synchrotron spectrum strongly effect the strength of the PWN effect on dust evolution. If the frequency of the spectral break is decreased, the effects of the PWN on dust are almost negligible outside of a small P-B parameter space, where the timescale effects are weakened but the affect on dust size is still strong. By using a more realistic spectrum and accounting for several spectral breaks, we find that the emission may be detectable earlier and further out, or it may be even harder to detect, depending on what the values of the spectral breaks are.

This model has a few assumptions and caveats. The strongest assumption in our model is to fix the optical/UV absorption emissivity to 1 and assume an infrared emission emissivity which is likely not valid over the entire range of dust sizes we examine, although since our PWN spectrum is very flat we do not expect the temperature of the dust to change by more than a factor of around 1.2 in most cases. Our model has spherical symmetry, which ignores inhomogeneity and clumping in the ejecta, is one-zone, which ignores the radial density profile of the ejecta, and does not completely account for effects such as sputtering and ionization. Despite this, these calculations can give some insight into the dust re-emission that can be expected and detectable from pulsar-driven supernovae, the timescales when observations may be feasible, and the fate of the dust as the supernova remnant evolves.

Chapter 6

Conclusions and Future Prospects

Given the results presented in Chapters 3 and 4, the verdict on the pulsar-driven model for SLSNe is somewhat inconclusive. There is one SLSN, PTF10hgi, that looks consistent with the pulsar-driven model, but our observations should have detected more sources if our model is numerically accurate and none of our assumptions were incorrect. It is incredibly difficult to constrain the pulsar-driven model entirely given the number of free parameters, and the difficulty of properly modelling the pulsar wind nebula emission numerically, and the time needed to produce each of the individual models. The results of Chapter 5 will likely not be vital to diagnose central engines until the presence and nature of the engine is firmly established, especially due to Spitzer no longer active the difficulty of getting observational time with the soon-to-be-launched JWST - these results, however, will be critical to constraining the energy output of the central engine in the optical/UV band once its nature is established, since most other processes either probe lower- or higher-energy emission. Due to the difficulty of modeling of the uncertainties in the models, the community will not give up on the pulsar-driven model just because of these non-detections, as this is by far the most studied model for SLSNe and the optical emission from most SLSNe can be fit with the pulsar-driven model (Nicholl et al. 2017b).

Our results may not have produced anything definitive, but they do provide valuable building blocks that can be expanded upon in future studies, and provide multiple paths forward for the pulsar-driven model given the current state of theory and observations. The limits of the radio model need to be more firmly estabilshed, as most models we have used so far have all been using a spectrum calibrated from the Crab Nebula, but this nebula is still almost 1000 years old, while our detected PWNe would be under ten years old and have much higher rotation rate and magnetic field, and therefore may have very different physical processes. The model likely needed to be simplified to be less computationally expensive, and then we could run parameter studies to find out what regions of parameter space are truely excluded - interesting parameter sets could then be cross-checked by running the full model again. For a basic synchrotron nebula, even an analytical toy model could give us some physical insight into where spectral breaks could be located and what fluxes to expect in different bands.

Better understanding of the optical light curve models and their output parameters will also be needed, since the results from using `MOSFiT` and the modified version of our model from Chapter 2 were still different. Ideally, we could use the physics from our model, which is likely more physically accurate, with the Bayesian parameter estimation of `MOSFiT` to provide full posteriors. More automated light curve modelling and parameter estimation will be required when future large scale surveys start taking data, since machine-learning methods of classifying SN based only on light curves are under development (Gomez et al. 2020). Once this is established, this optical code could be used in conjuction with a simplified radio code to do simultaneous optical-radio fitting for objects with multiwavelength detections, like PTF10hgi.

Recent observations, particularly in the optical regime, have made interesting discoveries. Observations of SN2012au, a close, energetic Type-Ib supernova similar to a hypernova (Kamble et al. 2013; Milisavljevic et al. 2013; Takaki et al. 2013), at 6.2 years post-explosion were presented by Milisavljevic et al. (2018). They found forbidden transition emission lines of sulfur and oxygen with expansion velocities of ≈ 2300 km/s, but no lines which would be evidence of ejecta-CSM interaction; they conculded that this is evidence of a photoionizing central PWN. Only few studies have presented nebular spectroscopy of SLSNe: Nicholl et al. (2019) overviews 41 spectra from 12 events, but mostly within one year of the explosion, and Nicholl et al. (2018) presents photometry and spectroscopy of one supernova, SN2015bn, at ~ 1000 days post-explosion, but found the spectrum changed little from observations at $\sim$ one year (Nicholl et al. 2016b). This may indicate that if the late spectrum of a pulsar-driven supernova is dominated by forbidden oxygen lines, the spectral evolution may happen on a timescale determined by the spin-down time of the pulsar. Due to the difficulty of doing radiative transfer simulations in the nebular phase, only two studies have published models on late-time SLSN spectra: one assuming a pair-instability supernova (Jerkstrand et al. 2016) and one assuming a central engine (Jerkstrand et al. 2017) - and these both focused on timescales of $\sim$ one year. No work has been done to study the effect of engine parameter variation on the spectra, and no characterization has been done on longer timescales - further radiative transfer simulations will be key to understanding how different central engines affect the spectra of different supernova.

Recent observational results regarding the optical polarization of SLSNe have also been interesting. Polarization is used as a probe of supernova asymmetry, and the detection of polarization would signal that the photosphere of the observed supernova has a distended, elongated geometry, likely due to energy input from a central engine. Several SLSNe have been observed using imaging polarimetry without a significant detection of polarization, including LSQ14mo at -6.9, 0.2, 8.2, 12.9, 18.5 days post-peak (Leloudas et al. 2015a); OGLE16dmu at 101.3 days post-peak (Cikota et al. 2018); PS17bek at -4.0, 2.8, 13.4, 21.0 days post-peak (Cikota et al. 2018); SN2018hti at -7, 8, and 15 days post-peak (Lee 2019); and SN2020ank at around 15 days post-peak (Lee 2020); suggesting these supernovae are not significantly non-spherical. Imaging (Leloudas et al. 2017) and spectropolarimetric (Inserra et al. 2016a) observations of SN2015bn both detected a significant increase in polarization 20 days post-peak; models and spectra suggest that SN2015bn underwent a "phase transition" at that time where the photosphere receded from an outer carbon and oxygen layer to a more aspherical core with mostly freshly nucleosynthesized material (Inserra et al. 2016a; Leloudas et al. 2017). Early imaging (Maund et al. 2019) and spectropolarimetric (Bose et al. 2018) observations of SN2017egm from one day pre-peak to 19 days post-peak did not find statistically significant polarization, but spectropolarimetric observations at 185 days post-peak do show signs of polarization (Saito et al. 2020); models here suggest that the early photosphere had a velocity of $\sim 10\,000$ km/s and an axial ratio of ~ 0.95, while the late photosphere had a velocity of ~ 5000 km/s and an axial ratio of ~ 0.85. Both of these results can be taken as evidence for a central engine, but do nothing to help constrain its properties or nature; to do so would likely require multi-dimensional hydrodynamics simulations, which have only started to be done recently (Chen et al. 2016, 2020b; Suzuki & Maeda 2017, 2019). With a suite of simulations with different ejecta parameters and compositions, engine luminosities, and injection geometries, one would be able to draw a much clearer line between the physical properties of the central engine and the observed polarization.

Modelling these also be useful in determining the falsifiability of the model. The non-detections so far do not falsify the model do to uncertainties in model predictions, but there are no model- or parameter-independent predictions outside of incredibly broad statements such as "the energy must be going somewhere". Since we know that pulsar luminosity decreases as t^{-2} (non including gravitational), and we can integrate the early luminosity to get limits on the pulsar energy, we know there is a minimum amount of energy that the PWN must be emitting, and by contraining multiple wavelengths, such as radio, X-ray, and optical together, we can determine if this energy is being emitted and thus falsify the model. Another model-independent qualitative prediction is that the ejecta will be accelerated by the PWN, so if spectroscopic determination of ejecta velocity shows that the ejecta has slowed down (as might be the case with an ejecta-CSM interaction), then the pulsar-driven model is false for that supernova; however, the recesssion of the photosphere needs to be accounted for, so even an accelerated ejecta may be observationally slowing down - comparing to hydrodynamic models should be sufficient to determine the dynamics of the ejecta as a whole. Neutrinos can also, in principle, be used to test for the presence or absence of a neutron star, which could distinguish the black hole fallback and pair-instability models from the pulsar-driven model, but this require either an extremely close SLSN or a neutrino detector orders of magnitude larger than anything currently available.

A new class of transient, the fast-blue optical transient (FBOT), and particularly the close FBOT AT2018cow (Prentice et al. 2018), may also shed some light on the observational parameter space spanned by the pulsar-driven model. AT2018cow is characterized by a SLSN-like peak luminosity, rapidly evolving light curve, a hot blackbody spectrum that is relatively unchanging and featureless over the first two weeks, and multiwavelength detections in radio/millimetre (Bietenholz et al. 2020; Ho et al. 2019; Margutti et al. 2019) and X-ray/gamma-ray (Kuin et al. 2019; Margutti et al. 2019; Rivera Sandoval et al. 2018). Several models have been proposed to explain the nature of AT2018cow, including PPISN (Leung et al. 2020), ejecta-CSM interaction (Fox & Smith 2019), tidal disruption event (TDE) of a white dwarf (Kuin et al. 2019) or main-sequence star (Perley et al. 2019), common envelope jets supernova (CEJSN) (Soker et al. 2019), electron-capture collapse of merged white dwarfs (Lyutikov & Toonen 2019), and of course, a central magnetar (Fang et al. 2019; Margutti et al. 2019; Mohan et al. 2020; Prentice et al. 2018). Fang et al. (2019) concluded that FBOTs are favorable targets compared to other engine-powered transients (e.g. SLSNe and gamma-ray bursts) for current and next-generation multi-messenger observatories, given their potentially higher volumetric rate.

X-ray and gamma-ray studies of many SLSNe put strong constraints on pulsar parameters (Margutti et al. 2018; Renault-Tinacci et al. 2018), with the x-ray study favoring large fields and ejecta masses (closer to our $P_{\rm min} = 1$ ms scenario), similar to what was inferred in Chapters 3. Radio observations have also put strong constraints on GRB-like outflows from SLSNe (Coppejans et al. 2018), and further radio observations of SLSNe remnants have also not detected any FRBs (Hilmarsson et al. 2020), but put strong constraints on their beaming fraction and burst rate.

Another logical next step is to try and predict unique emission or unique behaviour from another model, like from fallback accretion, calculate emission predictions, and propose observations of interesting candidates, much like we did here. Theorists should focus on what optical and spectral properties in the early emission could differentiate a pulsar-driven supernova from other energy sources, how the rates are affected by having multiple energy sources, and still, how to uniquely detect each energy source via their multiwavelength emission. Follow-up observations onto interesting sources will also be crucial, as investigating the time evolution of the flux and spectral breaks of sources like PTF10hgi and FRB121102 will be vital in characterizing their central engines, and radio detections from other interesting sources, such as SN2012au, will give us more chances to try and determine the nature of central engines in all supernovae. The final key is to combine multiwavelength observations on interesting sources, so that we can get more in depth characerization of different aspects of these sources. For example, follow-up on an interesting source might include spectroscopy and spectropolarimetry at regular intervals, X-ray observations at early times, infrared observations at late times, and millimetre and radio observations at later times. With multiwavelength models and observations, it is only a matter of time before we finally uncover the true nature of all exotic supernovae.

There is much that can be learned from studies of exotic supernovae and their engines. Since neutron stars formed within core-collapse supernovae are surrounded by ejecta, studying them during their infancy is normally near-impossible; only the most energetic ones will be able to be detected electromagnetically (these neutron stars will also emit continuous gravitational waves, which may be detectable by future ground- and space-based gravitational wave observatories (Sieniawska & Bejger 2019)) on short timescales, and these should be at the hearts of energetic supernovae such as SLSNe. Studying these early PWN can give us some clues about how neutron stars can generate extreme magnetic fields, which should give us some insight about the inner structure and composition of these objects. Since the progenitors of these exotic explosions are likely also exotic, and possibly more reflective of stars formed in the early universe, what we learn about these explosions can help us learn about star formation and feedback in early galaxies, which may have implications on our cosmological understanding of the universe. The lessons learned about neutron star structure could give some insight into the structure of matter in the pre-recombination era at $z > 1100$ (Ryden 2003; Tanabashi et al. 2018). Finding a connection between these explosions and FRBs would also be a major milestone for transient astronomy, and would allow us to learn about young neutron stars through two completely seperate transients. With the upcoming Vera C. Rubin Observatory, the sample of interesting exotic supernovae to study should be greatly increased, and can be followed-up on with next generation telescopes in multiple bands. The increased senstivity and localization precision of upcoming gravitational wave observatories will also increase the sample of neutron star mergers, which gives another method of studying exotic neutron stars formed by a completely different process. Drawing parallels between the observations from all sources (exotic supernovae, mergers, and FRBs) and implied neutron star physics will revolutionize our understanding of compact objects and the roles they can play in various transients.

Bibliography

Abbott, B. P., Abbott, R., Abbott, T. D., et al. 2017a, ApJ, 848, L13

—. 2017b, Physical Review Letters, 119, 161101

—. 2017c, ApJ, 848, L12

—. 2020a, ApJ, 892, L3

Abbott, R., Abbott, T. D., Abraham, S., et al. 2020b, arXiv e-prints, arXiv:2010.14527

Abdalla, H., Adam, R., Aharonian, F., et al. 2019, Nature, 575, 464

Abdikamalov, E., Ott, C. D., Radice, D., et al. 2015, ApJ, 808, 70

Abdo, A. A., Ackermann, M., Arimoto, M., et al. 2009, Science, 323, 1688

Abraham, F. 1974, Press, New York, 1974

Adler, S. L. 1971, Annals of Physics, 67, 599

Agnoletto, I., Benetti, S., Cappellaro, E., et al. 2009, ApJ, 691, 1348

Aguilera-Dena, D. R., Langer, N., Moriya, T. J., & Schootemeijer, A. 2018, ApJ, 858, 115

Akiyama, S., Wheeler, J. C., Meier, D. L., & Lichtenstadt, I. 2003, ApJ, 584, 954

Alexander, K. D., Berger, E., Fong, W., et al. 2017, ApJ, 848, L21

Alves, E. P., Grismayer, T., Fonseca, R. A., & Silva, L. O. 2014, New Journal of Physics, 16, 035007

An, T., Hong, X., Lao, B., et al. 2020, The Astronomer's Telegram, 13816, 1

Anderson, J. P., Pessi, P. J., Dessart, L., et al. 2018, A&A, 620, A67

Angus, C. R., Levan, A. J., Perley, D. A., et al. 2016, MNRAS, 458, 84

Aptekar, R., Frederiks, D., Golenetskii, S., et al. 2001, The Astrophysical Journal Supplement Series, 137, 227

Arcavi, I., Howell, D. A., Kasen, D., et al. 2017, Nature, 551, 210

Archibald, R. F., Kaspi, V. M., Tendulkar, S. P., & Scholz, P. 2018, ApJ, 869, 180

Archibald, R. F., Burgay, M., Lyutikov, M., et al. 2017, ApJ, 849, L20

Argyle, E., & Gower, J. F. R. 1972, ApJ, 175, L89

Arnett, W. D. 1982, ApJ, 253, 785

Arons, J. 1983, ApJ, 266, 215

Arons, J. 2002, in Astronomical Society of the Pacific Conference Series, Vol. 271, Neutron Stars in Supernova Remnants, ed. P. O. Slane & B. M. Gaensler, 71

—. 2003, ApJ, 589, 871

Arzoumanian, Z., Chernoff, D. F., & Cordes, J. M. 2002, ApJ, 568, 289

Atoyan, A. M., & Aharonian, F. A. 1996, MNRAS, 278, 525

Atteia, J.-L., Boer, M., Hurley, K., et al. 1987, The Astrophysical Journal, 320, L105

Baade, W. 1938, ApJ, 88, 285

Baade, W., & Zwicky, F. 1934, Proceedings of the National Academy of Science, 20, 254

Baade, W., & Zwicky, F. 1934, Physical Review, 46, 76

Bailer-Jones, C. A. L., Rybizki, J., Fouesneau, M., Mantelet, G., & Andrae, R. 2018, AJ, 156, 58

Bandura, K., Addison, G. E., Amiri, M., et al. 2014, in Society of Photo-Optical Instrumentation Engineers (SPIE) Conference Series, Vol. 9145, Ground-based and Airborne Telescopes V, ed. L. M. Stepp, R. Gilmozzi, & H. J. Hall, 914522

Bannister, K. W., Shannon, R. M., Macquart, J.-P., et al. 2017, ApJ, 841, L12

Bannister, K. W., Deller, A. T., Phillips, C., et al. 2019, Science, 365, 565

Barat, C., Hayles, R., Hurley, K., et al. 1983, Astronomy and Astrophysics, 126, 400

Baring, M. G., & Harding, A. K. 2007, Astrophysics and Space Science, 308, 109

Barkat, Z., Rakavy, G., & Sack, N. 1967, Phys. Rev. Lett., 18, 379

Barlow, M. J., Krause, O., Swinyard, B. M., et al. 2010, A&A, 518, L138

Barnes, J., Duffell, P. C., Liu, Y., et al. 2018, ApJ, 860, 38

Barrau, A., Rovelli, C., & Vidotto, F. 2014, Phys. Rev. D, 90, 127503

Bassa, C., Hessels, J., Kondratiev, V., et al. 2020, The Astronomer's Telegram, 13707, 1

Bassa, C. G., Tendulkar, S. P., Adams, E. A. K., et al. 2017, ApJ, 843, L8

Bastian, T. S., Benz, A. O., & Gary, D. E. 1998, ARA&A, 36, 131

Beckwith, S. V. W., & Sargent, A. I. 1991, ApJ, 381, 250

Begelman, M. C. 1998, ApJ, 493, 291

Begelman, M. C., & Li, Z.-Y. 1992, ApJ, 397, 187

Bégué, D., Burgess, J. M., & Greiner, J. 2017, ArXiv e-prints, arXiv:1710.07987

Beloborodov, A. M. 2017, ArXiv e-prints, arXiv:1702.08644

—. 2020, ApJ, 896, 142

Ben-Ami, S., Gal-Yam, A., Mazzali, P. A., et al. 2014, ApJ, 785, 37

Beniamini, P., Wadiasingh, Z., & Metzger, B. D. 2020, MNRAS, 496, 3390

Benli, O., & Ertan, Ü. 2018, MNRAS, 478, 4890

Bera, A., Mondal, S., Chandra, P., Tendulkar, S., & Roy, J. 2020, The Astronomer's Telegram, 13773, 1

Berger, E., Fong, W., & Chornock, R. 2013, ApJ, 774, L23

Berger, E., Soderberg, A. M., & Frail, D. A. 2003, GRB Coordinates Network, 2014

Bernal, C. G., Lee, W. H., & Page, D. 2010, Rev. Mexicana Astron. Astrofis., 46, 309

Bersten, M. C., Folatelli, G., García, F., et al. 2018, Nature, 554, 497

Bethe, H. A., Brown, G. E., Applegate, J., & Lattimer, J. M. 1979, Nuclear Physics A, 324, 487

Bevan, A., Barlow, M. J., & Milisavljevic, D. 2017, MNRAS, 465, 4044

Bhandari, S., Keane, E. F., Barr, E. D., et al. 2018, MNRAS, 475, 1427

Bhandari, S., Sadler, E. M., Prochaska, J. X., et al. 2020, ApJ, 895, L37

Bhattacharya, D., & Soni, V. 2007, ArXiv e-prints, arXiv:0705.0592

Bianchi, S., & Schneider, R. 2007, MNRAS, 378, 973

Bietenholz, M. F., & Bartel, N. 2017a, ApJ, 851, 124

—. 2017b, ApJ, 839, 10

—. 2017c, ApJ, 851, 7

Bietenholz, M. F., Margutti, R., Coppejans, D., et al. 2020, MNRAS, 491, 4735

Bisnovatyi-Kogan, G. S. 1971, Soviet Ast., 14, 652

Blanchard, P. K., Berger, E., Nicholl, M., & Villar, V. A. 2020, ApJ, 897, 114

Blanchard, P. K., Nicholl, M., Berger, E., et al. 2018, ApJ, 865, 9

Blander, M., & Katz, J. L. 1972, Journal of Statistical Physics, 4, 55

Blandford, R. D., Ostriker, J. P., Pacini, F., & Rees, M. J. 1973, A&A, 23, 145

Blinnikov, S. I., Eastman, R., Bartunov, O. S., Popolitov, V. A., & Woosley, S. E. 1998, ApJ, 496, 454

Blinnikov, S. I., Novikov, I. D., Perevodchikova, T. V., & Polnarev, A. G. 1984, Soviet Astronomy Letters, 10, 177

Blinnikov, S. I., Röpke, F. K., Sorokina, E. I., et al. 2006, A&A, 453, 229

Blondin, J. M., Chevalier, R. A., & Frierson, D. M. 2001, ApJ, 563, 806

Blondin, J. M., Mezzacappa, A., & DeMarino, C. 2003, ApJ, 584, 971

Bloom, J. S., Prochaska, J. X., Pooley, D., et al. 2006, ApJ, 638, 354

Bloom, J. S., Giannios, D., Metzger, B. D., et al. 2011, Science, 333, 203

Bochenek, C. D., Kulkarni, S. R., Ravi, V., et al. 2020a, The Astronomer's Telegram, 14077, 1

Bochenek, C. D., Ravi, V., Belov, K. V., et al. 2020b, Nature, 587, 59

Boër, M., Gendre, B., & Stratta, G. 2015, ApJ, 800, 16

Boggs, S. E., Zoglauer, A., Bellm, E., et al. 2007, The Astrophysical Journal, 661, 458

Bogovalov, S. V., Chechetkin, V. M., Koldoba, A. V., & Ustyugova, G. V. 2005, MNRAS, 358, 705

Boischot, A., & Clavelier, B. 1967, Astrophys. Lett., 1, 7

Bombaci, I. 1996, Astronomy and Astrophysics, 305, 871

Bonanno, A., Urpin, V., & Belvedere, G. 2005, A&A, 440, 199

Borghese, A., Rea, N., Coti Zelati, F., et al. 2020, The Astronomer's Telegram, 13720, 1

Borkowski, J., Gotz, D., Mereghetti, S., et al. 2004, GRB Coordinates Network, 2920

Bose, S., Dong, S., Pastorello, A., et al. 2018, ApJ, 853, 57

Bower, G. C., Metzger, B. D., Cenko, S. B., Silverman, J. M., & Bloom, J. S. 2013, ApJ, 763, 84

Bower, G. C., Chatterjee, S., Cordes, J., et al. 2018, in American Astronomical Society Meeting Abstracts, Vol. 231, American Astronomical Society Meeting Abstracts #231, 342.31

Brahe, T. 1573, Kopenhagen: Laurentius Benedictus

Bramante, J., & Linden, T. 2014, Physical Review Letters, 113, 191301

Branch, D., & Tammann, G. A. 1992, ARA&A, 30, 359

Brecher, K., Fesen, R. A., Maran, S. P., & Brandt, J. C. 1983, The Observatory, 103, 106

Bromberg, O., & Tchekhovskoy, A. 2016, MNRAS, 456, 1739

Bromberg, O., Tchekhovskoy, A., Gottlieb, O., Nakar, E., & Piran, T. 2017, ArXiv e-prints, arXiv:1710.05897

Brown, P. J., Breeveld, A. A., Holland, S., Kuin, P., & Pritchard, T. 2014, Ap&SS, 354, 89

Brownell, Jr., D. H., & Callaway, J. 1969, Nuovo Cimento B Serie, 60, 169

Brownlee, D. 2003, Rare Earth: Why complex life is uncommon in the Universe (Springer)

Bucciantini, N. 2012, in IAU Symposium, Vol. 279, Death of Massive Stars: Supernovae and Gamma-Ray Bursts, ed. P. Roming, N. Kawai, & E. Pian, 289–296

Bucciantini, N., Blondin, J. M., Del Zanna, L., & Amato, E. 2003, A&A, 405, 617

Bucciantini, N., Quataert, E., Arons, J., Metzger, B. D., & Thompson, T. A. 2007, MNRAS, 380, 1541

—. 2008, MNRAS, 383, L25

Bucciantini, N., Quataert, E., Metzger, B. D., et al. 2009, MNRAS, 396, 2038

Bucciantini, N., Thompson, T. A., Arons, J., Quataert, E., & Del Zanna, L. 2006, MNRAS, 368, 1717

Buckley, J. H., Bhupal Dev, P. S., Ferrer, F., & Huang, F. P. 2020, arXiv e-prints, arXiv:2004.06486

Buras, R., Rampp, M., Janka, H. T., & Kifonidis, K. 2003, Phys. Rev. Lett., 90, 241101

Buras, R., Rampp, M., Janka, H.-T., & Kifonidis, K. 2006, A&A, 447, 1049

Burgay, M., Pilia, M., Bernardi, G., et al. 2020, The Astronomer's Telegram, 13783, 1

Burgio, G., Baldo, M., Sahu, P., & Schulze, H.-J. 2002, Physical Review C, 66, 025802

Burrows, A., Dessart, L., Livne, E., Ott, C. D., & Murphy, J. 2007a, ApJ, 664, 416

Burrows, A., & Lattimer, J. M. 1986, ApJ, 307, 178

Burrows, A., Livne, E., Dessart, L., Ott, C. D., & Murphy, J. 2006a, ApJ, 640, 878

—. 2007b, ApJ, 655, 416

Burrows, D. N., Grupe, D., Capalbi, M., et al. 2006b, ApJ, 653, 468

Caleb, M., Spitler, L. G., & Stappers, B. W. 2018a, Nature Astronomy, 2, 839

Caleb, M., Flynn, C., Bailes, M., et al. 2017, MNRAS, 468, 3746

Caleb, M., Keane, E. F., van Straten, W., et al. 2018b, MNRAS, 478, 2046

Cameron, P., Chandra, P., Ray, A., et al. 2005, Nature, 434, 1112

Camilo, F., Ransom, S. M., Gaensler, B. M., et al. 2006, ApJ, 637, 456

Camilo, F., Ransom, S. M., Halpern, J. P., et al. 2016, ApJ, 820, 110

Campbell, P., Hill, M., Howe, R., et al. 2005, GRB Coordinates Network, 2932, 1

Cardelli, J. A., Clayton, G. C., & Mathis, J. S. 1989, ApJ, 345, 245

Chambers, K. C., Huber, M. E., Flewelling, H., et al. 2019, Transient Name Server Discovery Report, 2019-5, 1

Chamel, N., Haensel, P., Zdunik, J. L., & Fantina, A. 2013, International journal of modern physics E, 22, 1330018

Champion, D. J., Petroff, E., Kramer, M., et al. 2016, MNRAS, 460, L30

Chandra, P. 2018, Space Sci. Rev., 214, 27

Chandra, P., Ofek, E. O., Frail, D. A., et al. 2009, The Astronomer's Telegram, 2241, 1

—. 2010, The Astronomer's Telegram, 2367, 1

Chandrasekhar, S. 1931, ApJ, 74, 81

—. 1935, MNRAS, 95, 207

Chatterjee, S., Law, C. J., Wharton, R. S., et al. 2017, ArXiv e-prints, arXiv:1701.01098

Chattopadhyay, T., Misra, R., Chattopadhyay, A. K., & Naskar, M. 2007, ApJ, 667, 1017

Chatzopoulos, E., van Rossum, D. R., Craig, W. J., et al. 2015, ApJ, 799, 18

Chatzopoulos, E., & Wheeler, J. C. 2012, ApJ, 748, 42

Chatzopoulos, E., Wheeler, J. C., & Vinko, J. 2012, ApJ, 746, 121

Chatzopoulos, E., Wheeler, J. C., Vinko, J., Horvath, Z. L., & Nagy, A. 2013, ApJ, 773, 76

Chen, G., Ravi, V., & Lu, W. 2020a, ApJ, 897, 146

Chen, K.-J., Heger, A., Woosley, S., Almgren, A., & Whalen, D. J. 2014, ApJ, 792, 44

Chen, K.-J., Woosley, S. E., & Sukhbold, T. 2016, ApJ, 832, 73

Chen, K.-J., Woosley, S. E., & Whalen, D. J. 2020b, ApJ, 893, 99

Chen, T.-W., Smartt, S. J., Bresolin, F., et al. 2013, ApJ, 763, L28

Chen, T. W., Smartt, S. J., Jerkstrand, A., et al. 2015, MNRAS, 452, 1567

Chen, T.-W., Schady, P., Xiao, L., et al. 2017a, ApJ, 849, L4

Chen, T. W., Nicholl, M., Smartt, S. J., et al. 2017b, A&A, 602, A9

Chen, W.-C. 2020, PASJ, 72, L8

Cheng, B., Epstein, R. I., Guyer, R. A., & Young, A. C. 1996, Nature, 382, 518

Cheng, K. S., Ho, C., & Ruderman, M. 1986a, ApJ, 300, 500

—. 1986b, ApJ, 300, 522

Chevalier, R. A. 1977, in Astrophysics and Space Science Library, Vol. 66, Supernovae, ed. D. N. Schramm, 53

Chevalier, R. A. 1989, ApJ, 346, 847

—. 1998, ApJ, 499, 810

—. 2005, ApJ, 619, 839

Chevalier, R. A., & Fransson, C. 1992, ApJ, 395, 540

—. 1994, ApJ, 420, 268

Chevalier, R. A., & Irwin, C. M. 2011, ApJ, 729, L6

CHIME/FRB Collaboration, Amiri, M., Bandura, K., et al. 2018, ApJ, 863, 48

—. 2019a, Nature, 566, 235

CHIME/FRB Collaboration, Andersen, B. C., Bandura, K., et al. 2019b, ApJ, 885, L24

CHIME/FRB Collaboration, Amiri, M., Bandura, K., et al. 2019c, Nature, 566, 230

CHIME/FRB Collaboration, Amiri, M., Andersen, B. C., et al. 2020, Nature, 582, 351

Chin, Y.-N., & Huang, Y.-L. 1994, Nature, 371, 398

Chodorowski, M. J., Zdziarski, A. A., & Sikora, M. 1992, ApJ, 400, 181

Choi, Y.-B., Cho, H.-S., Lee, C.-H., & Kim, Y.-M. 2019, Journal of Korean Physical Society, 74, 842

Chomiuk, L., Soderberg, A., Margutti, R., et al. 2012, The Astronomer's Telegram, 3931, 1

Chomiuk, L., Chornock, R., Soderberg, A. M., et al. 2011, ApJ, 743, 114

Chornock, R., Bhirombhakdi, K., Katebi, R., et al. 2016, The Astronomer's Telegram, 8790, 1

Chugai, N. N., & Danziger, I. J. 1994, MNRAS, 268, 173

Cigan, P., Matsuura, M., Gomez, H. L., et al. 2019, ApJ, 886, 51

Cikota, A., Leloudas, G., Bulla, M., et al. 2018, MNRAS, 479, 4984

Clark, B. G. 1980, A&A, 89, 377

Clark, D. H., & Stephenson, F. R. 1977, The historical supernovae

Cline, D. B. 1996, Nuclear Physics A, 610, 500

Cline, T. 1980, Comments on Astrophysics, 9, 13

Cline, T., Desai, U., Teegarden, B., et al. 1982, The Astrophysical Journal, 255, L45

Coleiro, A., & Dornic, D. 2020, The Astronomer's Telegram, 13721, 1

Colgate, S. A. 1979, ApJ, 232, 404

Colgate, S. A., & McKee, C. 1969, ApJ, 157, 623

Condon, J. J., Cotton, W. D., Fomalont, E. B., et al. 2012, ApJ, 758, 23

Connor, L., Sievers, J., & Pen, U.-L. 2016, MNRAS, 458, L19

Cooke, J., Sullivan, M., Gal-Yam, A., et al. 2012, Nature, 491, 228

Cooke, R. J., Pettini, M., & Steidel, C. C. 2018, ApJ, 855, 102

Coppejans, D. L., Margutti, R., Guidorzi, C., et al. 2018, ApJ, 856, 56

Cordes, J. M., & Chatterjee, S. 2019, ARA&A, 57, 417

Cordes, J. M., & Lazio, T. J. W. 2002, astro-ph/0207156, astro-ph/0207156

Cordes, J. M., & Wasserman, I. 2016, MNRAS, 457, 232

Cornwell, T. J., Golap, K., & Bhatnagar, S. 2008, IEEE Journal of Selected Topics in Signal Processing, 2, 647

Costa, E., Frontera, F., Heise, J., et al. 1997, Nature, 387, 783

Cowperthwaite, P. S., Berger, E., Villar, V. A., et al. 2017, ApJ, 848, L17

Cox, D. P. 1972, ApJ, 178, 159

Crawford, F., Rane, A., Tran, L., et al. 2016, MNRAS, 460, 3370

Cromartie, H. T., Fonseca, E., Ransom, S. M., et al. 2020, Nature Astronomy, 4, 72

Cruces, M., Spitler, L. G., Scholz, P., et al. 2020, MNRAS, 500, 448

Cui, X.-H., Zhang, C.-M., Wang, S.-Q., et al. 2020, MNRAS, arXiv:2011.01339

Cutler, C. 2002, Phys. Rev. D, 66, 084025

Cutler, C., & Flanagan, É. E. 1994, Phys. Rev. D, 49, 2658

Cutler, C., & Jones, D. I. 2001, Phys. Rev. D, 63, 024002

Dai, S., Lu, J., Wang, C., et al. 2020, arXiv e-prints, arXiv:2011.03960

Dai, Z. G. 2020, ApJ, 897, L40

Dai, Z. G., Wang, J. S., Wu, X. F., & Huang, Y. F. 2016a, ApJ, 829, 27

Dai, Z. G., Wang, S. Q., Wang, J. S., Wang, L. J., & Yu, Y. W. 2016b, ApJ, 817, 132

Dalal, N., Griest, K., & Pruet, J. 2002, ApJ, 564, 209

Dale, D., & ngVLA Key Science Goal 3 Team. 2020, in American Astronomical Society Meeting Abstracts, American Astronomical Society Meeting Abstracts, 364.18

Dall'Osso, S., Shore, S. N., & Stella, L. 2009, MNRAS, 398, 1869

De Cia, A., Gal-Yam, A., Rubin, A., et al. 2018, ApJ, 860, 100

De Colle, F., Lu, W., Kumar, P., Ramirez-Ruiz, E., & Smoot, G. 2017, ArXiv e-prints, arXiv:1701.05198

de Jager, O. C., Harding, A. K., Michelson, P. F., et al. 1996, ApJ, 457, 253

De Luca, A. 2017, in Journal of Physics Conference Series, Vol. 932, Journal of Physics Conference Series, 012006

De Luca, A., Caraveo, P. A., Mereghetti, S., Tiengo, A., & Bignami, G. F. 2006, Science, 313, 814

de Mink, S. E., & King, A. 2017, ApJ, 839, L7

Del Zanna, L., Amato, E., & Bucciantini, N. 2004, A&A, 421, 1063

DeLaunay, J. J., Fox, D. B., Murase, K., et al. 2016, ApJ, 832, L1

Delgado, A., Harrison, D., Hodgkin, S., et al. 2017, Transient Name Server Discovery Report, 2017-873, 1

den Hartog, P. R. 2008

Deng, W., & Zhang, B. 2014, ApJ, 783, L35

Derishev, E., & Piran, T. 2019, ApJ, 880, L27

Dermer, C. D., Murase, K., & Takami, H. 2012, ApJ, 755, 147

Dessart, L., Hillier, D. J., Livne, E., et al. 2011, MNRAS, 414, 2985

Dessart, L., Hillier, D. J., Waldman, R., Livne, E., & Blondin, S. 2012, MNRAS, 426, L76

Dessart, L., Hillier, D. J., Woosley, S., et al. 2015, MNRAS, 453, 2189

Dessart, L., John Hillier, D., Yoon, S.-C., Waldman, R., & Livne, E. 2017, A&A, 603, A51

Dessart, L., Waldman, R., Livne, E., Hillier, D. J., & Blondin, S. 2013, MNRAS, 428, 3227

Dexter, J., & Kasen, D. 2013, ApJ, 772, 30

Di Francesco, J., Chalmers, D., Denman, N., et al. 2019, in Canadian Long Range Plan for Astronony and Astrophysics White Papers, Vol. 2020, 32

Draine, B. T., & Lee, H. M. 1984, ApJ, 285, 89

Draine, B. T., & Salpeter, E. E. 1979a, ApJ, 231, 438

—. 1979b, ApJ, 231, 77

Draine, B. T., Dale, D. A., Bendo, G., et al. 2007, ApJ, 663, 866

Drout, M. R., Soderberg, A. M., Gal-Yam, A., et al. 2011, ApJ, 741, 97

Duncan, R. C. 2001, arXiv preprint astro-ph/0103235

Duncan, R. C. 2004, in Cosmic explosions in three dimensions, ed. P. Höflich, P. Kumar, & J. C. Wheeler, 285

Duncan, R. C., & Thompson, C. 1992, The Astrophysical Journal, 392, L9

Durant, M., & van Kerkwijk, M. H. 2006, ApJ, 650, 1070

Dwek, E., & Arendt, R. G. 2015, ApJ, 810, 75

Dwek, E., Galliano, F., & Jones, A. P. 2007, ApJ, 662, 927

Eftekhari, T., Berger, E., Margalit, B., et al. 2019, ApJ, 876, L10

Eftekhari, T., Margalit, B., Omand, C. M. B., et al. 2020, arXiv e-prints, arXiv:2010.06612

Eichler, D., Livio, M., Piran, T., & Schramm, D. N. 1989, Nature, 340, 126

Elenbaas, C., Huppenkothen, D., Omand, C., et al. 2017, MNRAS, 471, 1856

Elshamouty, K. G., Heinke, C. O., Sivakoff, G. R., et al. 2013, ApJ, 777, 22

Elvis, M., Wilkes, B. J., McDowell, J. C., et al. 1994, ApJS, 95, 1

Epstein, R. I., Colgate, S. A., & Haxton, W. C. 1988, Physical Review Letters, 61, 2038

Falcke, H., & Rezzolla, L. 2014, A&A, 562, A137

Falk, S. W. 1978, ApJ, 225, L133

Falk, S. W., & Arnett, W. D. 1977, ApJS, 33, 515

Fang, K., Metzger, B. D., Murase, K., Bartos, I., & Kotera, K. 2019, ApJ, 878, 34

Farah, W., Bailes, M., Jameson, A., et al. 2017, The Astronomer's Telegram, 10867, 1

Farah, W., Flynn, C., Bailes, M., et al. 2018, MNRAS, 478, 1209

Fasano, M., Abdelsalhin, T., Maselli, A., & Ferrari, V. 2019, Phys. Rev. Lett., 123, 141101

Feroci, M., Hurley, K., Duncan, R., & Thompson, C. 2001, The Astrophysical Journal, 549, 1021

Ferrario, L., Melatos, A., & Zrake, J. 2015, Space Sci. Rev., 191, 77

Fewell, M. P. 1995, American Journal of Physics, 63, 653

Fishman, G. J., & Meegan, C. A. 1995, ARA&A, 33, 415

Flanagan, É. É., & Hughes, S. A. 1998, Phys. Rev. D, 57, 4535

Fonseca, E., Andersen, B. C., Bhardwaj, M., et al. 2020, ApJ, 891, L6

Foreman-Mackey, D., Hogg, D. W., Lang, D., & Goodman, J. 2013, PASP, 125, 306

Fox, O. D., & Smith, N. 2019, MNRAS, 488, 3772

Fraija, N., Barniol Duran, R., Dichiara, S., & Beniamini, P. 2019, ApJ, 883, 162

Frail, D., Kulkarni, S., & Bloom, J. 1999, Nature, 398, 127

Frail, D. A., Kulkarni, S. R., Nicastro, L., Feroci, M., & Taylor, G. B. 1997, Nature, 389, 261

Frail, D. A., Kulkarni, S. R., Sari, R., et al. 2001, ApJ, 562, L55

Fraley, G. S. 1968, Ap&SS, 2, 96

Fraser, M., & Boubert, D. 2019, ApJ, 871, 92

Frederiks, D., Aptekar, R., Cline, T., et al. 2008, in American Institute of Physics Conference Series, Vol. 1000, American Institute of Physics Conference Series, ed. M. Galassi, D. Palmer, & E. Fenimore, 271–275

Frontera, F., & Piro, L. 1999, A&AS, 138, 395

Fruchter, A. S., Levan, A. J., Strolger, L., et al. 2006, Nature, 441, 463

Fryer, C. L., Woosley, S. E., & Heger, A. 2001, ApJ, 550, 372

Fujimoto, S.-i., Nishimura, N., & Hashimoto, M.-a. 2008, ApJ, 680, 1350

Fuller, J., & Ott, C. D. 2015, MNRAS, 450, L71

Gaensler, B., Kouveliotou, C., Gelfand, J., et al. 2005, Nature, 434, 1104

Gaensler, B. M., & Slane, P. O. 2006, ARA&A, 44, 17

Gaensler, B. M., van der Swaluw, E., Camilo, F., et al. 2004, ApJ, 616, 383

Gajjar, V., Siemion, A. P. V., MacMahon, D. H. E., et al. 2017, The Astronomer's Telegram, 10675

Gajjar, V., Siemion, A. P. V., Price, D. C., et al. 2018, ApJ, 863, 2

Gal-Yam, A. 2012, Science, 337, 927

—. 2019, ARA&A, 57, 305

Gal-Yam, A., & Leonard, D. C. 2009, Nature, 458, 865

Gal-Yam, A., Mazzali, P., Ofek, E. O., et al. 2009, Nature, 462, 624

Galama, T. J., Vreeswijk, P. M., van Paradijs, J., et al. 1998, Nature, 395, 670

Gall, C., Hjorth, J., & Andersen, A. C. 2011, A&A Rev., 19, 43

Gaunt, J. A. 1930, Philosophical Transactions of the Royal Society of London Series A, 229, 163

Gavriil, F. P., Gonzalez, M. E., Gotthelf, E. V., et al. 2008, Science, 319, 1802

Gehrels, N., Sarazin, C. L., O'Brien, P. T., et al. 2005, Nature, 437, 851

Gelfand, J. D., Slane, P. O., & Zhang, W. 2009, ApJ, 703, 2051

Gelman, A., Hwang, J., & Vehtari, A. 2014, Statistics and computing, 24, 997

Gelman, A., & Rubin, D. B. 1992, Statistical Science, 7, 457

Gendre, B., Stratta, G., Atteia, J. L., et al. 2013, ApJ, 766, 30

Geng, J. J., & Huang, Y. F. 2015, ApJ, 809, 24

Geng, J.-J., Li, B., Li, L.-B., et al. 2020, ApJ, 898, L55

Georgy, C., Meynet, G., Ekström, S., et al. 2017, A&A, 599, L5

Ghisellini, G. 2016, arXiv:1609.04815, arXiv:1609.04815

Ghisellini, G., & Svensson, R. 1991, MNRAS, 252, 313

Giacconi, R., Gursky, H., Paolini, F. R., & Rossi, B. B. 1962, Physical Review Letters, 9, 439

Gilkis, A., Soker, N., & Papish, O. 2016, ApJ, 826, 178

Gilmer, M. S., Kozyreva, A., Hirschi, R., Fröhlich, C., & Yusof, N. 2017, ApJ, 846, 100

Gilmozzi, R., Cassatella, A., Clavel, J., et al. 1987, Nature, 328, 318

Ginzburg, S., & Balberg, S. 2012, ApJ, 757, 178

Ginzburg, V., & Syrovatskii, S. 1965, Annual Review of Astronomy and Astrophysics, 3, 297

Ginzburg, V. L., & Syrovatskii, S. I. 1965, ARA&A, 3, 297

Göğüş, E., Kouveliotou, C., Woods, P. M., et al. 2001, The Astrophysical Journal, 558, 228

Göğüş, E., Woods, P. M., Kouveliotou, C., et al. 1999, The Astrophysical Journal Letters, 526, L93

—. 2000, The Astrophysical Journal Letters, 532, L121

Gold, T. 1968, Nature, 218, 731

Goldreich, P., & Julian, W. H. 1969, ApJ, 157, 869

Goldreich, P., & Reisenegger, A. 1992, ApJ, 395, 250

Goldreich, P., & Weber, S. V. 1980, ApJ, 238, 991

Golenetskii, S., Ilyinskii, V., & Mazets, E. 1984

Gomez, H. L., Krause, O., Barlow, M. J., et al. 2012, ApJ, 760, 96

Gomez, S., Berger, E., Blanchard, P. K., et al. 2020, arXiv e-prints, arXiv:2009.01853

Good, D., & CHIME/FRB Collaboration. 2020, The Astronomer's Telegram, 14074, 1

Goodman, J., & Weare, J. 2010, Communications in Applied Mathematics and Computational Science, 5, 65

Gotthelf, E. V., & Halpern, J. P. 2009, ApJ, 695, L35

Gotthelf, E. V., Halpern, J. P., & Seward, F. D. 2005, ApJ, 627, 390

Gotthelf, E. V., Vasisht, G., Boylan-Kolchin, M., & Torii, K. 2000, ApJ, 542, L37

Gottlieb, O., Nakar, E., Piran, T., & Hotokezaka, K. 2017, ArXiv e-prints, arXiv:1710.05896

Götz, D., Mereghetti, S., Molkov, S., et al. 2006, Astronomy & Astrophysics, 445, 313

Goumans, T. P. M., & Bromley, S. T. 2012, MNRAS, 420, 3344

Göğüș, E., Woods, P. M., Kouveliotou, C., et al. 2000, ApJ, 532, L121

Granot, J., Panaitescu, A., Kumar, P., & Woosley, S. E. 2002, ApJ, 570, L61

Grasberg, E. K., & Nadyozhin, D. K. 1987, AZh, 64, 1199

Grassberg, E. K., Imshennik, V. S., & Nadyozhin, D. K. 1971, Ap&SS, 10, 28

Greiner, J., Mazzali, P. A., Kann, D. A., et al. 2015, Nature, 523, 189

Gruzinov, A. 2005, Physical Review Letters, 94, 021101

Gu, W.-M., Dong, Y.-Z., Liu, T., Ma, R., & Wang, J. 2016, ApJ, 823, L28

Gualtieri, L., Ciolfi, R., & Ferrari, V. 2011, Classical and Quantum Gravity, 28, 114014

Guillochon, J., Nicholl, M., Villar, V. A., et al. 2018, ApJS, 236, 6

Guillochon, J., Parrent, J., Kelley, L. Z., & Margutti, R. 2017, ApJ, 835, 64

Gupta, Y., Mitra, D., Green, D. A., & Acharyya, A. 2005, Current Science, 89, 853

Gutenberg, B., & Richter, C. F. 1956, Annals of Geophysics, 9, 1

Hackstein, S., Brüggen, M., Vazza, F., Gaensler, B. M., & Heesen, V. 2019, MNRAS, 488, 4220

Hackstein, S., Brüggen, M., Vazza, F., & Rodrigues, L. F. S. 2020, MNRAS, 498, 4811

Haensel, P., & Bonazzola, S. 1996, A&A, 314, 1017

Haensel, P., Potekhin, A. Y., & Yakovlev, D. G. 2007, Neutron stars 1: Equation of state and structure, Vol. 326 (Springer Science & Business Media)

Hakkila, J., Giblin, T. W., Roiger, R. J., et al. 2003, ApJ, 582, 320

Hallinan, G., Corsi, A., Mooley, K. P., et al. 2017, ArXiv e-prints, arXiv:1710.05435

Hamacher, D. W. 2014, Journal of Astronomical History and Heritage, 17, 161

Hamaker, J. P., Bregman, J. D., & Sault, R. J. 1996, A&AS, 117, 137

Hamilton, A. J. S., & Sarazin, C. L. 1984, ApJ, 287, 282

Hamuy, M., Phillips, M. M., Suntzeff, N. B., et al. 1996, AJ, 112, 2391

Hamuy, M., Maza, J., Phillips, M. M., et al. 1993, AJ, 106, 2392

Han, J. L., Manchester, R. N., van Straten, W., & Demorest, P. 2018, ApJS, 234, 11

Hankins, T. H., Kern, J. S., Weatherall, J. C., & Eilek, J. A. 2003, Nature, 422, 141

Harada, A., Nagakura, H., Iwakami, W., & Yamada, S. 2017, ApJ, 839, 28

Harding, A. K., Baring, M. G., & Gonthier, P. L. 1997, The Astrophysical Journal, 476, 246

Harding, A. K., & Lai, D. 2006, Reports on Progress in Physics, 69, 2631

Harding, A. K., & Muslimov, A. G. 1998, ApJ, 508, 328

Hatsukade, B., Tominaga, N., Hayashi, M., et al. 2018, ApJ, 857, 72

Haxton, W. C. 1988, Physical Review Letters, 60, 1999

Hayakawa, T., Iwamoto, N., Kajino, T., et al. 2006, ApJ, 648, L47

Hayakawa, T., & Maeda, K. 2018, ApJ, 854, 43

Heger, A., Fryer, C. L., Woosley, S. E., Langer, N., & Hartmann, D. H. 2003, ApJ, 591, 288

Heger, A., & Woosley, S. E. 2002, ApJ, 567, 532

Heintz, K. E., Prochaska, J. X., Simha, S., et al. 2020, ApJ, 903, 152

Hessels, J. W., Ransom, S. M., Stairs, I. H., et al. 2006, Science, 311, 1901

Hessels, J. W. T., Spitler, L. G., Seymour, A. D., et al. 2019, ApJ, 876, L23

Hester, J. J., Scowen, P. A., Sankrit, R., et al. 1995, ApJ, 448, 240

Hewish, A., Bell, S. J., Pilkington, J., Scott, P., & Collins, R. 1968, Nature, 217, 709

Hewish, A., & Okoye, S. 1965, Nature, 207, 59

Heyl, J. S., & Kulkarni, S. 1998, The Astrophysical Journal Letters, 506, L61

Hilmarsson, G. H., Spitler, L. G., Keane, E. F., et al. 2020, MNRAS, 493, 5170

Hirotani, K. 2006, ApJ, 652, 1475

Ho, A. Y. Q., Phinney, E. S., Ravi, V., et al. 2019, ApJ, 871, 73

Högbom, J. A. 1974, A&AS, 15, 417

Horváth, I. 1998, ApJ, 508, 757

Horváth, I., Balázs, L. G., Bagoly, Z., Ryde, F., & Mészáros, A. 2006, A&A, 447, 23

Horvath, I., Toth, B. G., Hakkila, J., et al. 2017, ArXiv e-prints, arXiv:1710.11509

Huang, Y.-J., Urata, Y., Huang, K., et al. 2020, ApJ, 897, 69

Huggins, W. 1866, MNRAS, 26, 275

Huijser, D., Goodman, J., & Brewer, B. J. 2015, arXiv e-prints, arXiv:1509.02230

Hulse, R. A., & Taylor, J. H. 1975, ApJ, 195, L51

Hurley, K., Cline, T., Mazets, E., et al. 1999, Nature, 397, 41

Hurley, K., Berger, E., Castro-Tirado, A., et al. 2002, ApJ, 567, 447

Hurley, K., Boggs, S. E., Smith, D. M., et al. 2005, Nature, 434, 1098

Hurley, K., Mitrofanov, I. G., Golovin, D., et al. 2020, GRB Coordinates Network, 27714, 1

Huygh, P. 1981, Science Digest

Inan, U., Lehtinen, N., Lev-Tov, S., et al. 1999, Geophysical Research Letters, 26, 3357

Inan, U. S., Lehtinen, N. G., Moore, R., et al. 2007, Geophysical research letters, 34

Indebetouw, R., Matsuura, M., Dwek, E., et al. 2014, ApJ, 782, L2

Inserra, C., Bulla, M., Sim, S. A., & Smartt, S. J. 2016a, ApJ, 831, 79

Inserra, C., Smartt, S. J., Jerkstrand, A., et al. 2013, ApJ, 770, 128

Inserra, C., Smartt, S. J., Gall, E. E. E., et al. 2016b, ArXiv e-prints, arXiv:1604.01226

Inserra, C., Nicholl, M., Chen, T.-W., et al. 2017, MNRAS, 468, 4642

Ioka, K., Hotokezaka, K., & Piran, T. 2016, ApJ, 833, 110

Ioka, K., & Nakamura, T. 2017, ArXiv e-prints, arXiv:1710.05905

Ioka, K., & Zhang, B. 2020, ApJ, 893, L26

Isella, A. 2020, in American Astronomical Society Meeting Abstracts, American Astronomical Society Meeting Abstracts, 364.15

Israel, G. L., Romano, P., Mangano, V., et al. 2008, ApJ, 685, 1114

Israel, G. L., Esposito, P., Rea, N., et al. 2016, MNRAS, 457, 3448

Israel, G. L., Burgay, M., Rea, N., et al. 2020, arXiv e-prints, arXiv:2011.06607

Ivezic, Z., Tyson, J., Abel, B., et al. 2008, arXiv preprint arXiv:0805.2366

Iwamoto, K., Mazzali, P. A., Nomoto, K., et al. 1998, Nature, 395, 672

Iwamoto, K., Nakamura, T., Nomoto, K., et al. 2000, ApJ, 534, 660

Jaeger, S. 2008, in Astronomical Society of the Pacific Conference Series, Vol. 394, Astronomical Data Analysis Software and Systems XVII, ed. R. W. Argyle, P. S. Bunclark, & J. R. Lewis, 623

Janka, H.-T. 2012, Annual Review of Nuclear and Particle Science, 62, 407

Janka, H.-T., Langanke, K., Marek, A., Martínez-Pinedo, G., & Müller, B. 2007, Phys. Rep., 442, 38

Japelj, J., Vergani, S. D., Salvaterra, R., Hunt, L. K., & Mannucci, F. 2016, A&A, 593, A115

Jerkstrand, A., Smartt, S. J., & Heger, A. 2016, MNRAS, 455, 3207

Jerkstrand, A., Smartt, S. J., Inserra, C., et al. 2017, ApJ, 835, 13

Joggerst, C. C., & Whalen, D. J. 2011, ApJ, 728, 129

Joglekar, H., Gangal, K., Vahia, M., & Sule, A. 2011, Puratattva-Bulletin of the Indian Archaeological Society, 41, 207

Johnston, S., & Romani, R. W. 2004, in IAU Symposium, Vol. 218, Young Neutron Stars and Their Environments, ed. F. Camilo & B. M. Gaensler, 315

Jones, A. P., Tielens, A. G. G. M., & Hollenbach, D. J. 1996, ApJ, 469, 740

Josephy, A., Chawla, P., Fonseca, E., et al. 2019, ApJ, 882, L18

Kalogera, V., & Baym, G. 1996, The Astrophysical Journal Letters, 470, L61

Kamble, A., Soderberg, A. M., Chomiuk, L., et al. 2013, arXiv e-prints, arXiv:1309.3573

Kardashev, N. S. 1964, AZh, 41, 807

Kasen, D., & Bildsten, L. 2010, ApJ, 717, 245

Kasen, D., Metzger, B. D., & Bildsten, L. 2016, ApJ, 821, 36

Kasen, D., Woosley, S. E., & Heger, A. 2011, ApJ, 734, 102

Kashiyama, K., Ioka, K., & Mészáros, P. 2013, ApJ, 776, L39

Kashiyama, K., & Murase, K. 2017, ApJ, 839, L3

Kashiyama, K., Murase, K., Bartos, I., Kiuchi, K., & Margutti, R. 2016, ApJ, 818, 94

Kaspi, V. M., & Beloborodov, A. M. 2017, ARA&A, 55, 261

Kasumov, F. K., Allahverdiyev, A. O., & Aydamirova, A. H. 2008, Azerbaijani Astronomical Journal, 3, 19

Katz, J. I. 2002, The biggest bangs : the mystery of gamma-ray bursts, the most violent explosions in the universe

—. 2014, Phys. Rev. D, 89, 103009

—. 2016, Modern Physics Letters A, 31, 1630013

—. 2020, MNRAS, 499, 2319

Keane, E. F., & Kramer, M. 2008, MNRAS, 391, 2009

Keane, E. F., & Petroff, E. 2015, MNRAS, 447, 2852

Kennel, C. F., & Coroniti, F. V. 1984, ApJ, 283, 710

Kepler, J. 1606, Opera Omnia, 2

Khokhlov, A. M., Höflich, P. A., Oran, E. S., et al. 1999, ApJ, 524, L107

Kilpatrick, C. D., Burchett, J. N., Jones, D. O., et al. 2020, arXiv e-prints, arXiv:2011.07561

Kirk, J. G., & Skjæraasen, O. 2003, ApJ, 591, 366

Kirk, J. G., & Skjaeraasen, O. 2004, in IAU Symposium, Vol. 218, Young Neutron Stars and Their Environments, ed. F. Camilo & B. M. Gaensler, 171

Kirsten, F., Jenkins, M., Snelders, M., et al. 2020a, The Astronomer's Telegram, 13735, 1

Kirsten, F., Snelders, M. P., Jenkins, M., et al. 2020b, Nature Astronomy, arXiv:2007.05101

Kisaka, S., Ioka, K., Kashiyama, K., & Nakamura, T. 2017, ArXiv e-prints, arXiv:1711.00243

Kiuchi, K., Kyutoku, K., Shibata, M., & Taniguchi, K. 2019, ApJ, 876, L31

Kiuchi, K., & Yoshida, S. 2008, Phys. Rev. D, 78, 044045

Klebesadel, R., Strong, I., & Olson, R. 1973, L85

Klebesadel, R. W., Strong, I. B., & Olson, R. A. 1973, ApJ, 182, L85

Klein, O., & Nishina, Y. 1929, Zeitschrift für Physik, 52, 853

Kleiser, I. K. W., & Kasen, D. 2014, MNRAS, 438, 318

Knop, R., Aldering, G., Deustua, S., et al. 1999, IAU Circ., 7128, 1

Kobayashi, H., Kimura, H., Watanabe, S.-i., Yamamoto, T., & Müller, S. 2011, Earth, Planets, and Space, 63, 1067

Komissarov, S. S., & Barkov, M. V. 2007, MNRAS, 382, 1029

Komissarov, S. S., & Lyubarsky, Y. E. 2004, MNRAS, 349, 779

Kong, A. K. H., Li, K. L., Kim, S., & Hui, C. Y. 2020, Research Notes of the American Astronomical Society, 4, 84

Kotera, K., Phinney, E. S., & Olinto, A. V. 2013, MNRAS, 432, 3228

Kouveliotou, C., Meegan, C. A., Fishman, G. J., et al. 1993, ApJ, 413, L101

Kouveliotou, C., Norris, J., Cline, T., et al. 1987, The Astrophysical Journal, 322, L21

Kouveliotou, C., Fishman, G., Meegan, C., et al. 1993, Nature, 362, 728

Kouveliotou, C., Dieters, S., Strohmayer, T., et al. 1998, Nature, 393, 235

Kozasa, T., & Hasegawa, H. 1987, Progress of Theoretical Physics, 77, 1402

Kozasa, T., Hasegawa, H., & Nomoto, K. 1989, ApJ, 344, 325

—. 1991, A&A, 249, 474

Kozasa, T., Nozawa, T., Tominaga, N., et al. 2009, in Astronomical Society of the Pacific Conference Series, Vol. 414, Cosmic Dust - Near and Far, ed. T. Henning, E. Grün, & J. Steinacker, 43

Kozyreva, A., & Blinnikov, S. 2015, MNRAS, 454, 4357

Kozyreva, A., Blinnikov, S., Langer, N., & Yoon, S. C. 2014, A&A, 565, A70

Kozyreva, A., Kromer, M., Noebauer, U. M., & Hirschi, R. 2018, MNRAS, 479, 3106

Kozyreva, A., Gilmer, M., Hirschi, R., et al. 2017, MNRAS, 464, 2854

Kramers, H. A. 1923, The London, Edinburgh, and Dublin Philosophical Magazine and Journal of Science, 46, 836

Krolik, J. H., & Piran, T. 2011, ApJ, 743, 134

Kuin, N. P. M., Wu, K., Oates, S., et al. 2019, MNRAS, 487, 2505

Kulkarni, S. R., Ofek, E. O., & Neill, J. D. 2015, ArXiv e-prints, arXiv:1511.09137

Kulkarni, S. R., Ofek, E. O., Neill, J. D., Zheng, Z., & Juric, M. 2014, ApJ, 797, 70

Kumar, P., & Bošnjak, Ž. 2020, MNRAS, 494, 2385

Kumar, P., Lu, W., & Bhattacharya, M. 2017, MNRAS, 468, 2726

Kumar, P., Narayan, R., & Johnson, J. L. 2008, MNRAS, 388, 1729

Kumar, P., Shannon, R. M., Osłowski, S., et al. 2019, ApJ, 887, L30

Kutschera, M., & Wójcik, W. 1989, Physics Letters B, 223, 11

Kuzmin, A. D. 2007, in WE-Heraeus Seminar on Neutron Stars and Pulsars 40 years after the Discovery, ed. W. Becker & H. H. Huang, 72

Lai, D. 2001, Reviews of Modern Physics, 73, 629

Lakićević, M., van Loon, J. T., Stanke, T., De Breuck, C., & Patat, F. 2012, A&A, 541, L1

Lamb, G. P., & Kobayashi, S. 2017, ArXiv e-prints, arXiv:1710.05857

Landau, L. 1957a, SOVIET PHYSICS JETP-USSR, 5, 101

—. 1957b, Soviet Physics Jetp-Ussr, 3, 920

Langer, N., Norman, C. A., de Koter, A., et al. 2007, A&A, 475, L19

Laros, J., Fenimore, E., Fikani, M., et al. 1986

Laros, J., Fenimore, E., Klebesadel, R., et al. 1987, The Astrophysical Journal, 320, L111

Lattimer, J. M., & Prakash, M. 2001, ApJ, 550, 426

—. 2007, Phys. Rep., 442, 109

Law, C. J. 2017, rfpipe: Radio interferometric transient search pipeline, ascl:1710.002

Law, C. J., Bower, G. C., Pokorny, M., Rupen, M. P., & Sowinski, K. 2012, ApJ, 760, 124

Law, C. J., Gaensler, B. M., Metzger, B. D., Ofek, E. O., & Sironi, L. 2018a, ApJ, 866, L22

Law, C. J., Abruzzo, M. W., Bassa, C. G., et al. 2017, ApJ, 850, 76

Law, C. J., Bower, G. C., Burke-Spolaor, S., et al. 2018b, ApJS, 236, 8

Law, C. J., Omand, C. M. B., Kashiyama, K., et al. 2019, ApJ, 886, 24

Law, C. J., Butler, B. J., Prochaska, J. X., et al. 2020, arXiv e-prints, arXiv:2007.02155

Lawrence, E., Vander Wiel, S., Law, C., Burke Spolaor, S., & Bower, G. C. 2017, AJ, 154, 117

Lazio, T., & ngVLA Key Science Case 5 Science Team. 2020, in American Astronomical Society Meeting Abstracts, American Astronomical Society Meeting Abstracts, 364.22

Lee, C.-H. 2019, ApJ, 875, 121

—. 2020, Astronomische Nachrichten, 341, 651

Leloudas, G., Chatzopoulos, E., Dilday, B., et al. 2012, A&A, 541, A129

Leloudas, G., Patat, F., Maund, J. R., et al. 2015a, ApJ, 815, L10

Leloudas, G., Schulze, S., Krühler, T., et al. 2015b, MNRAS, 449, 917

Leloudas, G., Maund, J. R., Gal-Yam, A., et al. 2017, ApJ, 837, L14

Leung, S.-C., Blinnikov, S., Nomoto, K., et al. 2020, ApJ, 903, 66

Levan, A. J., Tanvir, N. R., Cenko, S. B., et al. 2011, Science, 333, 199

Levan, A. J., Tanvir, N. R., Starling, R. L. C., et al. 2014, ApJ, 781, 13

Levesque, E. M. 2014, PASP, 126, 1

Levesque, E. M., Berger, E., Kewley, L. J., & Bagley, M. M. 2010a, AJ, 139, 694

Levesque, E. M., Kewley, L. J., Berger, E., & Zahid, H. J. 2010b, AJ, 140, 1557

Levin, Y., Beloborodov, A. M., & Bransgrove, A. 2020, ApJ, 895, L30

Levkov, D. G., Panin, A. G., & Tkachev, I. I. 2020, arXiv e-prints, arXiv:2010.15145

Li, C. K., Lin, L., Xiong, S. L., et al. 2020a, arXiv e-prints, arXiv:2005.11071

Li, C. K., Tuo, Y. L., Ge, M. Y., et al. 2020b, GRB Coordinates Network, 27679, 1

Li, Y., & Zhang, B. 2020, ApJ, 899, L6

Li, Z.-X., Gao, H., Ding, X.-H., Wang, G.-J., & Zhang, B. 2018, Nature Communications, 9, 3833

Lieb, E. H., & Yau, H.-T. 1987, ApJ, 323, 140

Liebendoerfer, M. 2005, JRASC, 99, 140

Lin, L., Zhang, C. F., Wang, P., et al. 2020a, The Astronomer's Telegram, 13697, 1

—. 2020b, Nature, 587, 63

Linder, E. V. 2020, Phys. Rev. D, 101, 103019

Lingam, M., & Loeb, A. 2017, ApJ, 837, L23

Liu, L.-D., Wang, L.-J., Wang, S.-Q., & Dai, Z.-G. 2017a, ArXiv e-prints, arXiv:1706.01783

—. 2018, ApJ, 856, 59

Liu, L.-D., Wang, S.-Q., Wang, L.-J., et al. 2017b, ApJ, 842, 26

Liu, T., Romero, G. E., Liu, M.-L., & Li, A. 2016, ApJ, 826, 82

Liu, Y.-Q., Modjaz, M., & Bianco, F. B. 2017c, ApJ, 845, 85

Loeb, A. 2016, ApJ, 819, L21

Long, K., & Pe'er, A. 2018, ApJ, 864, L12

Lorimer, D. R., Bailes, M., McLaughlin, M. A., Narkevic, D. J., & Crawford, F. 2007, Science, 318, 777

Lu, F. J., Aschenbach, B., & Song, L. M. 2001, A&A, 370, 570

Lu, W., & Kumar, P. 2018, MNRAS, 477, 2470

Lu, W., Kumar, P., & Zhang, B. 2020a, MNRAS, 498, 1397

Lu, W., Piro, A. L., & Waxman, E. 2020b, MNRAS, 498, 1973

Lunnan, R., Chornock, R., Berger, E., et al. 2014, ApJ, 787, 138

—. 2016, ApJ, 831, 144

Lunnan, R., Fransson, C., Vreeswijk, P. M., et al. 2018a, Nature Astronomy, 2, 887

Lunnan, R., Chornock, R., Berger, E., et al. 2018b, ApJ, 852, 81

Luo, R., Men, Y., Lee, K., et al. 2020, MNRAS, 494, 665

Lyman, J. D., Levan, A. J., Tanvir, N. R., et al. 2017, MNRAS, 467, 1795

Lyne, A., Graham-Smith, F., Weltevrede, P., et al. 2013, Science, 342, 598

Lyubarsky, Y. 2014, MNRAS, 442, L9

—. 2020, ApJ, 897, 1

Lyubarsky, Y., & Kirk, J. G. 2001, ApJ, 547, 437

Lyubarsky, Y. E. 2002, MNRAS, 329, L34

—. 2003, MNRAS, 345, 153

Lyutikov, M. 2002, ApJ, 580, L65

Lyutikov, M., Barkov, M. V., & Giannios, D. 2020, ApJ, 893, L39

Lyutikov, M., Burzawa, L., & Popov, S. B. 2016, MNRAS, 462, 941

Lyutikov, M., & Gavriil, F. P. 2006, MNRAS, 368, 690

Lyutikov, M., & Toonen, S. 2019, MNRAS, 487, 5618

MacFadyen, A. I., Ramirez-Ruiz, E., & Zhang, W. 2006, in American Institute of Physics Conference Series, Vol. 836, Gamma-Ray Bursts in the Swift Era, ed. S. S. Holt, N. Gehrels, & J. A. Nousek, 48–53

MacFadyen, A. I., & Woosley, S. E. 1999, ApJ, 524, 262

MacFadyen, A. I., Woosley, S. E., & Heger, A. 2001, ApJ, 550, 410

Macquart, J. P., Prochaska, J. X., McQuinn, M., et al. 2020, Nature, 581, 391

Madhavacheril, M. S., Battaglia, N., Smith, K. M., & Sievers, J. L. 2019, Phys. Rev. D, 100, 103532

Maeda, K., Nakamura, T., Nomoto, K., et al. 2002, ApJ, 565, 405

Maeda, K., Tanaka, M., Nomoto, K., et al. 2007, ApJ, 666, 1069

MAGIC Collaboration, Acciari, V. A., Ansoldi, S., et al. 2019a, Nature, 575, 459

—. 2019b, Nature, 575, 455

Manchester, R., Hobbs, G., Teoh, A., & Hobbs, M. 2005, VizieR Online Data Catalog, 7245, 105

Manchester, R. N. 2007, in American Institute of Physics Conference Series, Vol. 937, Supernova 1987A: 20 Years After: Supernovae and Gamma-Ray Bursters, ed. S. Immler, K. Weiler, & R. McCray, 134–143

Mandea, M., & Balasis, G. 2006, Geophysical Journal International, 167, 586

Mandelstam, S. 1958, Physical Review, 112, 1344

Mann, A. 2017, Proceedings of the National Academy of Science, 114, 3269

Marcote, B., Nimmo, K., Salafia, O. S., et al. 2019, ApJ, 876, L14

Marcote, B., Paragi, Z., Hessels, J. W. T., et al. 2017, ApJ, 834, L8

Marcote, B., Nimmo, K., Hessels, J. W. T., et al. 2020, Nature, 577, 190

Margalit, B., Beniamini, P., Sridhar, N., & Metzger, B. D. 2020a, ApJ, 899, L27

Margalit, B., Berger, E., & Metzger, B. D. 2019, ApJ, 886, 110

Margalit, B., & Metzger, B. D. 2017, ApJ, 850, L19

—. 2018, ApJ, 868, L4

—. 2019, ApJ, 880, L15

Margalit, B., Metzger, B. D., Berger, E., et al. 2018, MNRAS, 481, 2407

Margalit, B., Metzger, B. D., & Sironi, L. 2020b, MNRAS, 494, 4627

Margutti, R., Metzger, B. D., Chornock, R., et al. 2017, ApJ, 836, 25

Margutti, R., Chornock, R., Metzger, B. D., et al. 2018, ApJ, 864, 45

Margutti, R., Metzger, B. D., Chornock, R., et al. 2019, ApJ, 872, 18

Marschall, L. A. 1988, The supernova story

Marshall, F., & Swank, J. H. 2003, GRB Coordinates Network, 1996

Masui, K., Lin, H.-H., Sievers, J., et al. 2015, Nature, 528, 523

Matheson, H., & Safi-Harb, S. 2010, ApJ, 724, 572

Matheson, T., Garnavich, P., Olszewski, E. W., et al. 2003, GRB Coordinates Network, 2120

Matsuura, M., Dwek, E., Meixner, M., et al. 2011, Science, 333, 1258

Matsuura, M., Dwek, E., Barlow, M. J., et al. 2015, ApJ, 800, 50

Mattila, S., Fraser, M., Reynolds, T., et al. 2016, The Astronomer's Telegram, 9308, 1

Maund, J. R., Steele, I., Jermak, H., Wheeler, J. C., & Wiersema, K. 2019, MNRAS, 482, 4057

Maund, J. R., Wheeler, J. C., Patat, F., et al. 2007, MNRAS, 381, 201

Mazets, E., & Golenetskii, S. 1981, Astrophysics and Space Science, 75, 47

Mazets, E., Golenetskii, S., Il'Inskii, V., Guryan, Y. A., et al. 1979

Mazets, E., Golenetskii, S., Il'Inskii, V., et al. 1981, Astrophysics and Space Science, 80, 3

Mazzali, P. A., Sullivan, M., Pian, E., Greiner, J., & Kann, D. A. 2016, MNRAS, 458, 3455

McCray, R. 1993, ARA&A, 31, 175

McCray, R., & Fransson, C. 2016, ARA&A, 54, 19

McKinney, J. C. 2005, ApJ, 630, L5

McKinnon, M., Beasley, A., Murphy, E., et al. 2019, in BAAS, Vol. 51, 81

McMullin, J. P., Waters, B., Schiebel, D., Young, W., & Golap, K. 2007, in Astronomical Society of the Pacific Conference Series, Vol. 376, Astronomical Data Analysis Software and Systems XVI, ed. R. A. Shaw, F. Hill, & D. J. Bell, 127

Meegan, C. A., Fishman, G. J., Wilson, R. B., et al. 1992, Nature, 355, 143

Melikidze, G. I., Gil, J. A., & Pataraya, A. D. 2000, ApJ, 544, 1081

Melrose, D. B. 2017, Reviews of Modern Plasma Physics, 1, 5

Mereghetti, S., Savchenko, V., Ferrigno, C., et al. 2020, ApJ, 898, L29

Merloni, A., Heinz, S., & di Matteo, T. 2003, MNRAS, 345, 1057

Mestel, L. 1966, MNRAS, 133, 265

Mestel, L., & Takhar, H. S. 1972, MNRAS, 156, 419

Meszaros, P., & Rees, M. J. 1993, ApJ, 418, L59

Mészáros, P., & Ventura, J. 1979, Physical Review D, 19, 3565

Metzger, B. D. 2017, Living Reviews in Relativity, 20, 3

Metzger, B. D., Beniamini, P., & Giannios, D. 2018, ApJ, 857, 95

Metzger, B. D., Berger, E., & Margalit, B. 2017, ApJ, 841, 14

Metzger, B. D., & Bower, G. C. 2014, MNRAS, 437, 1821

Metzger, B. D., Giannios, D., Thompson, T. A., Bucciantini, N., & Quataert, E. 2011, MNRAS, 413, 2031

Metzger, B. D., Margalit, B., Kasen, D., & Quataert, E. 2015, MNRAS, 454, 3311

Metzger, B. D., Margalit, B., & Sironi, L. 2019, MNRAS, 485, 4091

Metzger, B. D., Vurm, I., Hascoët, R., & Beloborodov, A. M. 2014, MNRAS, 437, 703

Metzger, B. D., Martínez-Pinedo, G., Darbha, S., et al. 2010, MNRAS, 406, 2650

Micelotta, E. R., Dwek, E., & Slavin, J. D. 2016, A&A, 590, A65

Michanowsky, G. 1977, The once and future star: exploring the mysterious link between the great southern supernova (Vela X) and the origins of civilization.

Michel, F. C. 1988, Nature, 333, 644

Michilli, D., Seymour, A., Hessels, J. W. T., et al. 2018, Nature, 553, 182

Milisavljevic, D., Patnaude, D. J., Chevalier, R. A., et al. 2018, ApJ, 864, L36

Milisavljevic, D., Soderberg, A. M., Margutti, R., et al. 2013, ApJ, 770, L38

Min, M., Hovenier, J. W., & de Koter, A. 2003, in Astrophysics of Dust, 170

Minkowski, R., & Abell, G. 1963, Basic Astronomical Data: Stars and Stellar Systems

Mizuta, A., & Ioka, K. 2013, ApJ, 777, 162

Mochkovitch, R., Hernanz, M., Isern, J., & Martin, X. 1993, Nature, 361, 236

Mockler, B., Guillochon, J., & Ramirez-Ruiz, E. 2019, ApJ, 872, 151

Modjaz, M., Kewley, L., Kirshner, R. P., et al. 2008, AJ, 135, 1136

Mohan, P., An, T., & Yang, J. 2020, ApJ, 888, L24

Mondal, S., Bera, A., Chandra, P., & Das, B. 2020, arXiv e-prints, arXiv:2008.11375

Mooley, K. P., Nakar, E., Hotokezaka, K., et al. 2017, ArXiv e-prints, arXiv:1711.11573

Moriya, T., Tominaga, N., Tanaka, M., Maeda, K., & Nomoto, K. 2010, ApJ, 717, L83

Moriya, T. J., Blinnikov, S. I., Tominaga, N., et al. 2013, MNRAS, 428, 1020

Moriya, T. J., & Langer, N. 2015, A&A, 573, A18

Moriya, T. J., & Maeda, K. 2012, ApJ, 756, L22

Moriya, T. J., Nicholl, M., & Guillochon, J. 2018a, ApJ, 867, 113

Moriya, T. J., Sorokina, E. I., & Chevalier, R. A. 2018b, Space Sci. Rev., 214, 59

Moriya, T. J., Terreran, G., & Blinnikov, S. I. 2018c, MNRAS, 475, L11

Mösta, P., Richers, S., Ott, C. D., et al. 2014, ApJ, 785, L29

Mottez, F., & Zarka, P. 2014, A&A, 569, A86

Mottez, F., Zarka, P., & Voisin, G. 2020, arXiv e-prints, arXiv:2002.12834

Muñoz, J. B., Kovetz, E. D., Dai, L., & Kamionkowski, M. 2016, Phys. Rev. Lett., 117, 091301

Mukherjee, S., Feigelson, E. D., Jogesh Babu, G., et al. 1998, ApJ, 508, 314

Müller, B. 2015, MNRAS, 453, 287

Müller, B. 2017, in IAU Symposium, Vol. 329, The Lives and Death-Throes of Massive Stars, ed. J. J. Eldridge, J. C. Bray, L. A. S. McClelland, & L. Xiao, 17–24

Murase, K., Kashiyama, K., Kiuchi, K., & Bartos, I. 2015, ApJ, 805, 82

Murase, K., Kashiyama, K., & Mészáros, P. 2016, MNRAS, 461, 1498

—. 2017a, MNRAS, 467, 3542

Murase, K., Mészáros, P., & Fox, D. B. 2017b, ApJ, 836, L6

Murase, K., Thompson, T. A., & Ofek, E. O. 2014, MNRAS, 440, 2528

Murase, K., Toma, K., Yamazaki, R., & Mészáros, P. 2011, ApJ, 732, 77

Murase, K., Toma, K., Yamazaki, R., Nagataki, S., & Ioka, K. 2010, MNRAS, 402, L54

Murdin, P., & Murdin, L. 1985, Supernovae (Cambridge University Press)

Murdin, P., & Murdin, L. 2011, Supernovae

Muslimov, A., & Page, D. 1995, ApJ, 440, L77

Muslimov, A. G., & Harding, A. K. 2003, ApJ, 588, 430

Nadyozhin, D. K. 1994, ApJS, 92, 527

Nagakura, H., Iwakami, W., Furusawa, S., et al. 2017, ArXiv e-prints, arXiv:1702.01752

Nakar, E. 2007, Phys. Rep., 442, 166

Nakar, E., & Piran, T. 2011, Nature, 478, 82

—. 2017, ApJ, 834, 28

Nakar, E., Piran, T., & Granot, J. 2002, ApJ, 579, 699

Nakar, E., & Sari, R. 2010, ApJ, 725, 904

Naldi, G., Pilia, M., Bernardi, G., et al. 2020, The Astronomer's Telegram, 13739, 1

Narayan, R., Paczynski, B., & Piran, T. 1992, ApJ, 395, L83

Neill, J. D., Sullivan, M., Gal-Yam, A., et al. 2011, ApJ, 727, 15

Ng, C. Y., Gaensler, B. M., Chatterjee, S., & Johnston, S. 2010, ApJ, 712, 596

Nicholl, M., Berger, E., Blanchard, P. K., Gomez, S., & Chornock, R. 2019, ApJ, 871, 102

Nicholl, M., Berger, E., Margutti, R., et al. 2017a, ApJ, 835, L8

Nicholl, M., Guillochon, J., & Berger, E. 2017b, ApJ, 850, 55

Nicholl, M., & Smartt, S. J. 2016, MNRAS, 457, L79

Nicholl, M., Smartt, S. J., Jerkstrand, A., et al. 2013, Nature, 502, 346

—. 2014, MNRAS, 444, 2096

—. 2015a, ApJ, 807, L18

—. 2015b, MNRAS, 452, 3869

Nicholl, M., Berger, E., Smartt, S. J., et al. 2016a, ApJ, 826, 39

Nicholl, M., Berger, E., Margutti, R., et al. 2016b, ApJ, 828, L18

Nicholl, M., Berger, E., Kasen, D., et al. 2017c, ApJ, 848, L18

Nicholl, M., Blanchard, P. K., Berger, E., et al. 2018, ApJ, 866, L24

Nimmo, K., Marcote, B., Hessels, J. W. T., et al. 2020, The Astronomer's Telegram, 13786, 1

Nomoto, K., Tominaga, N., Umeda, H., Kobayashi, C., & Maeda, K. 2006, Nuclear Physics A, 777, 424

Norris, J., Hertz, P., Wood, K., & Kouveliotou, C. 1991, The Astrophysical Journal, 366, 240

Nozawa, T., & Kozasa, T. 2013, ApJ, 776, 24

Nozawa, T., Kozasa, T., & Habe, A. 2006, ApJ, 648, 435

Nozawa, T., Kozasa, T., Habe, A., et al. 2007, ApJ, 666, 955

Nozawa, T., Kozasa, T., Tominaga, N., et al. 2010, ApJ, 713, 356

Nozawa, T., Kozasa, T., Umeda, H., Maeda, K., & Nomoto, K. 2003, ApJ, 598, 785

Nozawa, T., Maeda, K., Kozasa, T., et al. 2011, ApJ, 736, 45

Nozawa, T., Kozasa, T., Tominaga, N., et al. 2008, ApJ, 684, 1343

Obergaulinger, M., Janka, H.-T., & Aloy, M. A. 2014, MNRAS, 445, 3169

O'Donnell, J. E. 1994, ApJ, 422, 158

Ofek, E. O. 2017, ApJ, 846, 44

Ofek, E. O., Fox, D., Cenko, S. B., et al. 2013, ApJ, 763, 42

Olausen, S., & Kaspi, V. 2014, The Astrophysical Journal Supplement Series, 212, 6

Olive, J. F., Hurley, K., Sakamoto, T., et al. 2004, ApJ, 616, 1148

Omand, C. M. B., Kashiyama, K., & Murase, K. 2018, MNRAS, 474, 573

—. 2019, MNRAS, 484, 5468

Oort, J. H., & van de Hulst, H. C. 1946, Bull. Astron. Inst. Netherlands, 10, 187

Oppenheimer, J. R., & Volkoff, G. M. 1939, Physical Review, 55, 374

Ørum, S. V., Ivens, D. L., Strand berg, P., et al. 2020, A&A, 643, A47

Osterbrock, D. E. 2001, in Bulletin of the American Astronomical Society, Vol. 33, American Astronomical Society Meeting Abstracts, 1330

Ostlie, D. A., & Carroll, B. W. 1996, An Introduction to Modern Stellar Astrophysics

Ostriker, J. P., & Gunn, J. E. 1969, ApJ, 157, 1395

—. 1971, ApJ, 164, L95

Ouyed, R., Kostka, M., Koning, N., Leahy, D. A., & Steffen, W. 2012, MNRAS, 423, 1652

Özel, F., & Freire, P. 2016, ARA&A, 54, 401

Pacini, F. 1967, Nature

—. 1968, Nature, 219, 145

Pacini, F., & Salvati, M. 1973, ApJ, 186, 249

Paczynski, B. 1986, ApJ, 308, L43

—. 1991, Acta Astron., 41, 257

—. 1992, Acta Astron., 42, 145

—. 1997, ArXiv Astrophysics e-prints, astro-ph/9712123

Paczynski, B., & Rhoads, J. E. 1993, ApJ, 418, L5

Page, D., Beznogov, M. V., Garibay, I., et al. 2020, ApJ, 898, 125

Palaniswamy, D., Li, Y., & Zhang, B. 2018, ApJ, 854, L12

Palla, M., Matteucci, F., Calura, F., & Longo, F. 2019, arXiv e-prints, arXiv:1903.01353

Palliyaguru, N., Aggarwal, K., & Agarwal, D. 2020, The Astronomer's Telegram, 13726, 1

Palmer, D. M., Barthelmy, S., Gehrels, N., et al. 2005, Nature, 434, 1107

Palmese, A., Hartley, W., Tarsitano, F., et al. 2017, ApJ, 849, L34

Pan, K.-C., Liebendörfer, M., Hempel, M., & Thielemann, F.-K. 2016, ApJ, 817, 72

Pastorello, A., Smartt, S. J., Botticella, M. T., et al. 2010, ApJ, 724, L16

Patat, F., Cappellaro, E., Danziger, J., et al. 2001, ApJ, 555, 900

Pavlov, G., & Shibanov, Y. A. 1979, Sov. Phys.-JETP (Engl. Transl.);(United States), 49

Pearlman, A. B., Majid, W. A., Prince, T. A., Naudet, C. J., & Kocz, J. 2020a, The Astronomer's Telegram, 13713, 1

Pearlman, A. B., Majid, W. A., Prince, T. A., et al. 2020b, arXiv e-prints, arXiv:2009.13559

Perley, D. A., Quimby, R. M., Yan, L., et al. 2016, ApJ, 830, 13

Perley, D. A., Mazzali, P. A., Yan, L., et al. 2019, MNRAS, 484, 1031

Perley, R. A., Chandler, C. J., Butler, B. J., & Wrobel, J. M. 2011, ApJ, 739, L1

Perley, R. A., Schwab, F. R., & Bridle, A. H. 1989, Synthesis imaging in radio astronomy: a collection of lectures from the third NRAO synthesis imaging summer school, Vol. 6

Perna, R., Soria, R., Pooley, D., & Stella, L. 2008, MNRAS, 384, 1638

Perna, R., & Stella, L. 2004, ApJ, 615, 222

Peterson, B. A., & Price, P. A. 2003, GRB Coordinates Network, 1985

Petroff, E., Hessels, J. W. T., & Lorimer, D. R. 2019, A&A Rev., 27, 4

Petroff, E., Bailes, M., Barr, E. D., et al. 2015, MNRAS, 447, 246

Petroff, E., Barr, E. D., Jameson, A., et al. 2016, PASA, 33, e045

Petropoulou, M., Kamble, A., & Sironi, L. 2016, MNRAS, 460, 44

Phillips, M. M. 1993, ApJ, 413, L105

Phinney, E. S. 1991, ApJ, 380, L17

Pilia, M., Burgay, M., Possenti, A., et al. 2020, ApJ, 896, L40

Pilkington, J., Hewish, A., Bell, S., & Cole, T. 1968, Nature, 218, 126

Piran, T. 2004, Reviews of Modern Physics, 76, 1143

Piro, A. L. 2015, ApJ, 808, L51

—. 2016, ApJ, 824, L32

Piro, A. L., & Kollmeier, J. A. 2017, ArXiv e-prints, arXiv:1710.05822

Planck Collaboration, Ade, P. A. R., Aghanim, N., et al. 2016, A&A, 594, A13

Platts, E., Weltman, A., Walters, A., et al. 2019, Phys. Rep., 821, 1

Pleunis, Z., & CHIME/FRB Collaboration. 2020, The Astronomer's Telegram, 14080, 1

Plotnikov, I., & Sironi, L. 2019, MNRAS, 485, 3816

Pons, J. A., & Geppert, U. 2007, A&A, 470, 303

Pons, J. A., Reddy, S., Prakash, M., Lattimer, J. M., & Miralles, J. A. 1999, ApJ, 513, 780

Pons, J. A., Viganò, D., & Rea, N. 2013, Nature Physics, 9, 431

Pontzen, A., Deason, A., Governato, F., et al. 2010, MNRAS, 402, 1523

Popov, S. B., & Postnov, K. A. 2010a, in Evolution of Cosmic Objects through their Physical Activity, ed. H. A. Harutyunian, A. M. Mickaelian, & Y. Terzian, 129–132

Popov, S. B., & Postnov, K. A. 2010b, in Evolution of Cosmic Objects through their Physical Activity, ed. H. A. Harutyunian, A. M. Mickaelian, & Y. Terzian, 129–132

Porth, O., Komissarov, S. S., & Keppens, R. 2013, MNRAS, 431, L48

Powell, J., & Müller, B. 2020, MNRAS, 494, 4665

Prajs, S., Sullivan, M., Smith, M., et al. 2017, MNRAS, 464, 3568

Prentice, S. J., Maguire, K., Smartt, S. J., et al. 2018, ApJ, 865, L3

Prochaska, J. X., & Zheng, Y. 2019, MNRAS, 485, 648

Prochaska, J. X., Bloom, J. S., Chen, H.-W., et al. 2006, ApJ, 642, 989

Prochaska, J. X., Macquart, J.-P., McQuinn, M., et al. 2019, Science, 366, 231

Quimby, R. M., Aldering, G., Wheeler, J. C., et al. 2007, ApJ, 668, L99

Quimby, R. M., Kulkarni, S. R., Kasliwal, M. M., et al. 2011, Nature, 474, 487

Rabinak, I., & Waxman, E. 2011, ApJ, 728, 63

Rafiei-Ravandi, M., Smith, K. M., & Masui, K. W. 2020, Phys. Rev. D, 102, 023528

Raithel, C. A. 2019, European Physical Journal A, 55, 80

Rajwade, K. M., Mickaliger, M. B., Stappers, B. W., et al. 2020, MNRAS, 495, 3551

Rakavy, G., & Shaviv, G. 1967, ApJ, 148, 803

Ramirez-Ruiz, E., Celotti, A., & Rees, M. J. 2002, MNRAS, 337, 1349

Rane, A., Lorimer, D. R., Bates, S. D., et al. 2016, MNRAS, 455, 2207

Rangelov, B., Pavlov, G. G., Kargaltsev, O., et al. 2016, ApJ, 831, 129

—. 2017, ApJ, 835, 264

Rasmussen, C. E., & Williams, C. K. I. 2006, Gaussian Processes for Machine Learning

Ravi, V. 2019, MNRAS, 482, 1966

Ravi, V., Hallinan, G., & Law, C. J. 2020a, The Astronomer's Telegram, 13693, 1

—. 2020b, The Astronomer's Telegram, 13690, 1

Ravi, V., & Lasky, P. D. 2014, MNRAS, 441, 2433

Ravi, V., Catha, M., D'Addario, L., et al. 2019, Nature, 572, 352

Razin, V. 1957, The dissertation

—. 1960, Izvestiya Vysshikh Uchebnykh Zavedenii. Radiofizika, 584

Rees, M. J., & Gunn, J. E. 1974, MNRAS, 167, 1

Reines, A. E., Greene, J. E., & Geha, M. 2013, ApJ, 775, 116

Remijan, A., Biggs, A., Cortes, P., et al. 2020, ALMA Doc, 8.3

Renault-Tinacci, N., Kotera, K., Neronov, A., & Ando, S. 2018, A&A, 611, A45

Reynolds, S. P. 2017, Dynamical Evolution and Radiative Processes of Supernova Remnants, ed. A. W. Alsabti & P. Murdin, 1981

Reynolds, S. P., & Chevalier, R. A. 1984, ApJ, 278, 630

Rezzolla, L., Most, E. R., & Weih, L. R. 2018, ApJ, 852, L25

Rhoads, J. E. 1997, ApJ, 487, L1

Ridnaia, A., Svinkin, D., Frederiks, D., et al. 2020a, arXiv e-prints, arXiv:2005.11178

Ridnaia, A., Golenetskii, S., Aptekar, R., et al. 2020b, GRB Coordinates Network, 27715, 1

Rivera Sandoval, L. E., Maccarone, T. J., Corsi, A., et al. 2018, MNRAS, 480, L146

Roberts, S., McQuillan, A., Reece, S., & Aigrain, S. 2013, MNRAS, 435, 3639

Romani, R. W. 1996, ApJ, 470, 469

Romani, R. W., & Yadigaroglu, I.-A. 1995, ApJ, 438, 314

Rosswog, S., & Brüggen, M. 2007, Introduction to high-energy astrophysics (Cambridge University Press Cambridge)

Roy, J., Tendulkar, S., Chandra, P., et al. 2020, The Astronomer's Telegram, 13778, 1

Ruderman, M. 1972, ARA&A, 10, 427

Ruderman, M. A., & Sutherland, P. G. 1975, ApJ, 196, 51

Rybicki, G. B., & Lightman, A. P. 1979, Radiative processes in astrophysics

Ryden, B. 2003, Introduction to cosmology

Rykoff, E. S., Aharonian, F., Akerlof, C. W., et al. 2009, ApJ, 702, 489

Saito, S., Tanaka, M., Moriya, T. J., et al. 2020, ApJ, 894, 154

Sandage, A., Saha, A., Tammann, G. A., Panagia, N., & Macchetto, D. 1992, ApJ, 401, L7

Sarangi, A., & Cherchneff, I. 2015, A&A, 575, A95

Sari, R., Piran, T., & Halpern, J. P. 1999, ApJ, 519, L17

Sault, R. J., Hamaker, J. P., & Bregman, J. D. 1996, A&AS, 117, 149

Sault, R. J., & Wieringa, M. H. 1994, A&AS, 108, 585

Savchenko, V., Ferrigno, C., Rodi, J., Mereghetti, S., & Gotz, D. 2020, The Astronomer's Telegram, 14087, 1

Scannapieco, E., Madau, P., Woosley, S., Heger, A., & Ferrara, A. 2005, ApJ, 633, 1031

Schieven, G. 2020, ALMA Doc, 8.1

Schilling, G. 2002, Flash! The Hunt for the Biggest Explosions in the Universe

Schlafly, E. F., & Finkbeiner, D. P. 2011, ApJ, 737, 103

Schnee, S., Enoch, M., Noriega-Crespo, A., et al. 2010, ApJ, 708, 127

Scholz, P., & CHIME/FRB Collaboration. 2020, The Astronomer's Telegram, 13681, 1

Scholz, P., Spitler, L. G., Hessels, J. W. T., et al. 2016, ApJ, 833, 177

Schreier, E., Levinson, R., Gursky, H., et al. 1972, ApJ, 172, L79

Schulze, S., Krühler, T., Leloudas, G., et al. 2018, MNRAS, 473, 1258

Schwab, F. R. 1984, AJ, 89, 1076

Sedov, L. I. 1946, Journal of Applied Mathematics and Mechanics, 10, 241

Shand, Z., Ouyed, A., Koning, N., & Ouyed, R. 2016, Research in Astronomy and Astrophysics, 16, 80

Shannon, R. M., Macquart, J. P., Bannister, K. W., et al. 2018, Nature, 562, 386

Shapiro, S. L., & Teukolsky, S. A. 1983, Black holes, white dwarfs, and neutron stars: The physics of compact objects

Sharma, A. K. 2000, Early Man in Jammu Kashmir and Ladakh (Agam Kala Prakashan)

Shigeyama, T., & Kashiyama, K. 2018, PASJ, 70, 107

Shklovskii, I. S. 1973, Soviet Ast., 16, 749

—. 1976, Soviet Ast., 19, 554

Shklovsky, I. 1967, The Astrophysical Journal, 148, L1

Shu, F. H. 1991, Physics of Astrophysics, Vol. I (University Science Books)

Sibthorpe, B., Ade, P. A. R., Bock, J. J., et al. 2010, ApJ, 719, 1553

Sieniawska, M., & Bejger, M. 2019, Universe, 5, 217

Silvia, D. W., Smith, B. D., & Shull, J. M. 2010, ApJ, 715, 1575

—. 2012, ApJ, 748, 12

Sironi, L., & Spitkovsky, A. 2011, ApJ, 741, 39

Skidmore, W., et al. 2015, Research in Astronomy and Astrophysics, 15, 1945

Skilling, J. 2004, in American Institute of Physics Conference Series, Vol. 735, American Institute of Physics Conference Series, ed. R. Fischer, R. Preuss, & U. V. Toussaint, 395–405

Slane, P. 2017, ArXiv e-prints, arXiv:1703.09311

Smartt, S. J., Chen, T.-W., Jerkstrand, A., et al. 2017, Nature, 551, 75

Smith, M., Sullivan, M., D'Andrea, C. B., et al. 2016, ApJ, 818, L8

Smith, N. 2014, ARA&A, 52, 487

Smith, N., Chornock, R., Li, W., et al. 2008, ApJ, 686, 467

Smith, N., Li, W., Silverman, J. M., Ganeshalingam, M., & Filippenko, A. V. 2011, MNRAS, 415, 773

Smith, N., & McCray, R. 2007, ApJ, 671, L17

Smith, N., Li, W., Foley, R. J., et al. 2007, ApJ, 666, 1116

Smith, N., Rest, A., Andrews, J. E., et al. 2018, MNRAS, 480, 1457

Soares-Santos, M., Holz, D. E., Annis, J., et al. 2017, ApJ, 848, L16

Soderberg, A. M., Frail, D. A., & Wieringa, M. H. 2004, ApJ, 607, L13

Soderberg, A. M., Berger, E., Page, K. L., et al. 2008, Nature, 453, 469

Soglasnov, V. A., Popov, M. V., Bartel, N., et al. 2004, ApJ, 616, 439

Soker, N., Grichener, A., & Gilkis, A. 2019, MNRAS, 484, 4972

Sorokina, E., Blinnikov, S., Nomoto, K., Quimby, R., & Tolstov, A. 2016, ApJ, 829, 17

Spitkovsky, A. 2006, ApJ, 648, L51

Spitler, L. G., Cordes, J. M., Hessels, J. W. T., et al. 2014, ApJ, 790, 101

Spitler, L. G., Scholz, P., Hessels, J. W. T., et al. 2016, Nature, 531, 202

Spruit, H. C. 2002, A&A, 381, 923

Spruit, H. C. 2009, in Cosmic Magnetic Fields: From Planets, to Stars and Galaxies, ed. K. G. Strassmeier, A. G. Kosovichev, & J. E. Beckman, Vol. 259, 61–74

Staelin, D. H., & Reifenstein, III, E. C. 1968, Science, 162, 1481

Stahler, S. W., & Palla, F. 2005, The Formation of Stars, 865

Stanek, K. Z., Matheson, T., Garnavich, P. M., et al. 2003, ApJ, 591, L17

Stella, L., Dall'Osso, S., Israel, G. L., & Vecchio, A. 2005, ApJ, 634, L165

Stephenson, F. R., & Clark, D. H. 1976, Scientific American, 234, 100

Stephenson, F. R., & Green, D. A. 2003, S&T, 105

—. 2005, Journal for the History of Astronomy, 36, 217

Stothers, R. 1977, Isis, 68, 443

Straal, S., Maan, Y., Gelfand, J., van Leeuwen, J., & Kouveliotou, C. 2020, The Astronomer's Telegram, 14151, 1

Sukhbold, T., & Woosley, S. E. 2016, ApJ, 820, L38

Surnis, M., Joshi, B. C., Bagchi, M., et al. 2020a, The Astronomer's Telegram, 13769, 1

—. 2020b, The Astronomer's Telegram, 13777, 1

—. 2020c, The Astronomer's Telegram, 13799, 1

Suzuki, A., & Maeda, K. 2017, MNRAS, 466, 2633

—. 2018, MNRAS, 478, 110

—. 2019, ApJ, 880, 150

Tabor, E., & Loeb, A. 2020, ApJ, 902, L17

Taggart, K., & Perley, D. 2019, arXiv e-prints, arXiv:1911.09112

Takahashi, K., Yoshida, T., Umeda, H., Sumiyoshi, K., & Yamada, S. 2016, MNRAS, 456, 1320

Takaki, K., Kawabata, K. S., Yamanaka, M., et al. 2013, ApJ, 772, L17

Tan, C. M., & Chime/Pulsar Collaboration. 2020, The Astronomer's Telegram, 13838, 1

Tanabashi, M., Hagiwara, K., Hikasa, K., et al. 2018, Phys. Rev. D, 98, 030001

Tanaka, M., Kawabata, K. S., Hattori, T., et al. 2012, ApJ, 754, 63

Tanaka, M., Utsumi, Y., Mazzali, P. A., et al. 2017, PASJ, 69, 102

Tanaka, S. J. 2017, in Journal of Physics Conference Series, Vol. 932, Journal of Physics Conference Series, 012052

Tanaka, S. J., & Takahara, F. 2010, ApJ, 715, 1248

—. 2013, MNRAS, 429, 2945

Tananbaum, H., Gursky, H., Kellogg, E. M., et al. 1972, ApJ, 174, L143

Tanvir, N. R., Levan, A. J., Fruchter, A. S., et al. 2013, Nature, 500, 547

Tauris, T. M., Langer, N., & Podsiadlowski, P. 2015, MNRAS, 451, 2123

Tauris, T. M., & Manchester, R. N. 1998, MNRAS, 298, 625

Tavani, M., Casentini, C., Ursi, A., et al. 2020a, arXiv e-prints, arXiv:2005.12164

Tavani, M., Verrecchia, F., Casentini, C., et al. 2020b, ApJ, 893, L42

Taylor, G. B., Carilli, C. L., & Perley, R. A. 1999, Astronomical Society of the Pacific Conference Series, 180

Tchekhovskoy, A., Spitkovsky, A., & Li, J. G. 2013, MNRAS, 435, L1

Temim, T., Dwek, E., Arendt, R. G., et al. 2017, ApJ, 836, 129

Temim, T., Slane, P., Arendt, R. G., & Dwek, E. 2012a, ApJ, 745, 46

Temim, T., Slane, P., Reynolds, S. P., Raymond, J. C., & Borkowski, K. J. 2010, ApJ, 710, 309

Temim, T., Sonneborn, G., Dwek, E., et al. 2012b, ApJ, 753, 72

Tendulkar, S. P., Kaspi, V. M., & Patel, C. 2016, arXiv:1602.02188, arXiv:1602.02188

Tendulkar, S. P., Bassa, C. G., Cordes, J. M., et al. 2017, ApJ, 834, L7

Tendulkar, S. P., Gil de Paz, A., Kirichenko, A. Y., et al. 2020, arXiv e-prints, arXiv:2011.03257

Terasawa, T., Tanaka, Y. T., Takei, Y., et al. 2005, Nature, 434, 1110

Terreran, G., Pumo, M. L., Chen, T.-W., et al. 2017, Nature Astronomy, 1, 713

The CHIME/FRB Collaboration, Andersen, B. C., Bandura, K. M., Bhardwaj, M., et al. 2020, Nature, 587, 54

Thielemann, F.-K., Hashimoto, M.-A., & Nomoto, K. 1990, ApJ, 349, 222

Thirumalai, A., & Heyl, J. S. 2009, Physical Review A, 79, 012514

Thompson, C., & Duncan, R. C. 1993, ApJ, 408, 194

Thompson, C., & Duncan, R. C. 1995, Monthly Notices of the Royal Astronomical Society, 275, 255

Thompson, C., & Duncan, R. C. 1995, MNRAS, 275, 255

Thompson, C., & Duncan, R. C. 1996, The Astrophysical Journal, 473, 322

—. 2001, The Astrophysical Journal, 561, 980

Thompson, C., Lyutikov, M., & Kulkarni, S. 2002, The Astrophysical Journal, 574, 332

Thompson, T. A., Burrows, A., & Meyer, B. S. 2001, ApJ, 562, 887

Thompson, T. A., Chang, P., & Quataert, E. 2004, ApJ, 611, 380

Thornton, D., Stappers, B., Bailes, M., et al. 2013, Science, 341, 53

Timokhin, A. N., & Harding, A. K. 2015, ApJ, 810, 144

Todini, P., & Ferrara, A. 2001, MNRAS, 325, 726

Tohuvavohu, A. 2020a, The Astronomer's Telegram, 13748, 1

—. 2020b, The Astronomer's Telegram, 13758, 1

—. 2020c, The Astronomer's Telegram, 14075, 1

—. 2020d, The Astronomer's Telegram, 14076, 1

Tolman, R. C. 1939, Physical Review, 55, 364

Tolstov, A., Nomoto, K., Blinnikov, S., et al. 2017a, ApJ, 835, 266

Tolstov, A., Zhiglo, A., Nomoto, K., et al. 2017b, ApJ, 845, L2

Tong, H., & Yu, C. 2017, ArXiv e-prints, arXiv:1711.06593

Tonry, J., Denneau, L., Heinze, A., et al. 2018a, Transient Name Server Discovery Report, 2018-1680, 1

—. 2018b, Transient Name Server Discovery Report, 2018-1722, 1

Torres, D. F., Cillis, A., Martín, J., & de Oña Wilhelmi, E. 2014, Journal of High Energy Astrophysics, 1, 31

Torres-Forné, A., Cerdá-Durán, P., Pons, J. A., & Font, J. A. 2016, MNRAS, 456, 3813

Totani, T. 2013, PASJ, 65, arXiv:1307.4985

Totani, T., & Panaitescu, A. 2002, ApJ, 576, 120

Troja, E., Cusumano, G., O'Brien, P. T., et al. 2007, ApJ, 665, 599

Truelove, J. K., & McKee, C. F. 1999, ApJS, 120, 299

Tsytovich, V. 1951, Vestn. Mosk. Univ. Ser. Phys., 11, 27

Umeda, H., & Nomoto, K. 2008, ApJ, 673, 1014

Urata, Y., Huang, K., Yamazaki, R., & Sakamoto, T. 2015, ApJ, 806, 222

Usov, V. 1996, arXiv preprint astro-ph/9612091

Usov, V. V. 1992, Nature, 357, 472

Usov, V. V., & Melrose, D. B. 1995, Australian Journal of Physics, 48, 571

Utsumi, Y., Tanaka, M., Tominaga, N., et al. 2017, PASJ, 69, 101

Valenti, S., David, Sand, J., et al. 2017, ApJ, 848, L24

van der Horst, A. J., Kouveliotou, C., Gorgone, N. M., et al. 2012, ApJ, 749, 122

van der Swaluw, E. 2003, A&A, 404, 939

Van Der Swaluw, E., Achterberg, A., & Gallant, Y. A. 1998, Mem. Soc. Astron. Italiana, 69, 1017

van der Swaluw, E., Achterberg, A., Gallant, Y. A., & Tóth, G. 2001, A&A, 380, 309

van der Swaluw, E., Downes, T. P., & Keegan, R. 2004, A&A, 420, 937

van Gorkom, J. H., Knapp, G. R., Raimond, E., Faber, S. M., & Gallagher, J. S. 1986, AJ, 91, 791 van Paradijs, J., Groot, P. J., Galama, T., et al. 1997, Nature, 386, 686

Vandenbroucke, J. 2020, The Astronomer's Telegram, 13689, 1

Vanderspek, R., Crew, G., Doty, J., et al. 2003, GRB Coordinates Network, 1997

Venter, C., & de Jager, O. C. 2007, in WE-Heraeus Seminar on Neutron Stars and Pulsars 40 years after the Discovery, ed. W. Becker & H. H. Huang, 40

Vietri, M., & Stella, L. 1998, ApJ, 507, L45

Villar, V. A., Berger, E., Metzger, B. D., & Guillochon, J. 2017a, ApJ, 849, 70

Villar, V. A., Guillochon, J., Berger, E., et al. 2017b, ApJ, 851, L21

Vink, J., Bleeker, J., van der Heyden, K., et al. 2006, ApJ, 648, L33

Vinko, J., Zheng, W., Pandey, S. B., et al. 2012, in American Astronomical Society Meeting Abstracts, Vol. 219, American Astronomical Society Meeting Abstracts #219, 436.04

Virgili, F. J., Liang, E.-W., & Zhang, B. 2009, MNRAS, 392, 91

Virgili, F. J., Mundell, C. G., Pal'shin, V., et al. 2013, ApJ, 778, 54

Vlasis, A., Dessart, L., & Audit, E. 2016, MNRAS, 458, 1253

Vreeswijk, P., Tanvir, N., & Galama, T. 2000, The Newsletter of the Isaac Newton Group of Telescopes, 2, 5

Vreeswijk, P. M., Savaglio, S., Gal-Yam, A., et al. 2014, ApJ, 797, 24

Vreeswijk, P. M., Leloudas, G., Gal-Yam, A., et al. 2017, ApJ, 835, 58

Wadiasingh, Z., Beniamini, P., Timokhin, A., et al. 2020, ApJ, 891, 82

Wadiasingh, Z., & Timokhin, A. 2019, ApJ, 879, 4

Wang, L., Howell, D. A., Höflich, P., & Wheeler, J. C. 2001, ApJ, 550, 1030

Wang, M.-H., Ai, S.-K., Li, Z.-X., et al. 2020, ApJ, 891, L39

Wang, S.-Q., Wang, L.-J., & Dai, Z.-G. 2019a, Research in Astronomy and Astrophysics, 19, 063

Wang, S. Q., Wang, L. J., Dai, Z. G., & Wu, X. F. 2015, ApJ, 807, 147

Wang, X.-Y., Liu, R.-Y., Zhang, H.-M., Xi, S.-Q., & Zhang, B. 2019b, ApJ, 884, 117

Watanabe, S., & Opper, M. 2010, Journal of machine learning research, 11

Watts, A. L., Kouveliotou, C., van der Horst, A. e. J., et al. 2010, ApJ, 719, 190

Watts, A. L., Andersson, N., Chakrabarty, D., et al. 2016, Reviews of Modern Physics, 88, 021001

Waxman, E. 2017, ApJ, 842, 34

Waxman, E., & Draine, B. T. 2000, ApJ, 537, 796

Waxman, E., & Mészáros, P. 2003, ApJ, 584, 390

Weber, F., Negreiros, R., Rosenfield, P., & Stejner, M. 2007, Progress in Particle and Nuclear Physics, 59, 94

Wesson, R., Barlow, M. J., Matsuura, M., & Ercolano, B. 2015, MNRAS, 446, 2089

Whalen, D. J., Smidt, J., Heger, A., et al. 2014, ApJ, 797, 9

Wheeler, J. C., & Akiyama, S. 2010, New A Rev., 54, 183

Wheeler, J. C., Yi, I., Höflich, P., & Wang, L. 2000, ApJ, 537, 810

Wijers, R. A. M. J., & Galama, T. J. 1999, ApJ, 523, 177

Williams, P. K. G., Clavel, M., Newton, E., & Ryzhkov, D. 2017, pwkit: Astronomical utilities in Python, ascl:1704.001

Wilner, D., & ngVLA Key Science Goal 1 Science Team. 2020, in American Astronomical Society Meeting Abstracts, American Astronomical Society Meeting Abstracts, 364.14

Winkler, P. F., Gupta, G., & Long, K. S. 2003, The Astrophysical Journal, 585, 324

Winterberg, F. 2001, Zeitschrift Naturforschung Teil A, 56, 889

Wolszczan, A., Prószyński, M., Graham, D. A., & Wright, G. A. E. 1984, in BAAS, Vol. 16, Bulletin of the American Astronomical Society, 728

Wooden, D. H., Rank, D. M., Bregman, J. D., et al. 1993, ApJS, 88, 477

Woods, P. M., Kouveliotou, C., van Paradijs, J., et al. 1999, The Astrophysical Journal Letters, 519, L139

Woosley, S. E. 1993, ApJ, 405, 273

—. 2010, ApJ, 719, L204

—. 2017, ApJ, 836, 244

Woosley, S. E., & Bloom, J. S. 2006, ARA&A, 44, 507

Woosley, S. E., Eastman, R. G., & Schmidt, B. P. 1999, ApJ, 516, 788

Woosley, S. E., Hartmann, D. H., Hoffman, R. D., & Haxton, W. C. 1990, ApJ, 356, 272

Woosley, S. E., & Haxton, W. C. 1988, Nature, 334, 45

Woosley, S. E., Pinto, P. A., & Weaver, T. A. 1988, Proceedings of the Astronomical Society of Australia, 7, 355

Wucknitz, O., Spitler, L. G., & Pen, U. L. 2020, arXiv e-prints, arXiv:2004.11643

Wyrzykowski, L., & Gromadzki, M. 2017, Transient Name Server Discovery Report, 2017-1442, 1

Wyrzykowski, L., Kostrzewa-Rutkowska, Z., Klencki, J., et al. 2015, The Astronomer's Telegram, 8485, 1

Xu, S., & Zhang, B. 2020, ApJ, 898, L48

Yamasaki, S., Kashiyama, K., & Murase, K. 2020a, arXiv e-prints, arXiv:2008.03634

Yamasaki, S., Kisaka, S., Terasawa, T., & Enoto, T. 2019, MNRAS, 483, 4175

Yamasaki, S., Lyubarsky, Y., Granot, J., & Göğüş, E. 2020b, MNRAS, 498, 484

Yamasaki, S., Totani, T., & Kiuchi, K. 2020c, arXiv e-prints, arXiv:2010.07796

Yamazaki, R., Ioka, K., & Nakamura, T. 2002, ApJ, 571, L31

—. 2003, ApJ, 593, 941

Yan, L., Quimby, R., Ofek, E., et al. 2015, ApJ, 814, 108

Yan, L., Lunnan, R., Perley, D. A., et al. 2017, ApJ, 848, 6

Yang, H., & Zou, Y.-C. 2020, ApJ, 893, L31

Yang, Y.-P., & Zhang, B. 2018, ApJ, 868, 31

Yang, Y.-P., Zhang, B., & Dai, Z.-G. 2016, ApJ, 819, L12

Yang, Y.-P., Zhu, J.-P., Zhang, B., & Wu, X.-F. 2020, ApJ, 901, L13

Yaron, O., & Gal-Yam, A. 2012, PASP, 124, 668

Yasuda, Y., & Kozasa, T. 2012, ApJ, 745, 159

Yoon, S. C., Dierks, A., & Langer, N. 2012, A&A, 542, A113

Yoon, S.-C., Woosley, S. E., & Langer, N. 2010, ApJ, 725, 940

Younes, G., Baring, M. G., Kouveliotou, C., et al. 2020, arXiv e-prints, arXiv:2006.11358

Yuan, Y., Beloborodov, A. M., Chen, A. Y., & Levin, Y. 2020, ApJ, 900, L21

Yusof, N., Hirschi, R., Meynet, G., et al. 2013, MNRAS, 433, 1114

Zanazzi, J. J., & Lai, D. 2020, ApJ, 892, L15

Zavlin, V. E., Pavlov, G. G., Sanwal, D., & Trümper, J. 2000, ApJ, 540, L25

Zeilik, M., & van Panhuys Smith, E. 1987, Philadelphia: Saunders College Pub., c1987. 2nd ed., 1

Zhang, B. 2014, ApJ, 780, L21

—. 2016, ApJ, 827, L31

—. 2017, ApJ, 836, L32

—. 2019, Nature, 575, 448

—. 2020a, Nature, 587, 45

—. 2020b, Nature, 582, 344

Zhang, B., & Mészáros, P. 2001, ApJ, 552, L35

Zhang, C. F., Jiang, J. C., Men, Y. P., et al. 2020a, The Astronomer's Telegram, 13699, 1

Zhang, S. N., Li, X. B., Li, C. K., et al. 2020b, The Astronomer's Telegram, 13729, 1

Zhang, W., Woosley, S. E., & MacFadyen, A. I. 2003, ApJ, 586, 356

Zhao, F.-Y., Strom, R. G., & Jiang, S.-Y. 2006, Chinese J. Astron. Astrophys., 6, 635

Zhou, B., Li, X., Wang, T., Fan, Y.-Z., & Wei, D.-M. 2014, Phys. Rev. D, 89, 107303

Zhou, P., Vink, J., Safi-Harb, S., & Miceli, M. 2019, A&A, 629, A51

Zhu, W., Wang, B., Zhou, D., et al. 2020, The Astronomer's Telegram, 14084, 1